IMPERIAL COLLEGE, LONDON

THEORY BASED ON DEVICE CURRENT CLIPPING TO EXPLAIN AND PREDICT PERFORMANCE INCLUDING DISTORTION OF POWER AMPLIFIERS FOR WIRELESS COMMUNICATION SYSTEMS

A dissertation submitted in partial satisfaction of the

requirements for the degree Doctor of Philosophy

in

Electrical & Electronic Engineering

Circuits and Systems Group

by

YunJia Tian

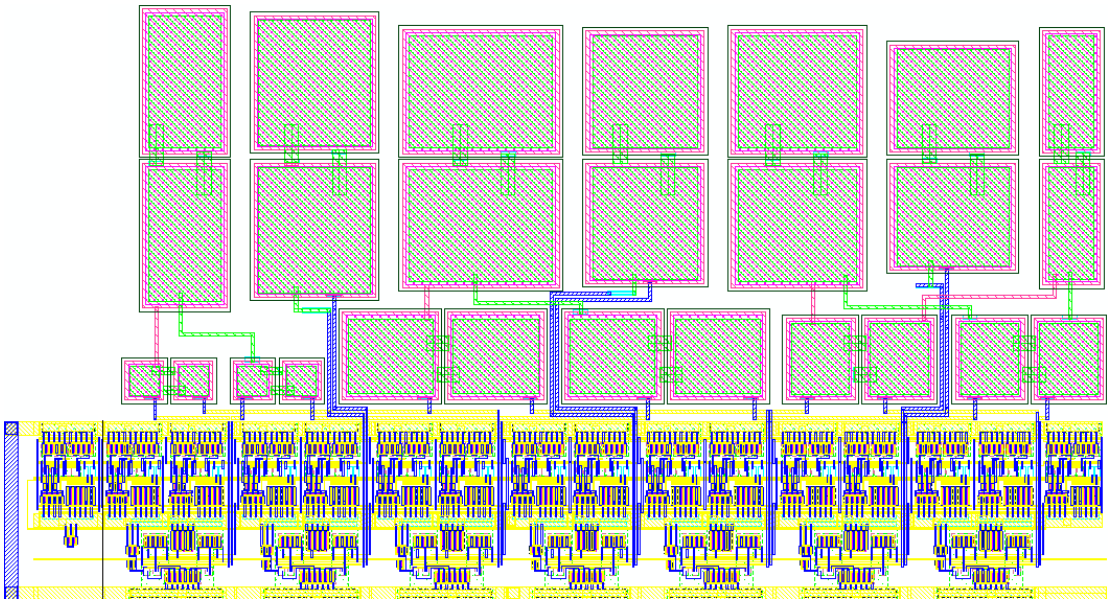

Layout of first filter chip for wireless communication systems designed for Lime Microsystems to fund the work described in this thesis.

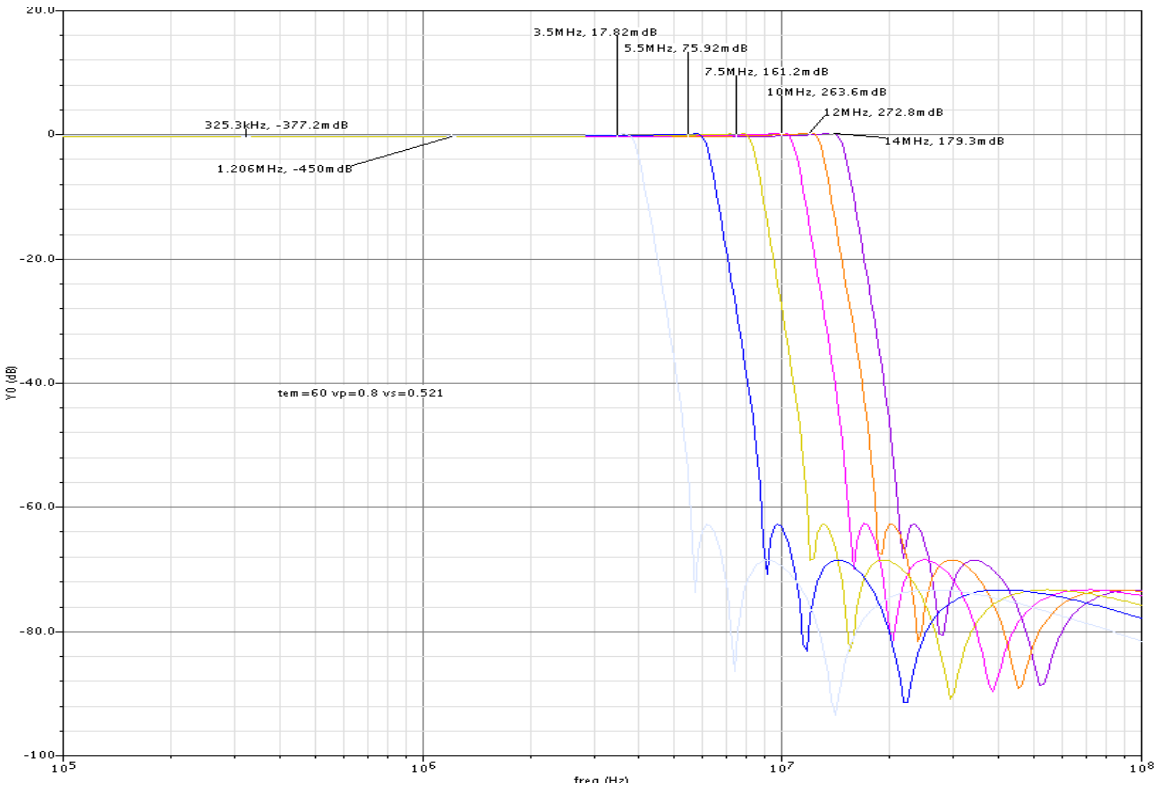

Simulation of second filter chip fully extracted from layout showing wide-range programming of cut-off frequency.

For my Mum, Dad, Brother and Sister

& 给我的父母，兄长和姐姐 &

ABSTRACT

Power amplifiers are critical components in wireless communication systems that need to have high efficiency, in order to conserve battery life and minimise heat generation, and at the same time low distortion, in order to prevent increase of bit error rate due to constellation errors and adjacent channel interference. This thesis is aimed at meeting a need for greater understanding of distortion generated by power amplifiers of any technology, in order to help designers manage better the trade-off between obtaining high efficiency and low distortion. The theory proposed in this thesis to explain and predict the performance of power amplifiers, including distortion, is based on analysis of clipping of the power amplifier device current, and it is a major extension of previous clipping analyses, that introduces many key definitions and concepts. Distortion and other power amplifier metrics are determined in the form of 3-D surfaces that are plotted against PA class, which is determined by bias voltage, and input signal power level. It is shown that the surface of distortion exhibits very high levels due to clipping in the region where efficiency is high. This area of high distortion is intersected by a valley that is 'L'-shaped. The 'L'-shaped valley is subject to a rotation that depends on the softness of the cut-off of the power amplifier device transfer characteristic. The distortion surface with rotated 'L'-shaped valley leads to predicted curves for distortion versus input signal power that match published measured curves for power amplifiers even using very simple device models. The distortion versus input signal power curves have types that are independent of technology. In class C, there is a single deep null. In the class AB range, that is divided into three sub-ranges, there may be two deep nulls (sub-range AB(B)), a ledge (sub-range AB(A)) or a shallow null with varying depth (sub-range AB(AB)).

ACKNOWLEDGEMENTS

It is my great pleasure to take this opportunity to appreciate everyone who made this thesis possible.

First and foremost, I would like to express my sincere gratitude and appreciation to my supervisor Dr. David G Haigh for his continuous and invaluable guidance, support inspiration and encouragement during my research study. Dr. Haigh's knowledge and dedication on research influence and inspire me to become a good researcher.

Special thanks to Danny Webster for his advice on the power amplifier work. His knowledge and industrial experience really broadens the project and inspires more thought.

I appreciate the opportunity of cooperating with Professor Yasuhiro Sugimoto. I would thank Dr. Tom Clarks for his advice on the transmission line driver project and the load line project. I appreciate Assad Borjak for his valuable advice on filter design and patient support on VLSI circuit layout.

I would like to thank Ebrahim Bushehri and Lime Microsystems Ltd for finical support. I also thank Lime Microsystems Ltd for their technology support that meant that we finished the low pass filter project on time. I also appreciated the finical support from Bob Brewer of Analogue Devices (UK).

A special round of thanks goes to my colleagues who gave me lot of support on academic matters and Cadence. I would especially like to acknowledge: Francesco Cannillo, Sofia Vatti and Xu Min.

YunJia Tian

April, 2008

TABLE OF CONTENT

LIST OF FIGURES

LIST OF TABLES

LIST OF ABBREVIATIONS

ACI	Adjacent channel interference
ACPR	Adjacent channel power ratio
BER	Bit error rate
C/I	Carrier-to-interference ratio
ECA	Effective conduction angle
EVM	Error vector magnitude
FPP	Full power point
FPCA	Full power conduction angle
IMD	Intermodulation distortion
IMD3	3rd order intermodulation distortion
PA	Power amplifier
R0	No clipping region
R1	Single clipping region
R2	Double clipping region
Rf	Full clipping region
SNR	Signal to noise ratio
2-D	Two dimension
3-D	Three dimension

LIST OF SYMBOLS

α	Cut-off clipping angle
β	Knee clipping angle
C_D	Resonate capacitor to povide a low impedance at harmonic frequencies
C_G	Coupling capacitor
C_L	Capacitor to provide current to the load resistors
G	Transconductance of the linear model
η	Drain efficiency
η_{PA}	Power added efficiency
i_D	Drain current
i_{DL}	A limit value of drain current
i_L	Current flow to the load resistors
K	Tranconducatnce of the suqre law model
L_D	Resonate inductor to provide device bias current.
L_G	Inductor for gate bias voltage
P_{DC}	DC power
P_{in}	Input power
P_{out}	Output power
γ	Conduction angle
γ_F	Full power conduction angle
γ_{FT1}	The first transition FPCA
γ_{FT2}	The second transition FPCA
R_L	Load resistor
v_D	Drain voltage
V_{GG}	Gate bias voltage
V_{GGe}	Effective gate bias voltage
v_G	Gate input signal
$\hat{v}_G$	Input signal amplitude

v_{GC}	Clipped input voltage
$\hat{v}_{GC}$	Clipped input voltage amplitude
v_{GCmax}	Maximum clipped input voltage
v_{GCmin}	Minimum clipped input voltage
v_{GL}	Limit value of input voltage
v_{in}	Input signal
v_L	Voltage on load resistors
V_T	Device threshold voltage
V_{TE}	Effective threshold voltage

CHAPTER 1

INTRODUCTION

1.1. Wireless Communication Systems

The development of wireless communication is proceeding rapidly. Systems such as Wi-Fi based on CDMA (Code Division Multiple Access) [1][2], mobile phone based on GSM (Global System for Mobile Communication) [3][4] and mobile multimedia unit based on today's 3G and future 4G [5] − [8] wireless systems are being developed. This constantly growing market drives an intense effort to develop improved wireless standards and system architectures, as well as reduce implementation costs by using low-cost technologies and higher level of integration. These systems contain a wireless transmitter and receiver that are called transceiver. A highly integrated transceiver system in one integrated circuit chip is called for in order to minimize cost and reduce size.

The block diagram of a typical transceiver with transmitter and receiver chains is shown in Figure 1.1 [9] − [13]. All of the blocks shown are challenging analogue designs and are the subject of much current research, including low noise amplifier [9] − [16], variable gain amplifier (VGA) [17] − [19], mixers [9][14][20][21], transmitter and receiver low pass filters [9] − [13][22], switch [9][10][23], frequency synthesiser [9][10], power amplifier [9] − [16][21][24] − [47] and ADC-DAC [9][10][48] − [50]. The power amplifier is the subject of study in this thesis.

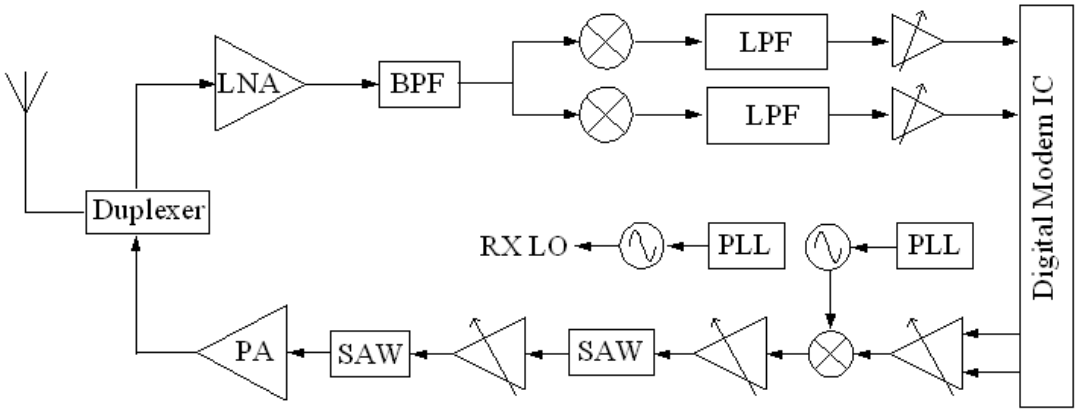

Figure 1.1 Typical architecture of wireless transceiver [9] − [13].

1.2. Power Amplifier Requirements

The essence of the function of the power amplifier (PA), as shown for example in Figure 1.1, is to convert DC power from the battery or power supply into RF power in the antenna. The power amplifier is usually the most power hungry block in the transmitter, and therefore it is crucial to design it in order to preserve battery life and minimize heat generation. This can be achieved by designing the PA to have maximum efficiency, which may be defined as the ratio of power delivered to load to DC power consumption [47][51] − [54] [1].

$$\eta = \frac{P_{out}}{P_{DC}} \tag{1.1}$$

Power amplifiers are classified into different categories. The maximum efficiency is one of common methods [24][47]. Bias voltage and conduction angle [15][24][47] [52][53] are also used to classify PAs. This will be reviewed briefly in the next sub-section.

[1] The efficiency defined in (1.1) is *drain efficiency*. Efficiency is often defined as *power added efficiency*, $\eta_{PA} = \frac{P_{out} - p_{in}}{P_{DC}} = \eta\left(1 - G^{-1}\right)$, where P_{in} is input power and gain $G = P_{out}/P_{in}$.

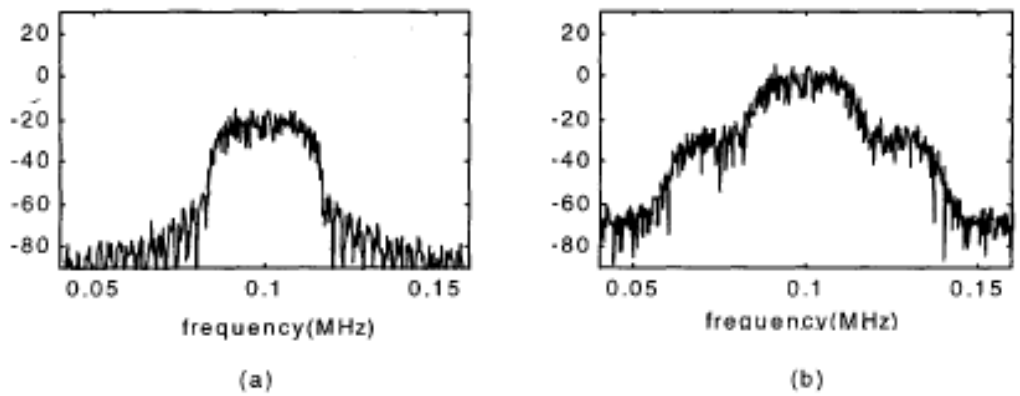

Figure 1.2 (a) input power spectrum; (b) output power spectrum showing 3rd and 5th order distortion [65].

Recently, many wireless communication systems adopt sophisticated modulation schemes such as QAM (Quadrature amplitude modulation) [55] − [57], QPSK (Quadrature Phase Shift Keying) [58] − [60], and BPSK (Binary Phase Shift Keying) [61][62] for high spectral efficiency and channel capacity in an environment of growing demand on available spectrum [63]. However, these modulation formats have signals with highly time-varying envelopes with high peak-to-average ratio [64]. With such a signal, nonlinearity in the PA, which is inevitable since the PA is based on a device that is nonlinear, has two very serious effects on system performance.

Adjacent channel interference (ACI) is caused by 3rd and higher odd order intermodulation distortion (IMD[2]) products generated by the tones comprised of a modulated spectrum [47][54][65] − [70]. For the signal at the input of the PA, only the RF band signal exists, as shown in Figure 1.2(a) [65]. 3rd and 5th order intermodulation distortion products generated by PA nonlinearity cause adjacent channel interference in the PA output signal, as shown in Figure 1.2(b) [65]. Adjacent channel power channel power ratio (ACPR) is used to specify ACI, which quantifies out-of-band interference of wireless handsets [54][65][70]. ACI reduces the signal-to-noise ratio (SNR) for the adjacent channel, thus increasing the bit error rate (BER) [71] − [73]. In order to prevent unacceptable level of interference between adjacent channels, wireless communication systems specify strict requirements on power transmitted into adjacent channels [47][54][65][70].

[2] IMD is defined to be the sideband components at mixing frequency[47].

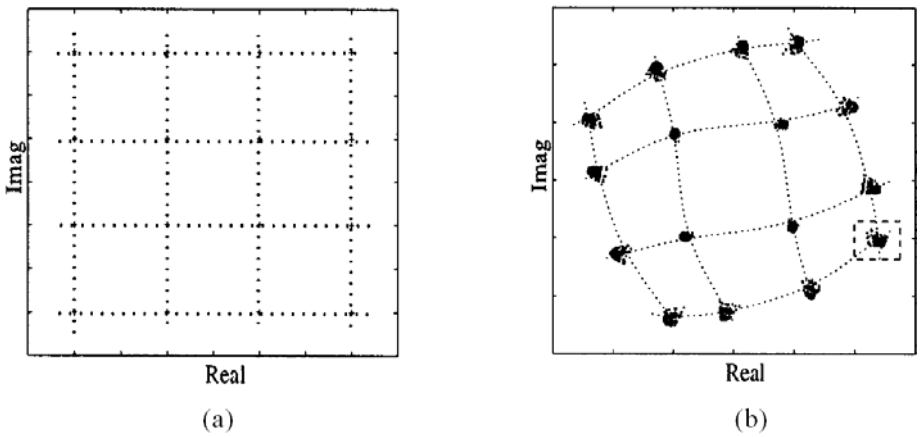

Figure 1.3 (a) Original symbol constellation; (b) Received Symbol constellation with effect of nonlinear distortion [69].

Third order distortion in the PA also results in constellation errors. The symbol constellation for a signal in a system before the PA [69] is shown in Figure 1.3(a). 3rd order non-linearity in the PA causes signal amplitude-dependent changes in PA gain and phase that corrupt the constellation as shown in Figure 1.3(b) [69]. This in-band distortion effect increases BER and is quantified using error vector magnitude (EVM) [47][54][65][69][70].

Thus it is vitally important that PAs have simultaneously high efficiency and high linearity. Unfortunately these two requirements are contradictory. This leads to a trade-off which has been the subject of much study [74]. The PA is now looked at in more detail.

1.3. Power Amplifier Circuit and Performance Overview

The basic circuit of a power amplifier is shown in Figure 1.4 [67][75]. The PA is based around a device that is shown here as a field effect transistor, with input voltage v_G, output voltage v_D and output current i_D. The input signal v_{in} is coupled to the input terminal of the device via coupling capacitor C_G. Inductor L_G supplies the input signal bias voltage V_{GG} that defines the class of operation for the PA [15][47][52][53]. The output terminal of the device is coupled to load resistor R_L and biased from supply voltage V_{DD} via a bias/matching circuit that may take several

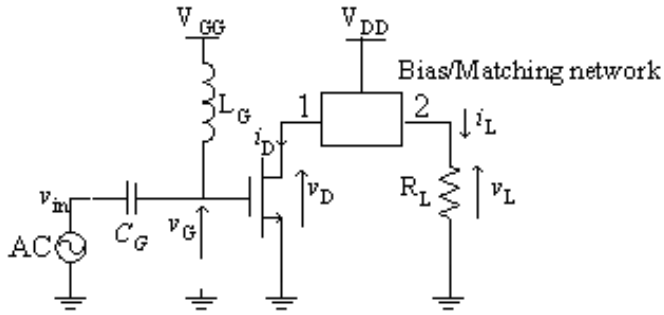

Figure 1.4 Schematic of PA with bias/matching networks [67][75].

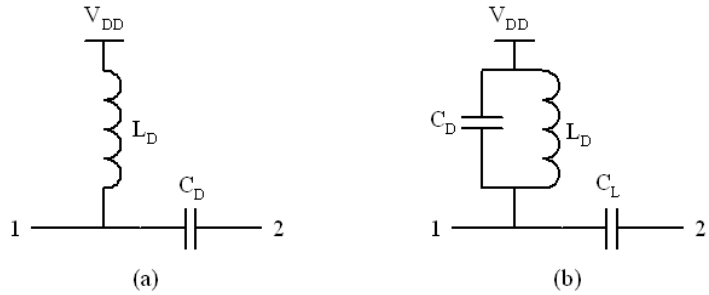

Figure 1.5 Bias/matching circuits, (a) simple; (b) tuned [54][76].

different forms. Two common forms for the bias/matching circuit are shown in Figure 1.5 [54][76]. In the simple circuit in Figure 1.5(a), the device output signal is coupled to the load resistor via C_D and inductor L_D provides bias current for the device output terminal [54][76]. In the circuit in Figure 1.5(b), L_D and C_D are designed to resonate in the PA operating frequency band to provide high impedance, but C_D provides low impedance at harmonic frequencies [76] and L_D provides device bias current.

The device in the PA schematic of Figure 1.4 may be described by

$$i_D = f\left(v_G, v_D\right) \tag{1.2}$$

This relationship is usually expressed in the form of a set of device output characteristics, as shown in Figure 1.6 [75], where i_D is plotted against v_D for a set of values of v_G. Assuming ideal bias elements in Figure 1.4 ($L \rightarrow \infty$, $C \rightarrow \infty$), the effective value of the load resistor in Figure 1.4, as seen at the output terminal of the device, may be represented by a linear relation and this may be represented in Figure 1.6 as a load line. The value of V_{DD} in Figure 1.4 affects the position of the load line

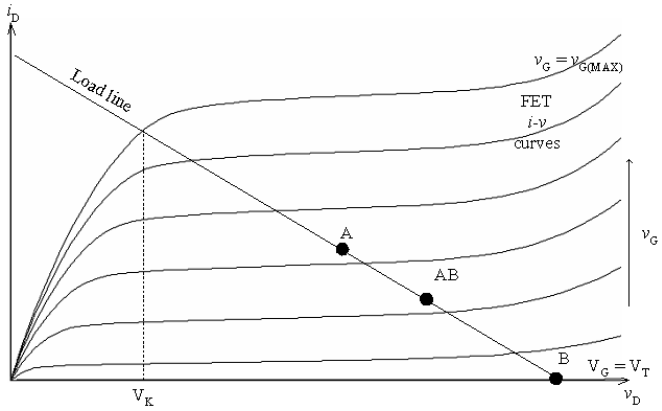

Figure 1.6 Device *i* −*v* curves load line and operation points for Class A, AB and B [75].

and the effective load resistance as seen at the output terminal of the device affects its slope. The value of V_{GG} in Figure 1.4 determines the position of the quiescent or bias operating point on the load line. In response to the time dependent variation of the input signal v_{in} in Figure 1.4, the dynamic operating point moves periodically up and down the load line about the quiescent operating point.

The class of a PA is governed by the quiescent operating point that is set by V_{GG} in Figure 1.4 and is designated by one or more letters. A number of cases are marked in Figure 1.6. For Class A operation, the operating point is in the middle of the load line. For Class B, the operating point is at the bottom of the load line where the device output current just reaches zero [47][54]. The device input voltage v_G that makes the output current just zero is called the threshold voltage V_T. So Class B operation is obtained for $V_{GG} = V_T$. PAs with operating points between those for Class A and B are designated Class AB [47][54], which is an operation range. Another class of PA is Class C [47][54]. For Class C, the quiescent operation point is set by putting V_{GG} below V_T. Since at this quiescent point, i_D is zero, in the load line representation in Figure 1.6 the Class C operating point is on top of the Class B operating point and cannot be distinguished from it. In order to do that, we can generalise the representation in Figure 1.6 into three dimensions as proposed by the author in [75].

The $i - v$ curves in Figure 1.6 show i_D of the PA device as a function of v_D with v_G a parameter. Rather than being expressed as a set of parametric curves, this

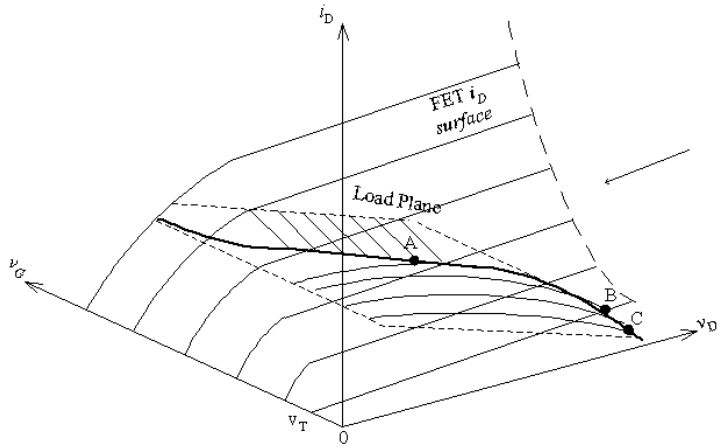

Figure 1.7 FET I /V curves and load line represented in 3 − D with gate operating points OPG [75].

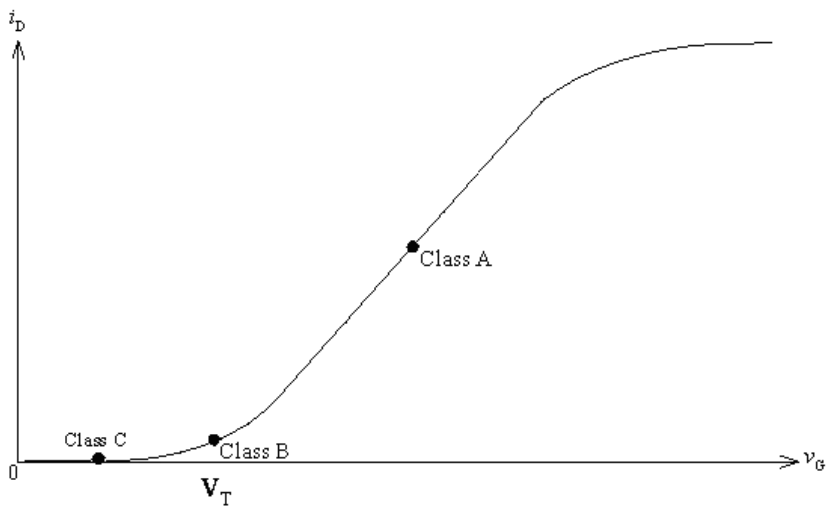

Figure 1.8 Device transfer characteristic and quiescent operating point for Class A, B and C operation [75].

relationship may be represented instead as a 3-D surface of i_D as a function of v_G and v_D as shown in Figure 1.7. Since the relationship governed by the load resistor that gives the load line in Figure 1.6 is independent of v_G, it is represented in 3-dimensions by a *load plane* that is parallel to the v_G axis, as in Figure 1.7. Now since the PA circuit comprises both the device and the load resistor, the quiescent operating point and the dynamic operating point must lie on the intersection of the load plane with the device surface. This intersection gives an 'S'− shaped curve in 3-D space, as shown

in Figure 1.7 [75]. Now all of the three operating points, including Class C, for which $V_{GG} < V_T$, may be represented distinctively, as shown in Figure 1.7.

The device transfer characteristic is the dependence of device current i_D on input voltage v_G. It may be obtained by projecting the 'S'− shaped intersection curve in Figure 1.7 onto the $i_D - v_G$ plane, or equivalently, by viewing it along the v_D axis, as indicated by the arrow. The resulting transfer characteristic is shown in Figure 1.8 [75], together with quiescent operating points for Class A, B and C.

The device transfer characteristic in Figure 1.8 may be approximated using a piece-wise linear approach, and this technique has been used to derive some basic results for PA efficiency [51][52]. In this approach, for $v_G \leq V_T$, i_D is treated as zero, for v_G greater than a limit value v_{GL}, i_D is treated as constant, and for $V_T \leq v_G \leq v_{GL}$, i_D is treated as a linear function of v_G. Device output currents for the cases of Class A, B and C using the piecewise linear model and a sinusoidal input voltage are shown in Figure 1.9 [47]. Note that only in the case of Class A can the device output current be

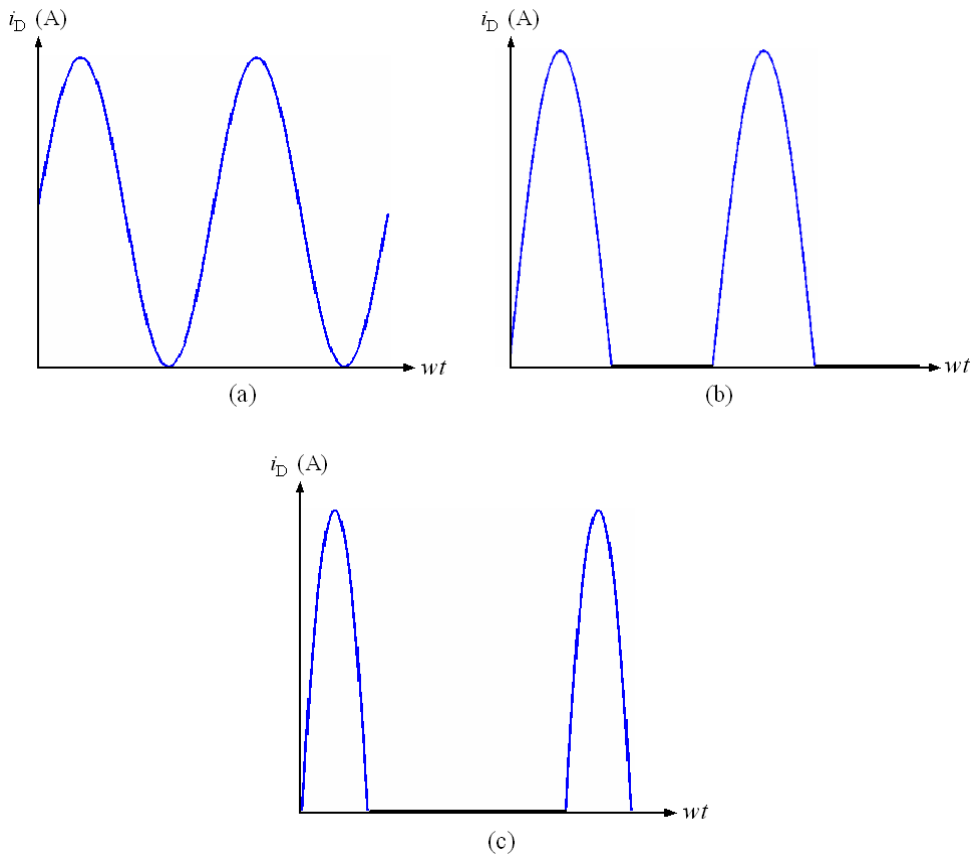

Figure 1.9 PA device output current waveforms from [47][67], (a) Class A; (b) Class B and (c) Class C.

sinusoidal. However, in the case of non-sinusoidal device output current, use of the tuned bias circuit in Figure 1.5(b) will provide a very low impedance path to V_{DD} for the harmonics of i_D allowing just the fundamental component to pass to the load, generating a sinusoidal output voltage.

Under the assumption of an ideal tuned bias circuit and piecewise-linear device model, and some other basic assumptions about signal amplitude [51][52], efficiencies of Class A, B and C amplifiers have been determined and the figures are given in Table 1.1 [47][51][3,4]. It can be seen from Table 1.1 that in moving from Class A to Class C, *i.e.* for operating point moving to the left on the transfer characteristic in Figure 1.8, efficiency increases from 50 % to 100 %. This can be explained by the fact that the mean values of the current waveforms in Figure 1.9, which determine the PA DC supply current [75], reduce in going from Class A to Class C.

However, as efficiency increases in going from Class A to Class C, the other critical performance parameter for the PA, nonlinearity, deteriorates [47]. This constitutes the problem of the great trade-off in PA design. In order to be able to optimise this trade-off, it is necessary to have a good understanding about PA efficiency and about PA nonlinearity. A lot of information is available in the literature about PA efficiency [47][51][52]. This thesis focuses specifically on understanding the nonlinearity of the PA.

Table 1.1 Comparison of efficiency for PA operating classes [51]

Operating Class	Efficiency	
	Maximum	In practice
Class A	50%	30%
Class AB	50% − 78.5%	30% − 60%
Class B	78.5%	60%
Class C	78.5 − 100%	70%

[3] As well as Class A, B and C, PAs may also operate in Class D, E, F and S [47]. In Class D, E,F and S, the device operates as a switch and efficiency very close to 100% may be obtained at the cost of very poor linearity [47].

[4] Table 1.1 shows that PA efficiencies obtained in practice are somewhat below those calculated from the simple theory [51]. There are several reasons fot this including the non-zero knee voltage in the device $i - v$ charatcteristics, V_K in Figure 1.6.

1.4. Conclusions

In this chapter, some background about the need for PAs in communication systems and their requirements has been presented. Also, some simple concepts concerning the basic operation have been reviewed. The next chapter will present background on advanced methods of analysing PAs, especially their nonlinearity performance. This background will lead to a statement of the motivation of this thesis and the layout of the remaining chapters.

CHAPTER 2

BACKGROUND ON ADVANCED METHODS FOR DETERMINING PA PERFORMANCE

2.1. Introduction

In this chapter, advanced methods for determination of PA performance will be reviewed. The chapter begins with reviewing device current clipping analysis methods for deriving efficiency of PA. Then general methods of determining small-signal PA distortion from derivatives of transconductance and output conductance will be considered. This is followed by methodologies for predicting large-signal distortion performance based on the actual device transfer characteristic. Finally, examples of published measured and simulated PA performance will be examined, leading to a statement of the aim of this research work and the layout of the remaining chapters.

2.2. Simple Device Current Clipping Analysis [51]

In this analysis, proposed by Pedro [51], the device input voltage is assumed to be sinusoidal and the device transfer characteristic is approximated by a piecewise linear function, as shown in Figure 2.1, which also shows the clipped output current

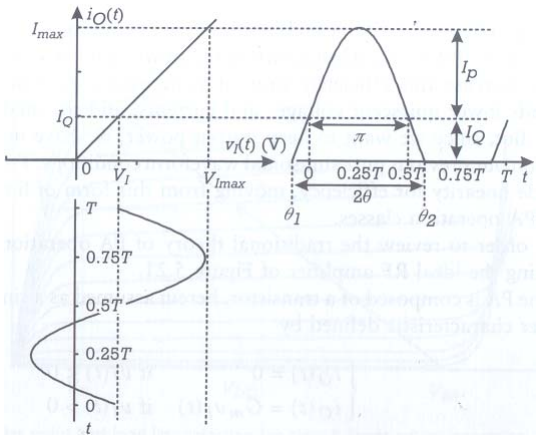

Figure 2.1 PA input voltage and output current with piecewise linear device transfer characteristic [51].

define the class of a PA. Conduction angles (2θ) of 2π, 3π/2, π, π/2 and 0 correspond to operating classes of A, AB, B, C and limit case of Class C, respectively.

The 0th and 1st order Fourier series coefficients of device output current in Figure 2.1**,** which determine DC supply power and fundamental signal power in the load, are derived for a range of conduction angles. These quantities together with their ratio, which is efficiency according to (1.1), are calculated for various conduction angles and presented in the form of Table 2.1. Pedro uses these results to argue that Class C operation is not very attractive because, although efficiency is very high, output power is low, and there are other problems [51].

Then the piecewise linear device transfer characteristic in Figure 2.1 is replaced by two other functions having a softer form of cut-off, one describing a FET and the other a BJT [51]. Pedro shows that DC power, output power and efficiency as functions of conduction angle are not much changed [51].

Table 2.1 Maximum output power, DC power consumption and efficiency [51].

2θ	R_L	P_{DC}	P_{RFmax}	η_{max} (%)
2π	2 V_{DD} / I_{max}	0.5 $V_{DD}I_{max}$	0.25 $V_{DD}I_{max}$	50
3π/2	1.88 V_{DD} / I_{max}	0.44 $V_{DD}I_{max}$	0.26 $V_{DD}I_{max}$	60.1
π	2 V_{DD} / I_{max}	0.32 $V_{DD}I_{max}$	0.25 $V_{DD}I_{max}$	78.5
π/2	3.22 V_{DD} / I_{max}	0.16 $V_{DD}I_{max}$	0.15 $V_{DD}I_{max}$	94
0	∞	0	0	100

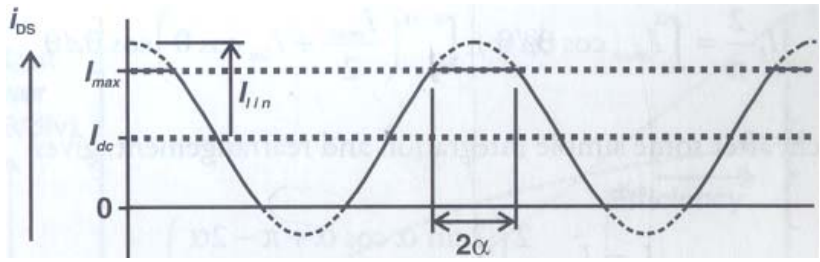

Figure 2.2 Conduction angle definition for overdriven Class A PA [52].

Pedro then introduces a second turning point into the device transfer characteristic that gives a maximum output current limit, as shown in Figure 1.8 [51]. For this device model, Pedro takes the case of heavy overdrive, for which all classes of operation have the same device output current waveform, which is a square wave, and he derives an expression for efficiency. The idea of deriving PA performance by analysis of the clipped device output current waveform has been further developed by Cripps [52].

2.3. Device current Clipping Analysis with Symmetrical Clipping for Class A PA [52]

In [52], Cripps presents a method to determine the performance of the overdriven class A PA by analysis of device current clipping. Here, the input signal is assumed to be a pure sinusoidal signal and the output current and output voltage waveforms are clipped waveforms with symmetrical clipping angles 2α, as shown in Figure 2.2. By determining 0th and 1st order Fourier series coefficients for the device current waveform, DC power and output power are derived as functions of input power.

Output power and efficiency against input power for the overdriven Class A PA are shown in Figure 2.3. The output power gradually reaches the saturation level as current waveform clipping increases. At the 1-dB compression point, the efficiency is about 63%, which is similar to that for Class AB. At the 3dB compression point, efficiency is about 71%. Cripps shows that, as the input power increases, conduction angle reduces, leading to the increase in efficiency. The overdriven Class A PA

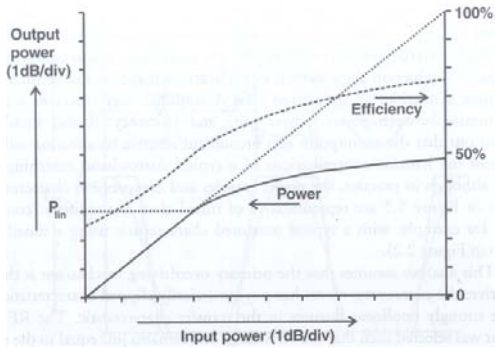

Figure 2.3 Output power and efficiency of Class A PA with symmetrical clipping angles [52].

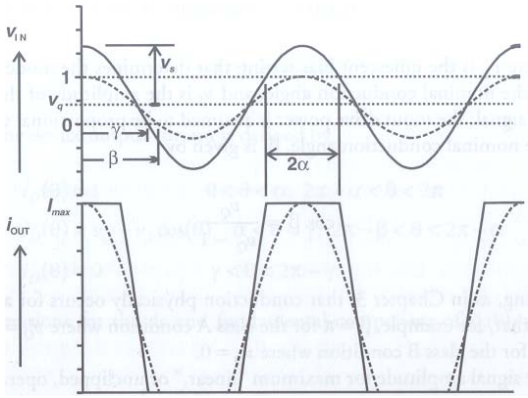

Figure 2.4 Input voltage and output current waveforms for Class AB PA with normal device level (- - -) and overdriven (──) [52].

provides an interesting trade-off between output power, efficiency and gain. However, the nonlinearity becomes worse. The above results naturally led Cripps to analysis of other classes with reduced conduction angle.

2.4. Device Current Clipping Analysis with Unsymmetrical Clipping for any PA Class from A to C [52]

The device input voltage and output current corresponding to Class AB case is shown in Figure 2.4 [52]. The dashed lines denote normal operation and solid lines denote overdriven operation with more extensive clipping [52]. The device current

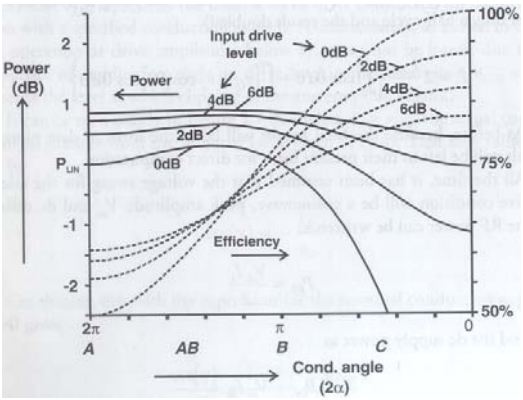

Figure 2.5 Output power (—) and efficiency (- - -) of PA from [52] versus conduction angle (*i.e.* class) for different input signal power levels.

waveforms are defined mathematically in three segments, cut-off, saturation and quasi-linear. In cut-off segment, the current is zero, in saturation segment, the current is at the maximum (I_{max}) and in the quasi-linear segment, the current waveform is part of a cosine waveform.

Using these definitions of device current as a function of conduction angle in the three segments, DC and fundamental components of the device output current are obtained from Fourier series coefficients [52]. Output power and efficiency with different input power levels (0, 2, 4 and 6 dB) are plotted against conduction angle from 0 to 2π in Figure 2.5. Normalisation is adopted that makes the output power 0 dB at conduction angle of 2π (Class A) when the normalised input power is 0 dB.

The results in Figure 2.5 show some interesting conclusions. Reduction of conduction angle (going in the direction from Class A towards Class C) always increases efficiency. Increase in input power level may increase or decrease efficiency, dependenting on class. Reducing conduction angle, *i.e.* moving towards Class C reduces output power except for the case of high conduction angle and low power. Figure 2.5 is a very important result because it shows the dependence of two very important PA performance parameters, output power and efficiency, as a function of two independent variables, namely class (conduction angle) and input power level that are crucial parameters to choose in the design and operation of a PA.

In sections 2.2 to 2.4, work that determines PA performance by analysis of device current clipping has been described. The analyses led to prediction of PA

output power and efficiency under certain assumptions. This thesis, however, is primarily about PA distortions, so methods of determining PA distortion are now reviewed.

2.5. Distortion, Derivatives and Soft Pinch-off Function [77]

PA non-linearity is caused primarily by the non-linearity of the PA device transfer characteristic. It can be seen from the example transfer characteristic in Figure 1.8 that non-linearity is strongly dependent on operating point, which determines PA class. For example, for Class A operation, it is possible to avoid the strong nonlinearities that occur in the curve for $v_G = V_T$ and for where i_D saturates at high vales of v_G. Third order intermodulation distortion (IMD3) that causes ACI and constellation errors in a communication system, is very sensitive to the trajectory of the device transfer characteristic, such as that in Figure 1.8. As a result, it has not been possible to come up with a device model transfer characteristic expression that can predict how IMD3 varies with PA input voltage amplitude for different classes of operation. In order to help towards solving this problem, the idea of using *derivatives* has been adopted [77][78].

For any bias voltage v_G in Figure 1.8, the small-signal linear approximation consists in approximating the relationship using $i_D = g_m v_G$, where g_m is the gradient of the curve [77][78]. The small signal *non-linear* approximation for a given point on the device transfer characteristic is

$$i_D = g_1 v_G + g_2 v_G^2 + g_3 v_G^3 + \cdots \tag{2.1}$$

where,

$$g_i = \frac{1}{i!}\frac{\partial^i i_D}{\partial v_G^i} \tag{2.2}$$

is the ith order derivative of the i_D versus v_G relationship [77][78]. Note that the g_i vary with bias point in Figure 1.8. They are referred to as bias-dependent small-signal

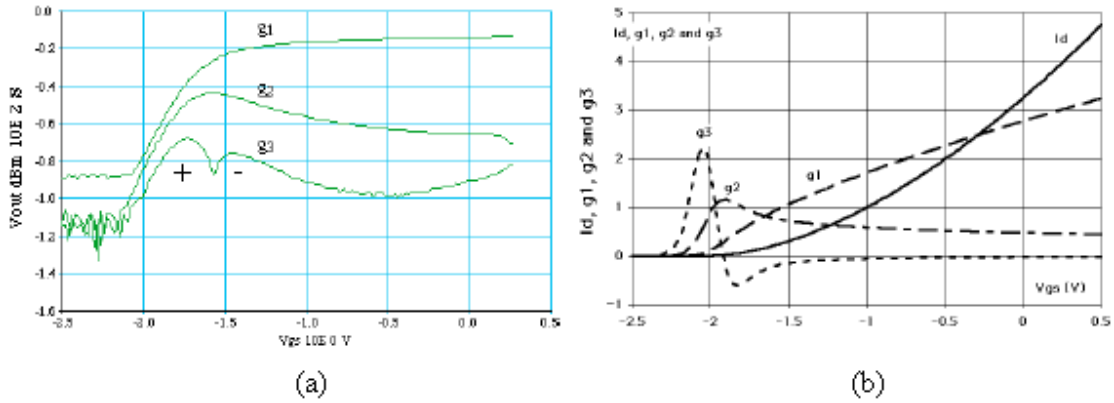

Figure 2.6 Plots of PA device drain current derivatives, (a) measured using dB scale; (b) predicted using Q-law model with soft pinch-off function (linear scale) [77][78].

derivatives, or just derivatives, for short. Derivatives describe the curvature of the transfer characteristic at any bias voltage and how the curvature is changing. The piece-wise linear device model transfer characteristic in Figure 2.1 has gradient discontinuities; therefore, its transconductance g_1 has step discontinuities and g_2 and g_3 have spike discontinuities. The square law model, $i_D = K\,(v_G - V_T)^2$ is continuous, but its g_m (g_1) has gradient discontinuities, g_2 has a step discontinuity and g_3 has spike discontinuities [77]. Similar statements apply to the Q-law model where the power 2 in the model expression becomes a constant Q [77][78].

The current $i_D = f\,(v_G)$ and the first few derivatives for a real device [77][78] are shown in Figure 2.6(a) using a vertical scale in dB. It can be seen that the derivatives of the real device are continuous and finite.

The poor match between the derivatives of a real device and the model derivatives has been largely overcome by introducing into the device model equation a function called the *soft pinch-off function* [77][79][80]. v_G in the device model expression is replaced by

$$v_G^{'} = V_T + V_{ST} \ln\left| e^{(v_{GS} - V_T)/V_{ST}} + 1 \right| \tag{2.3}$$

This has the effect of making the model derivatives finite and continuous. For example, the derivatives for the Q-law model with Q = 1.7 using the soft-pinch-off

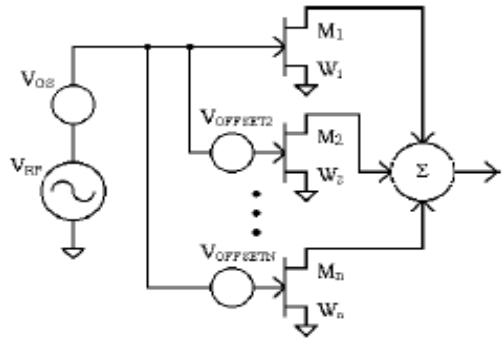

Figure 2.7 Derivative superposition amplifier architecture [77][78].

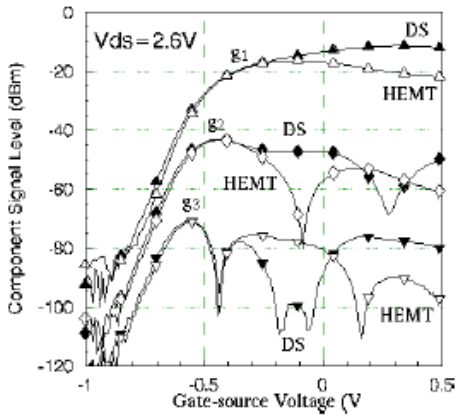

Figure 2.8 Comparison of measured derivatives g_1, g_2 and g_3 for a 4-HEMT DS amplifier and for a single HEMT [77][78].

function with V_{ST} = 0.07 are shown in Figure 2.6(b) using a linear vertical scale [77], providing a reasonable match with the measured derivatives in Figure 2.6(a). The soft-pinch function is used in all high quality device models [79][80]. As well as providing derivatives that are continuous, finite and realistic, it also provides correct modelling of the sub-threshold (or weak inversion) mode of device operation. Although the soft pinch-off function is a very important development, it must be remembered that derivatives describe small-signal nonlinearity. The PA is a large signal device and it has not been possible to model correctly the variation of 3rd order distortion with class over the full signal power range of interest.

Some idea about large signal distortion behaviour can be obtained by the concept of time dependence of derivatives through a signal cycle [77][78]. This idea has been applied successfully in the context of an amplifier distortion reduction technique called *derivative superposition* that is now described. In the derivative superposition

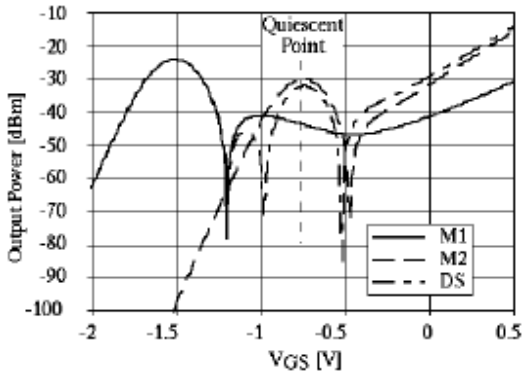

Figure 2.9 3rd order derivatives for phase reversal form of derivative superposition [77][78].

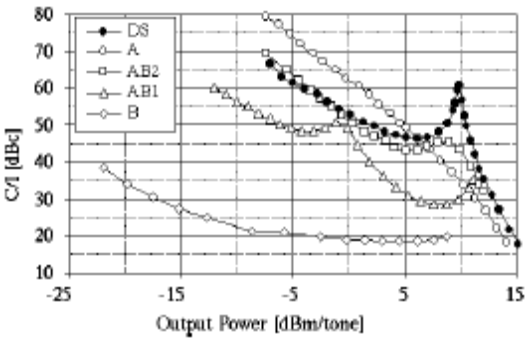

Figure 2.10 Measured 1-tone C/I ratio for DS amplifier and single FET for different operating points [77][78].

approach, a number of devices are arranged so that their output currents add, as shown in Figure 2.7 [77][78]. Each device has the same AC input signal but its input bias voltage is independent. By choice of the device bias voltages and gate widths, it is possible to obtain cancellation between positive and negative parts of the device g_3 curves, leading to a region of very low small-signal 3rd order distortion, as illustrated in Figure 2.8 [77][78].

The extension of the derivative superposition idea to large signals is illustrated in Figure 2.9 [77][78]. In this case, the aim is not to obtain very low g_3, but to ensure that for a chosen input voltage bias and amplitude, g_3 has opposite signs for equal parts of the signal period [77][78]. This leads to a null in 3rd order distortion for a specific large signal amplitude. This can be seen as a peak in carrier-to-interference ration (C / I) in Figure 2.10 [77][78]. Thus the idea of time-dependent derivatives

allows some limited capability to predict and control a feature of the large-signal distortion behaviour of a PA.

2.6. 2-D Talyor Series Representation for PA device [77][78]

Change in the value of the load resistor of a PA affects small-signal distortion and some interesting work has been done on this [77][78]. Change of load resistance can be represented as a change of the slope of the load plane in the 3-D PA representation in Figure 1.7. This situation can be handled by replacing the i_D (v_G) expression (2.1) for small signal variations about a chosen operation point by the 2-dimensional dependence [77][78], given by

$$\begin{aligned} i_D &= g_1 v_{GS} + g_2 v_{GS}^2 + g_3 v_{GS}^3 + \cdots \\ &\quad + g_{d1} v_{DS} + g_{d2} v_{DS}^2 + g_{d3} v_{DS}^3 + \cdots \\ &\quad m_{11} v_{GS} v_{DS} + m_{12} v_{GS}^2 v_{DS} + m_{21} v_{GS} v_{DS}^2 + \cdots \\ &= g_1 v_{GS} + g_2 v_{GS}^2 + g_3 v_{GS}^3 + \cdots \\ &\quad + g_{d1} A v_{GS} + g_{d2} A^2 v_{GS}^2 + g_{d3} A^3 v_{GS}^3 + \cdots \\ &\quad m_{11} A v_{GS}^2 + m_{12} A v_{GS}^3 + m_{21} A^2 v_{GS}^3 + \cdots \end{aligned} \tag{2.4}$$

where A[5] is voltage gain with $A = g_1/(R_L^{-1} + g_{d1})$ and R_L is the effective load resistance. In (2.4), g_1 is the transconductance, g_2 and g_3 are 2nd and 3rd order transconductance coefficients. g_{d1} is the output conductance and g_{d2} and g_{d3} are non-linear output conductance coefficients; the m terms are called mixing terms [77][78]. Equation (2.4) makes it possible to determine PA distortion as a function of effective load resistance for a given input signal bias voltage (*i.e.* class) for small signal variation about an operating point in Figure 1.7, for which the coefficients in (2.4) are treated as constants. In [81], nonlinearity for a PA in CMOS technology mainly due to transconductance and output conductance is analysed. The results may be expressed as 3-D plots of 2nd and 3rd order distortion versus load resistance and input

[5] Here, only dominated term in drain current (i_D) is considered, $i_D \approx g_1 v_{GS}$ in order to determine v_{DS}. Therefore, the relationship between v_{GS} and v_{DS} is assumed to be linear.

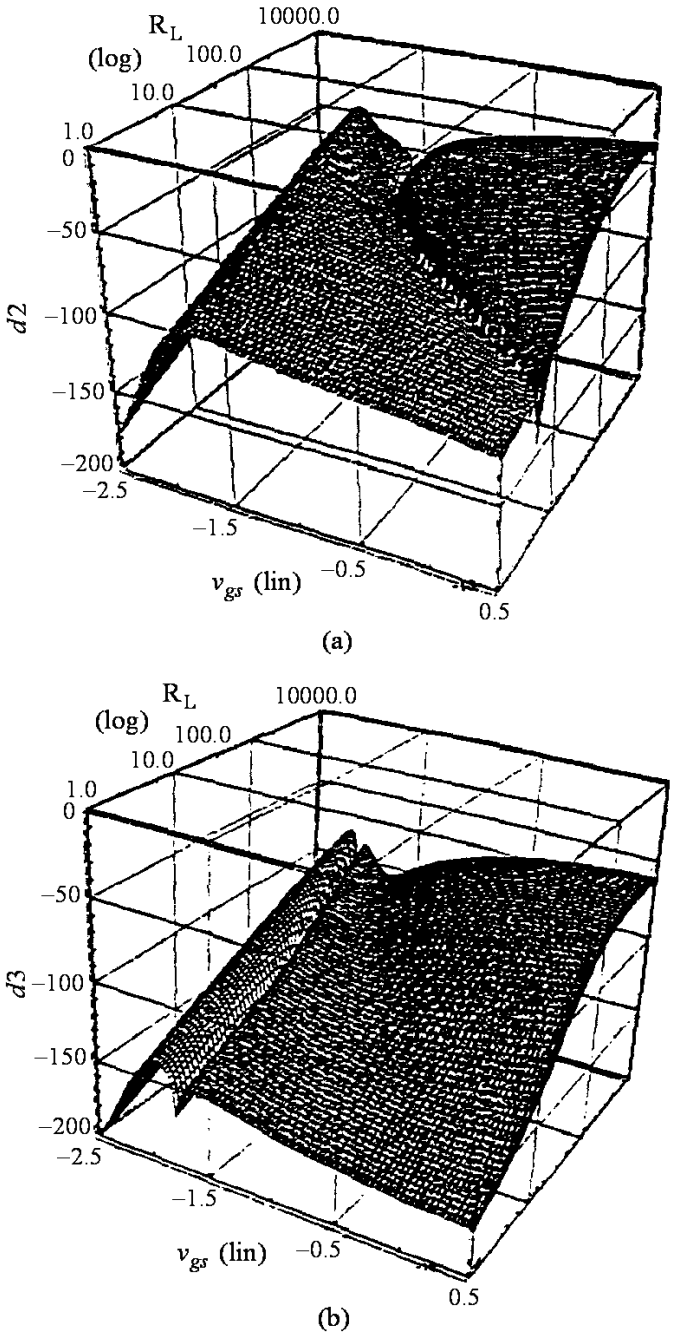

Figure 2.11 2nd and 3rd order distortion levels in the saturation region versus bias and load resistance, (a) 2nd harmonic level; (b) 3rd harmonic level [82].

signal bias voltage (*i.e.* class), as shown in Figure 2.11[82]. The 3-D plots imply a deep null for 2nd and a shallow null for 3rd order distortion when plotted against load resistance. The predictions have been confirmed by measurements on a real PA, as shown in Figure 2.12 [82].

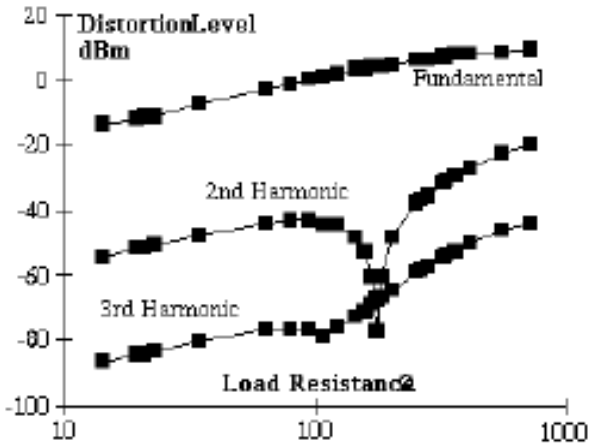

Figure 2.12 Measured distortion versus load resistance for a PA [82].

The ideas in section 2.5 and in this section have served to increase understanding about distortion in PAs. However, apart from the ability to predict a null in large signal 3rd order distortion in the modified derivative superposition method, these ideas really relate to small-signal distortion. But the PA is essentially a large signal device and prediction of distortion up to the edge of and beyond saturation is needed. In the next two sections of this chapter, techniques for obtaining large signal PA distortion are reviewed.

2.7. Impulse Model for 3rd Derivative of Device Transfer Characteristic [83]

The first method of predicting PA distortion is based on modelling the 3rd derivative of the PA device transfer characteristic using impulses. For example, the g_3 curve in Figure 2.6(b) could be modelled by impulses, one with a positive weighting just below $v_{GS} = V_T$ and one with a smaller negative weighting just above V_T. A g_3 derivative such as that in Figure 2.6 (b) corresponds to a device transfer characteristic with a single discontinuity around V_T, as shown in Figure 2.1. In practice, PAs have load resistance that can be represented by a loadline or load plane, as shown in Figures 1.6 and 1.7. This causes device output current to saturate for high v_G, as shown in the device transfer characteristic of Figure 1.8. This in turn causes

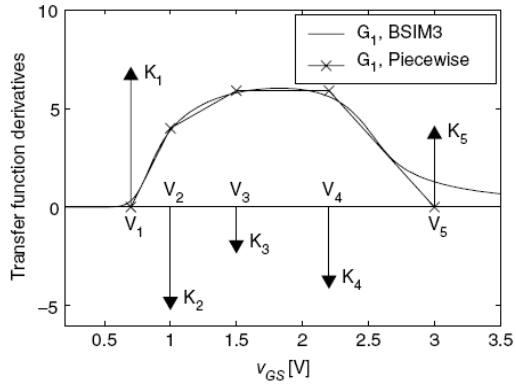

Figure 2.13 Transconductance characteristic, its piecewise linear approximation and an impulse model for the 3rd derivative [83].

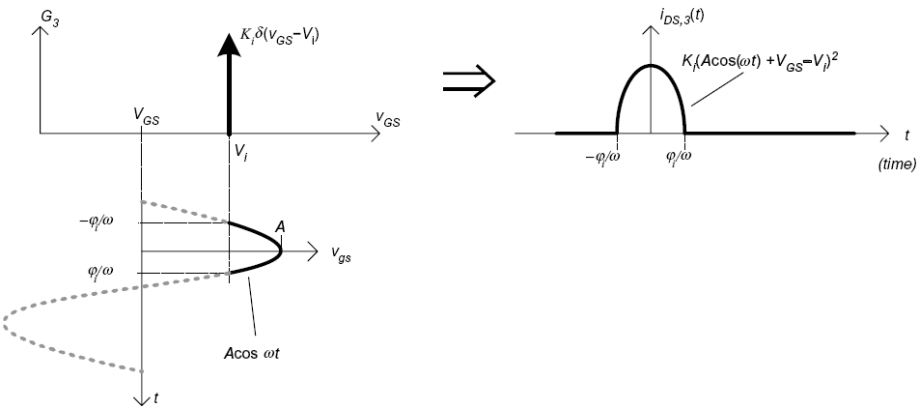

Figure 2.14 Illustration of input signal peak transversing a g_3 impulse and the corresponding current response [83].

transconductance g_m, or g_1, to fall at high v_G, as shown by the smooth curve in Figure 2.13. The fall in g_1 for high v_G causes further positive and negative peaks in the g_3 characteristic.

This first method of predicting PA distortion is based on a piecewise linear approximation to the transconductance, as shown by the angular trace in Figure 2.13. This implies a 3rd derivative of the device transfer characteristic that may be modelled as a superposition of impulses K_i as shown in Figure 2.13. The weighting of the impulses is related to the amount by which the gradient of the transconductance changes at the break points. For a given bias point, *i.e.* value of v_G in Figure 2.13, as the amplitude of the input signal increases, so its peaks encounter more impulses, each of which generates a component, as shown in Figure 2.14. These current

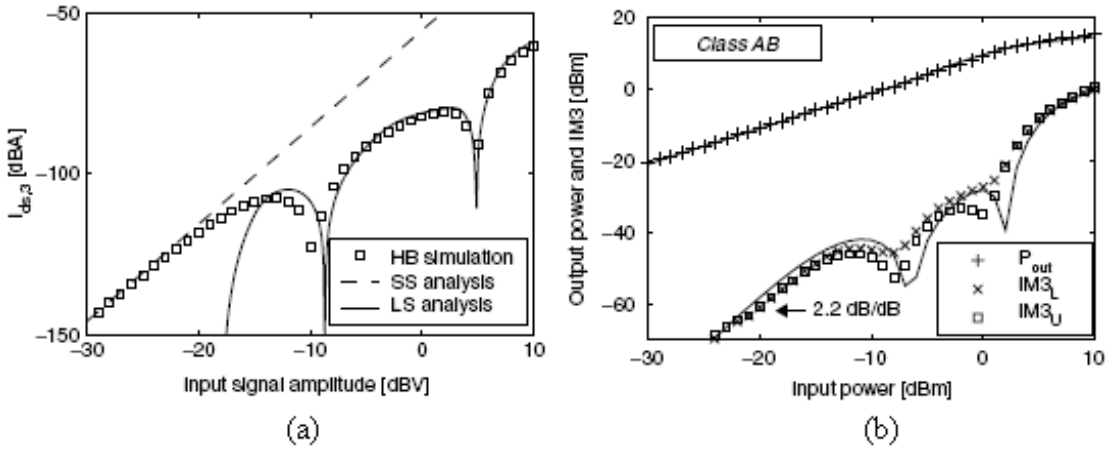

Figure 2.15 (a) Simulated 3rd harmonices component of Class AB PA at V_{GS} = 0.875V; (b) measured output power and IM3 of Class AB PA at V_{GS} = 0.875V [83].

components contribute to large signal IMD3, which can be determined from their Fourier series. This method in [83] leads to prediction of large signal IMD3 behaviour for all classes of operation from Class A to C. An example of a curve of predicted 3rd order distortion versus input signal power is shown in Figure 2.15(a) for Class AB, together with a simulation using a good device model [83]. The technique gives some understanding of the relationship between a device transfer characteristic, via its transconductance and 3rd derivative characteristic and impulse model, and features in the distortion power sweep, such as the presence of nulls.

Although, the impulse method can predict large signal PA distortion, it relies on measurement or simulation of the device transfer characteristic for a specific device and a decision on amplitude and position of every impulse (K_i) used to model it. Note that this impulse model method for predicting large signal distortion can predict only large-signal distortion. In Figure 2.15(a) [83], the small signal distortion obtained from the simulation is predicted by Volterra analysis[6] [51][97]. The measured IMD3 for the same PA is shown in Figure 2.15(b), confirming the shape of the IMD3 curve with its two nulls [83].

The impulse modelling method of predicting PA distortion is essentially a numerical transformation between the device transfer characteristic (represented by its 1st derivative, or transconductance, curve in Figure 2.13), to PA large signal

[6] Volterra analysis uses a closed form to express the response of a weak nonlinear system.

distortion (in Figure 2.15(a)) via the simplified impulse model for g_3 in Figure 2.13. However, the method provides considerable insight, since starting from a chosen bias point (or class of operation) along the horizontal axis in Figure 2.13, as signal amplitude increases, its positive and negative peaks encounter impulses, which may be positive or negative, which give rise to the nulls, or absence of nulls, is the PA distortion curve (e.g. Figure 2.15(a)) [83]. In next section, three purely numerical methods [86][87][89] used to analysis IMD3 performance of PA will be reviewed.

2.8. Numerical Methods for Analysing IMD performance [86][87][89]

The method in [86] starts from the measured transfer characteristic of a LDMOS FET as shown in Figure 2.16. At every gate bias point along the horizontal axis, the output current can be represented using Taylor series expansion. The odd order coefficients of Taylor series are retained up to 11th order. Since the excitation voltage for the transfer characteristic is gate bias voltage plus input signal, coefficients can be considered to be a function of gate-bias voltage. After simple mathematical replacement, the fundamental components and 3rd order IMD3 components of the output current are derived as a function of gate bias voltage and input signal amplitude. Thus, the author of [86] can present a 3-D plot of IMD3 against input signal power and bias gate voltage (that defines PA class) and this is shown in Figure 2.17(a).

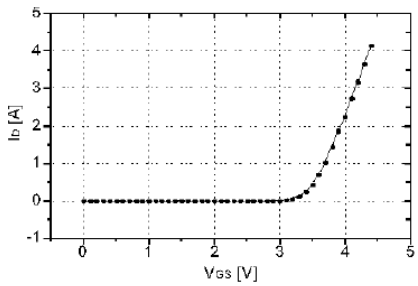

Figure 2.16 Measured transfer function of LDMOS FET [86].

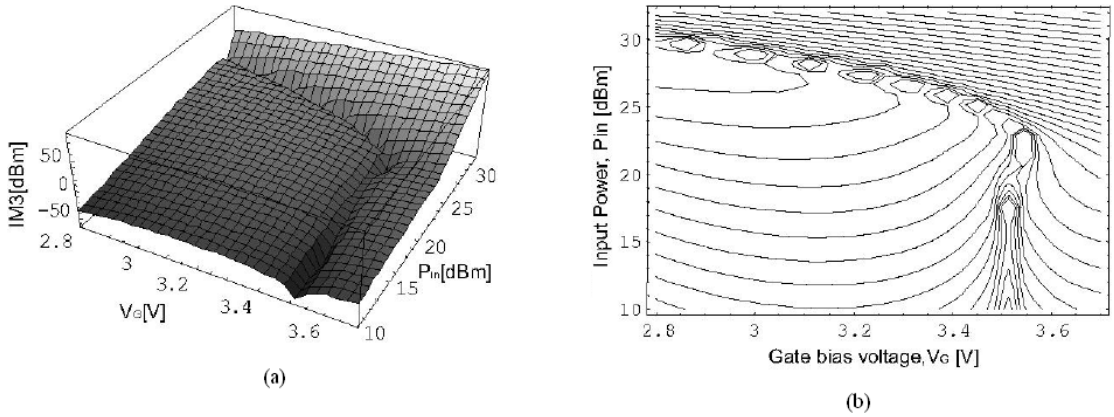

Figure 2.17 IMD3 surface and corresponding contour plot [86].

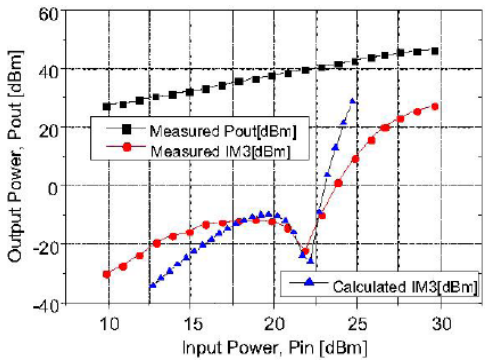

Figure 2.18 Measured output power and IMD3 power, and predicted IMD3 power [86].

The type of plot in Figure 2.17(a) is considered as an important development. The impact on PA performance of two key parameters that the PA designer has at his disposal, bias (*i.e.* class) and degree of backoff (*i.e.* input signal amplitude) can be clearly seen. Perhaps the amount of computation required has prevented wider use of this approach. Another advantage of the 3-D plot is that it provides a bird's eye view that increases understanding. In the case of Figure 2.17(a), it can be seen that the surface of high IMD3 values is crossed by a deep valley. From the contour plot of IMD3 obtained from the 3D plot in Figure 2.17(b), it can be see that the valley is 'L'-shaped. It can be seen that for a certain bias voltage, referred to as Class AB in [86], below a certain input signal power level, one part of the valley is parallel to the input power axis. Such a condition is attractive and called in [86] a sweet spot. The IMD3 sweet spot is determined by the sum of odd coefficients in the analysis. Figure 2.18

shows a prediction of IMD3 versus input signal power for a particular bias voltage obtained from the 3D plot in Figure 2.17(a) together with the measured curve. Although the position of the null is well predicted, this is not the case for the IMD3 levels each side of the null. Thus in spite of the achievement in [86] of having identified the 'L'-shaped distortion valley in Figure 2.17(a), the method still has some limitation.

The next method of transformation from device transfer characteristic is described in [87]. In this method, a large-signal current source device model with 15 parameters is obtained by empirically fitting to small-signal transconductance and measured pulsed and static drain current characteristics. Transconductance curve is fitted in four regions, including sub-threshold, quadratic, linear and compression regions. Large and small signal IMD behaviour is investigated using Fourier and Volterra series analysis, respectively [87][88]. Using this approach, the measured distortion-power sweep for a Class AB LDMOS PA is well predicted, including sweep spots [87]. In addition, device nonlinear parasitic capacitances are shown to affect the IMD sweet-spots [87].

The last method of transformation from nonlinear device transfer characteristic to PA distortion is presented in [89]. In this paper, GaAs MESFET distortion is predicted mathematically by combining Volterra series analyses for small signal and two sinusoidal input describing function (TSIDF) for large signal. TSIDF function includes the saturation shape of transfer characteristic in Figure 1.8. Using this method, good agreement was obtained between predicted and measured IMD3 for a PA using a MESFET device operated in Class AB and B.

In sections 2.5 to 2.6 and in sections 2.7 to 2.8, techniques for predicting small-signal and large-signal PA distortion, respectively, have been reviewed. All of these methods start from a description, or model, of the nonlinearity of the device, in the form of a transfer characteristic, a transconductance characteristic or a derivative. Thus these techniques are really transformations between the given non-linearity of a device and the resulting distortion behaviour of a PA incorporating that device. Before stating the aim of this present thesis, published measured PA distortion data is reviewed, in order to learn more about the nature of PA distortion characteristics.

2.9. Published Measured and Simulated Distortion Data

Measured 3rd order intermodulation distortion (IMD3) and output power versus input signal power are given in [83] for a CMOS PA operating in four different classes. The gate bias voltage for the four classes is given in Table 2.2. Two are in Class AB, one is in Class C and one is in Class A. The Class AB cases are designated AB_- and AB_+, according to the value of the bias voltage. The measured output power and 3rd order IMD data for this PA from [83] is shown replotted in Figure 2.19.

The drain voltage for the power MOSFET used in this PA is 3 V and the gate width is 1200 μm. The IMD data is measured using two sinusoidal signals spaced by 1 MHz and centred at 950 MHz. The four distortion curves in Figure 2.19 exhibit quite different features. Even the curves for the two class AB cases are different, that for AB_- having two nulls and that for AB_+ having a ledge. For Class C, there is a single null and the curve for Class A is monotonic increasing. Before commenting further on this variation of characteristics, we consider other technologies.

Table 2.2 PA bias voltage and operating classes for Figures 2.19 − 2.22.

Technology	Ref	Bias voltage V_{GG} (V)	Class	Figure
CMOS measurement	[83]	0.675 0.875 1.1 2.0	C AB_- AB_+ A	Figure 2.19
LDMOS measurement	[87]	0.9 1.2 1.3 2.5	C AB_- AB_+ A	Figure 2.20
MESFET measurement	[89]	− 1.24 − 0.61	B AB	Figure 2.21
CMOS simulation	[83]	0.675 0.875 0.925 2.0	C AB_- AB_+ A	Figure 2.22

Measured IMD3 and output power for an LDMOS PA operating in four different classes is given in [87]. The gate bias voltage for the four classes is given in Table 2.2. As for the LDMOS PA, two are in Class AB, one in Class C and one in Class A. The drain bias voltage is 20 V and the IMD3 test signal spacing is 1MHz centred at 100MHz. The measured IMD3 and output power for this PA from [87] for the four classes of operation are shown replotted in Figure 2.20. As for the CMOS PA just described, the Class C and Class A distortion curves have a single null and are monotonic, respectively. However, in this case, both of the Class AB curves have two nulls but the null spacings are very different. The AB_+ case with the higher bias voltage has a much narrower null spacing.

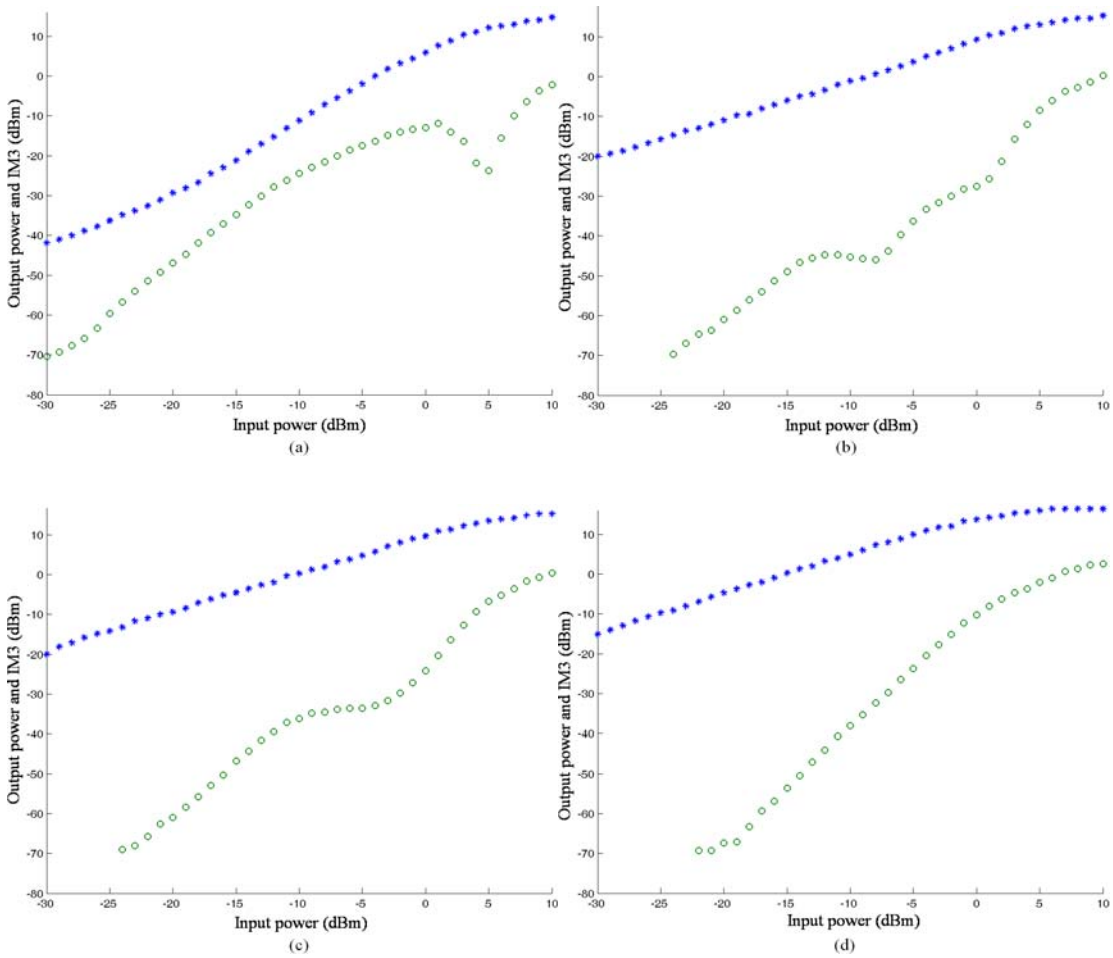

Figure 2.19 Measured IMD3 (o) and output power (*) for CMOS PA from [83] classes are (a) C; (b) AB_-; (c) AB_+ and (d) A.

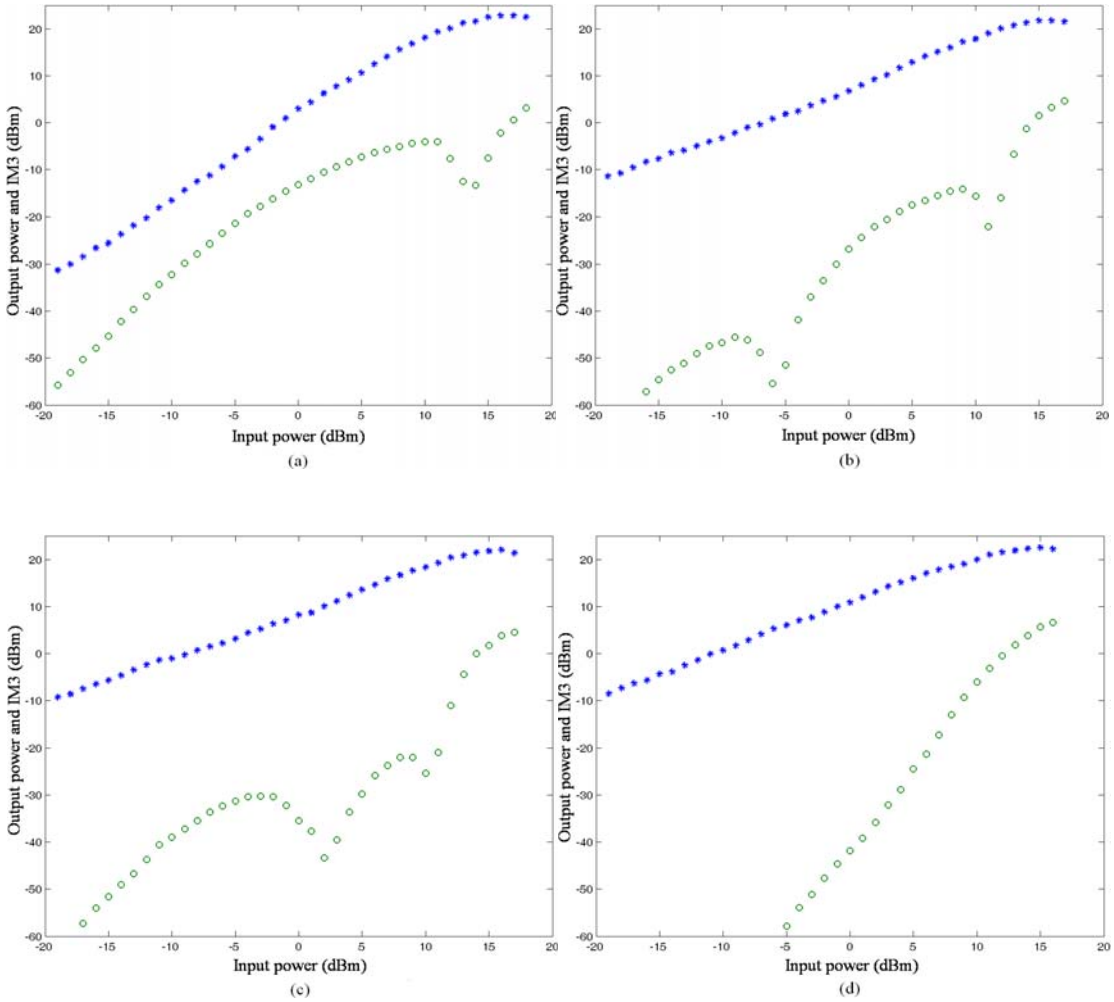

Figure 2.20 Measured IMD3 (o) and output power (*) for LDMOS PA from [87]; classes are (a) C; (b) AB_-; (c) AB_+ and (d) A.

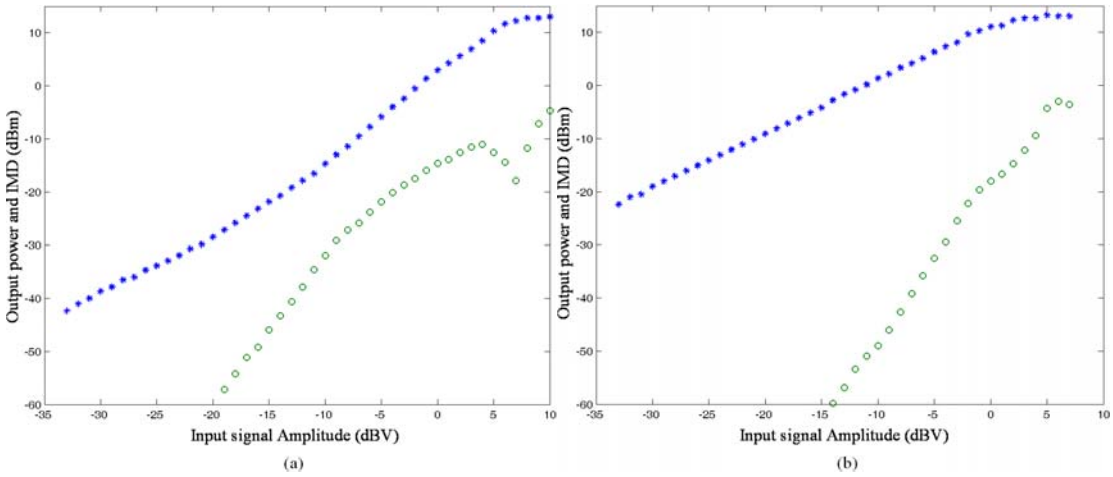

Figure 2.21 Measured IMD3 (o) and output power (*) for MESFET PA from [89]; classes are (a) B; (b) AB_+.

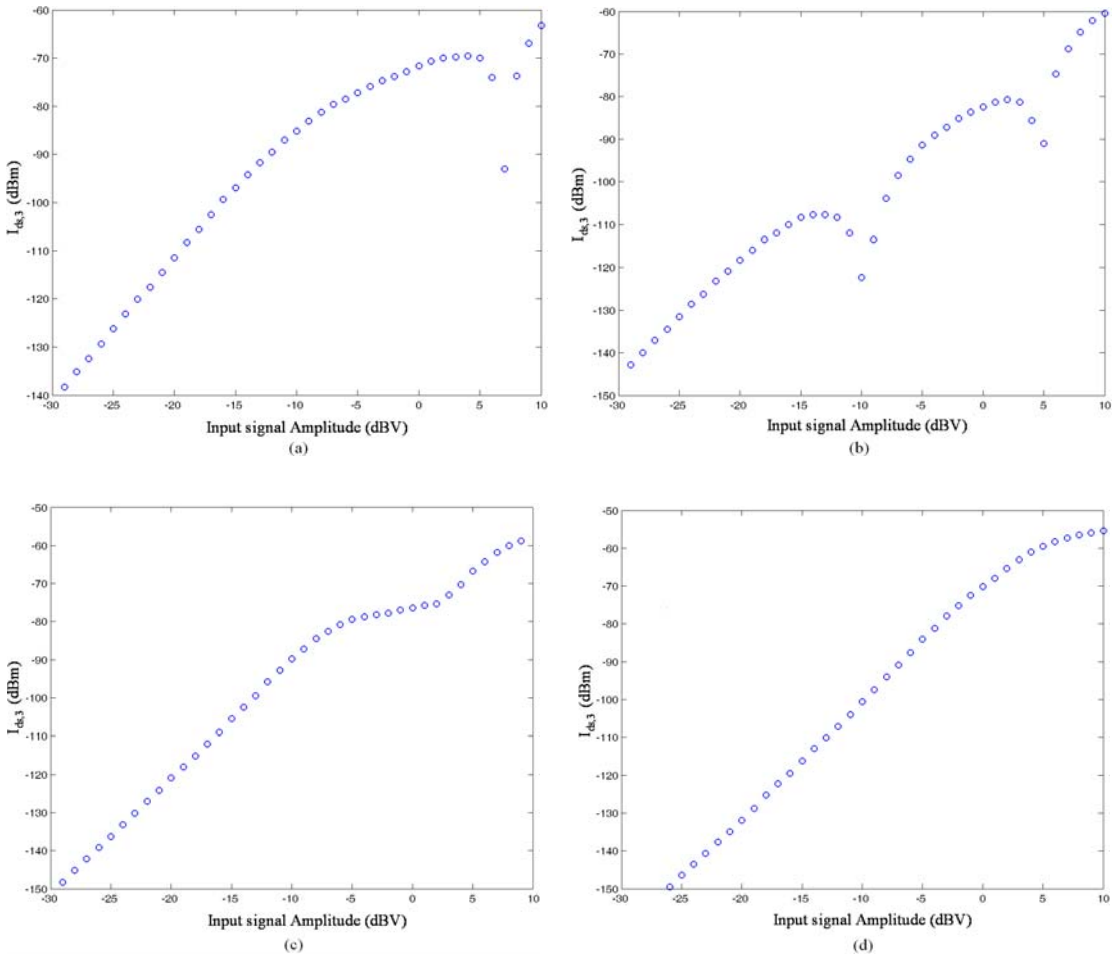

Figure 2.22 Simulated IMD3 for CMOS PA from [83] classes are (a) C; (b) AB_-; (c) AB_+; (d) A.

Measured IMD3 and output power for a GaAs MESFET PA operating in two different classes, Class B and Class AB, is given in [89]. The gate bias voltage used is given in Table 2.2. Measured output power and IMD3 from [89] is shown replotted in Figure 2.21. The IMD3 test frequencies were spaced by 0.1 GHz at 2 GHz. An input matching network was tuned for maximum gain. An output matching network provided the optimum Cripps load [52] for the fundamental and a short circuit for the baseband and 2nd harmonic components. From Figure 2.21, it can be seen the IMD3 curve for the Class B case has a single null. The IMD3 curve for Class AB has a slight ledge.

For the CMOS PA, whose measured IMD3 and output power characteristics from [83] were shown in Figure 2.19, the authors of [83] give also simulated performance using a very high quality device model. However, the simulation

assumed a totally integrated PA with MOSFET gate width of 60 μm. The input signal bias voltages for the four different classes of operation considered are given in Table 2.2. The method of analysis used for the computer simulation is harmonic balance [83]. The simulated output power and IMD3 for the CMOS PA in [83] are shown replotted in Figure 2.22**.** The characteristics are generally similar to those obtained from measurement in Figure 2.19, except that the nulls are much deeper. Having reviewed published distortion data for PAs of three different technologies, CMOS, LDMOS and GaAs MESFET, some conclusions can now be drawn.

For Class C PAs (CMOS − Figure 2.19(a) and Figure 2.22(a); LDMOS − Figure 2.20(a)), the distortion power sweep always exhibits a single null. For Class A PAs (CMOS − Figure 2.19(d) and Figure 2.22(d); LDMOS − Figure 2.20(d)), the distortion power sweep always increases monotonically. For Class AB PAs, two types of behaviour are observed. For CMOS (Figure 2.19(b) and Figure 2.22(b) and for LDMOS (Figure 2.20(b) and (c)), there may be two nulls in the distortion power sweep. The alternative Class AB distortion power sweep behaviour is a ledge. This is exhibited for the CMOS PA in Figures 2.19(c) and 2.22(c) and for the GaAs MESFET PA in Figure 2.21(b).

The conclusion from these published results of PA data is that across all three technologies (CMOS, LDMOS and GaAs), the form of the distortion power sweep in Class AB has just two types (double null and ledge), in Class C has a single type (single null) and in Class A has single type (monotonic increasing). Against the background of this surprising uniformity of PA distortion characteristics across three different technologies, the aim of this thesis can now be stated.

2.10. Project Motivation and Organisation of Thesis

It has been seen that there appear to be just four types of distortion power sweep curve for a PA of any technology, namely double null (with variable null spacing), single null, ledge (with variable width and depth) and monotonically increasing. This fact suggests strongly that there might be a theory that can explain distortion in PAs that is technology-independent.

The methods of predicting large signal PA distortion reviewed in sections 2.7 and 2.8 do predict the observed forms of distortion power sweeps, but their starting point is a set of coefficient values that describe device current, transconductance or 3rd derivative over a range of operating points. Thus these methods fall short of a general technology-independent theory to explain PA distortion.

Perhaps the greatest insight on PA distortion is given by the methods of time-dependent g_3 derivative and the impulse model for the 3rd derivative, reviewed in sections 2.5 and 2.7, respectively. With these methods, it is possible to see, starting from a particular bias point, *i.e.* PA class, how increase of signal amplitude can bring in components of opposite sign, producing distortion nulls. However, both methods are based on a particular device characteristic, and therefore lack full generality. The project described in this thesis was aimed at developing a general theory for distortion in PAs that is technology independent. In order to develop such a general theory, it is necessary to know the cause of distortion in PAs. This cause is not hard to find.

Consider the PA device output current waveforms for different classes of operation in Figure 1.9. All of these waveforms, apart from that for Class A, are heavily clipped sinewaves that have high levels of harmonics. For example, for the case of Class C, the sinewave in Figure 1.9(c) has a 3rd harmonic to fundamental ratio of 0.584 or − 10.758 dB. PAs are usually operated with a tuned load matching/coupling network as in Figure 1.5(b), in which case, the harmonic components of the device current are ideally shorted to V_{DD} and only the fundamental component flows in the load. However, any idea that this solves the problem is fallacious. It is shown in Appendix A, for a nonlinear device described by a polynomial, that 3rd order intermodulation distortion (IMD3) tone level relative to wanted signal tone level is the same as 3rd harmonic level relative to fundamental. Therefore when the PA whose output waveforms for sinusoidal input signal are as shown in Figure 1.9 is operated with narrowband multi-tone signals, the level of IMD3 components generated will be at the same high level as the harmonic components in Figure 1.9. Moreover, these IMD3 components generated at high level will be close in frequency to the input signals, and therefore they will not be shorted to V_{DD} by the tuned-circuit in Figure 1.5(b) but rather will flow straight into the load resistor. The idea that device current clipping is the major cause of distortion in PAs

is supported by the fact that such clipping is independent of the technology of the device used to realise the PA, just as the types of distortion characteristics of real PAs are technology-independent.

The project described in this thesis sought to develop a theory of device current clipping in order to explain the observed distortion characteristics of real PAs. The project is aimed therefore at a major extension of the device current clipping analysis methods reviewed in sections 2.2 to 2.4. The PA device current clipping theory developed in this thesis starts from key definitions and concepts (in Chapter 3), derives results that are independent of device model (Chapter 4), considers the linear and square law device models (Chapters 5 and 6), introduces a model that is transitional between linear and square law (Chapter 7) and compares predicted PA performance with published measured data (Chapter 8), before presenting conclusions and ideas for further work (in Chapter 9).

CHAPTER 3

DEVICE CURRENT CLIPPING THEORY

3.1. Introduction

In this chapter, some key definitions and concepts that relate to how clipping effects operate in a PA are given in order to provide a rigorous basis for a theory. These concepts lead towards a simple system model for a PA with clipping that will allow considerable development of the theory in subsequent chapters.

In order to be able to propose a satisfactory general theory for PA performance based on device current clipping, it will clearly be necessary, at the beginning of this chapter, to attempt to identify different types of clipping and to define associated clipping angles. These clipping angles must be related to conduction angle, which is used in the literature. It will be necessary to identify different PA input signal power ranges where different mathematical conditions apply and the critical transition point that divides them. Conduction angle at this transition point will be used in order to provide an unambiguous definition of the class of a PA.

3.2. Definitions

3.2.1. Input Voltage v_G, Output Current i_D, Knee and Cut-off Clipping

A typical PA with input signal bias network L_G and C_G, bias network A, and output matching load coupling network B is shown in Figure 3.1. Under the

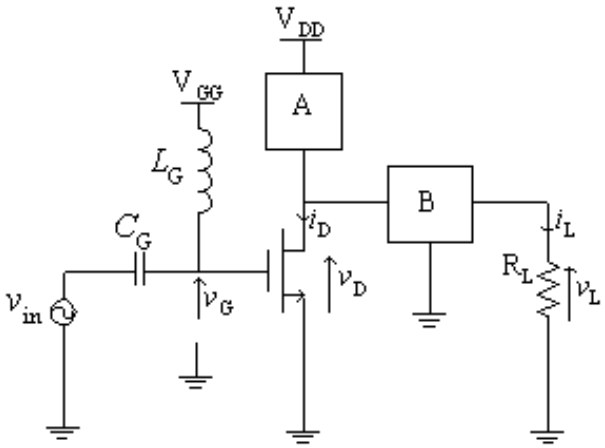

Figure 3.1 Circuit diagram of PA, A: Drain current feed circuit; B: Load coupling matching circuit.

assumption that L_G and C_G are asymptotically large, that V_{GG} is a DC voltage and that v_{in} is an AC voltage, we have

$$v_G = V_{GG} + v_{in} \tag{3.1}$$

The input signal is assumed to have the form

$$v_{in} = \hat{v}_G \cos \omega_o t \tag{3.2}$$

Hence

$$v_G = V_{GG} + \hat{v}_G \cos \varphi \tag{3.3}$$

where $\varphi = \omega_o t$. V_{GG} is termed input signal bias voltage and $\hat{v}_G$ is termed peak value of the input voltage ($\hat{v}_G \geq 0$).

Consider Figure 3.2(a), which shows the device input voltage waveform v_G (bottom left), output current waveform i_D (right) and the device v_G to i_D transfer characteristic. The waveforms correspond to a class C amplifier with about 6 dB of backoff[7] [84]. The transfer characteristic in Figure 3.2 (a) is assumed to be such that

[7] It can be calculated from $20\log\left[\left(v_{peak} - V_T\right)/\left(v_{GL} - V_T\right)\right]$. Here, v_{peak} is the peak value of input signal.

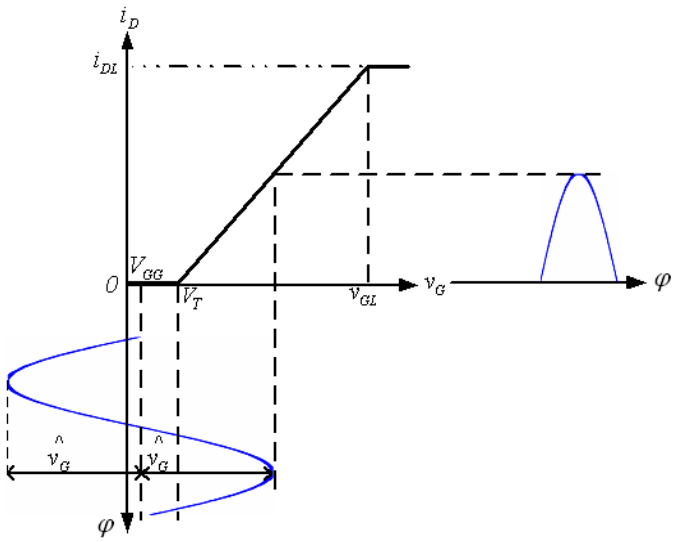

(a)

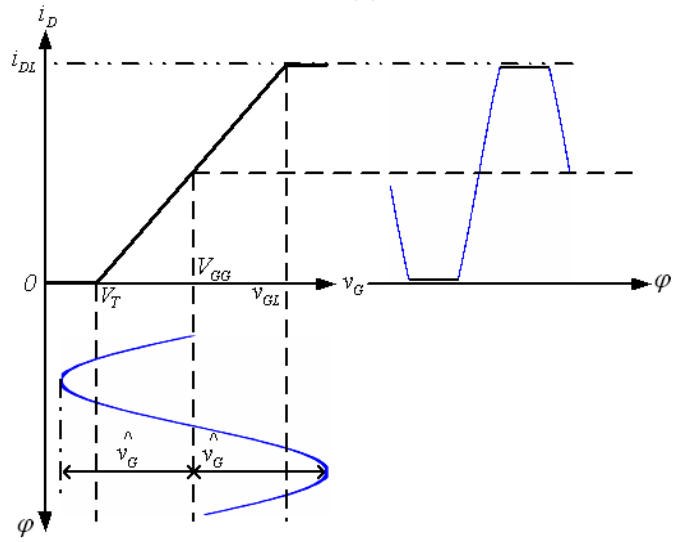

(b)

Figure 3.2 v_G and i_D waveforms with device transfer characteristic (a) case of single cut-off clipping, class C; (b) case of double clipping, class A.

for $v_G \leq V_T$, output current is zero. This effect causes clipping of i_D that we denote *cut-off clipping*. For $v_G \geq v_{GL}$, drain current reaches a limit value i_{DL} causing a form of clipping of i_D, which we denote device *knee clipping*. The case where both types of clipping occur is illustrated in Figure 3.2(b), which is for the case of a Class A amplifier overdriven by about 2 dB. The case where only cut-off clipping occurs in Figure 3.2(a) is referred to as *single clipping* and the case, where there is device knee

clipping as well as cut-off clipping as in Figure 3.2(b) is referred to as *double clipping*. The device transfer characteristic in Figure 3.2 is shown as linear, but other forms of device model will be considered in Chapters 5, 6 and 7. The device model characteristic in Figure 3.2 is termed linear here, but is referred to in [52] as the ideal non-linear model[8].

Cut-off clipping is dependent on the input voltage and the device threshold voltage V_T. Knee clipping, on the other hand, depends on the intersection of the load line of the PA with the outer edge of the triode region part of the device i_D–v_D characteristic, where i_D saturates (the knee point), as shown in Figures 1.6 and 1.7. It is therefore dependent on many factors including load resistance and supply voltage. In this thesis, whatever the class of a PA, the load line is assumed to be chosen so that the maximum output current is set to a value which is safely below the maximum limit but sufficiently high that current swing is adequate. Hence i_{DL} in Figure 3.2 is treated as a constant. This same assumption is made in the earlier clipping analyses in [51][52]. Once i_{DL} in Figure 3.2 is set in this way, the corresponding value, v_{GL}, for the input voltage is determined from the device transfer characteristic.

It follows from these considerations that it is possible to consider the i_D waveforms in Figure 3.2 to be generated from clipped versions of the input voltage, v_G. This is illustrated in Figure 3.3, which is a redrawing of Figure 3.2, but showing clipped input voltage v_{GC} in place of v_G. Note that when the concept of clipped input voltage is introduced, the form of the device transfer characteristic for $v_G < V_T$ and $v_G > v_{GL}$ becomes irrelevant. So the transfer characteristic is shown in Figure 3.3 only for the range $V_T \leq v_G \leq v_{GL}$. The concept of clipped input voltage allows us to separate the clipping effect from the device model as represented in the system block diagram of Figure 3.4. Although simple, the concept of clipped input voltage allows a more elegant mathematical description of the PA and can generate some interesting preliminary results that are independent of device model, which will be presented in Chapter 4. Note that the clipped input voltage in Figure 3.4 is hypothetical and does not exist in the actual circuit of Figure 3.1.

[8] Since all device models considered in these thesis will have cut-off and knee clipping, they are in a sense all non-linear. But we prefer to denote the model in Figure 3.2 as 'linear' because it is linear for $V_T \leq v_G \leq v_{GL}$.

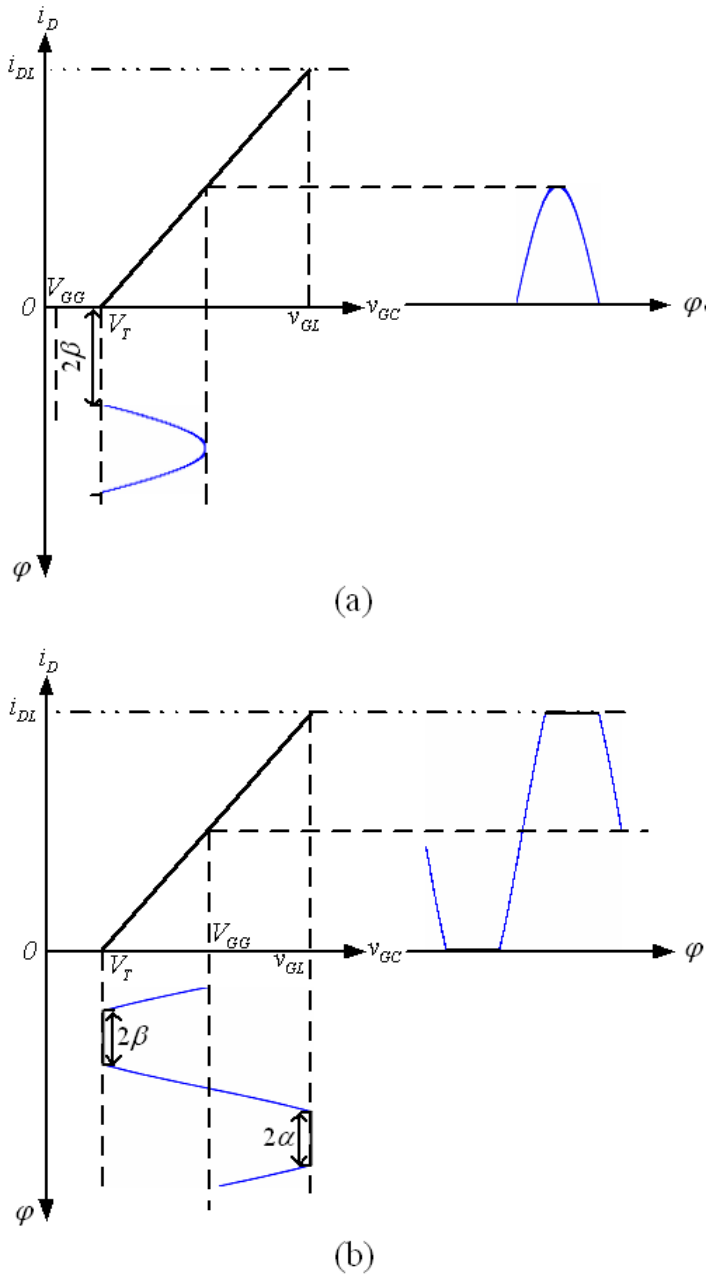

Figure 3.3 v_{GC} and i_D waveforms with device transfer characteristic (a) case of single cut-off clipping, class C; (b) case of double clipping, class A.

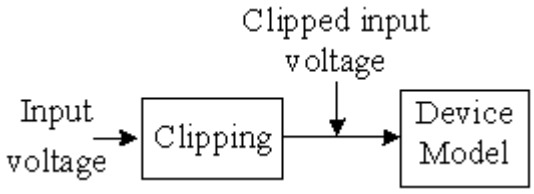

Figure 3.4 Illustration of concept of clipped device input voltage as a PA system model.

3.2.2. Knee Clipping Angle, Cut-off Clipping Angle and Conduction Angle

Angle 2α in Figure 3.3 is denoted as the *knee clipping angle*. It can be seen from Figure 3.2 that knee clipping occurs for

$$\hat{v}_G \geq v_{GL} - V_{GG} \tag{3.4}$$

From Figures 3.2(b) and 3.3(b), knee clipping angle is given by,

$$\cos\alpha = \frac{v_{GL} - V_{GG}}{\hat{v}_G} \tag{3.5}$$

In the case of, where $\hat{v}_G < v_{GL} - V_{GG}$, there is no knee clipping and $\alpha = 0$. Since in practice $V_{GG} < v_{GL}$, knee clipping angle is governed by the constraint $0 \leq 2\alpha \leq \pi$.

Angle 2β in Figure 3.3 is denoted as the *cut-off clipping angle*. For cut-off clipping, two cases should be considered. If $V_{GG} \geq V_T$ (as in Figures 3.2(b) and 3.3(b)), then cut-off clipping occurs for,

$$\hat{v}_G \geq V_{GG} - V_T \tag{3.6}$$

If $V_{GG} \leq V_T$ (as in Figures 3.2(a) and 3.3(a)), cut-off clipping occurs for,

$$\hat{v}_G \geq V_T - V_{GG} \tag{3.7}$$

In both cases, cut-off clipping angle as a function of peak input voltage is given by,

$$\cos\beta = \frac{V_{GG} - V_T}{\hat{v}_G} \tag{3.8}$$

In the case, where $V_{GG} \geq V_T$ and (3.6) applies, then β is governed by $0 \leq 2\beta \leq \pi$. When $V_{GG} \geq V_T$ and (3.6) does not apply, then $\beta = 0$ and it may be said that there is no clipping. In the case, where $V_{GG} \leq V_T$ and (3.7) applies, then β is governed by $\pi \leq 2\beta \leq 2\pi$. When $V_{GG} \leq V_T$ and (3.7) does not apply, then $\beta = \pi$ ($2\beta = 2\pi$) and the v_{GC} waveform may be described as fully clipped at which point it vanishes.

Conduction angle is commonly used in discussions about PA operation [51][52]. It is only during cut-off clipping that the PA device is not conducting current, and therefore conduction angle is given by,

$$\gamma = 2(\pi - \beta) \tag{3.9}$$

Hence,

$$\cos\frac{\gamma}{2} = -\cos\beta \tag{3.10}$$

Substituting (3.8) into (3.10), conduction angle is given by

$$\cos\frac{\gamma}{2} = \frac{V_T - V_{GG}}{\hat{v}_G} \tag{3.11}$$

Equation (3.11) showing dependence of PA conduction angle on device bias voltage and amplitude of input signal is very important. The effect of clipping as input signal amplitude changes is now considered, beginning with same key definitions.

3.2.3. Full Power Point, Saturation and Quasi-linear Input Power Ranges

Full power point (FPP) is defined as the critical transition point at which knee clipping just starts to occur, *i.e.* at which knee clipping angle α changes from zero to a non-zero value. Clipped input voltage waveforms for PAs of different classes at the FPP are illustrated in the upper part of Figure 3.5. Since what is commonly referred to as a class C PA [52] can have conduction angle anywhere between π (class B) and 0 (limit case of class C), here, it is designated as *class BC*. This emphasises that it is actually a range, like Class AB, rather than a precisely defined single class, like Class A or B.

Now the power range of a PA may be sub-divided. The range above the FPP is termed the *saturation range*. The range below the FPP is termed the *quasi-linear*

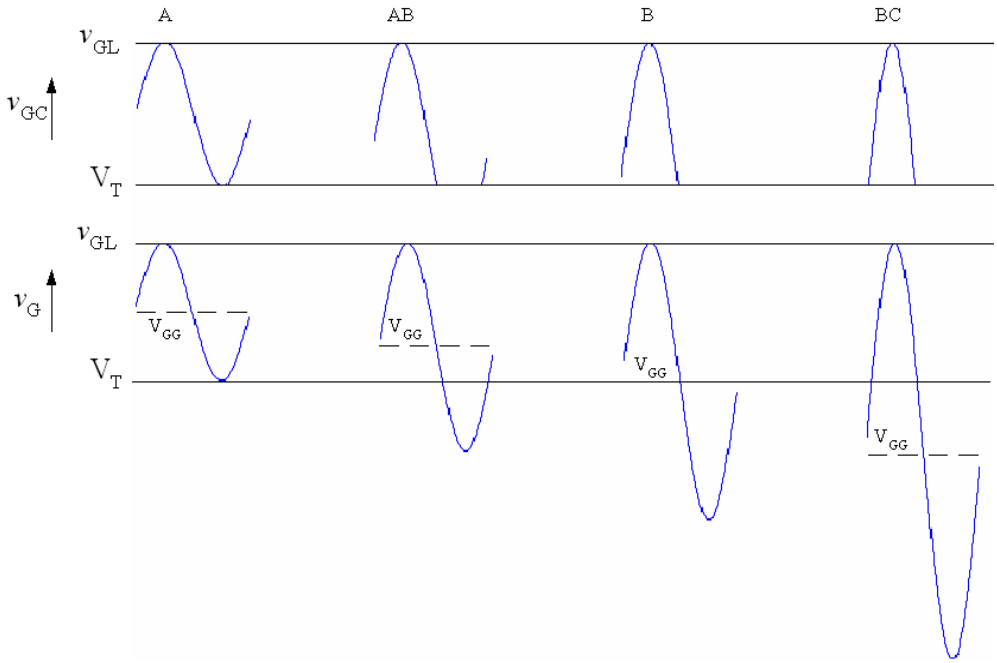

Figure 3.5 Clipped input voltage v_{GC} and input voltage v_G for PAs of different class at the FPP.

range [52], because it is over this range that the closest approach to linear behaviour is sought. In the saturation range, double clipping occurs, but in the quasi-linear range, only cut-off clipping occurs. For the clipped input voltages for different classes of PA in the upper part of Figure 3.5, the actual input voltage waveforms with the input signal bias voltage are shown in the lower part of the figure. Conditions on V_{GG} for the four cases are given in Table 3.1. The fact that for the four classes (A, AB, B and BC), input signal bias voltages are so different leads to quite different behaviour patterns when input power is reduced.

This difference of behaviour is illustrated in Figure 3.6, where the FPP conditions for the four PA classes from the top row of Figure 3.5, are shown in the

Table 3.1 V_{GG} and γ_F conditions for operation of PAs in different classes and class ranges.

Class	Class range	V_{GG}	FPCA γ_F
A		$V_{GG} = (v_{GL} + V_T)/2$	2π
	AB	$V_T < V_{GG} < (v_{GL} + V_T)/2$	$\pi \leq \gamma_F \leq 2\pi$
B		$V_{GG} = V_T$	π
	BC	$V_{GG} < V_T$	$0 \leq \gamma_F \leq \pi$

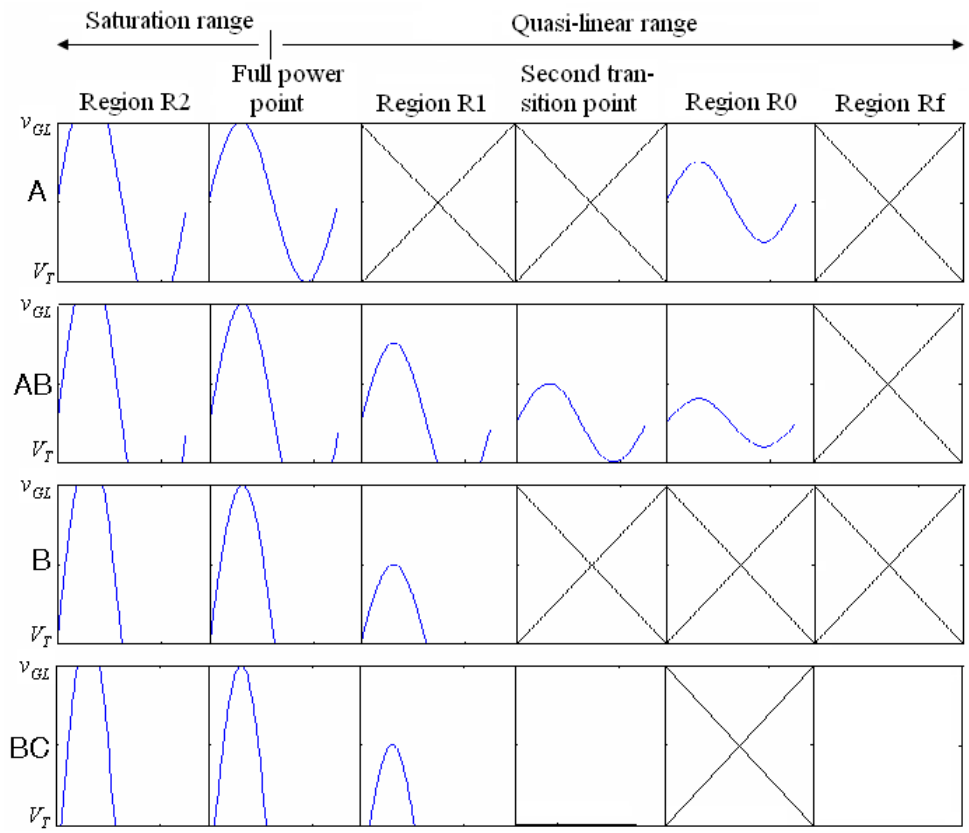

Figure 3.6 Clipped input voltage waveforms for different classes and power levels.

second column. The effect of reducing power below the FPP for different classes is shown in the third and subsequent columns of Figure 3.6. For class A and B, as the signal level is reduced, the waveshape does not change. There is a single mode of behaviour denoted region R0 for class A, as there is no clipping, and region R1 for class B, as there is single clipping. For class AB, however, there is a critical second transition point where the signal becomes a sinewave. For Class BC, there is also a critical second transition point, but at that point the signal becomes zero. This difference between Class AB and BC can be understood from the lower part of Figure 3.5 by imagining that the amplitude of the input signal is reduced for the two cases. Reducing the PA input signal amplitude beyond the second transition point leads to a further region in Figure 3.6 (region R0) for Class AB, where the sinewave amplitude reduces. For Class BC the signal remains zero, and, since in this region, the knee clipping angle 2β in Figure 3.3(a) is 2π, the signal is fully clipped and the region denoted Rf as shown in Figure 3.6.

The first column of Figure 3.6 shows the clipped gate voltage for gate voltage amplitude about 3 dB higher than the FPP. The region above FPP, where double clipping occurs is denoted R2. In the limit as gate voltage amplitude is increased, the waveforms for all classes converge to a square wave with peak-to-peak amplitude $v_{GL} - V_T$ and therefore become identical.

The definition of FPP as it has been given provides a boundary between the saturation and quasi-linear power range. For input voltage amplitude above the FPP, the peak-to-peak value of output current must remain constant, so the fundamental component of output current can increase only by a few dB due to change in waveshape. On the other hand, below the FPP, it is obvious that peak output current must change strongly with input signal amplitude.

The function of a boundary between the saturation and quasi-linear power ranges is normally performed by the 1 dB compression point, but 1 dB compression point does not have the mathematical properties needed here. The definition of FPP, on the other hand, is mathematically straightforward and allows this theory to be developed in an elegant way as will be shown in Chapter 4.

3.2.4. Full Power Conduction Angle and Class Definition

In the literature [51][52], the class of a PA is defined using conduction angle. However, (3.11) shows that conduction angle γ is dependent on PA input voltage amplitude $\hat{v}_G$. This is a difficulty that can create considerable confusion about the class that a PA is actually operating in. However, this problem may be overcome by introducing an important definition. *Full power conduction angle* (FPCA), γ_F, is defined as the conduction angle γ, according to (3.11), but specifically at the full power point as defined in section 3.2.3. The concept of FPCA allows a strict formal definition of the class of a PA. The class definitions and corresponding values of γ_F are given in Table 3.1.

From Table 3.1, the point $\gamma_F = \pi$ rads divides the entire class range from A to C into two ranges that are denoted here as the *AB class range* and the *BC class range*. The definition of the class of a PA using the conduction angle at the full power point (γ_F) is a key idea that makes possible the mathematical development that will begin in Chapter 4. The definition of PA class may differ slightly from that based on 1 dB

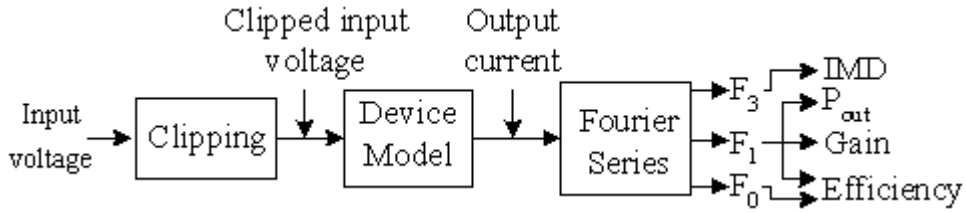

Figure 3.7 System model for PA biased on clipping.

compression point, but no alternative to the FPP and γ_F as a basis for a very general mathematical approach, such as will be presented here, has been found.

3.3. Equivalent System Model for Predicting PA Performance

In section 3.2.1, it has been shown that the clipping effects that occur in a PA may be regarded as being applied to the PA input voltage and this concept led to the system representation in Figure 3.4 that models part of the PA operation. Figure 3.4 may now be completed by extending it to the form shown in Figure 3.7, where Fourier series coefficients for the output current of the device are included. Assuming a single tone sinusoidal input voltage, the first order Fourier series coefficient gives the output signal power and gain. From the zero and first order coefficients, efficiency is obtained. From the third order coefficient, 3rd order distortion is derived. Different device models will be introduced and the corresponding Fourier coefficients will be derived in later chapters. Before this, some fundamental results that are independent of device model will be developed in the next chapter.

3.4. Conclusion

In this chapter, important foundations for a comprehensive theory of PA device current clipping have been laid. Some key definitions have been given and an equivalent block diagram model for the PA system behaviour has been proposed.

Firstly, two types of clipping, cut-off and knee clipping, have been identified. It has been shown that the clipped device output current may be considered to be

generated from a clipped version of the device input voltage. Then mathematical expressions for general cut-off and knee clipping angles were derived and related to conduction angle. Full power point (FPP) was defined as the point where knee clipping just starts to occur. The power range above FPP is denoted the saturation range, whereas that below the FPP is denoted the quasi-linear range. The effect of reducing and increasing input signal power with respect to the FPP for different classes of PA was considered. It was found that there were large changes in conduction angle and changes of state between no clipping, single clipping, double clipping and full clipping. The difficulty in formal definition of the class of a PA due to variation of conduction angle with input voltage amplitude was solved by introducing the concept of full power conduction angle, γ_F, which is the conduction angle at the FPP.

This idea led to a proposal of a system block diagram model for predicting PA performance that will form the basis for the approach in this thesis. This diagram includes the concept of considering clipping to be applied to the device input voltage, which is key to this theory. It also includes aspects that will be considered in future chapters, such as the form of the device model and the derivation of Fourier series coefficients of the device output current waveform in order to obtain PA performance prediction.

Key aspects of the fundamental theory have been laid in this chapter. In the next chapter, the theory will be developed to obtain some preliminary results that are independent of the form of the device model.

CHAPTER 4

RESULTS THAT ARE INDEPENDENT OF DEVICE MODEL

4.1. Introduction

In the last chapter, an equivalent block diagram model for PA system performance has been proposed based on the key definitions and concepts developed. The system model includes the device model. However, at this stage it is possible to derive some very important results that are independent of device model. These results are interesting and useful in themselves and also will provide a good foundation for the introduction of device models in the following three chapters.

The results in this chapter include the device input bias voltage for any class of operation, the amplitude of the input signal that corresponds to the full power point and the precise way in which clipping and conduction angles vary with class and input signal amplitude.

4.2. Device Bias Voltage

PA class is determined by γ_F, or conduction angle γ at the FPP condition. The FPP is the borderline between single clipping (or in the case of Class A no clipping) and double clipping where the inequality (3.4) becomes an equality:

$$\hat{v}_G = v_{GL} - V_{GG} \tag{4.1}$$

Setting $\gamma = \gamma_F$ in (3.11) and substituting (4.1) into it, the FPCA as a function of input signal and the bias voltage can be derived,

$$\cos\frac{\gamma_F}{2} = \frac{V_T - V_{GG}}{v_{GL} - V_{GG}} \tag{4.2}$$

Rearranging (4.2), V_{GG} as a function of γ_F is given

$$V_{GG} = \frac{V_T - v_{GL}\cos\frac{\gamma_F}{2}}{1 - \cos\frac{\gamma_F}{2}} \tag{4.3}$$

In order to make prediction results from the theory as general as possible so that they can be applied to any practical PA, from this point, normalisation is applied to the input voltage. The normalisation is such that the maximum input voltage, v_{GL} in Figures 3.2 and 3.3, is set to be V_T + 2 V. With this method of normalisations, the peak-to-peak clipped input voltage at the FPP is 2 V for a PA of any class and the peak clipped input voltage, $\hat{v}_{GC}$, is 1 V.

Adopting this normalisation and rearranging (4.3), the effective gate bias voltage V_{GGe} is obtained,

$$\begin{aligned} V_{GGe} &= V_{GG} - V_T \\ &= \frac{2\cos\frac{\gamma_F}{2}}{\cos\frac{\gamma_F}{2} - 1} \end{aligned} \tag{4.4}$$

A plot of V_{GGe} as a function of γ_F is shown in Figure 4.1. When $\gamma_F = \pi$ (class B), $V_{GGe} = 0$ which implies that the DC bias voltage V_{GG} is equal to the threshold voltage V_T. When $\gamma_F = 2\pi$ (class A), V_{GGe} is 1 V, half of the maximum limit value, as expected. When $\gamma_F < \pi$ (BC class range), the PA needs a large negative DC bias voltage, which has been recognised in [52].

The extrapolation function, to be discussed next, is a function that is fundamental to the theory of PA behaviour that is to be presented.

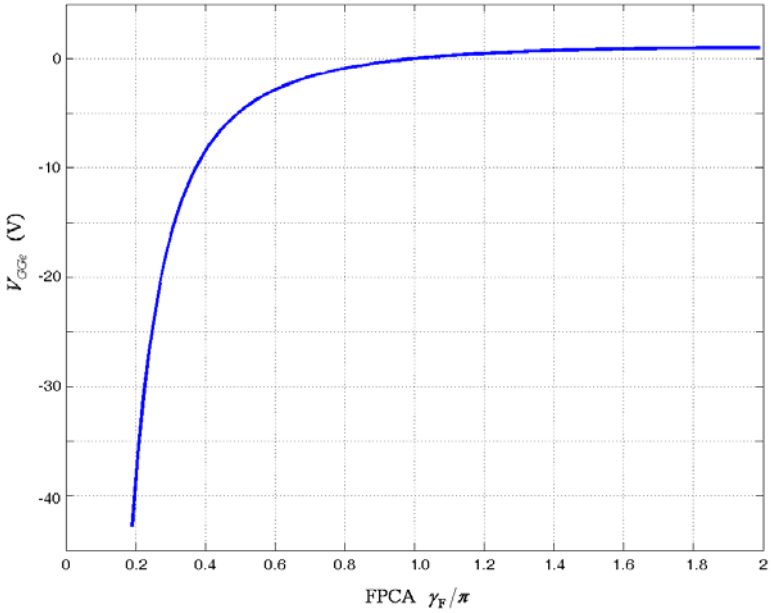

Figure 4.1 Input voltage varies with the conduction angle.

4.3. Extrapolation Function

The extrapolation function (F_e) is defined as the ratio of the peak amplitude $\hat{v}_{GC}$ of the clipped PA input voltage v_{GC} to the peak amplitude $\hat{v}_G$ of the input voltage v_G,

$$F_e = \frac{\hat{v}_{GC}}{\hat{v}_G} \tag{4.5}$$

$\hat{v}_G$ is defined in (3.3) and in Figure 3.3. $\hat{v}_{GC}$ is defined as half of the peak-to-peak value of the clipped input voltage v_{GC}. For the four types of clipping identified in Chapter 3, no clipping and single, double and full clipping, the clipped input voltage and the definition of $\hat{v}_{GC}$ is illustrated in Figure 4.2. In order to evaluate (4.5), it is helpful to define the maximum and minimum values, v_{GCmax} and v_{GCmin} of the clipped input voltage, shown on the right side of each waveform in Figure 4.2. If there is no knee clipping, then $v_{GCmax} = V_{GG} + \hat{v}_G$; otherwise, $v_{GCmax} = v_{GL}$. If there is no cut-off clipping then $v_{GCmin} = V_{GG} - \hat{v}_G$; otherwise $v_{GCmax} = V_T$. Note that case of full clipping shown in Figure 4.2(d), where $V_{GG} + \hat{v}_G$ is smaller than V_T, for the clipped

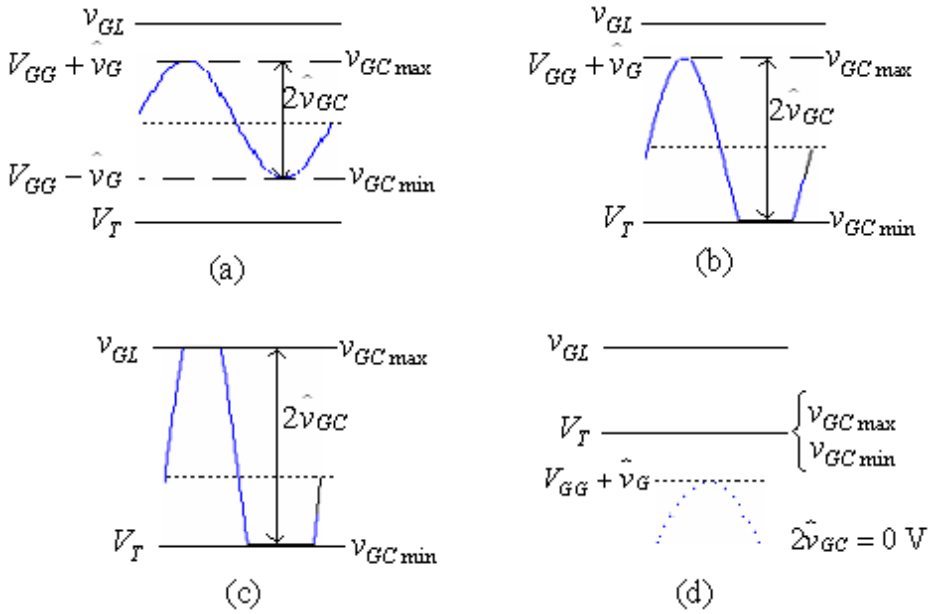

Figure 4.2 Clipped PA input voltage in three cases; (a) no clipping; (b) single clipping; (c) double clipping; (d) full clipping.

input voltage waveform vanishes and $\hat{v}_{GC}$ = 0. From Figure 4.2, it is evident that in all four cases,

$$2\hat{v}_{GC} = v_{GC\,\max} - v_{GC\,\min} \tag{4.6}$$

The concepts of v_{GCmax} and v_{GCmin} can be used to unite (3.5) and (3.8) in a form that applies in all four cases in Figure 4.2.

$$\cos\alpha = \frac{v_{GC\,\max} - V_{GG}}{\hat{v}_G} \tag{4.7}$$

$$\cos\beta = \frac{V_{GG} - v_{GC\,\min}}{\hat{v}_G} \tag{4.8}$$

Rearranging (4.5) - (4.8) leads to

$$F_e = \frac{1}{2}\left(\cos\alpha + \cos\beta\right) \tag{4.9}$$

This expression for the extrapolation function in terms of knee and cut-off clipping angles underlies the further results that will be obtained in this chapter. Some idea of the significance of the extrapolation function may be gained from Figure 3.5. From (4.5), F_e is the ratio of $\hat{v}_{GC}$ to $\hat{v}_G$ in Figure 3.5. But whereas Figure 3.5 shows waveforms for all classes only at the FPP, F_e in (4.9) applies not only to all classes but to all types of clipping and therefore to all power levels.

In the special case of the quasi-linear range of PA operation that includes the FPP, $\alpha = 0$, and the extrapolation function becomes,

$$F_{eL} = \frac{1}{2}\left(1 + \cos\beta\right) \tag{4.10}$$

Then from (3.9), β may be expressed in terms of conduction angle,

$$F_{eL} = \frac{1}{2}\left(1 - \cos\frac{\gamma}{2}\right) \tag{4.11}$$

This expression will be applied in order to derive some very important results in the following sections.

4.4. Amplitude of PA Input Voltage Corresponding to FPP for Any Class of PA

From (4.5), PA input voltage amplitude may be expressed in terms of the amplitude of the hypothetical clipped input voltage, by:

$$\hat{v}_G = \frac{\hat{v}_{GC}}{F_e} \tag{4.12}$$

Using normalisation, as described in section 4.2, for v_G, then, at the FPP, $\hat{v}_{GC}$ in (4.12) becomes 1 V. The value of $\hat{v}_G$ at the FPP, denoted $\hat{v}_{GF}$, is obtained by substituting (4.11) into (4.12) and by setting $\gamma = \gamma_F$,

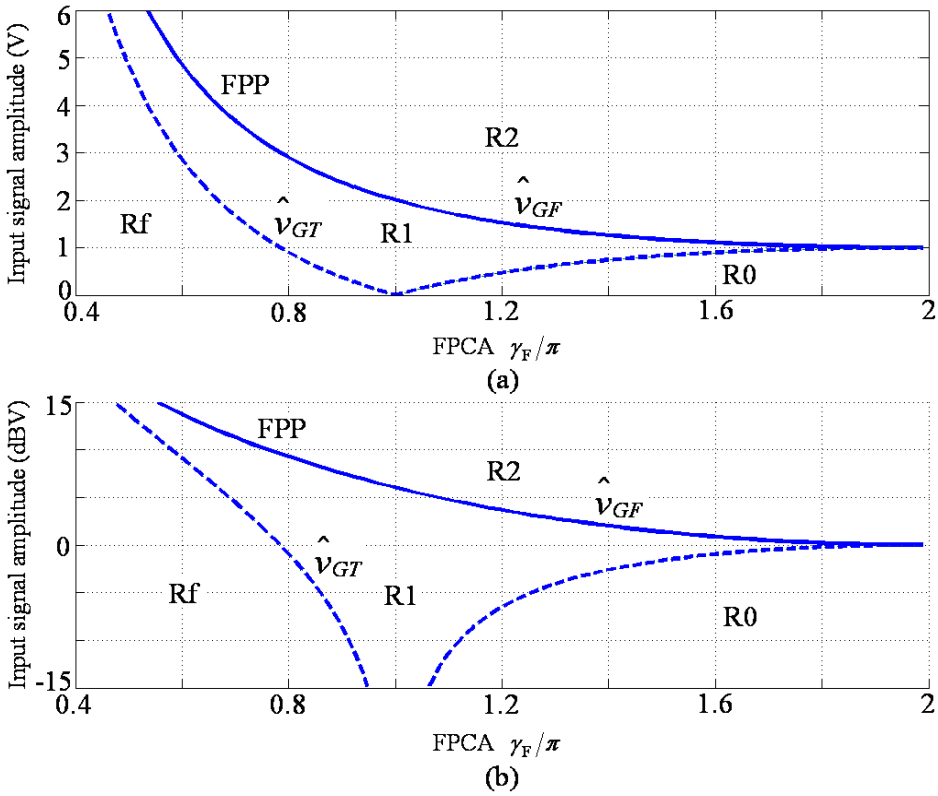

Figure 4.3 Regions of PA operation defined in $\hat{v}_G - \gamma_F$ space in the terms of clipping. (a) using units of V for $\hat{v}_G$; (b) using units of dBV for $\hat{v}_G$.

$$\hat{v}_{GF} = \frac{2}{1-\cos\frac{\gamma_F}{2}} \tag{4.13}$$

A plot of $\hat{v}_{GF}$ versus γ_F is shown by the solid line in Figure 4.3(a). This shows that for a Class B PA ($\gamma_F = \pi$), the input voltage needed at the FPP is double that for class A ($\gamma_F = 2\pi$). For class BC ($0 \le \gamma_F \le \pi$) considerable input voltage amplitudes are required as γ_F is reduced in this range. As indicated in Figure 4.3(a), (4.13) constitutes a boundary between the region of the plot (R2) corresponding to the saturation range of operation where there is double clipping and the quasi-linear region (R1) where there is single clipping. Since the $\hat{v}_{GF}$ curve in Figure 4.3(a) relates input signal amplitude at the full power point to γ_F, in Figure 4.3(a) and in subsequent graphs it will be labelled as the FPP contour.

4.5. Subdivision of Quasi-Linear Region

It can be seen from Figure 3.6 that the second transition point that occurs in the quasi-linear region for class range AB and BC corresponds to a change from single clipping to no clipping or to full clipping, respectively. This point is defined by the inequalities (3.6) and (3.7) governing the occurrence of cut-off clipping becoming equalities,

$$\hat{v}_{GT} = \pm\left(V_{GG} - V_T\right) \tag{4.14}$$

where $\hat{v}_{GT}$ is the input voltage amplitude corresponding to the second transition point and the '+' and '−' signs are for $V_{GG} \geq V_T$ (AB class range) and $V_{GG} \leq V_T$ (BC class range), respectively. Substituting for V_{GG} in (4.14) in terms of γ_F using (4.3), the cut-off clipping boundary is given by

$$\begin{aligned}\hat{v}_{GT} &= \left|\frac{V_T - v_{GL}\cos\frac{\gamma_F}{2}}{1-\cos\frac{\gamma_F}{2}} - V_T\right| \\ &= \left|\frac{\left(V_T - v_{GL}\right)\cdot\cos\frac{\gamma_F}{2}}{1-\cos\frac{\gamma_F}{2}}\right|\end{aligned} \tag{4.15}$$

Normalising v_G by setting $v_{GL} = V_T + 2$ V,

$$\hat{v}_{GT} = \left|\frac{2\cos\frac{\gamma_F}{2}}{1-\cos\frac{\gamma_F}{2}}\right| \tag{4.16}$$

Equation (4.16) is plotted in Figure 4.3(a) using a dashed line. For the BC class range ($\gamma_F \leq \pi$), (4.16) defines the boundary between single clipping (R1) and the region (Rf) of full clipping (no conduction); for the AB class range ($\gamma_F \geq \pi$), it defines the boundary between single clipping (R1) and no clipping (R0). Thus, the entire $\hat{v}_G$

$-\gamma_F$ space in Figure 4.3(a) is divided into four distinct regions depending on the type of clipping that occurs. Figure 4.3(a) quantifies what was shown in Figure 3.6. For sufficiently high input voltage amplitude, PAs of all classes operate in region R2. As input voltage is reduced, the Class A PA goes directly into the R0 region at the FPP. All other classes go into the R1 region at the FPP. Then for even lower input voltage, PAs in the AB class range go from region R1 into region R0, of no clipping and those in the BC class range from region R1 into region Rf of full clipping.

Figure 4.3(a) shows that for all classes of PA except class A, the FPP is bordered in the quasi-linear region by a region of single clipping. This region is critically important for PA performance, especially IMD, as will be shown. Figure 4.3(b) shows the data from Figure 4.3(a) but using a scale for input signal amplitude $\hat{v}_G$ in units of dBV. $\hat{v}_G$ at the FPP for classes A and B is now 0 dBV and 6 dBV, respectively. The axes of Figure 4.3(b), input signal amplitude, $\hat{v}_G$, and PA class, γ_F, are the two key parameters, which critically affect all aspects of PA performance. Thus, from this point in this thesis, Figure 4.3(b) will be used as a base on which to present 3-D plots of PA performance metrics.

It can be observed that the expression for $\hat{v}_{GT}$ in (4.16) is just the magnitude of the effective gate bias voltage in (4.4). This may be simply explained by the fact that at the border line between single clipping and either no clipping or full clipping, the input signal amplitude $\hat{v}_{GT}$ is equal to $\pm (V_{GG} - V_T)$, according to (4.14).

4.6. Peak Clipped Gate Voltage versus Input Signal Amplitude and Class

The peak value of the clipped input voltage waveform, $\hat{v}_{GC}$, as illustrated in Figure 4.2 is now investigated as a function of independent variables γ_F (PA class) and $\hat{v}_G$ (input signal amplitude) *i.e.* as a function of the variables of Figure 4.3(b). For the single clipping region R1, $\alpha = 0$, and the peak clipped gate voltage may be written, using (4.5) and (4.10) as

$$\begin{aligned}\hat{v}_{GC} &= F_{eL}\hat{v}_G \\ &= \frac{1}{2}\left(1+\cos\beta\right)\hat{v}_G\end{aligned} \tag{4.17}$$

Nonlinearity arises, in general, from the dependence of cosβ on $\hat{v}_G$ according to (3.8). $\hat{v}_{GC}$ as a function of γ_F is given by substituting for cosβ using (3.8) and then for V_{GG} using (4.3),

$$\begin{aligned}\hat{v}_{GC} &= \frac{1}{2}\left[\hat{v}_G + \frac{V_T - v_{GL}\cos\frac{\gamma_F}{2}}{1-\cos\frac{\gamma_F}{2}} - V_T\right] \\ &= \frac{1}{2}\left[\hat{v}_G + \frac{\left(V_T - v_{GL}\right)\cos\frac{\gamma_F}{2}}{1-\cos\frac{\gamma_F}{2}}\right]\end{aligned} \tag{4.18}$$

Normalising v_G by setting $v_{GL} = V_T + 2V$ leads to,

$$\hat{v}_{GC} = \frac{\hat{v}_G}{2} - \frac{\cos\frac{\gamma_F}{2}}{1-\cos\frac{\gamma_F}{2}} \tag{4.19}$$

A 3-D plot of $\hat{v}_{GC}$ versus $\hat{v}_G$ and γ_F for region R1, according to (4.19), is shown in Figure 4.4. The units for $\hat{v}_{GC}$ are dBV and $\hat{v}_G$ and γ_F coordinates that form the base for the plot are the same as in Figure 4.3(b). The four regions of Figure 4.3(b) and the contours dividing them, FPP and $\hat{v}_{GT}$, can be clearly seen in Figure 4.4. Now consider how the remaining regions (R2 and R0) in Figure 4.4 may be plotted.

At the FPP, which is the boundary between regions R1 and R2, substitution of $\hat{v}_G = \hat{v}_{GF}$ according to (4.13), into (4.19) gives $\hat{v}_{GC} = 1$. This applies for $\hat{v}_G > \hat{v}_{GF}$, as can be seen in Figure 3.6. The boundary between regions R1, R0 and Rf occurs for $\hat{v}_G = \hat{v}_{GT}$ given by (4.16). Substituting $\hat{v}_G = \hat{v}_{GT}$ from (4.16) into (4.19) gives for $\gamma_F \geq \pi$ ('+' sign in (4.16)) $\hat{v}_G = \hat{v}_{GC}$, and for $\gamma_F \leq \pi$ ('−' sign in (4.16)) $\hat{v}_{GC} = 0$. This

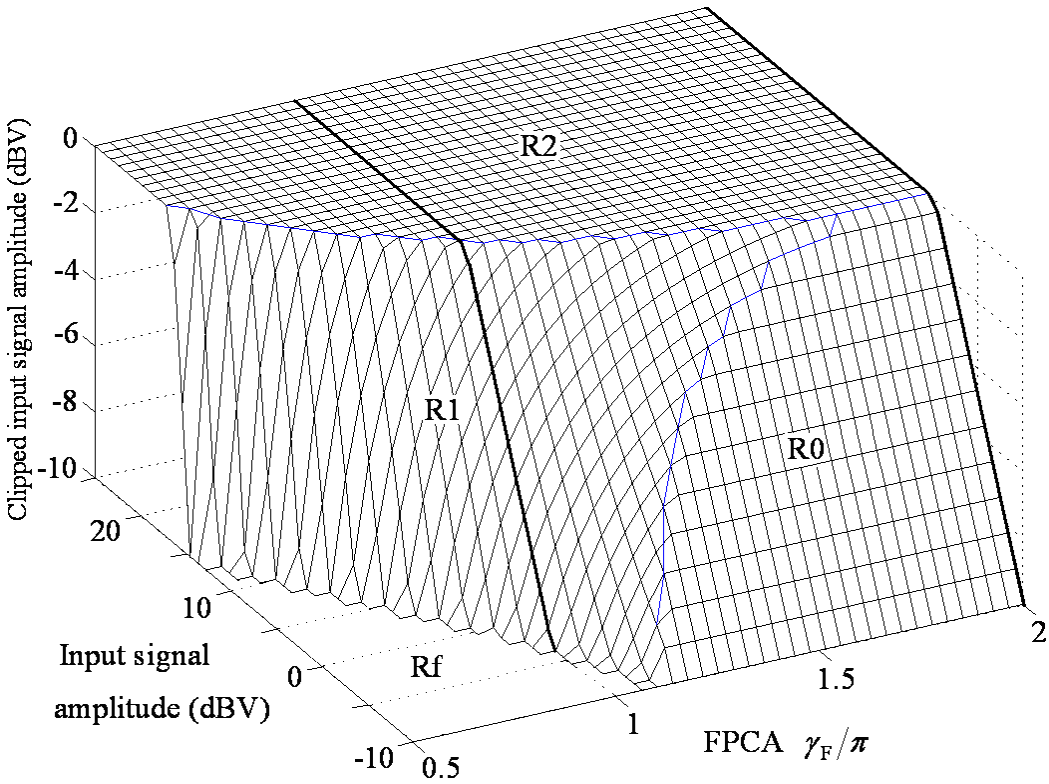

Figure 4.4 Clipped peak input signal versus FPCA γ_F and input signal amplitude $\hat{v}_G$.

allows the plot in Figure 4.4 to be completed for the remaining regions R2, R0 and RF.

The PA system model in Figure 3.7 shows that the effect of clipping, that can be considered to be applied to the PA input signal, is an inescapable underlying factor affecting PA performance. Thus, features from Figure 4.4 can all be observed in the output power characteristics of a real PA. These features include, in the quasi-linear range, the linear behaviour for class A and B, reduction in slope in region R1 in the AB class range ($\gamma_F \geq \pi$) and increase in slope in region R1 in the BC class range ($\gamma_F \leq \pi$).

The device model and Fourier series blocks in the system model of Figure 3.7 modify these fundamental aspects of PA performance, as will be shown when device models will be introduced in Chapters 5, 6 and 7.

4.7. Clipping and Conduction Angles versus Input Signal Amplitude and Class

In the R2 region, in which knee clipping occurs, using (3.5) and (4.3) , the knee clipping angle is given by

$$\begin{aligned}\alpha &= \arccos\frac{v_{GL}-V_{GG}}{\hat{v}_G}\\ &= \arccos\left[\frac{v_{GL}}{\hat{v}_G}-\frac{V_T-v_{GL}\cos\frac{\gamma_F}{2}}{\hat{v}_G\left(1-\cos\frac{\gamma_F}{2}\right)}\right]\\ &= \arccos\frac{v_{GL}-V_T}{\hat{v}_G\left(1-\cos\frac{\gamma_F}{2}\right)}\end{aligned} \tag{4.20}$$

The knee clipping angle below the FPP is always zero. Normalising the gate voltage (4.20) becomes

$$\alpha = \arccos\frac{2}{\hat{v}_G\left(1-\cos\frac{\gamma_F}{2}\right)} \tag{4.21}$$

Using (3.8) and (4.3), the cut-off clipping angle in the R1 and R2 regions is given by

$$\begin{aligned}\beta &= \arccos\frac{V_{GG}-V_T}{\hat{v}_G}\\ &= \arccos\left(\frac{V_T-v_{GL}\cos\frac{\gamma_F}{2}}{\hat{v}_G\left(1-\cos\frac{\gamma_F}{2}\right)}-\frac{V_T}{\hat{v}_G}\right)\end{aligned} \tag{4.22}$$

$$= \arccos \frac{\left(V_T - v_{GL}\right)\cos\frac{\gamma_F}{2}}{\hat{v}_G\left(1-\cos\frac{\gamma_F}{2}\right)}$$

Normalising the gate voltage by setting $v_{GL} = V_T + 2V$ gives,

$$\beta = \arccos \frac{-2\cos\frac{\gamma_F}{2}}{\hat{v}_G\left(1-\cos\frac{\gamma_F}{2}\right)} \tag{4.23}$$

The cut-off clipping angle in region R0 is $\beta = 0$ and in region Rf is $\beta = \pi$ rads. The values of the clipping angles α and β in all four regions of Figure 4.3 are summarized in Table 4.1.

Substituting (4.23) into (3.9), conduction angle, with normalisation, is given by

$$\gamma = 2\pi - 2\arccos \frac{-2\cos\frac{\gamma_F}{2}}{\hat{v}_G\left(1-\cos\frac{\gamma_F}{2}\right)} \tag{4.24}$$

Figure 4.5(a), (b) and (c) show α, β and γ from (4.21), (4.23) and (4.24) as a function of input signal amplitude $\hat{v}_G$ and γ_F, respectively.

Table 4.1 Clipping angles in four clipping regions.

Region	Clipping	α	β
R2	Double	(4.21)	(4.23)
R1	Single	0	(4.23)
R0	No	0	0
Rf	Full	0	π

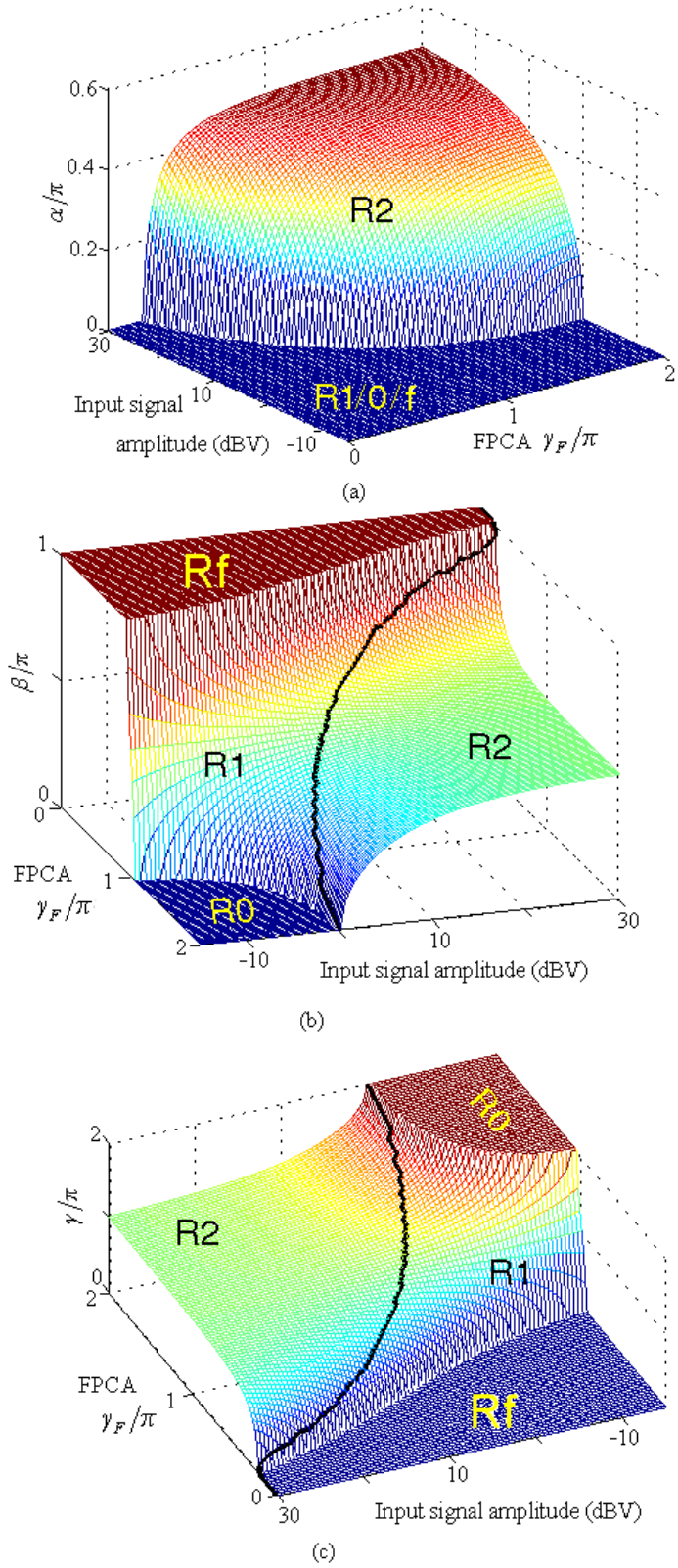

Figure 4.5 Clipping angles and conduction angel versus FPCA γ_F and input signal amplitude $\hat{v}_G$. (a) α; (b) β; (c) γ.

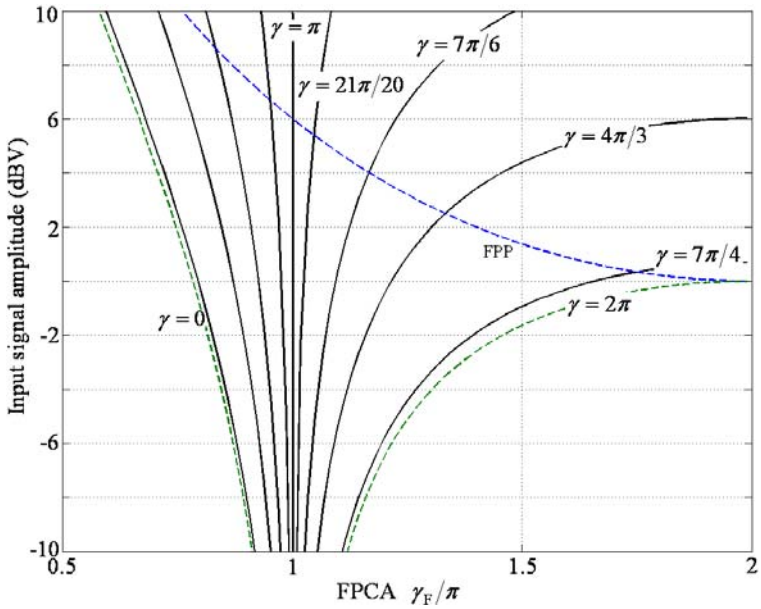

Figure 4.6 Contours of constant conduction angle (γ) versus input signal amplitude $\hat{v}_G$ and FPCA γ_F.

From Figure 4.5(a), α is zero except in the R2 region, as expected. As the input signal increases, α increase up to a limit of π/2. From Figure 4.5(b), β keeps constant at 0 in the R0 region. In the Rf region, β is π. In the R2 region, as $\hat{v}_G$ increases, β reaches a limit of π/2. This limit is approached from 0 in the class AB range ($\gamma_F \geq \pi$) and from π in the class BC range ($\gamma_F \geq \pi$). From Figure 4.5(c), conduction angle γ decreases for class A ($\gamma_F = 2\pi$ rads) from 2π to π rads in the saturation region R2 has been observed in [52].

The dependence of conduction angle on input signal power is further emphasised in Figure 4.6, which shows a contour plot of constant γ values derived from Figure 4.5(c) plotted against input signal amplitude $\hat{v}_G$ and full power conduction angle, γ_F. The distinction between conduction angle γ and full power conduction angle γ_F is critical to the approach developed in this work. Note in Figure 4.6 that conduction angle is equal to full power conduction angle only on the FPP contour. Figure 4.6 shows that conduction angle does not change with input signal power for class A in the quasi-linear region ($\gamma = \gamma_F = 2\pi$) rads, or for class B in all regions ($\gamma = \gamma_F = \pi$) rads. However for γ_F close to π rads in the quasi-linear region and for γ_F close to

zero or 2π rads in the saturation region, the change in γ with signal power is very considerable and approaches π rads.

4.8. Conclusions

In this chapter, some preliminary mathematical results independent of device model have been presented. The possibility of obtaining such results flows from the idea, proposed in Chapter 3, of regarding clipping as being applied to the PA device input voltage.

First, an expression for device input signal bias voltage was derived as a function of full power conduction angle γ_F, which defines the class of the PA. A plot of this expression confirmed the very large negative bias needed for a PA in the BC class range with small γ_F, mentioned in [52]. Then, the extrapolation function, which underlies the mathematical description of the clipping effect in PAs, has been introduced and evaluated as a function of clipping and conduction angles. The extrapolation function was used to determine the amplitude of PA input voltage corresponding to FPP for any class of PA. It made it possible to plot the FPP as a contour in a graph of input signal power versus full power conduction angle γ_F, *i.e.* PA class, and it constitutes a boundary between the regions of the plot corresponding to the saturation and quasi-linear operation regions. Then, the quasi-linear region was subdivided into regions with single clipping, no clipping and full clipping. Thus, the space with dimensions of input voltage amplitude and γ_F (or class) was divided into four distinct regions, governed by four types of clipping (double, single, full and none) that had been identified in Chapter 3. Expressions for peak clipped input voltage as a function of input signal amplitude and class were determined and a 3-D plot showing this dependence was produced. Many characteristics of the output power of a real PA as a function of class and input power were already evident in that plot. Finally, expressions for clipping and conduction angles as functions of input signal amplitude and class were derived. 3-D plots show the very significant variation of these angles with input signal power.

Key aspects of the device current clipping theory for PAs have been laid in the last two chapters. The understanding of clipping effects and preliminary mathematical results now provide a platform for the introduction of device models, and this will be done in the next three chapters.

CHAPTER 5

LINEAR DEVICE MODEL AND PA PERFORMANCE

5.1. Introduction

The last two chapters proposed a comprehensive device current clipping theory for PA behaviour and derived some preliminary results that are independent of device model. In this chapter and the following two chapters, the device model block in the PA system diagram of Figure 3.7 will be introduced. This chapter is devoted to introducing the linear device model and using Fourier series to derive PA performance metrics.

The chapter begins by laying some mathematical foundations for what follows. The linear device model is described and the Fourier coefficients of the resulting output current derived analytically. Then PA metrics will be evaluated mathematically and presented as 3-D plots. This will lead to an assessment of the linear model with respect to how the predicted PA metrics compare with published metrics.

5.2. General

5.2.1. Assumptions

As stated in Chapter 3 (section 3.2.1) and illustrated in Figure 3.2, the models

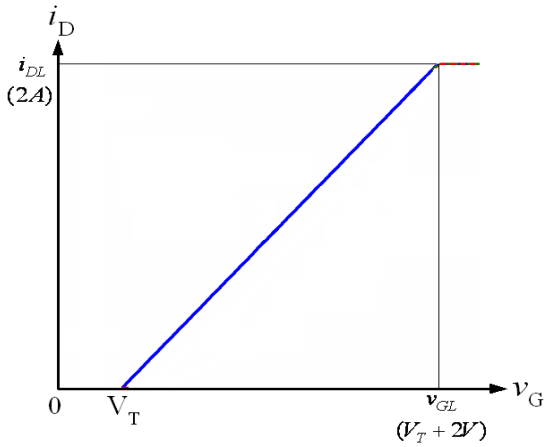

Figure 5.1 Transfer characteristic for the linear device model showing normalisation.

that are considered in this thesis are DC models subject to some simple constraints. These are:

1) For PA input voltage v_G equal to or less than device threshold voltage V_T, the device output current i_D is zero, as illustrated again in Figure 5.1.
2) Device output current is limited to a maximum value i_{DL}, as in Figure 5.1. The value of PA input voltage for which i_D reaches its limit is denoted v_{GL}.

Just as PA input voltage was normalised in Chapter 4 (section 4.2), the output current is now normalised. The limit value of i_D, i_{DL}, is set to be 2A. The normalised limit value of device output current and the corresponding normalised value of device input voltage are given in brackets in Figure 5.1. With this normalisation, for any class of PA at the FPP, the peak-to-peak output current is 2 A and the peak-to-peak clipped input voltage is 2V. Thus, at the FPP, the peak clipped input voltage amplitude $\hat{v}_{GC}$ is 1 V and the peak output current $\hat{i}_D$ is 1 A, where peak output current is defined as one half of the peak-to-peak value.

It is obvious from the way in which device output current is derived from the input voltage via a transfer characteristic, as illustrated in Figure 3.2 that both the positive and negative peaks of the output current waveform will have even symmetry. In order to make the whole waveform an even function, the $\varphi = 0$ reference for the device input voltage may be chosen as the value corresponding to the positive peak value, as shown in Figure 5.2(a). This allows some simplifications in deriving the Fourier series coefficients, as will be shown in the next sub-section.

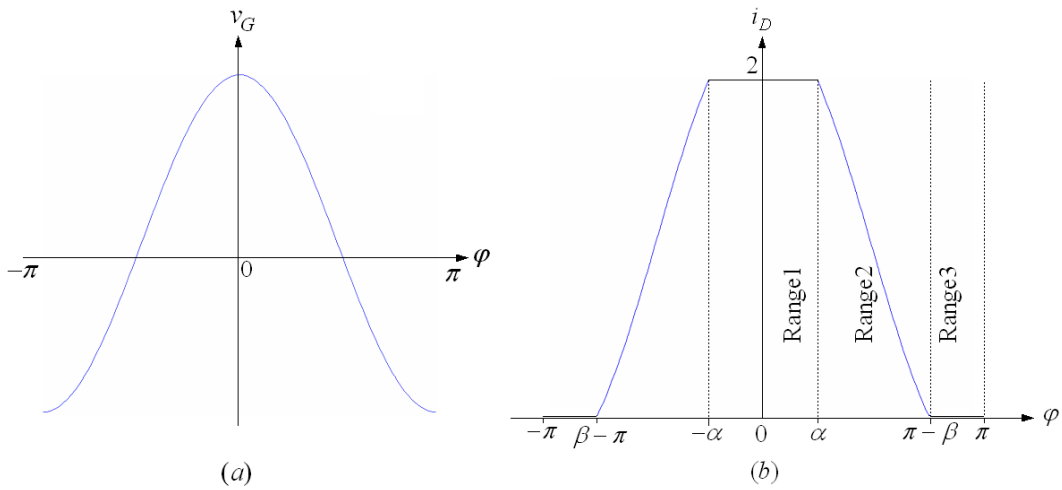

Figure 5.2 (a) Illustration of the φ = 0 reference point showing one period of input voltage waveform; (b) illustration of the three ranges of the drain current waveform.

Now consider device output current. If there is no clipping, then $\varphi = 0$ and $\varphi = \pi$ correspond to the maximum and minimum of the current waveform that results from the device input voltage waveform of Figure 5.2(a). If there is clipping (cut-off, knee or both), then $\varphi = 0$ and $\varphi = \pi$ correspond to the mid-points of the clipped parts of the current waveform, as shown in Figure 5.2(b). Angles α and β may be regarded as knee and cut-off clipping angles for a half-period of the even-symmetric waveform.

In general, the device output current waveform can be divided into three ranges, as shown in Figure 5.2(b).

Range 1: $i_D = 2$ $\quad 0 \le \varphi \le \alpha$ (5.1)

Range 2: i_D depends on device model $\quad \alpha \le \varphi \le \pi - \beta$ (5.2)

Range 3: $i_D = 0$ $\quad \pi - \beta \le \varphi \le \pi$ (5.3)

These three ranges, 1, 2 and 3, correspond to the three parts of the device transfer characteristic in Figure 5.1, namely $v_G > v_{GL}$, $V_T \le v_G \le v_{GL}$ and $v_G < V_T$, respectively. Device output current in ranges 1 and 3 is independent of device model. Only in range 2, does the choice of model affect the current waveform.

5.2.2. Fourier Series

Fourier series [90] can be used to represent a periodic signal *f(t)* with period T_0 in terms of a DC component, fundamental component with frequency $\omega_0 = 1/T_0$ and harmonic components at frequency $k\omega_0$, [90]

$$f(t) = F_0 + \sum_{k=1}^{\infty}\left(F_k \cos k\omega_0 t + K_k \sin k\omega_0 t\right) \tag{5.4}$$

where

$$F_0 = \frac{1}{2\pi}\int_0^{2\pi} f(t)\,d\varphi \tag{5.5}$$

$$F_k = \frac{1}{\pi}\int_0^{2\pi} f(t)\cos k\varphi d\varphi \tag{5.6}$$

$$K_k = \frac{1}{\pi}\int_0^{2\pi} f(t)\sin k\varphi d\varphi \tag{5.7}$$

$$k = 1, 2 \cdots\cdots n$$

As mentioned above, PA output current $f(t) = i_D(\varphi)$ has been defined to be an even periodic function and this makes the coefficients K_k always equal to zero. Furthermore, in (5.5) and (5.6), the integration range may be taken from 0 to π and result doubled [91]. The DC component of $i_D(\varphi)$ then becomes

$$F_0 = \frac{1}{\pi}\int_0^{\pi} i_D(\varphi)\,d\varphi \tag{5.8}$$

and the fundamental ($k = 1$) and harmonic ($k > 1$) components are

$$F_k = \frac{2}{\pi}\int_0^{\pi} i_D(\varphi)\cos k\varphi d\varphi \tag{5.9}$$

Device output current, $i_D(\varphi)$ in (5.8) and (5.9), exists in three different ranges, as defined in (5.1) − (5.3) and in Figure 5.2(b). Hence the integration ranges may be

split accordingly. Since $i_D(\varphi)$ is zero in range 3, this range makes no contribution to the total integration. Therefore, (5.8) and (5.9) become

$$F_0 = \frac{1}{\pi}\left[\int_0^{\alpha} 2d\varphi + \int_{\alpha}^{\pi-\beta} i_D(\varphi)\,d\varphi\right] = \frac{2\alpha}{\pi} + I_0 \tag{5.10}$$

where, I_0 given by

$$I_0 = \frac{1}{\pi}\int_{\alpha}^{\pi-\beta} i_D(\varphi)\,d\varphi \tag{5.11}$$

and

$$F_K = \frac{2}{\pi}\left[\int_0^{\alpha} 2\cos k\varphi\, d\varphi + \int_{\alpha}^{\pi-\beta} i_D(\varphi)\cos k\varphi\, d\varphi\right] = \frac{4\sin k\alpha}{k\pi} + I_K \tag{5.12}$$

where, I_k given by

$$I_K = \frac{2}{\pi}\int_{\alpha}^{\pi-\beta} i_D(\varphi)\cos k\varphi\, d\varphi \tag{5.13}$$

Since the first terms in (5.10) and (5.12), which are independent of device model, have now been evaluated, in what follows, only expressions (5.11) and (5.13) that are model dependent need to be evaluated.

5.3. Linear Device Model

5.3.1. Model Description

The linear device model is given by,

$$i_D = G\left(v_G - V_T\right) \tag{5.14}$$

With normalisation of v_G and i_D such that i_D = 2 A when v_G = V_T + 2 V, then G = 1 AV^{-1}. The normalised form of the linear device model is,

$$i_D = v_G - V_T \tag{5.15}$$

A graph of the model transfer characteristic has been used for illustration in Figures 3.2 and 3.3 and is shown also in Figure 5.1. Substituting for v_G from (3.3) into (5.15), device output current is given by

$$\begin{aligned} i_D\left(\varphi\right) &= V_{GG} - V_T + \hat{v}_G \cos\varphi \\ &= V_{GGe} + \hat{v}_G \cos\varphi \end{aligned} \tag{5.16}$$

Effective device bias voltage, v_{GGe}, is given as a function of FPCA γ_F by (4.4),

$$V_{GGe} = \frac{2\cos\frac{\gamma_F}{2}}{\cos\frac{\gamma_F}{2} - 1} \tag{5.17}$$

In the four regions of PA operation, R0, R1, R2 and Rf, defined in Figure 4.3, the knee and cut-off clipping angles α and β, needed in (5.10) − (5.13), were given in Table 4.1, which is repeated in Table 5.1 with formulas. Equation (5.16) together with (5.17) and Table 5.1 will be used in the following sections to derive DC, fundamental and third harmonic components for the output current of the device.

Figure 5.3 shows three waveforms that are a cosinewave, a half-wave rectified cosine wave and a square wave, respectively. The three waveforms represent PA device output current assuming a linear device model in three interesting cases. The first is Class A PA at the FPP (Figure 3.6: 1st row, 2nd column). Figure 5.3(b) is class B PA at the FPP (Figure 3.6: 3rd row, 2nd column). Figure 5.3(c) is PA of any class with the limiting case of very large saturating input voltage amplitude. The DC, fundamental and third harmonic components, F_0, F_1 and F_3 for these three waveforms are given in Table 5.2 [91].

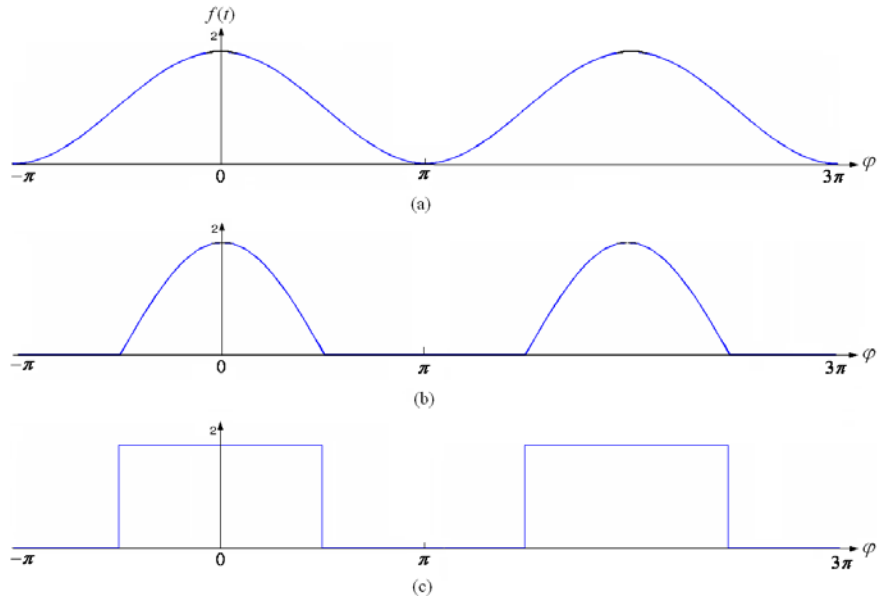

Figure 5.3 Three specific cases of device output current waveforms, (a) Class A at FPP; (b) Class B at FPP; (c) saturated (any class).

Table 5.1 Clipping angles in four clipping regions

Region	Clipping	α	β
R2	Double	$\arccos\dfrac{2}{\hat{v}_G\left(1-\cos\dfrac{\gamma_F}{2}\right)}$	$\arccos\dfrac{-2\cos\dfrac{\gamma_F}{2}}{\hat{v}_G\left(1-\cos\dfrac{\gamma_F}{2}\right)}$
R1	Single	0	$\arccos\dfrac{-2\cos\dfrac{\gamma_F}{2}}{\hat{v}_G\left(1-\cos\dfrac{\gamma_F}{2}\right)}$
R0	No	0	0
Rf	Full	0	π

Table 5.2 DC, fundamental and third harmonic components for waveforms in Figure 5.3 [91].

Signal	F_0	F_1	F_1 (dB)	F_3	F_3 (dB)	α	β
Sine	1	1	0	0	− ∞	0	0
Half sine	2/π	1	0	0	− ∞	0	π/2
Square	1	1.273	2.098	0.424	− 7.444	π/2	π/2

Table 5.2 also gives F_1 and F_3 in dB units. The corresponding knee and cut-off clipping angles α and β are also given. The values F_0, F_1 (dB) and F_3 (dB) will be used to confirm Fourier coefficient results in the following sections. The three waveforms in Figure 5.3 will be referred to as test waveforms A, B, and C, as indicated in Table 5.1.

5.3.2. DC and Fundamental Fourier Coefficients for Device Output Current

The DC component of device current, F_0 is given by (5.10) that contains the integral I_0 given in (5.11). Substituting model equation (5.16) into (5.11), then

$$\begin{aligned} I_0 &= \frac{1}{\pi}\int_{\alpha}^{\pi-\beta}\left(V_{GGe}+\hat{v}_G\cos\varphi\right)d\varphi \\ &= V_{GGe}\left[1-\frac{1}{\pi}\left(\alpha+\beta\right)\right]+\frac{\hat{v}_G}{\pi}\left(\sin\beta-\sin\alpha\right) \end{aligned} \tag{5.18}$$

The expression for DC component of the device output current, F_0, follows by introducing the model independent term from (5.10) and using (5.17) and the α and β values in Table 5.1. This makes it possible to plot DC component of the device current as a 3-D plot against FPCA γ_F and input signal amplitude $\hat{v}_G$ and the plot is shown in Figure 5.4(a). Points corresponding to the test waveforms 'A', 'B' and 'C' in Figure 5.3, are indicated in Figure 5.4(a) and gives values of 1.00, 0.63 and 1.00, respectively, which agree well with Table 5.2. It can be observed that for any value of $\hat{v}_G$, the DC component falls as γ_F is reduced. For a Class A PA, for which $\gamma_F = 2\pi$, and for a Class AB PA in region R0, the DC component of the device current is invariant with $\hat{v}_G$. In other regions, the DC component always falls as $\hat{v}_G$ is reduced.

The fundamental component of the device output current, F_1, is given by substituting $k = 1$ in (5.12) and (5.13). Substituting (5.16) into (5.13), the integral, I_1 is given by,

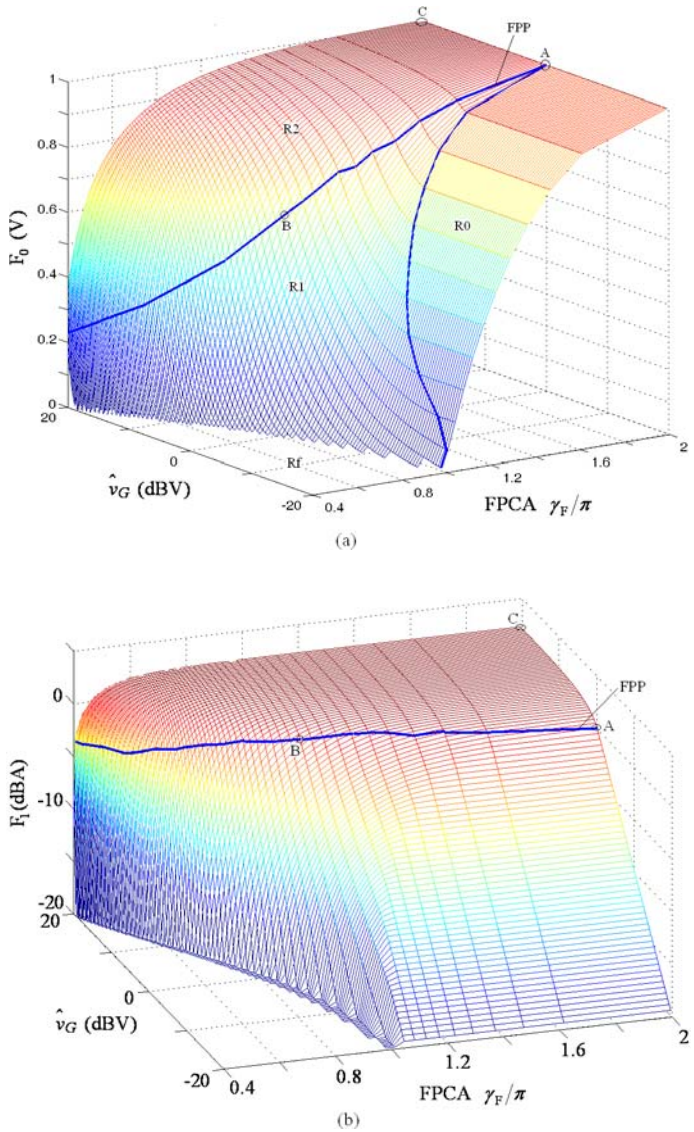

Figure 5.4 Harmonic components of device output current versus $\hat{v}_G$ and FPCA γ_F, (a) DC component, (b) fundamental component.

$$
\begin{aligned}
I_1 &= \frac{2}{\pi}\int_{\alpha}^{\pi-\beta}\left(V_{GGe}+\hat{v}_G\cos\varphi\right)\cos\varphi d\varphi \\
&= \frac{2V_{GGe}}{\pi}\left(\sin\beta-\sin\alpha\right)+\hat{v}_G\left[1-\frac{1}{\pi}\left(\alpha+\beta\right)-\frac{1}{2\pi}\left(\sin 2\alpha+\sin 2\beta\right)\right]
\end{aligned}
\tag{5.19}
$$

By introducing the model independent term from (5.12) with k = 1, and using (5.17) and Table 5.1, the fundamental component of device output current as a function of γ_F and $\hat{v}_G$ is obtained and its 3D plot is shown in Figure 5.4(b). At 'A',

'B' and 'C' points in Figure 5.4(b), the F_1 values are 0.00, 0.00 and 2.10 dB that agree with values in Table 5.2.

It is interesting to compare amplitude of the fundamental component of the device output current in Figure 5.4(b) with the plot for the amplitude of the clipped device input voltage in Figure 4.4. With a linear model, the device output current waveform is essentially the same as the clipped input voltage waveform and the differences between the plots arise only from the Fourier series coefficient. At the FPP in Figure 5.4(b), there is now a smooth transition between the saturation and quasi-linear power ranges as beyond the FPP, in the saturation region, the fundamental component in Figure 5.4(b) now increases by a few dB. Below the FPP, the surface in Figure 5.4(b) is essentially very similar to that in Figure 4.4, which has already been discussed in section 4.4.5, including the features of linear behaviour in region R0 and for Class B $\gamma_F = \pi$, and a varying gradient in region R1, which is ≤ 1 for $\gamma_F \geq \pi$ (class range AB) and ≥ 1 for $\gamma_F \leq \pi$ (class range BC).

5.3.3. 3rd Order Fourier Coefficient versus Clipping Angles

It is shown in Appendix A that the level of IMD3 that causes ACI and constellation errors in a PA, relative to the wanted signal for a multi-tone input signal is the same as the level of 3rd harmonic relative to fundamental for single tone excitation. Therefore the 3rd order Fourier series coefficient of the device output current waveform is of special interest. As will be shown, the 3-D plot of F_3 against γ_F and $\hat{v}_G$ has an interesting surface that varies between very high and very low values. For these reasons, analysis of F_3 is approached in a different way than that adopted for F_0 and F_1. Thus, in this section, F_3 is evaluated for the general case of a clipped waveform that has a fixed peak-to-peak amplitude and that is defined by its clipping angles α and β. A plot of F_3 versus γ_F and $\hat{v}_G$ will be obtained in the following section (5.3.4). The peak-to-peak waveform amplitude assumed in this section is 2 A.

A peak-to-peak current waveform amplitude of 2 A implies a peak amplitude $\hat{i}_D$ of 1 A. The corresponding peak clipped input voltage $\hat{v}_{GC}$ must be 1 V. Relationship between input voltage amplitude and amplitude of clipped input voltage was derived in section 3.2.2 via the extrapolation function as in (4.5),

$$\hat{v}_G = \frac{\hat{v}_{GC}}{F_e} \tag{5.20}$$

where, the extrapolation function is given by (4.9). Setting $\hat{v}_{GC}$ = 1 in (5.20) and substituting for F_e using (4.9), $\hat{v}_G$ is given by

$$\hat{v}_G = \frac{2}{\cos\alpha + \cos\beta} \tag{5.21}$$

This expression applies to any device model, including the linear model.

For the linear device model, the third harmonic component of the device output current, F_3, is given by substituting $k = 3$ in (5.12) and (5.13). Substituting the linear model equation (5.16) into (5.13), the integral, I_3, is given by,

$$I_3 = \frac{2}{\pi}\int_{\alpha}^{\pi-\beta}\left(V_{GGe} + \hat{v}_G\cos\varphi\right)\cos 3\varphi \, d\varphi \tag{5.22}$$

After the integration, I_3 is given by,

$$I_3 = \frac{2}{3\pi}V_{GGe}\left(\sin 3\beta - \sin 3\alpha\right) - \frac{\hat{v}_G}{2\pi}\left(\sin 2\alpha + \sin 2\beta + \frac{\sin 4\alpha + \sin 4\beta}{2}\right) \tag{5.23}$$

In order to derive F_3 as a function of α and β, we do not express V_{GGe} as a function of γ_F using (5.17) but rather use (3.8). Then $\hat{v}_G$ in (5.23) is substituted for using (5.21),

$$I_3 = \frac{\sin 4\beta - 2\sin 2\beta - 6\sin 2\alpha - 3\sin 4\alpha - 8\sin 3\beta\cos\alpha}{6\pi\left(\cos\alpha + \cos\beta\right)} \tag{5.24}$$

Introducing the model independent term from (5.12) with $k = 3$, then F_3 is given by

$$\begin{aligned} F_3 &= \frac{4\sin 3\alpha}{3\pi} + \frac{\sin 4\beta - 2\sin 2\beta - 6\sin 2\alpha - 3\sin 4\alpha - 8\sin 3\beta\cos\alpha}{6\pi\left(\cos\alpha + \cos\beta\right)} \\ &= \frac{\sin 2\alpha\left(\cos 2\alpha - 1\right) + \sin 2\beta\left(\cos 2\beta - 1\right)}{3\pi\left(\cos\alpha + \cos\beta\right)} \end{aligned} \tag{5.25}$$

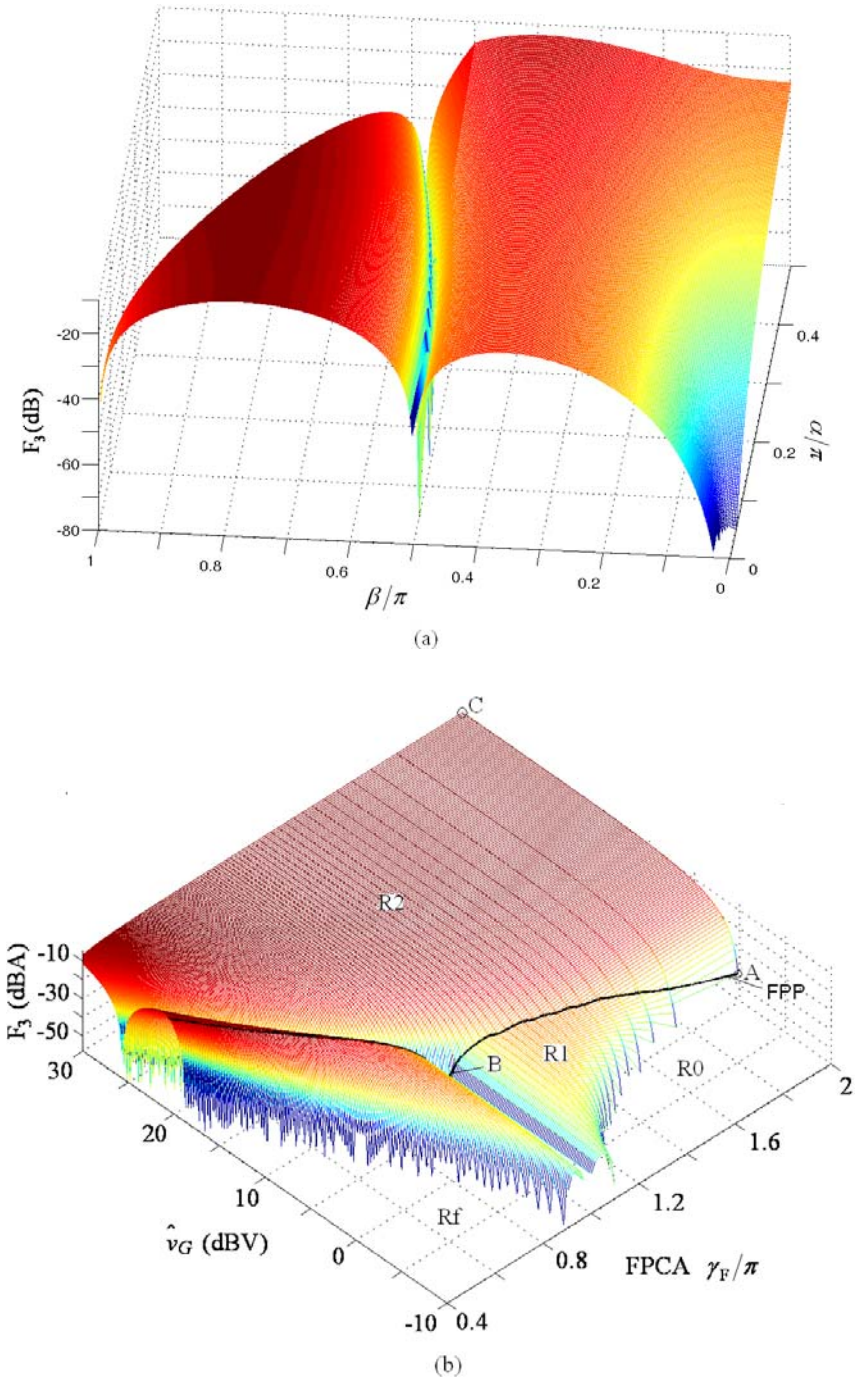

Figure 5.5 Third harmonic components (a) versus clipping angles; (b) versus $\hat{v}_G$ and FPCA γ_F.

A plot of F_3 against α and β is shown in Figure 5.5(a). By definition $\alpha + \beta \leq \pi$, and the range of the plot has been restricted accordingly. A very significant feature of this plot is that a deep valley crosses the surface. When $\alpha = 0$, the valley gives a deep null at $\beta = \pi/2$. Once α increases above 0, the null at $\beta = \pi/2$ shifts into the range of β

> $\pi/2$. This can be understood from mathematical analysis. A deep null occurs for $F_3 = 0$, as this corresponds to $20\log(F_3) \rightarrow -\infty$. Therefore, in (5.25), a null occurs only if the following condition is satisfied,

$$\sin 2\alpha\left(\cos 2\alpha - 1\right) + \sin 2\beta\left(\cos 2\beta - 1\right) = 0$$
$$\cos\alpha + \cos\beta \neq 0 \tag{5.26}$$

It is obvious that when $\alpha = 0$, $\beta = \pi/2$ satisfies (5.26). Now consider the case of $\alpha > 0$. For $\alpha \neq 0$ and $\beta \neq 0$, it is always true that $\cos 2\alpha - 1 < 0$, $\cos 2\beta - 1 < 0$. Since these terms have the same sign, it is necessary in order to satisfy (5.26) that $\sin 2\alpha$ and $\sin 2\beta$ have opposite signs. Since $\alpha \in [0, \pi/2]$, then $\sin 2\alpha > 0$. Therefore, when $\alpha \neq 0$, the null can only occur where $\sin 2\beta < 0$. Since $\beta \in [0, \pi]$, then $2\beta > \pi$. Thus the null occurs for $\beta > \pi/2$ for $\alpha > 0$.

Having obtained the plot of F_3 for the fixed amplitude clipped device current waveform as a function of its clipping angles and explored its feature of a deep valley, F_3 is now derived as a function of γ_F and $\hat{v}_G$.

5.3.4. 3rd Order Fourier Coefficient Versus γ_F and $\hat{v}_G$

The third harmonic component of device output current as a function of FPCA γ_F and input signal amplitude $\hat{v}_G$ may be derived by starting from the integral I_3 in (5.23), introducing the model independent term (5.12) with $k = 3$, and then using (5.17) and Table 5.1 in order to substitute for α, β and V_{GGe}. The corresponding 3D plot is shown in Figure 5.5(b). At the 'A', 'B' and 'C' points in Figure 5.5(b), the F_3 values are − Inf, − Inf, − 7.44 dB that agree with Table 5.2**.**

The plot of F_3 versus γ_F and $\hat{v}_G$ in Figure 5.5(b) is crossed by a deep valley but, unlike that in Figure 5.5(a), the valley has a sharp bend in it. We refer to this valley as the 'L'-shaped valley. The four clipping regions in Figure 4.3, R2, R1, R0 and Rf, can be clearly seen in Figure 5.5(b) as indicated. A result of great practical significance is that for all γ_F except $\gamma_F = 2\pi$ (class A), and $\gamma_F = \pi$ (class B), the FPP is bordered in

the quasi-linear power region by the region R1 where distortion is very high. Now the relationship between the plots in Figure 5.5(a) and (b) is considered.

In the quasi-linear region, knee clipping angle $\alpha = 0$, as shown in Figure 4.5(a). Therefore distortion in this region is governed by the cross-section through the surface of Figure 5.5(a) for $\alpha = 0$, i.e. by the curve corresponding to the front edge of the surface. This curve has a null at $\beta = \pi/2$. From Figure 4.5(b), for $\gamma_F = \pi$, β remains at $\pi/2$ through the whole of the quasi-linear power range. Therefore, for $\gamma_F = \pi$, *i.e.* for a class B PA, the null at $\beta = \pi/2$ for $\alpha = 0$ in Figure 5.5(a) must manifest itself as a deep valley throughout the whole of the quasi-linear range, as indeed is the case in Figure 5.5(b). This part of the 'L'-shaped valley in Figure 5.5(b) will be referred to as the *class B part of the valley*. A null in distortion that is maintained over a wide range of input signal power is referred to as a *sweet spot* [51].

Figure 5.5(b) shows that at the FPP, *i.e.* at the beginning of the saturation range, this valley turns sharply to the left into the BC class range. This feature can be predicted from Figure 5.5(a) by the following argument. Figure 4.5(a) shows that, at the FPP, α starts to increase from zero. In Figure 5.5(a), the condition for the valley as α increases above zero, is that $\beta > \pi/2$, as has also been proved mathematically in the previous sub-section. From Figure 4.5(b), in the R2 region, β approaches its limit value of $\pi/2$ by increasing from 0 in the AB class range and by decreasing from π in the BC class range. It follows that at the FPP, the valley must cross the surface through the BC class range and therefore turn to the left. This part of the 'L'-shaped valley in Figure 5.5(b) that is above the FPP and turns into the BC class range will be called the *class BC part of the valley*. Figure 5.5(b) shows that although there is no valley in the AB class range, there is a ledge where rate of change of distortion becomes less once the FPP is crossed and the quasi-linear range begins.

In section 5.3.6, 2-D plots of distortion versus input signal power for different PA classes will be obtained from the 3-D plot in Figure 5.5(b). But firstly, 3-D plots of gain and efficiency will be presented.

5.3.5. Gain and Efficiency

In section 5.3.2, DC and fundamental components of device output current were derived, and shown as 3-D plots in Figure 5.4. This section will derive further PA metrics based on those results.

Gain is defined as the ratio of the fundamental component of the output current to the peak input voltage,

$$G_N = \frac{F_1}{\hat{v}_G} \tag{5.27}$$

The gain is normalised because $\hat{v}_G$ is normalised and F_1 is the fundamental component of a normalised current. With this method of normalisation for the gain, a class A PA at the FPP has a G_N value of 0 dB. Denormalisation of G_N in order to apply it to practical PAs is discussed Appendix B.

Using (5.12) with $k = 1$ and (5.19), gain is given by

$$G_N = \frac{4\sin\alpha}{\pi\hat{v}_G} + \frac{2V_{GGe}}{\pi\hat{v}_G}\left(\sin\beta - \sin\alpha\right) + 1 - \frac{\alpha+\beta}{\pi} - \frac{1}{2\pi}\left(\sin 2\alpha + \sin 2\beta\right) \tag{5.28}$$

V_{GGe} and α, β are given as function of γ_F and $\hat{v}_G$ by (5.17) and Table 5.1, respectively.

The 3-D plot of gain versus FPCA γ_F and input signal amplitude $\hat{v}_G$ is shown in Figure 5.6. It is constant (at 0 dB) only in the R0 region where there is no clipping and it falls to zero in the Rf region. Normalised gain is − 6 dB at the FPP for class B and falls to much lower values in the R1 region in the BC class range. For all classes, above the FPP in the saturation (R2) range, gain reduces approximately linearly as the input voltage increases but the output current saturates.

PA efficiency is defined, in general, to be

$$\eta = \frac{1}{2}\frac{\hat{i}_{D1}\hat{v}_{D1}}{I_{DD}V_{DD}} \tag{5.29}$$

where η is drain efficiency, $\hat{i}_{D1}$ and $\hat{v}_{D1}$ are fundamental Fourier components of device output current and voltage, respectively, and I_{DD} and V_{DD} are supply current

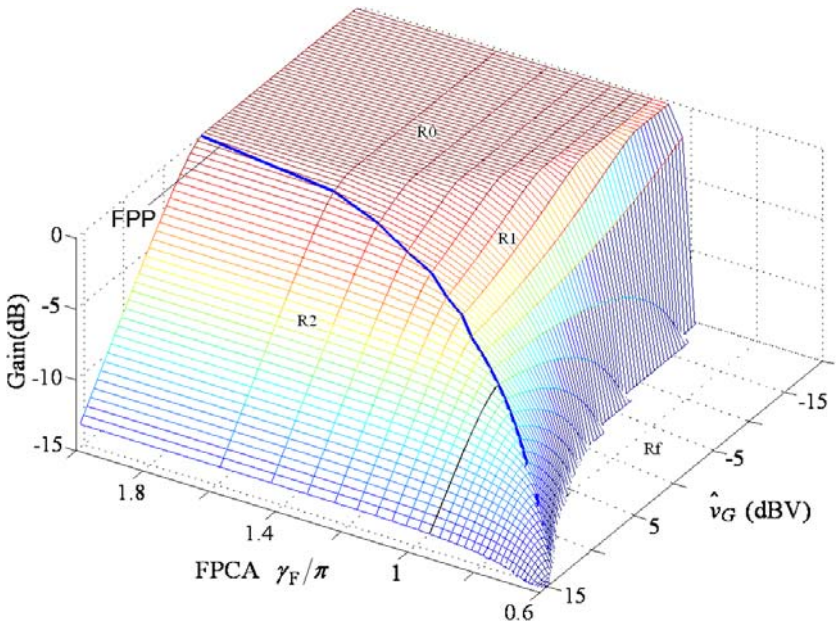

Figure 5.6 Gain versus input signal amplitude $\hat{v}_G$ and FPCA γ_F.

and voltage, respectively. It is shown in [51][52] that $I_{DD} = \overline{i_D}$, where $\overline{i_D}$ is average value of the output current. For load resistance R_L, (5.29) then becomes

$$\eta = \frac{1}{2}\frac{\hat{i}_{D1}^2 R_L}{\overline{i_D} V_{DD}} \tag{5.30}$$

For maximum efficiency, PA design should be such that V_{DD} lies in the middle of the range of v_D. In this case and assuming zero knee voltage, then

$$V_{DD} = \hat{v}_{D1} = \hat{i}_{D1} R_L \tag{5.31}$$

As current in (5.30) is normalised, then at the FPP for a class A PA, $\hat{i}_{D1}$ = 1 A, and (5.31) implies that $V_{DD} = R_L$. In this case, (5.30) becomes

$$\eta = \frac{1}{2}\frac{\hat{i}_{D1}^2}{\overline{i_D}} \tag{5.32}$$

In terms of Fourier series coefficients for normalised current, (5.32) is

$$\eta = \frac{1}{2}\frac{F_1^2}{F_0} \tag{5.33}$$

Equation (5.31) assumes that the v_D waveform is symmetrical [52] and this can be satisfied by biasing the device via a parallel tuned circuit as in Figure 1.5(b) that acts as a short- circuit to harmonic components of device output current.

Substituting (5.18) and (5.19) with their corresponding model independent term form (5.10) and (5.12) (with $K = 1$) into (5.33), η is given by

$$\eta = \frac{1}{2}\frac{\left\{\frac{4\sin\alpha}{\pi} + \frac{2V_{GGe}}{\pi}\left(\sin\beta - \sin\alpha\right) + \hat{v}_G\left[1 - \frac{\alpha+\beta}{\pi} - \frac{1}{2\pi}\left(\sin 2\alpha + \sin 2\beta\right)\right]\right\}^2}{\frac{2\alpha}{\pi} + V_{GGe}\left[1 - \frac{1}{\pi}\left(\alpha+\beta\right)\right] + \frac{\hat{v}_G}{\pi}\left(\sin\beta - \sin\alpha\right)} \tag{5.34}$$

Substituting for V_{GGe} using (5.17) and for α and β using Table 5.1, efficiency can be expressed as a function of FPCA γ_F and input signal amplitude $\hat{v}_G$. The corresponding 3-D plot is shown in Figure 5.7(a). It yields the classical results of 50% for class A and 78.5% for class B at the FPP. For class A, the efficiency increases from 50% at the FPP to a limit of 80% above the FPP. This is called the *overdriven class A* mode as proposed in [52]. However, Figures 5.5(b) and 5.6 clearly show severe penalties of considerable increase in distortion and reduction of gain associated with this mode of operation. In practice, efficiency is less than that predicted in Figure 5.7(a) because of the effect of the device knee voltage. It can be seen from Figure 5.7(a) that the efficiency has a maximum with respect to $\hat{v}_G$ in the BC class range and for part of the AB class range. The path of the maximum is shown by the contour plot corresponding to the 3-D plot in Figure 5.7(a) that is shown in Figure 5.7(b). It can be seen that the maximum efficiency for all classes occurs well above the FPP (in the R2 region).

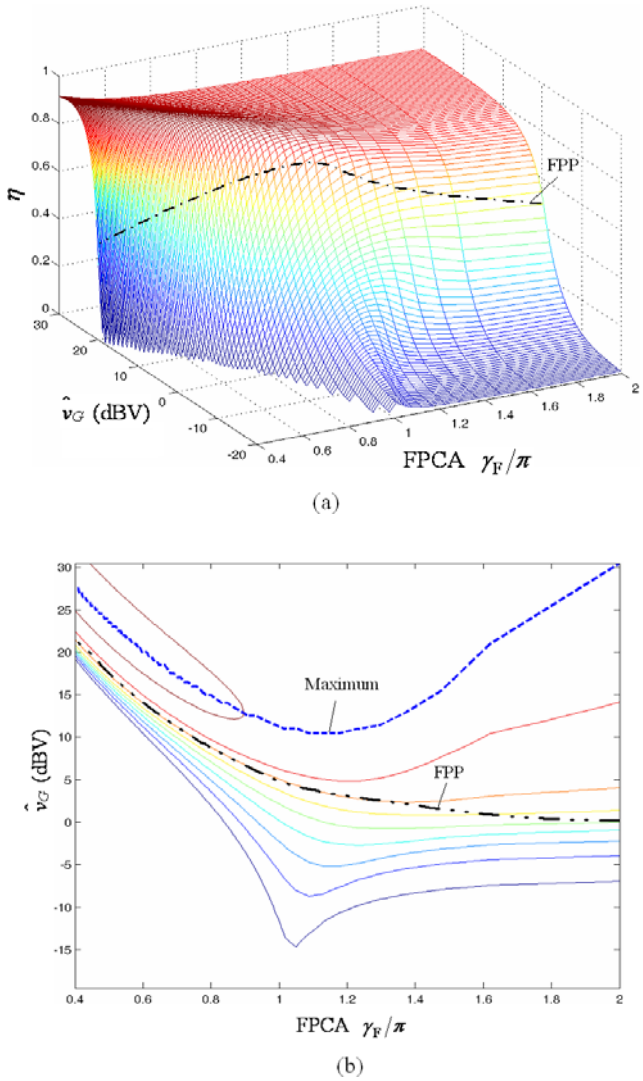

Figure 5.7 Efficiency versus input signal amplitude $\hat{v}_G$ and FPCA γ_F (a) 3-D plot; (b) contour plot.

5.3.6. Power Sweeps

3-D plots have been given for the fundamental and 3rd harmonic of device output current, gain and efficiency versus $\hat{v}_G$ and γ_F, in Figures 5.4(b), 5.5(b), 5.6 and 5.7(a), respectively. It is usual to plot these PA performance metrics against $\hat{v}_G$, to produce so-called power sweeps. We now derive such power sweeps by taking cross-sections, or slices, from the 3-D plots parallel to the $\hat{v}_G$ axis for specified values of γ_F. The γ_F values for all power sweeps for the linear device model are the same and are given in Table 5.3. In all power sweeps, full power point is indicated by the symbol

Table 5.3 Values of γ_F for PA performance power sweeps in Figures 5.8 − 5.11.

Class	γ_F (π)
A	2
AB1	1.3
AB2	1.1
B	1
BC1	0.9
BC2	0.8

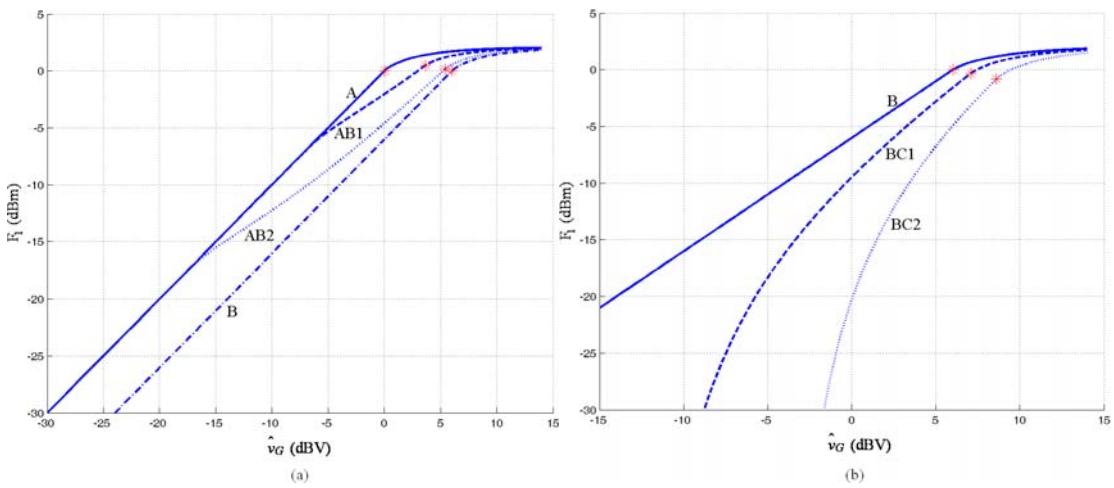

Figure 5.8 Predicted power sweeps from Figure 5.4 (b), (a) AB class range; (b) BC class range.

' * '. All power sweeps are presented as two graphs ((a) and (b)) that cover the AB and BC class ranges separately; the curve for Class B ($\gamma_F = \pi$) occurs in both graphs. Figure 5.8 shows the power sweeps for output power obtained from Figure 5.4(b). Due to the normalisation used in this thesis, the output current at FPP for Class A is 0 dBA when the input voltage is 0 dBV. The output power curve for class B appears parallel with that for class A but shifted by 6 dB [52] on the $\hat{v}_G$ axis. The performance of class B can regarded to be linear behaviour, like Class A as mentioned in [52]. At the FPP, output power is the same for class A and B and slightly higher for class AB. The change of slope below FPP for class AB is due to cut-off clipping in the R1 region. For class BC, output power reduces very nonlinearly as input power is reduced and becomes zero when entering the Rf region.

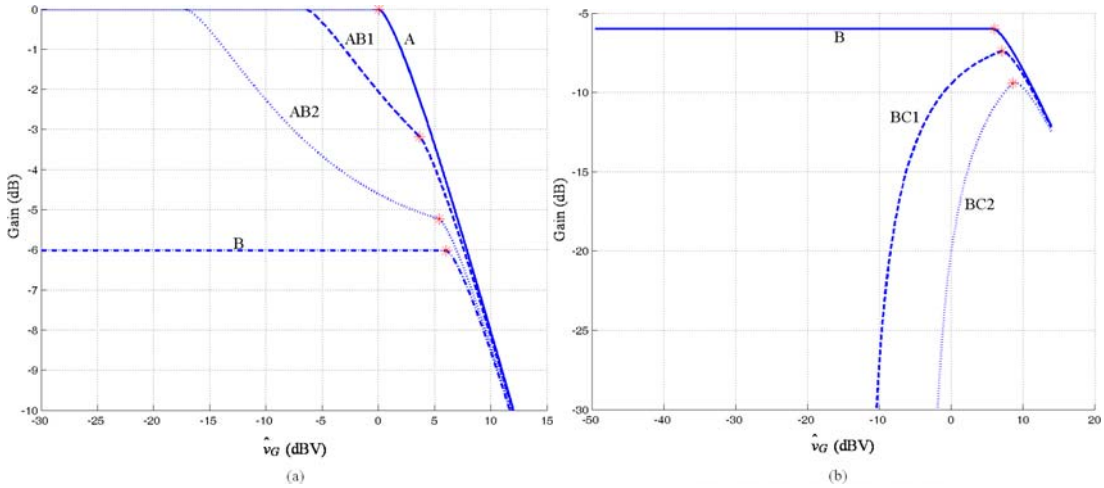

Figure 5.9 Predicted gain-power sweeps from Figure 5.6, (a) AB class range; (b) BC class range.

After the FPP, output current for all classes tends to be saturated at the same level of 2.1 dBA.

Figure 5.9 shows sweeps for normalised gain obtained from Figure 5.6. For classes A and AB in R0 region, gain is 0 dB. For class B, gain in the quasi-linear range is – 6 dB. For class AB in the R1 region, the slope changes due to cut-off clipping. For class BC, gain drops quickly at both low and high input power. In the BC class range, maximum gain is close to the FPP.

Figure 5.10 shows efficiency sweeps obtained from Figure 5.7(a). For class A, efficiency is 50% at the FPP and it approaches a limit of about 80% under heavy overdrive. The efficiency for class B is 78.5% at FPP. The maximum efficiency for class BC1 and BC2 in Figure 5.10(b) is around 90%. As conduction angle γ_F is reduced towards zero, the i_D pulse narrows. This reduces the DC component of i_D, but at the same time reduces the fundamental component $\hat{i}_{D1}$, preventing a rapid approach of η to a limit value of 100%. As conduction angle is reduced in the BC class range, efficiency at the FPP reduces. The maximum efficiency at the FPP is that for class B at 78.5%.

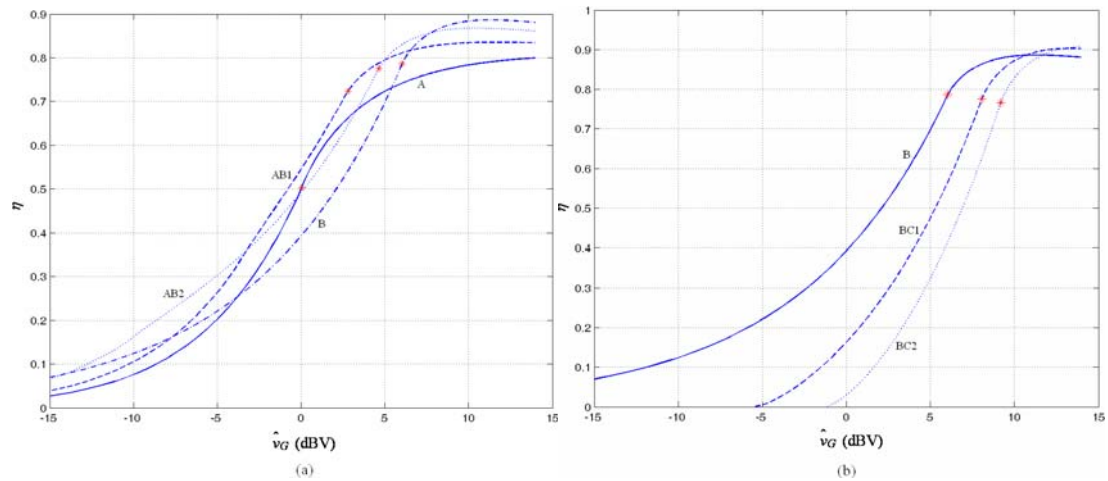

Figure 5.10 Predicted efficiency-power sweeps from Figure 5.7, (a) AB class range; (b) BC class range.

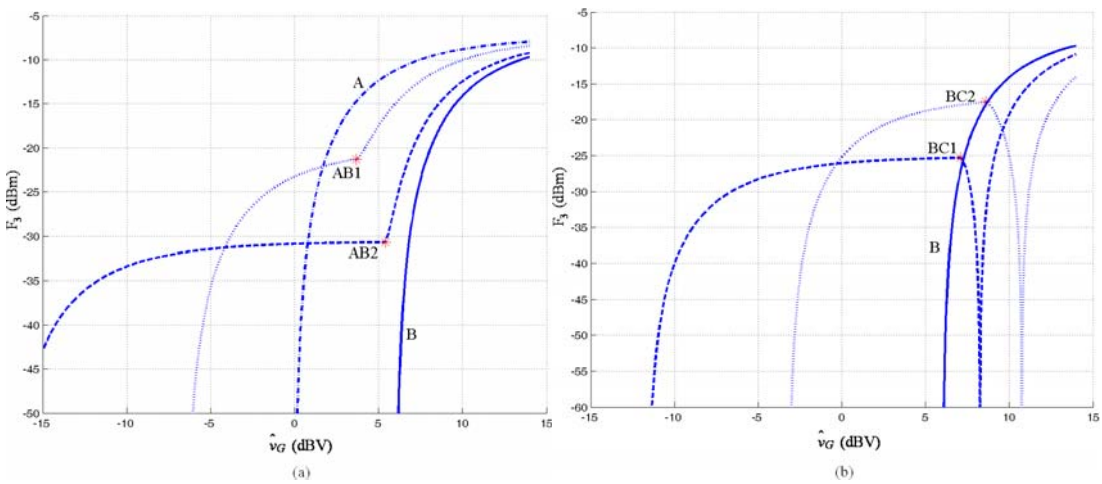

Figure 5.11 Predicted IMD-power sweeps from Figure 5.5(b), (a) AB class range; (b) BC class range.

Summarising Figures 5.8 – 5.10, class A has highest output power and gain across all power levels, but low efficiency, especially at the FPP. Class BC has high efficiency at high input power, but suffers from low output power and gain.

Figure 5.11 shows slices of the 3rd order distortion 3-D plot in Figure 5.5(b). Class A and B have no distortion at the FPP and below. For class AB range, there is a ledge that becomes higher and narrower as γ_F increases. In the BC class range; there is a deep null that shifts to higher power with γ_F decreasing. There is a ledge below the bull that, at the same time, becomes higher and narrower.

5.4. Assessment of Linear Model

The 3-D surface in Figure 5.5(b) is similar to that predicted for a PA based on a LDMOS device in [86] using small-signal bias-dependent derivatives obtained from measurement of the LDMOS devices, as reviewed in section 2.11 and shown in Figure 2.17. However, the valley in Figure 2.17 from [86], appears more 'L'-shaped than that in Figure 5.5(b) because it is plotted against V_{GG} rather than against γ_F.

Compared with [86], the present work has same distinctive features. It shows clearly that the class BC part of the 'L'-shaped valley is above the FPP and therefore caused by knee clipping. It also shows that the 'L'-shaped valley is not a feature of the model of the particular device used but is a fundamental property of a PA that is due to single and double clipping of the device current waveform and can be predicted by means of Fourier series for even the simplest possible device model, *i.e.* for one that is linear and for which meaningful derivatives do not exist. Practical confirmation in [86] of the predicted distortion surface derived is limited to part of one distortion-power sweep in the vicinity of a predicted null. The existence of the null is verified but this falls far that of a verification of the form of the whole distortion surface. But the apparent similarity between Figure 5.5(b) and the predicted distortion surface for the LDMOS device in Figure 2.17 from [86] suggests that the transfer characteristic of the LDMOS device in [86] must be behaving in a rather linear fashion.

Figure 5.11 shows that, for the linear device model, the clipping theory predicts a single null in the distortion-power sweep in the class BC range and a ledge in the class AB range.

If the predicted distortion surface in [86] could be confirmed by detailed measurements, then similar distortion power sweeps would be expected for the LDMOS PA in [86]. However, it is necessary to make comparison not only with the rather linear device in [86] but also with other published data. PA designs using CMOS, LDMOS and GaAs MESFET technologies reported in [83][87][89] and reviewed in section 2.9 exhibit a wide variety of 3rd order distortion-power sweep curves, as shown in Figures 2.19, 2.20 and 2.21. Especially, in the AB class range a double null is frequently seen.

Thus, although clipping theory and the linear device model predict the 'L'-shaped valley predicted in the distortion surface for the rather linear LDMOS PA in [86], the clipping theory and linear device model cannot replicate the distortion power sweeps for PAs using less specialised devices. In order to predict the double null in the distortion power sweep in the AB class range, it is necessary to consider use of models other than the linear model used so far, and this approach will be followed in the following chapter.

5.5. Conclusion

In this chapter, one PA device model has been introduced, namely the linear device model. For this model Fourier series coefficients of the device current waveform have been evaluated used in order to derive PA performance metrics, including output power, efficiency, gain and 3rd order distortion. Results have been presented in the form of 3-D plots and power sweeps obtained from them. The linear model was studied first because it is the simplest model and it exemplifies the effect of clipping is a pure way.

The 3-D graphs of output power, gain and efficiency versus input voltage amplitude $\hat{v}_G$ and FPCA γ_F, reveal some interesting results. These include the very rapid reduction of output power and gain as FPCA γ_F is reduced in the BC class range and the rapid reduction of efficiency as $\hat{v}_G$ is reduced in the BC class range. Similar results can be found in a general way in the literature [83][87], but the systematic way in which PA performance metrics are presented as 3-D plots versus $\hat{v}_G$ and γ_F is very revealing and allow fully informed choice of PA class and degree of back-off to be made in a practical PA design. Another result that emerged was the maximum in efficiency with respect to $\hat{v}_G$ in the BC and in part of the AB class range. Although the surfaces of output power, gain and efficiency are interesting, the far more interesting result is the surface of 3rd order distortion. The surface shows very high distortion in the R2 and R1 regions, above and below the FPP, respectively. This high distortion region is crossed by a deep valley that is 'L'-shaped. Below the FPP, in the quasi-linear input power range, the valley is parallel to the $\hat{v}_G$ axis and yields a

distortion-power sweep for Class B ($\gamma_F = \pi$) that has no distortion, *i.e.* it has a sweet spot. This part of the valley is caused by single clipping. At the FPP, the deep valley turns sharply to the left into the BC class range. Hence, in the BC class range, distortion-power sweeps with a single deep null at high power are predicted. This part of the valley is caused by double clipping. In the AB class range, there is no valley, but only a ledge close to the FPP. Hence, distortion-power sweeps throughout the AB class range are predicted to have a ledge.

The 'L'-shaped valley predicted in the distortion surface of a PA with a linear device model due to device current clipping is very similar to the published distortion surface for a PA with a LDMOS device predicted from the device transfer characteristic. However, there is insufficient measured data in that publication to confirm the existence of the 'L'-shaped valley. A more serious problem is that other published data for CMOS, LDMOS and GaAs MESFET PAs shows measured distortion sweeps with two deep nulls for the AB class range and a single deep null for Class B, and these distortion power sweeps are inconsistent with the 'L'-shaped valley predicted by clipping theory using the linear model.

This assessment of the linear model calls for a necessarity to investigate the performances of other kinds of device model. The square law device model is used and is of interest because it approximately describes devices with relatively longer channel lengths. In next chapter, the square law model will be investigated.

CHAPTER 6

SQUARE LAW DEVICE MODEL AND PA PERFORMANCE

6.1. Introduction

The last chapter presented an analysis of PA performance with the linear device model. However, the predicted sweep of 3rd order distortion versus input signal power did not exhibit the double null in the AB class range which is often seen in published PA data due to device current clipping. This chapter is focused on investigating performance of PAs with the square law model.

The analysis on the square law model follows the same method as that used in Chapter 5 for the linear model. 3-D plots of output power, gain, efficiency and 3rd order distortion will be presented. Comparison between PA performance with the linear and square law models will lead to assessment of both models and inspire speculation on how the device model modifies the effect of clipping and determines PA performance. This will set the direction for the following chapter.

6.2. Model Description

The square law device model expression is,

$$i_D = K\left(v_G - V_T\right)^2 \tag{6.1}$$

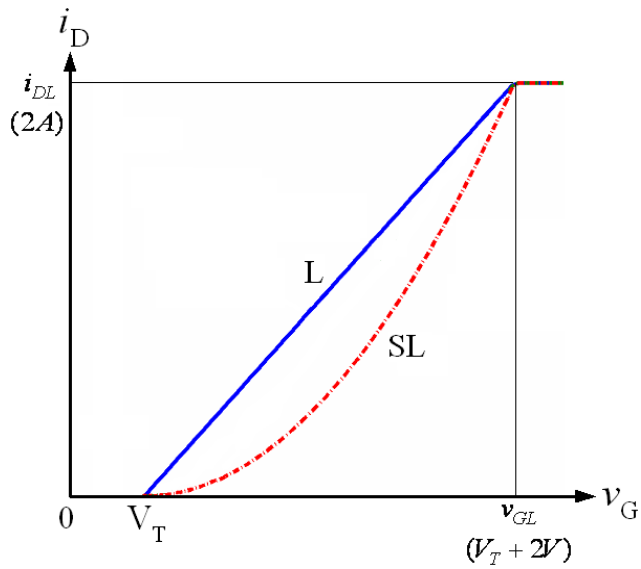

Figure 6.1 Transfer characteristic for the linear and square law device models showing normalisation.

where, K is a transconductance factor. Normalising i_D and v_G as for the linear model, $K = 1/2$ AV^{-2} and we have

$$i_D = \frac{1}{2}\left(v_G - V_T\right)^2 \tag{6.2}$$

The transfer characteristic is shown in Figure 6.1, as curve 'SL'. Substituting for v_G using (3.3), (6.2) becomes,

$$i_D = \frac{1}{2}\left(V_{GGe} + \hat{v}_G \cos\varphi\right)^2 \tag{6.3}$$

For the linear device model, the three waveforms shown in Figure 5.3 were used as test points for the Fourier series coefficients. They corresponded to a Class A PA at the FPP, Class B PA at the FPP and heavily overdriven PA (any class), respectively. The waveforms for these conditions using the square law model are shown in Figure 6.2. Figure 6.2(c) is identical with Figure 5.3(c). Figure 5.3(a) describes $i_D = (1+\cos\varphi)^2/2$ ((6.3)) with V_{GGe} = 1 V and $\hat{v}_G$ = 1 V). Figure 5.3(b) describes $i_D = 2\cos^2\varphi$, truncated to the range $-\pi/2$ to $\pi/2$ (V_{GGe} = 0 and $\hat{v}_G$ = 2 V in

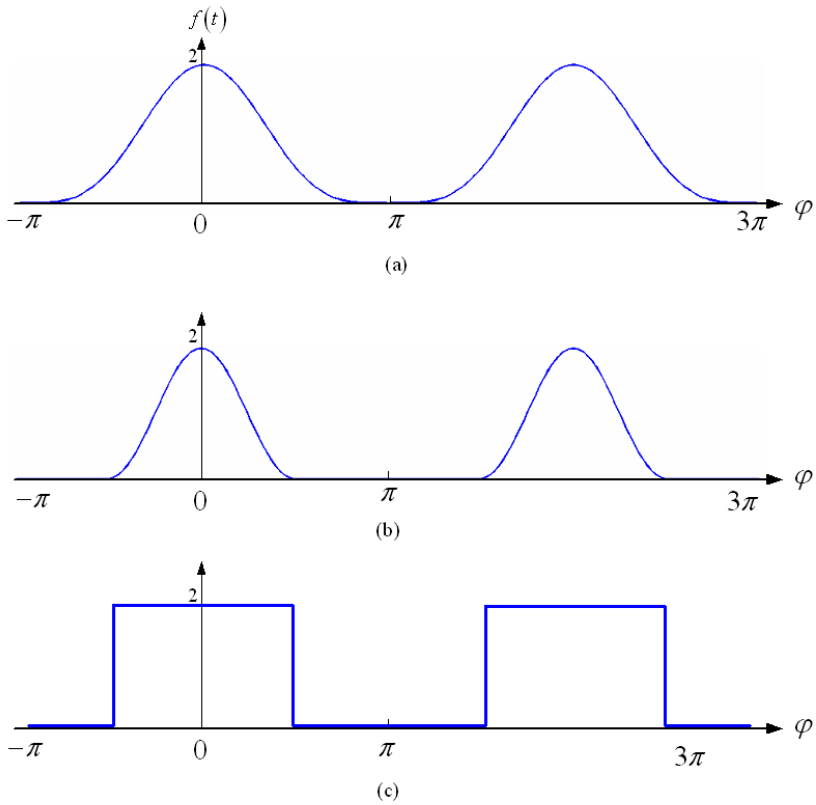

Figure 6.2 Three specific cases of device output current waveforms, (a) Class A at FPP; (b) Class B at FPP; (c) saturated (any class).

((6.3)). The Fourier series coefficients for the test waveforms and other relevant data are given in Table 6.1.

6.2.1. DC and Fundamental Fourier Coefficients for Device Output Current

We use the same methods as used for the linear model in Chapter 5. For DC component of the device current F_0 is given by (5.10) and the integral I_0 is given by (5.11). Substituting model expression (6.3) into (5.11), I_0 for the square law model is,

Table 6.1 DC, fundamental and third harmonic components for waveforms in Figure 6.2.

Test	F_0	F_1	F_1 (dB)	F_3	F_3 (dB)	α	β
A	0.50	1.00	0.00	0.00	− ∞	0	0
B	0.50	0.84	− 1.43	0.34	− 9.38	0	π/2
C	1.00	1.273	2.10	0.42	− 7.44	π/2	π/2

$$I_0 = \frac{1}{2\pi}\int_{\alpha}^{\pi-\beta}\left(V_{GGe} + \hat{v}_G \cos\varphi\right)^2 d\varphi$$

$$= \frac{V_{GGe}^{\ 2}}{2}\left(1 - \frac{\alpha+\beta}{\pi}\right) + \frac{V_{GGe}\hat{v}_G}{\pi}\left(\sin\beta - \sin\alpha\right) + \hat{v}_G^2\left(\frac{1}{4} - \frac{\alpha+\beta}{4\pi} - \frac{\sin 2\beta + \sin 2\alpha}{8\pi}\right)$$

(6.4)

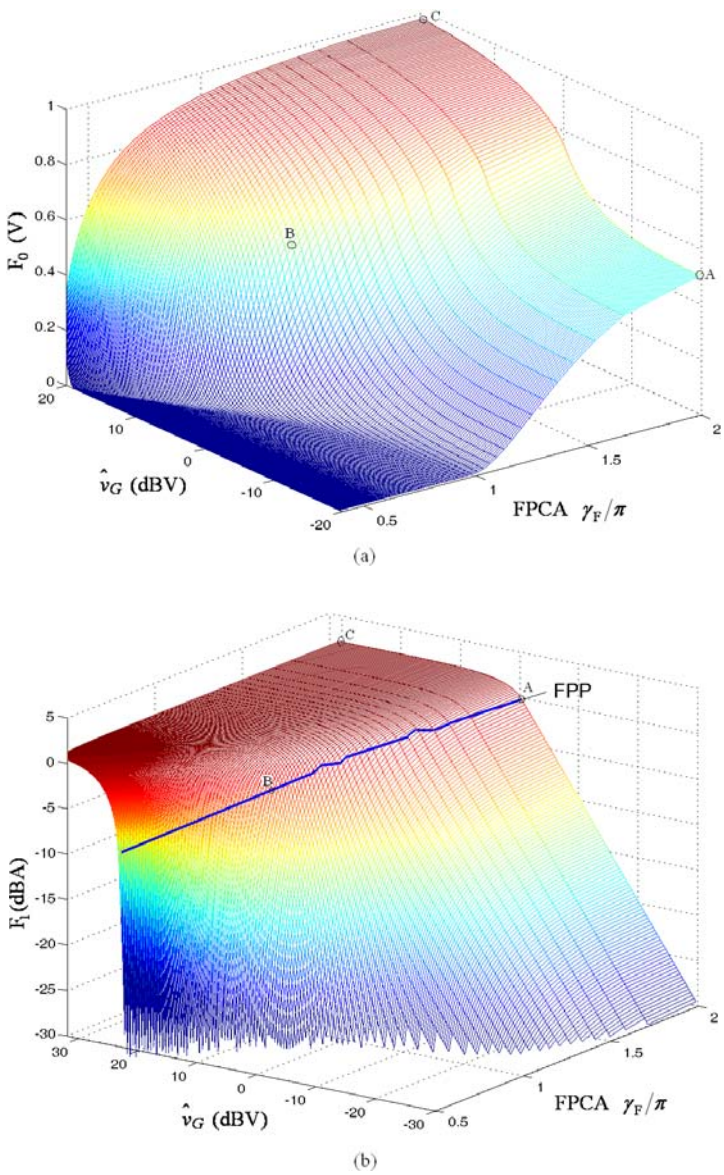

Figure 6.3 Harmonic components of device output current versus $\hat{v}_G$ and FPCA γ_F, (a) DC component; (b) fundamental component.

The fundamental component of the device output current, F_1, is given by substituting $k = 1$ in (5.12) and (5.13). The integral, I_1, in (5.13) is given by,

$$I_1 = \frac{1}{\pi}\int_{\alpha}^{\pi-\beta}\left(V_{GGe} + \hat{v}_G \cos\varphi\right)^2 \cos\varphi \, d\varphi$$

$$= \frac{1}{\pi}\left[V_{GGe}\hat{v}_G\left(\pi - \beta - \alpha - \frac{\sin 2\beta + \sin 2\alpha}{2}\right) + \right. \tag{6.5}$$

$$\left. V_{GGe}{}^2\left(\sin\beta - \sin\alpha\right) + \hat{v}_G^2 \frac{\sin 3\beta - \sin 3\alpha + 9\left(\sin\beta - \sin\alpha\right)}{12}\right]$$

F_0 and F_1 follow from (6.4) and (6.5) by introducing the model independent terms from (5.10) and (5.12) (with $k = 1$), using (5.17) and the α and β expressions in Table 5.1. DC and fundamental components are plotted versus $\hat{v}_G$ and γ_F in Figure 6.3(a) and (b).

From Figure 6.3(a), the DC component approaches 0.5 when $\gamma_F = 2\pi$ (class A) and input signal amplitude becomes small. As input signal amplitude increases, DC component increases for any class of operation. Compared with DC component of the linear model in Figure 5.4(a), the effect of the nonlinear model can be clearly observed in the case of class A; for $\gamma_F = 2\pi$ for the linear model, the DC components is constant at 1.00. This implies that model non-linearity of drain current has a significant effect. For the test point 'C' in Table 6.1 and Figure 6.2, the waveform becomes a square wave for any model. Therefore, the Fourier series coefficients are the same for any model; however the limit is approached rather gradually in Figure 6.3(a). At test points A and B in Figure 6.3(a), the values of F_0 are 0.50 and 0.50, which compare well with the expected values in Table 6.1.

From Figure 6.3(b), the fundamental component is roughly similar to that for the linear model in Figure 6.3(b), except that F_1 falls more rapidly for $\gamma_F < 2\pi$. This can be seen by comparing the surfaces in the region $\gamma_F = \pi$. The comparison will be shown more clearly by power sweeps to be presented in section 6.2.5.

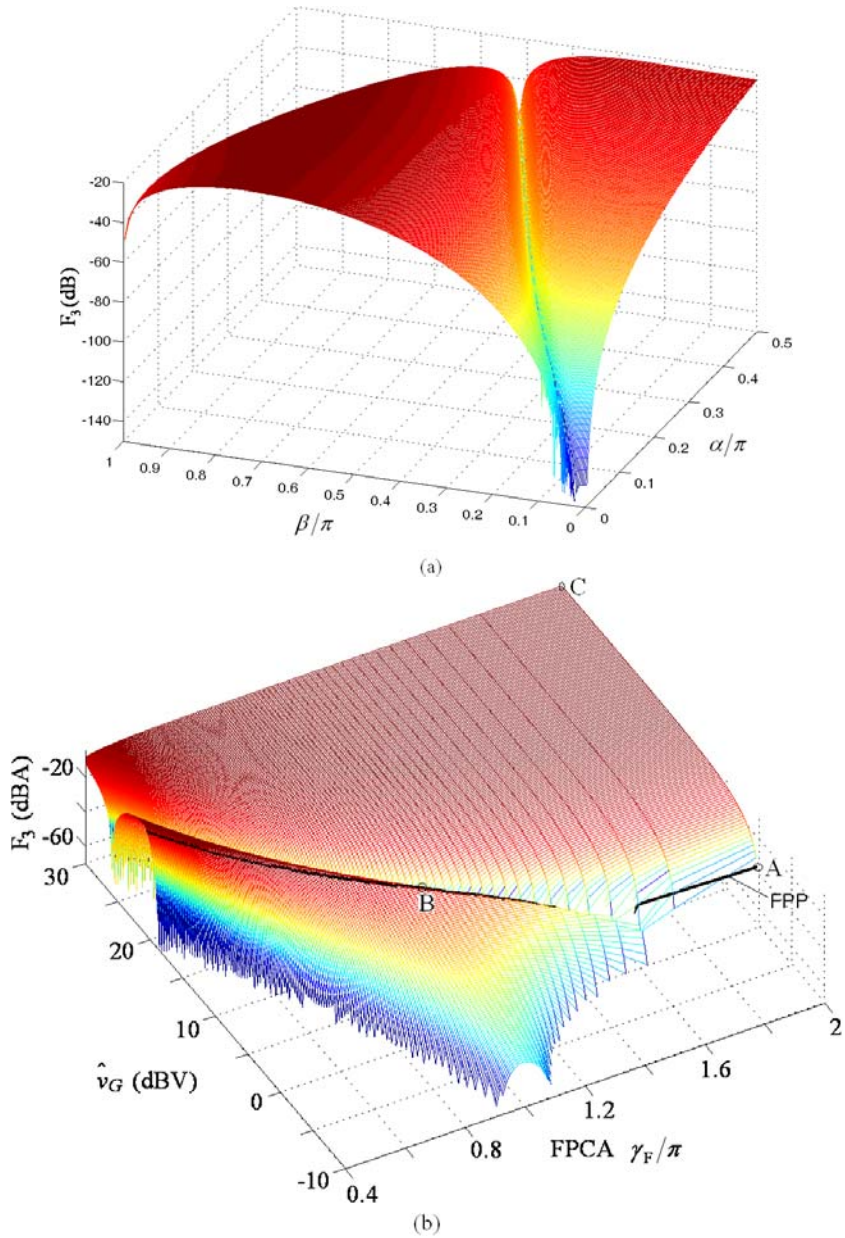

Figure 6.4 3rd harmonic component of drain current versus, (a) clipping angles; (b) $\hat{v}_G$ and FPCA γ_F.

6.2.2. 3rd Order Fourier Coefficient Versus Clipping Angles

First, F_3 as a function of clipping angles α and β is derived for a constant amplitude waveform by following the same method as for the linear model in section 5.3.3. Substituting (6.3) into (5.13) (with $k = 3$), the integral I_3 is given by,

$$I_3 = \frac{1}{\pi}\int_{\alpha}^{\pi-\beta}\left(V_{GGe} + \hat{v}_G \cos\varphi\right)^2 \cos 3\varphi \, d\varphi \tag{6.6}$$

After the integration, I_3 becomes,

$$I_3 = \hat{v}_G^2\left(\frac{\sin 3\beta - \sin 3\alpha}{3\pi} + \frac{\sin 5\beta - \sin 5\alpha}{10\pi} + \frac{\sin\beta - \sin\alpha}{2\pi}\right) + 2V_{GGe}^2\frac{\sin 3\beta - \sin 3\alpha}{3\pi} - V_{GGe}\hat{v}_G\left(\frac{\sin 4\beta + \sin 4\alpha}{2\pi} + \frac{\sin 2\beta + \sin 2\alpha}{\pi}\right) \tag{6.7}$$

Substituting (3.8) and (5.21) into (6.7), in order to eliminate V_{GGe} and $\hat{v}_G$, leads to

$$I_3 = \frac{4}{\pi\left(\cos\alpha + \cos\beta\right)^2}\left[\frac{\sin 3\beta - \sin 3\alpha}{6} + \frac{\sin 5\beta - \sin 5\alpha}{20} + \frac{\sin\beta - \sin\alpha}{4} + \cos^2\beta\frac{\sin 3\beta - \sin 3\alpha}{3} - \cos\beta\left(\frac{\sin 4\beta + \sin 4\alpha}{4} + \frac{\sin 2\alpha + \sin 2\beta}{2}\right)\right] \tag{6.8}$$

Introducing the model independent term from (5.12) (with k = 3), F_3 as a function of clipping angles is given by,

$$F_3 = \frac{4\sin 3\alpha}{3\pi} + \frac{4}{\pi\left(\cos\alpha + \cos\beta\right)^2}\left[\frac{\sin 3\beta - \sin 3\alpha}{6} + \frac{\sin 5\beta - \sin 5\alpha}{20} + \frac{\sin\beta - \sin\alpha}{4} + \cos^2\beta\frac{\sin 3\beta - \sin 3\alpha}{3} - \cos\beta\left(\frac{\sin 4\beta + \sin 4\alpha}{4} + \frac{\sin 2\beta + \sin 2\alpha}{2}\right)\right]$$

$$= \frac{4}{\pi\left(\cos\alpha + \cos\beta\right)^2}\left[\frac{\sin 3\beta - \sin 3\alpha}{6} + \frac{\sin 5\beta - \sin 5\alpha}{20} + \frac{\sin\beta - \sin\alpha}{4} + \frac{\sin 3\alpha\cos\alpha\left(\cos\alpha + \cos\beta\right)}{3} - \cos\beta\frac{\sin 4\alpha + \sin 4\beta + 4\left(\sin 2\alpha + \sin 2\beta\right)}{12}\right] \tag{6.9}$$

F_3 versus α and β is shown plotted in Figure 6.4(a). Compared with the corresponding plot for linear model in Figure 5.5(a), the deep valley has shifted to the right for low α value. For the linear model plot in Figure 5.5(a), the valley caused a null for $\alpha = 0$ at $\beta = \pi/2$ that caused a sweet spot in Figure 5.5(b) that was a dominant feature of the PA behaviour in the quasi-linear region of operation. Since there is no null at $\beta = \pi/2$ for $\alpha = 0$ in Figure 6.4(a), this means that there can be no class B sweet spot in the case of the square law model. This will be verified by deriving F_3 as a function of $\hat{v}_G$ and γ_F in the next section.

6.2.3. 3rd Order Fourier Coefficient Versus γ_F and $\hat{v}_G$

The third harmonic component of device output current as a function of FPCA γ_F and input signal amplitude $\hat{v}_G$ may be derived from (6.7) by introducing the model independent term (5.12) with $k = 3$, and using (4.4) and Table 5.1. The result is shown as a 3-D plot in Figure 6.4(b). At the 'A', 'B' and 'C' points in Figure 6.4(b), the F_3 values are − Inf, − 9.38, − 7.44 that agree with Table 6.1.

As expected from Figure 6.4(a), the valley giving the class B sweet spot for the linear model (in Figure 5.5(b)) no longer exists in Figure 6.4(b). In the BC class range ($\gamma_F \leq \pi$), the plots in Figures 5.5(b) and 6.4(b) for the two models are similar having a valley that is parallel to the FPP in the saturation range. This is not surprising as the plots in Figures 5.5(a) and 6.4(a) become similar $\beta \leq \pi/2$ as α increases above zero. However, for the square law model, instead of having a ledge naming through the AB class range, as in Figure 5.5(b), there is a deep valley that is a continuation of the class BC valley. The fact that F_3 surfaces for both models are crossed by a deep continuous valley is interesting and will be discussed in section 7.2.2.

6.2.4. Gain and Efficiency

PA gain, as defined in (5.27) and using the F_1 expression based on (6.5) as discussed in section 6.2.1, is shown in Figure 6.5. Above the FPP, the gain reduces as does that in Figure 5.6 for the linear model. In contract to the linear model, the gain falls in R0 region for the square law model when $\gamma_F < 2\pi$.

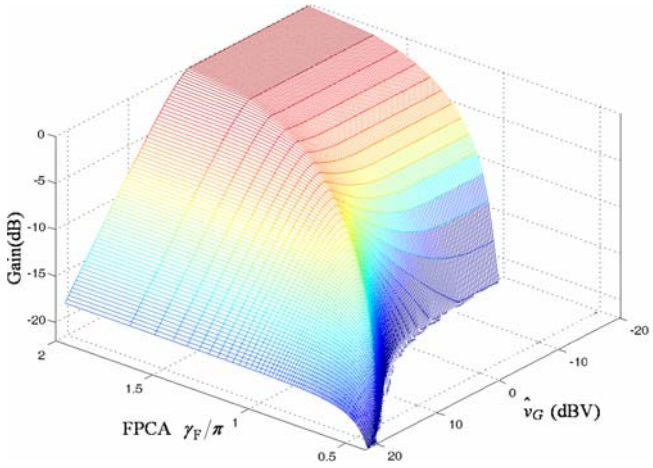

Figure 6.5 Gain versus input signal amplitude $\hat{v}_G$ and FPCA γ_F.

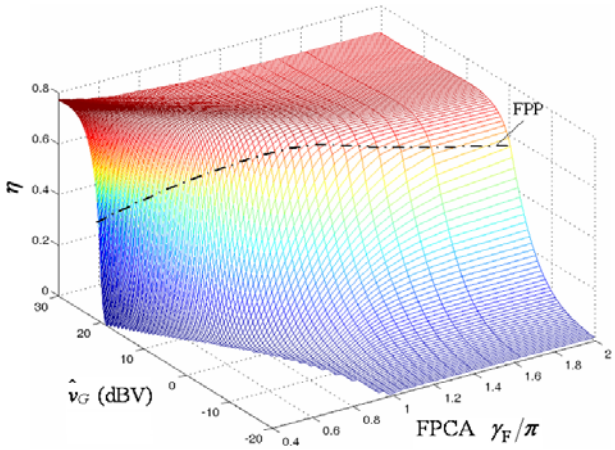

(a)

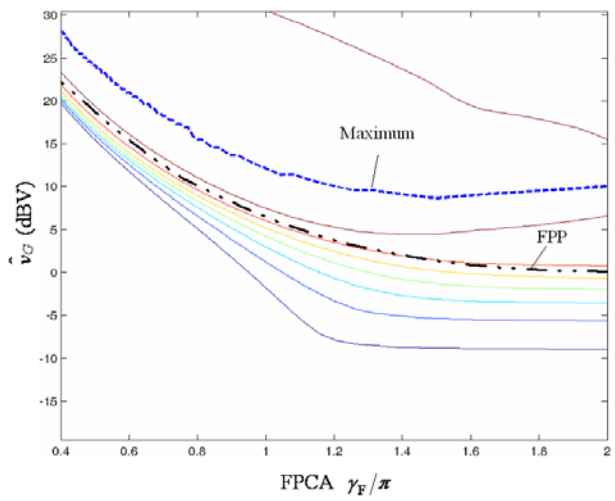

(b)

Figure 6.6 Efficiency versus $\hat{v}_G$ and FPCA γ_F, (a) 3-D plot; (b) contour plot.

The efficiency for the square law model, as defined in (5.33), and using F_0 and F_1 expressions derived in section 6.2.1, is shown in Figure 6.6(a). This appears to be similar to that for the linear model in Figure 6.6(a), except that efficiency falls more rapidly with reducing $\hat{v}_G$ for all classes. As for the linear device model, the efficiency has a maximum with respect to $\hat{v}_G$. The path of the maximum is shown more clearly in contour plot of Figure 6.6(b).

6.2.5. Power Sweeps

For the square law device model, 3-D plots of fundamental and 3rd harmonic of device output current, gain and efficiency have been given in Figures 6.3(b), 6.4(b), 6.5 and 6.6(a), respectively. Sweeps of output power, gain and efficiency obtained from these 3-D plots are shown in Figures 6.7, 6.8 and 6.9. The γ_F values for these sweeps for the square law model are given in Table 6.2.

Comparing the output power plots in Figure 6.7 with these for the linear model in Figure 5.8, the following statement can be made. Except for Class A, the output power at the FPP for the square law model is reduced significantly. In class AB, the change from region R0 to R1 is less abrupt, and there is an increase in slope rather than reduction in slope. The output power in class BC range of the square law model follows the same features as that of the linear model except that gain is reduced more. The slope of the gain curve in Class B is 2, showing very nonlinear behaviour.

Gain sweeps for the square law model in Figure 6.8 shows major differences from the linear model results in Figure 5.9. Due to the nonlinearity of the model, small signal gain in the class AB range depends on γ_F, and peaks close to the FPP. These differences suggest the model effect on PA performance is significant.

Table 6.2 values of γ_F for PA performance power sweeps in Figures 6.7 − 6.10.

Class	γ_F (π)
A	2
AB1	1.2
AB2	1.05
B	1
BC1	0.9
BC2	0.8

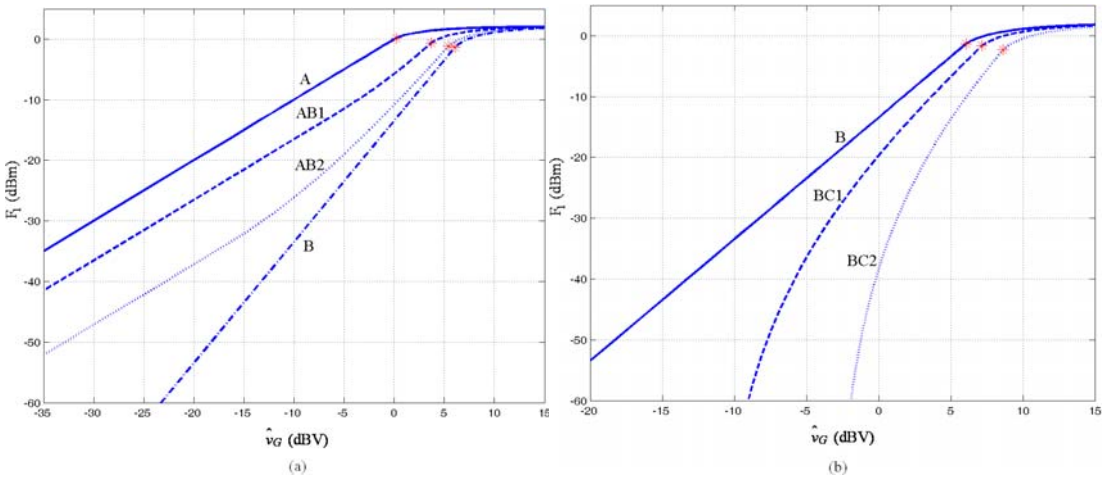

Figure 6.7 Predicted power sweeps from Figure 6.3 (b), (a) AB class range; (b) Class BC range.

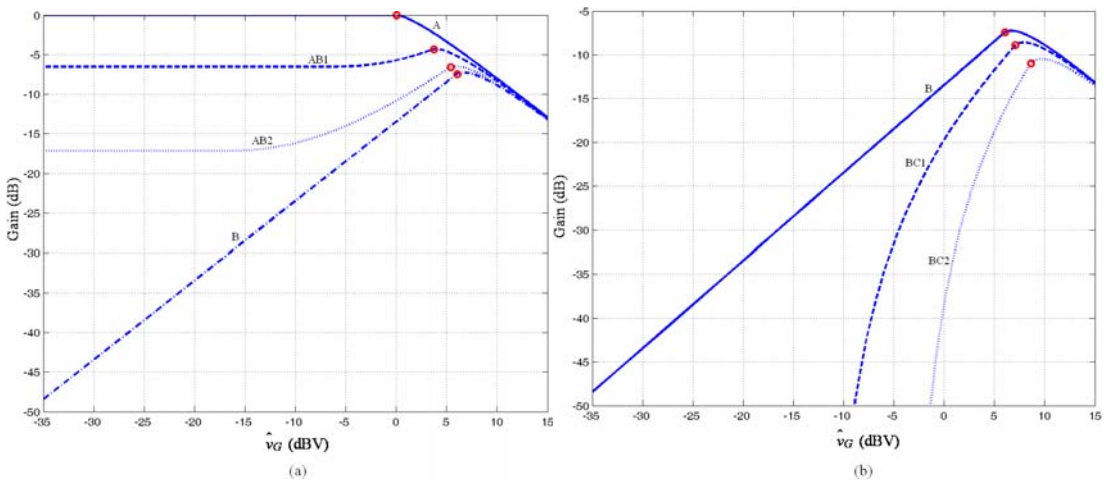

Figure 6.8 Predicted gain sweeps from Figure 6.5 (a), (a) AB class range, (b) BC class range.

PA efficiency sweeps for the square law model in Figure 6.9, show the efficiency for Class A at the FPP point has increased from 50% to 68%. The efficiency for Class B at the FPP point is less changed at 74%. Maximum efficiency at the FPP now occurs for Class AB1, rather than for Class B in Figure 5.9. Class A now has the highest efficiency in the low power range. Class AB and B are better in the high power range.

The 3-D plot of 3rd order PA distortion using the square law model was shown in Figure 6.4(b). Distortion sweeps obtained from this plot are shown in Figure 6.10. Compared with the linear model curves in Figure 5.11, the ledges in the class AB

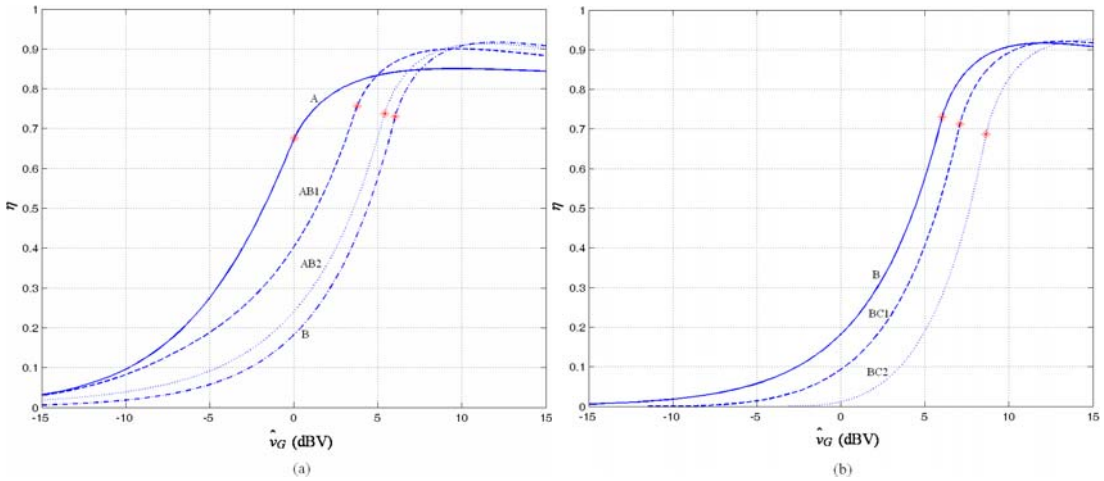

Figure 6.9 Predicted efficiency sweeps from Figure 6.6 (a), (a) AB class range, (b) BC class range.

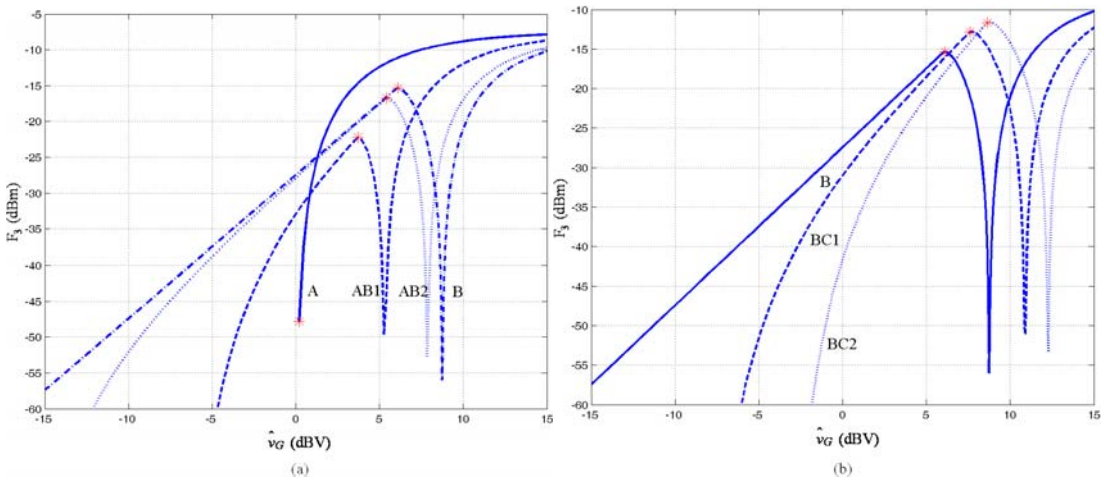

Figure 6.10 Predicted IMD power sweeps from Figure 6.4 (b), (a) AB class range, (b) BC class range.

range have become deep nulls that are above the FPP. For class B, as expected, there is now no sweet spot, but instead a deep null above the FPP, and a region of very high distortion in the quasi-linear range. Generally, distortion levels for the square law model are very high compared to those for the linear model in Figure 5.11.

6.3. Assessment of the Linear and Square Law Device Models

As mentioned in Chapter 2, IMD3 power sweep for PAs in the literature exhibit

a wide variety of behaviour patterns. In the BC class range ($0 < \gamma_F \leq \pi$), IMD3-power sweeps for practical PAs exhibit a single null. The single null was the form of distortion-power sweep predicted due to drain current clipping in Figure 5.11(b). For the square law device model, it can be seen from Figure 6.10(b) that, in this class range, the form of the distortion power sweep is similar. Thus, in the BC class range, the change of device model from linear to square law does not change the general form of the predicted distortion-power sweep. In the AB class range ($\pi \leq \gamma_F \leq 2\pi$), distortion-power sweeps for real PAs exhibit a wide variety of forms including the double null, the single null and the ledge. The linear model was able to predict the ledge but neither the double null nor the single null (Figure 5.11). However, it can now be seen from Figure 6.10 that the square law model only predicts a single null in the class AB range and neither the ledge nor the double null. Thus, neither of the two simple models that has been considered so far can predict observed distortion sweeps for real PAs in the AB class range. It can be concluded that the form of the distortion-power sweep for a PA in the AB class range is very sensitive to device model, which is not the case for the BC class range. In order to correctly predict the distortion characteristics of real PAs, we will need to study in detail the relationship between the distortion surfaces obtained using two simple models in Figures 5.5(b) and 6.4(b) and this will lead us to consider, in the next chapter, a more flexible form of device model.

6.4. Conclusion

In this chapter, the square law device model and a full analysis of PA output power, efficiency, gain and 3rd order distortion obtained using it were presented.

The difference between DC components of output current of the linear and square law models, shown as a 3-D plot versus $\hat{v}_G$ and γ_F, demonstrated the effect of the model on performance of PAs. For fundamental component, the slope of output power versus input power is rather different, except for Class A case. The case of Class B showed nonlinearity that decreases output power in low power range. For two Class AB cases, the gain expansion effect has been presented after the linear increase

range and below saturation. Therefore, the efficiency sweeps for two models present distinctive features.

However, the most significant result was the distortion performance comparison for two models. For the linear model, there is a deep null for class B for the quasi-linear range, a ledge for class AB and a valley in the BC class range. For the square law model, the valley in the 3rd order distortion extends from the BC class range straight across into the class AB range rather than making a turn into Class B. The common feature between the two models is that the valley appears in the 3rd order distortion surface. But the difference is the position of valley, especially in the class AB range. It would illustrate an important result that the clipping results in the appearance of the valley, whereas the model transfer characteristic determines the path of the valley. The mechanism understanding the different performance of two models will be presented in the next chapter.

However, the linear and square law models are two extreme cases of device transfer characteristics. They cannot realistically represent the characteristics of real devices. In next chapter, more flexible models will be investigated, which can present the features of real devices. Because 3rd order distortion characteristics have shown significant change due to the different device transfer characteristics, the investigation will be focused on 3rd order distortion in the following chapter.

CHAPTER 7

TRANSITIONAL DEVICE MODELS AND PA PERFORMANCE

7.1. Introduction

In Chapters 5 and 6, the PA device current clipping theory of Chapter 3 and 4 was used to derive the key PA performance parameters that are determined by device output current clipping, namely, output power, gain, efficiency and 3rd order distortion, for two types of device model, the linear one and the square law. All PA performance parameters have been plotted as 3-D surfaces as a function of FPCA γ_F, that defines PA class, and input signal amplitude, $\hat{v}_G$. The surfaces for output power, efficiency and gain have similar general forms for the two device models, and differ only in the degree of slope of the surface. For 3rd order distortion, on the other hand, the situation is different. Although both models produce a very high level of distortion in the double and single clipping regions, R2 and R1, which is crossed by a deep valley, the valley path is quite different for the two models. For the linear model, the valley is 'L'-shaped, but for the square law model the valley traverses the surface in a smooth curve. This difference leads to quite different distortion-power sweep predictions for the two models.

The 'L'-shaped valley obtained for the linear model is quite similar to that observed in the literature for a LDMOS device whose transfer characteristic is

approximately linear [86]. But most PA devices, including those based on CMOS and GaAs technologies, have quite different distortion-power sweeps that exhibit a variety of features depending on class, including single null, double null and ledge. This wide variety of distortion characteristics could be predicted from the 3-D distortion surface for neither the linear nor the square law model.

The purpose of this chapter is to try to derive a device model that can predict the wide variety of distortion characteristics of real PAs. This task is begun by trying to explain the reason behind the very great change in distortion characteristics obtained for the linear and for the square law device model.

7.2. Relationship between Linear and Square Law Model Distortion Surfaces

7.2.1. Objective

3-D plots of 3rd order PA distortion for the linear and square law device models that are now studied were derived in chapters 5 and 6 as Figures 5.5(b) and 6.4(b), respectively, and they are shown again in Figure 7.1(a) and (b). In both cases, a deep valley crosses the entire surface. The path of the valley is similar in the BC class range. But the path of the valley is quite different for Class B and in the AB class range. The path of a valley is shown most clearly by contour plots and contour plots

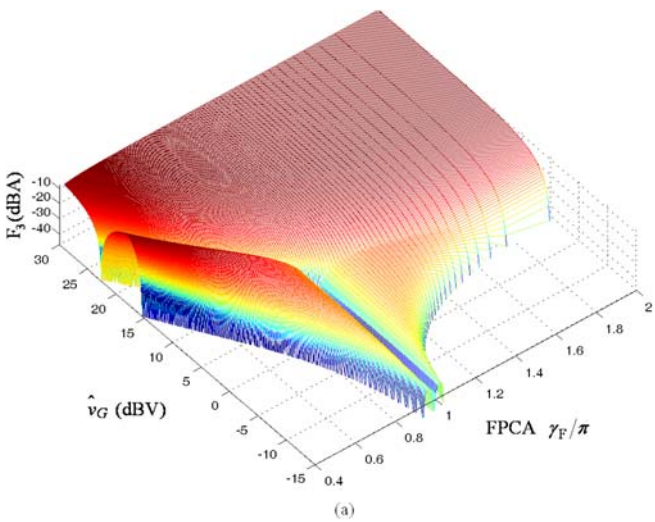

(a)

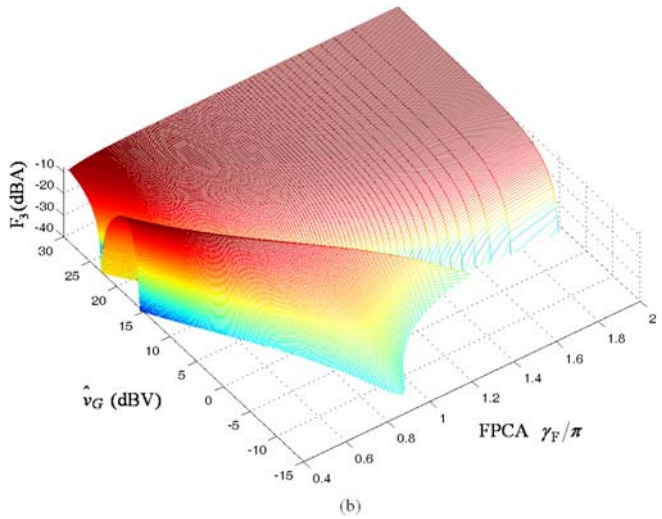

Figure 7.1 3rd order distortion 3-D plots for (a) linear device model, (b) square law model.

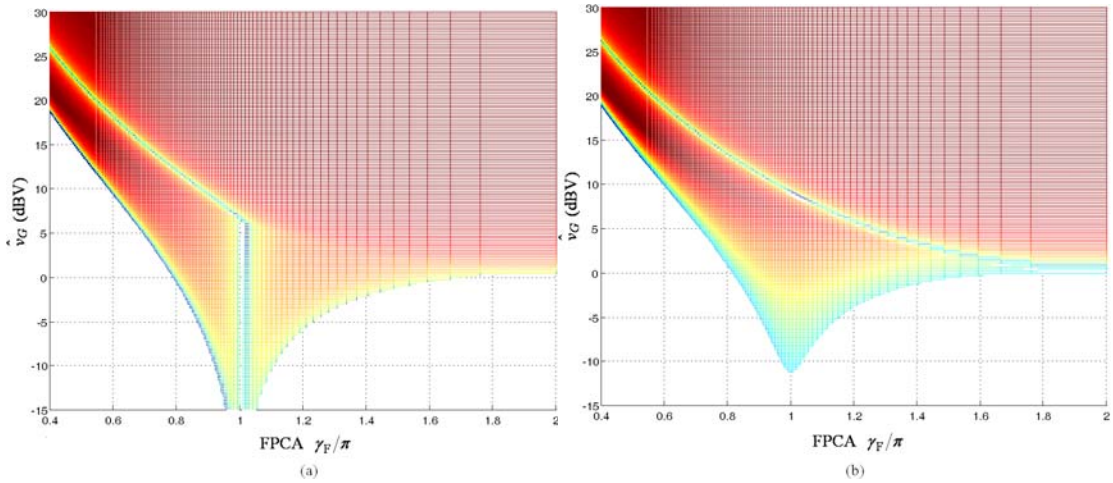

Figure 7.2 3rd order distortion contour plots for (a) linear device model; (b) square law model.

corresponding to the 3-D plots in Figure 7.1(a) and (b) are shown in Figure 7.2(a) and (b), respectively. In order to try to understand why the position of the valley has changed in the way shown clearly in Figure 7.2, some general properties of such valleys will be derived.

7.2.2. Principle of Valley Continuity

On each side of a deep valley in a distortion plot that is expressed in dB units, the original Fourier coefficient must have opposite signs since, in the valley, the

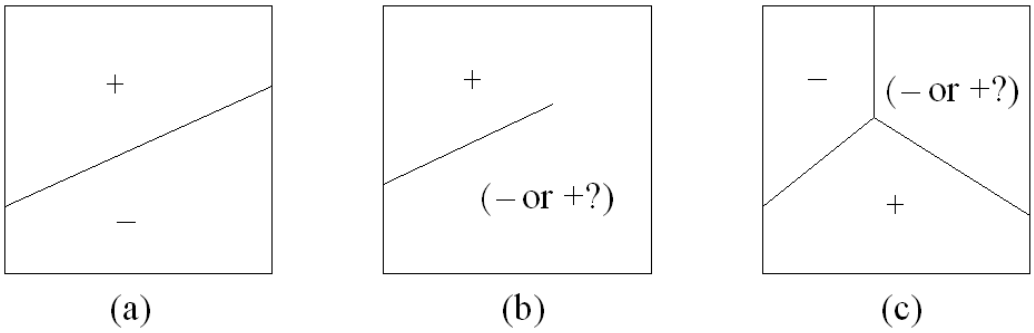

Figure 7.3 Permissible and impermissible conditions on a deep valley, (a) permissible; (b) and (c) impermissible.

Fourier series coefficient is zero. Thus valleys divide such plots into regions with opposite signs. The need for each region to have a unique sign imposes some general constraints on the path of a valley.

1) A valley may cross an entire surface dividing it into two regions where the Fourier series coefficient has opposite signs, as shown in Figure 7.3(a).
2) There are no restrictions, in general, on the way in which such a valley may turn or bend.
3) A valley can never terminate in the middle of a surface because then no unique set of suitable signs exists, as illustrated in Figure 7.3(b). A valley can never split into two valleys, as is illustrated in Figure 7.3(c), for the same reason.

The fact, that in both contour plots in Figure 7.2, the valley crosses the entire surface, is consistent with the principle of valley continuity. Understanding the effect of device model on distortion is approached by introducing a new definition.

7.2.3. Idea of Effective Threshold Voltage

The transfer characteristics for the linear and square law device models that were shown in Chapter 6 as Figure 6.1 are shown again in Figure 7.4. For the linear model, the on-set of conduction at the cut-off point ($v_G = V_T$) is abrupt, but for the square law model, it is gradual. For a square law model device operated with large signal amplitudes, the curved characteristic that occurs around $i_D = 0$ must be less significant in determining i_D than the shape of the curve for higher values of i_D. Hence, PA behaviour with a square law device model may be approximated by that for a

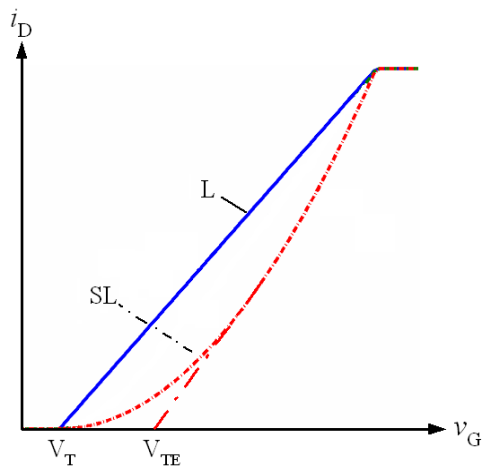

Figure 7.4 Explanation of effective threshold voltage, with transfer characteristics for linear device model 'L' and square law model 'SL'.

linear model with an *effective threshold voltage* V_{TE} that is significantly higher than the actual V_T, as shown in Figure 7.4.

The idea of extrapolating the high − i_D part of the i_D curve in this way is not a precise concept. In order to approximately match large i_D behaviour for the square law model, it would strictly be necessary to increase G in the linear model equation (5.14) as well as increase V_T, as Figure 7.4 shows that the gradient of the model transfer characteristic is increased. Thus the concept of effective threshold voltage is rather empirical and is based on the idea that the effect of shift of V_T on distortion, which effects clipping behaviour, is the most significant factor. The usefulness of the concept will be shown in due course.

By using the concept of effective threshold voltage, the effect of a nonlinear device model on clipping and conduction angle can be approximately evaluated. From (3.8), increase in V_T to V_{TE} will reduce cosβ. This corresponds to an increase in the effective value of β. It can be shown from (3.9) that this causes a reduction in effective conduction angle γ. The result that the square law model reduces the effective conduction angle may be reached in an alternative way by considering the idea of effective conduction angle more directly, in the context of the device current waveform.

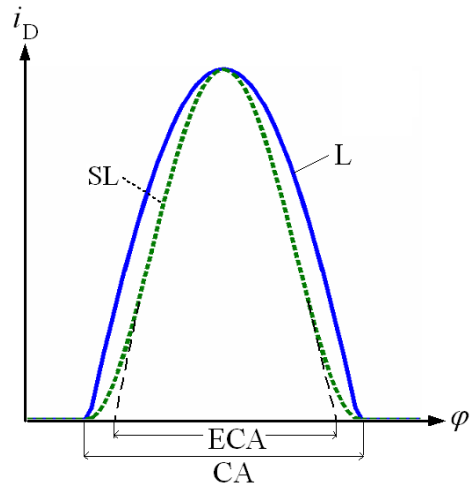

Figure 7.5 Relationship between effective conduction angle (ECA) and conduction angle (CA) showing device current waveforms for linear (L) and square law (SL) device models.

7.2.4. Idea of Effective Conduction Angle

Figure 7.5 shows a sketch of two device output current waveforms, one for a linear device model and one for a square law model. The conduction angles for both waveforms are the same, so i_D reaches zero at the same time instants. However, in the case of the square law model, the current pulse is significantly narrower. In an informal way, the main part of the pulse may be extrapolated to the φ axis, in order to define an *effective conduction angle*, ECA. For the square law model, ECA is always less than CA. Thus, the conclusion is the same as that reached in section 7.2.3 using the concept of effective threshold voltage, namely that use of the square law device model reduces effective conduction angle γ below the actual conduction angle.

7.2.5. Significance of Change in Effective Conduction Angle

The task is best approached through the contour plot of constant values of conduction angle γ versus input signal amplitude $\hat{v}_G$ and FPCA γ_F which was derived in chapter 4 (section 4.7) as Figure 4.6, and is shown again in Figure 7.6.

The clear distinction made between γ_F that defines PA class, and γ for a given class (value of γ_F) that varies with $\hat{v}_G$, is key to the approach developed in this thesis. In general, for any class of PA, *i.e.* value of γ_F, γ is equal to γ_F only at the FPP. The

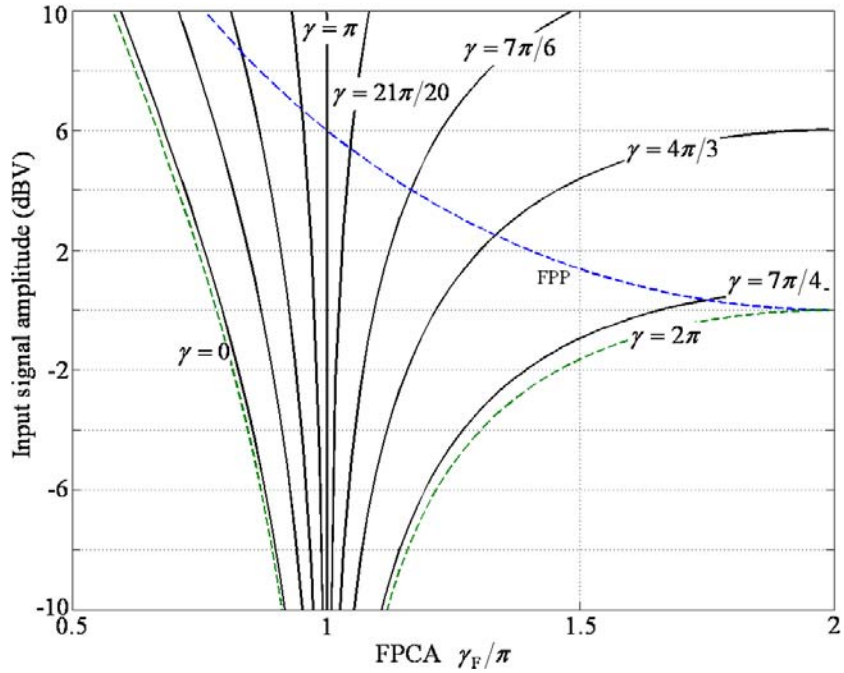

Figure 7.6 Contours of constant conduction angle (γ) versus input signal amplitude $\hat{v}_G$ and FPCA γ_F.

value of γ varies with $\hat{v}_G$ above the FPP in the R2 region and below the FPP in the R1 region; the only exception is Class B, for which $\gamma = \gamma_F = \pi$ for all input signal amplitudes. Thus, the effect of using the square law device model in reducing the effective conduction angle, as was shown in the previous subsections, cannot be simplistically interpreted simply as a change in the class of a PA. It must be interpreted within the framework of the constant γ contours in Figure 7.6.

Consider now a 3-D plot of some PA performance parameter, such as distortion, versus input signal amplitude $\hat{v}_G$ and FPCA γ_F when a linear device model is assumed. Consider further, a feature of the PA performance surface that occurs for particular values of $\hat{v}_G$ and γ_F. From the contour plot in Figure 7.6, the value of γ at the values of $\hat{v}_G$ and γ_F corresponding to that feature may be obtained. If now a square law model is assumed that reduces the effective value of γ, then the feature must now occur at a point to the right of the original point on a new γ contour for a higher value of γ such that the reduction of effective γ due to the square law model yields the

original γ value. This approach can now be applied in order to explore the relationship between the distortion surface in Figures 7.1(a) and (b).

7.2.6. Relationship between Distortion Surfaces

Consider the Class B part of the valley in the distortion contour plot of Figure 7.2(a) for the linear device model. We showed in section 5.3.4 that the class B valley in Figure 7.2(a) follows the $\gamma = \pi$ contour in Figure 7.6 in the quasi-linear region, *i.e.* up to the FPP. Consider now the effect of introducing a nonlinear device model, the square law model.

From the argument in section 7.2.5, we would expect the same feature to occur, but for a higher value of conduction angle γ. Therefore the valley should now follow a contour for $\gamma > \pi$ in Figure 7.6. Thus it should rotate clockwise and become curved. In the limit of extreme non-linearity, the valley would end up following the $\gamma = 2\pi$ contour. We can see from Figures 7.6 and 4.3(b) that the valley would then be following the boundary between the R1 and R0 regions. Since there is no distortion in the R0 region for either model (see Figure 7.2), at that point the valley will have effectively disappeared into the R0 region, where there is no distortion.

Consider now the class BC part of the valley in Figure 7.2(a). The principle of valley continuity of section 7.2.2 requires that this part of the valley cannot terminate in the middle of a surface. Therefore it must extend to keep its connection with the rotated class B valley. The result is that, for a highly nonlinear model, the class BC valley must extend right across the surface. The rotation and curving of the class B part of the valley until it disappears into the no-distortion R0 region and the extension of the class BC part of the valley as described would lead precisely to the surface features in Figure 7.2(b).

The relationship between the 3-D distortion surfaces obtained with the linear and square law models has been explained in general terms by introducing the concepts of effective threshold voltage and effective conduction angle. Although this is a contribution to general understanding, it is necessary to remember what was shown in Chapters 5 and 6, that neither of these distortion plots can predict the distortion-power sweeps of real PAs. Next, the ideas that have been introduced will

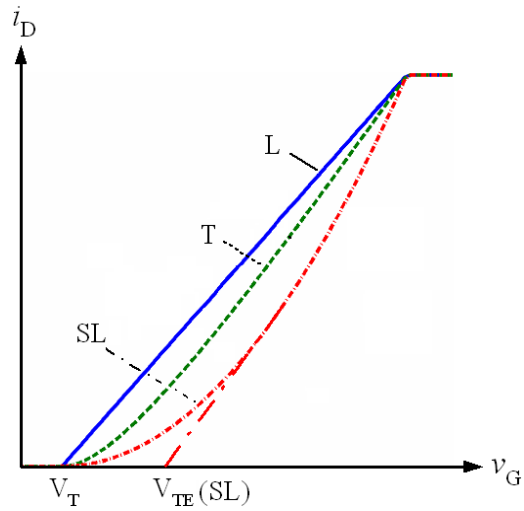

Figure 7.7 Transfer characteristics for linear device model 'L', square law model 'SL' and transitional model 'T'.

be developed further in order to try to arrive at an idea for a type of model that can predict the distortion behaviour of real PAs.

7.3. Idea of Transitional Device Model

Consider a general kind of device model [9] whose transfer characteristic lies between those for the linear and square law models, as exemplified by curve 'T' in Figure 7.7, where 'T' denotes *transitional model*. Because the effective threshold voltage for the transitional model lies between V_T and V_{TE}, the reduction of the effective value of γ due to model non-linearity will be less severe than that for the square law model. Therefore the class B part of the distortion valley would be expected to not follow the $\gamma = 2\pi$ contour in Figure 7.6, but rather to follow an intermediate curve, such as that for $\gamma = 7\pi/6$ or $4\pi/3$.

The shape of the whole distortion valley expected, including the extension of the class BC valley to meet up with the rotated class B valley, as required by the

[9] The square law model is normally inaccurate, expecially for short-channel FET in high-frequency. In [77], reducing power of the Q-law model from 2 to 1.7 has been demonstrated to describe second and third order derivatives more realistically.

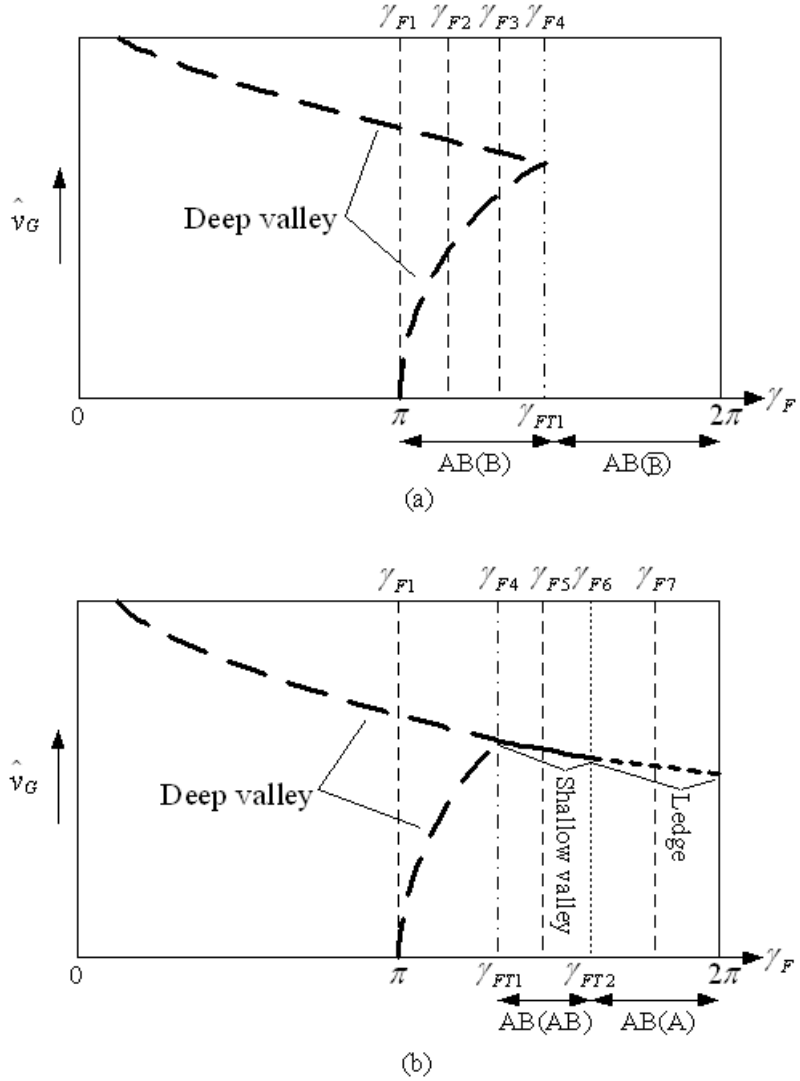

Figure 7.8 Sketch of rotated valley and slices for distortion sweeps, (a) division of AB class range; (b) sub-division of AB($\overline{\mathrm{B}}$) class range.

principle of valley continuity, is sketched in Figure 7.8(a). In the following section, the implications for distortion sweeps of the rotated 'L'-shaped valley in Figure 7.8(a) will be fully explored. But it can be noted already, that a power sweep for the γ_F values γ_{F2} and γ_{F3} in Figure 7.8(a) will certainly cross the deep valley twice and therefore yield the double null which is frequently observed in the distortion characteristic of real PAs operating in class AB, and which cannot be obtained from the linear and square law model distortion surfaces in Figure 7.1.

7.4. Sub-divisions of the AB Class Range

7.4.1. Principal Sub-division

In section 3.2.4, the total range of PA class, from $\gamma_F = 0$ (limit case of Class C) to $\gamma_F = 2\pi$ (Class A) was subdivided into the AB and BC class ranges, based on different clipping behaviour. Based on the hypothesis of the rotation of the 'L'-shaped valley, as sketched in Figure 7.8(a) and which will be verified in later sub-sections of this chapter, it is now possible to make a further sub-division within the AB class range.

First, the value of γ_F corresponding to the 'corner' of the 'L'-shaped valley in Figure 7.8(a) is termed a transition FPCA γ_{FT1}. It provides a natural way of sub-dividing the AB class range that is mathematically precise and has tremendous practical engineering significance. The parts of the AB class range to the left and right of γ_{FT1} are denoted AB(B) and AB($\overline{B}$) class ranges, respectively as indicated in Figure 7.8(a). AB(B) denotes part of AB class range adjacent to Class B and AB($\overline{B}$) denotes part of AB class range away from Class B. Superimposed on the sketch of the rotated valley in Figure 7.8(a) are lines representing distortion-power sweeps for different values of γ_F in the AB(B) class range.

The lower limit of the AB(B) class range is for $\gamma_F = \pi$ (class B). For this value of γ_F, there is a null in the saturation region for high input power. For lower power, the valley becomes parallel to the $\hat{v}_G$ axis, causing a sweet spot, but for very low input power only.

The upper limit of the AB(B) class range, $\gamma_F = \gamma_{FT1}$, is characterised by a single null, which is the convergence in the limit of two nulls that come from the class B and BC parts of the rotated valley. At this precise point, the direction of the valley becomes parallel to the $\hat{v}_G$ axis as the valley turns. Therefore, this deep null is expected to be unusually wide, and it will be referred to as the *wide null*. Each side of the wide null, the original F_3 function has the same sign.

For the range between $\gamma_F = \pi$ and $\gamma_F = \gamma_{FT1}$, the 'L'-shaped valley is crossed twice in distortion sweeps and that gives rise to two deep nulls. The spacing between the nulls reduces as γ_F increases in this range. For example, choosing γ_F in Figure

7.8(a) to be γ_{F2} and γ_{F3} will give rise to double nulls, with wide and narrow input power spacing, respectively.

7.4.2. Subdivision of AB($\overline{B}$) Class Range

Consider Figure 7.8(b) that shows the AB($\overline{B}$) class range in Figure 7.8(a) in more detail. It has been shows that there is a deep null in the distortion sweep at the transition point $\gamma_F = \gamma_{FT1}$. For distortion-power sweeps in the part of the AB($\overline{B}$) region close to γ_{FT1}, the null at γ_{FT1} must produce a minimum. This minimum cannot be a deep minimum, because the deep valley turns back on itself at $\gamma_F = \gamma_{FT1}$ and does not exist for $\gamma_F > \gamma_{FT1}$, as has been explained. The feature that occupies the part of the AB($\overline{B}$) range close to $\gamma_F = \gamma_{FT1}$ is referred to as a *shallow valley*. The part of the AB($\overline{B}$) range close to $\gamma_F = \gamma_{FT1}$ where there is a shallow valley is denoted the *AB(AB) class range*. As γ_F increases above γ_{FT1}, the depth of the shallow valley will gradually reduce. The signs of F_3 each side of this shallow valley are the same.

In the part of the AB ($\overline{B}$) class range close to $\gamma_F = 2\pi$ (Class A), there must be a ledge, as is the case for the linear model and is visible in Figure 7.2(a). This part of the AB ($\overline{B}$) class range is denoted the *AB(A) class range*, as shown in Figure 7.8(b).

Hence, the AB ($\overline{B}$) class range may be divided into sub-ranges AB(AB) and AB(A), according to whether there is a shallow null or a ledge, respectively. The dividing point between the two sub-ranges is denoted a second transition FPCA, γ_{FT2}, as indicated in Figure 7.8(b). For $\gamma_F \leq \gamma_{FT2}$, where there is a shallow valley, the slope of the distortion surface with respect to $\hat{v}_G$ suffers a change in sign. For $\gamma_F \geq \gamma_{FT2}$, there is no such change of sign. The transition point γ_{FT2} may thus be precisely defined, mathematically. The subdivision of the AB ($\overline{B}$) class range into regions of shallow valley and ledge is obviously of considerable practical engineering significance.

Thus, it can be seen that the rotated 'L'-shaped valley concept could in principle, predict the wide variety of IMD3-power sweep types that are observed in practical PAs in the class AB region, including the double null, single deep null, single shallow null and ledge. The following sections will introduce some examples of transitional device models and derive the distortion performance obtained from them in order to test the speculative ideas and concepts that have been proposed.

7.5. Transitional Device Models

7.5.1. Q – Law Model

The Q-law model is given by

$$i_D = K\left(v_G - V_T\right)^Q \tag{7.1}$$

The Q-law model has been used as a starting point from which advanced models for GaAs MESFETs have been developed [92]. Applying the same normalisation method for i_D and v_G as that used for the linear and square law models in chapters 5 and 6, i_D is set to be 2A when v_G is V_T + 2V. Then, in (7.1), $K = 2^{(1-Q)}$ AV^{-Q}. Thus the normalised form of (7.1) is

$$i_D = 2^{1-Q}\left(v_G - V_T\right)^Q \tag{7.2}$$

When the transition parameter Q is 1, the expression is identical to that for the linear model in (5.15). When Q is 2, it becomes the square law expression of (6.2). When Q lies between 1 and 2, a transitional transfer characteristic between linear and square law forms is expected.

7.5.2. Velocity Saturation Model

The velocity saturation model is given by

$$i_D = K\frac{\left(v_G - V_T\right)^2}{1+\theta\left(v_G - V_T\right)} \tag{7.3}$$

This form of model is commonly used to represent the effect of carrier velocity saturation in a device, in which case θ is termed the velocity saturation parameter [93]. Normalising i_D to be 2A when v_G is V_T + 2V, then, in (7.3), $K = \theta + 1/2$ AV^{-2}. Thus the normalised form of (7.3) is

$$i_D = \left(\theta + 1/2\right)\frac{\left(v_G - V_T\right)^2}{1+\theta\left(v_G - V_T\right)} \tag{7.4}$$

When the transition parameter θ approaches infinity, the model approaches the linear model of (5.15) and when θ equals zero, the model becomes the square law model of (6.2). Note that θ in (7.4) is not necessarily used to represent the velocity saturation effect in a device. It is now regarded simply as a transition parameter in the model equation.

7.5.3. Comparison of Transitional Models

Plots of i_D versus v_G for the Q-law model from (7.2) and for the velocity saturation model from (7.4) are given in Figures 7.9(a) and (b), respectively. The

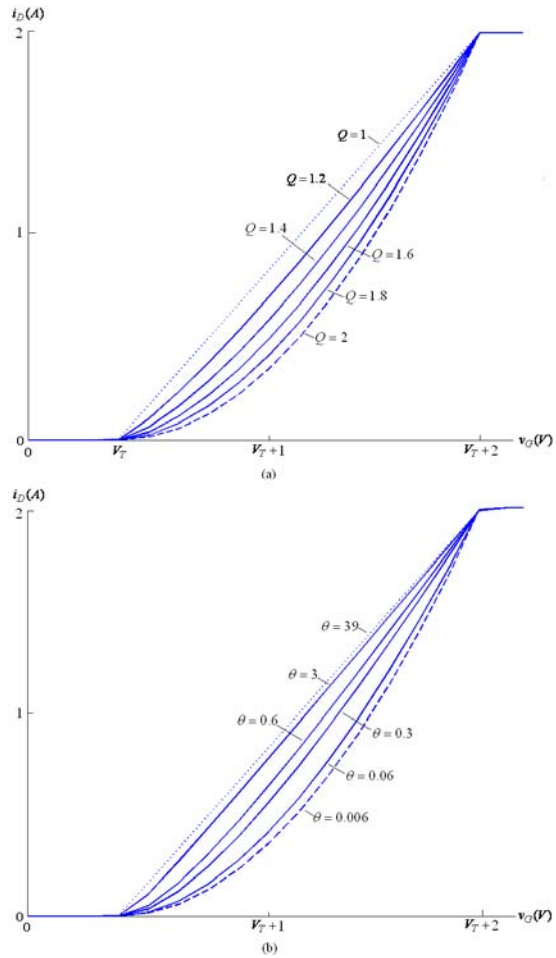

Figure 7.9 Transfer characteristics for transitional models, (a) Q-law model, (b) velocity saturation model.

range of Q-values and θ-values used is stated in the figure. The limiting cases of the linear model (Q = 1, $\theta \rightarrow \infty$) and square law model (Q = 2, θ = 0) are included, exactly or as close approximations.

It can be seen from Figure 7.9 that both transitional models produce a smooth curve that can change in a continuous fashion between the linear and square law curves. The curves in Figure 7.9 may be linearly extrapolated, in the way shown in Figure 7.4, and this will lead to a wide range of values of effective threshold voltage, V_{TE}. Thus both models appear to satisfy the requirements for a transitional model, as discussed in section 7.3 and sketched in Figure 7.7.

However, there are some differences between the sets of curves for the two models in Figures 7.9(a) and (b) that follow from their defining expressions. In the limiting case Q = 1 and $\theta \rightarrow \infty$, both models give a linear relationship between v_G and i_D. However, if we exclude the linear case, *i.e.* applying restrictions Q > 1 and $\theta < \infty$, (7.4) shows that the relationship between v_G and i_D for the velocity saturation model

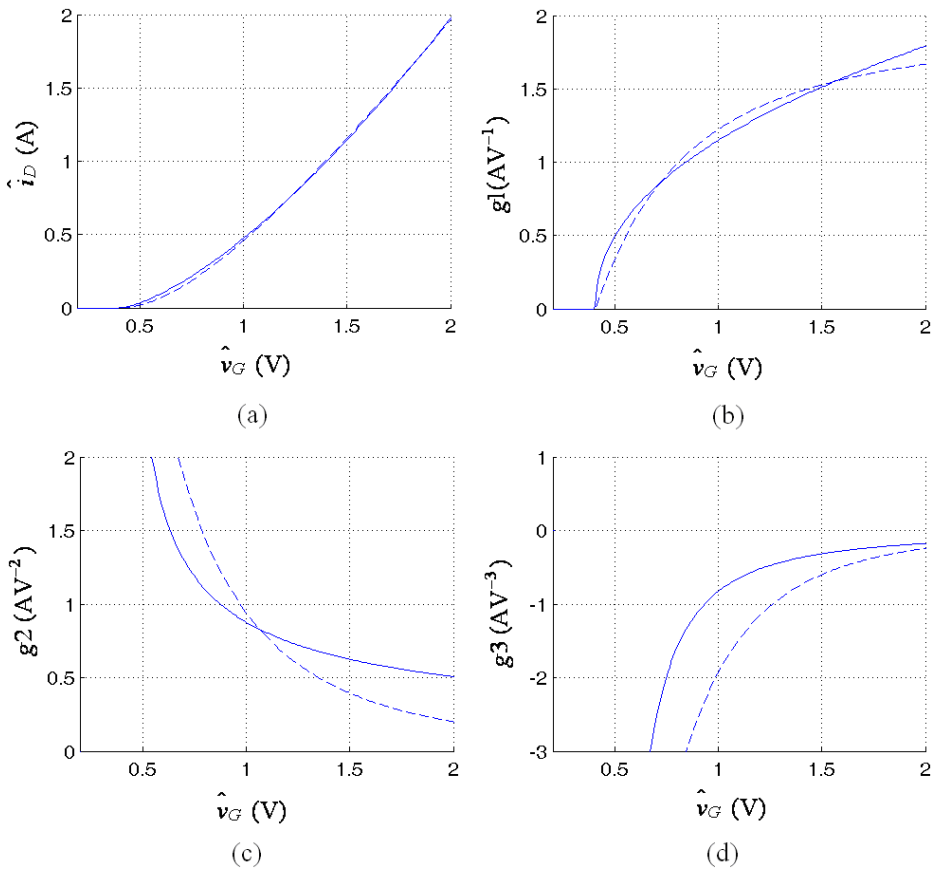

Figure 7.10 Comparison of transitional models for Q = 1.45 (—) and θ = 0.30 (- -), (a) i_D, (b) first derivative, (c) second derivative, (d) third derivative.

always tends towards a linear one for large v_G, which is not the case for the Q-law model of (7.2). This effect can be observed in Figure 7.9, by taking a pair of Q and θ values that give roughly the same transitional curve overall, such as Q = 1.4 and θ = 0.3. For this case, the linearizing effect in the upper half of the curve can be clearly seen in Figure 7.9(b), whereas that part of the corresponding curve in Figure 7.9(a) is more curved. Thus although both models satisfy the requirement of being transitional models, they also do have individual features.

More precise comparison between the Q-law and velocity saturation model transfer characteristics in Figure 7.9 may be made by plotting curves for particular Q and θ values on the same graph and also by comparing their small-signal bias-dependent derivatives, as shown in Figures 7.10 − 7.12. Since both models have derivatives with step or spike discontinuities for $v_G = V_T$ and for $v_G = v_{GL}$, only the intermediate range $V_T < v_G < v_{GL}$ is plotted. In Figures 7.10 and 7.11, a value for the transition parameter θ of 0.3 was set, corresponding to the middle of the transition

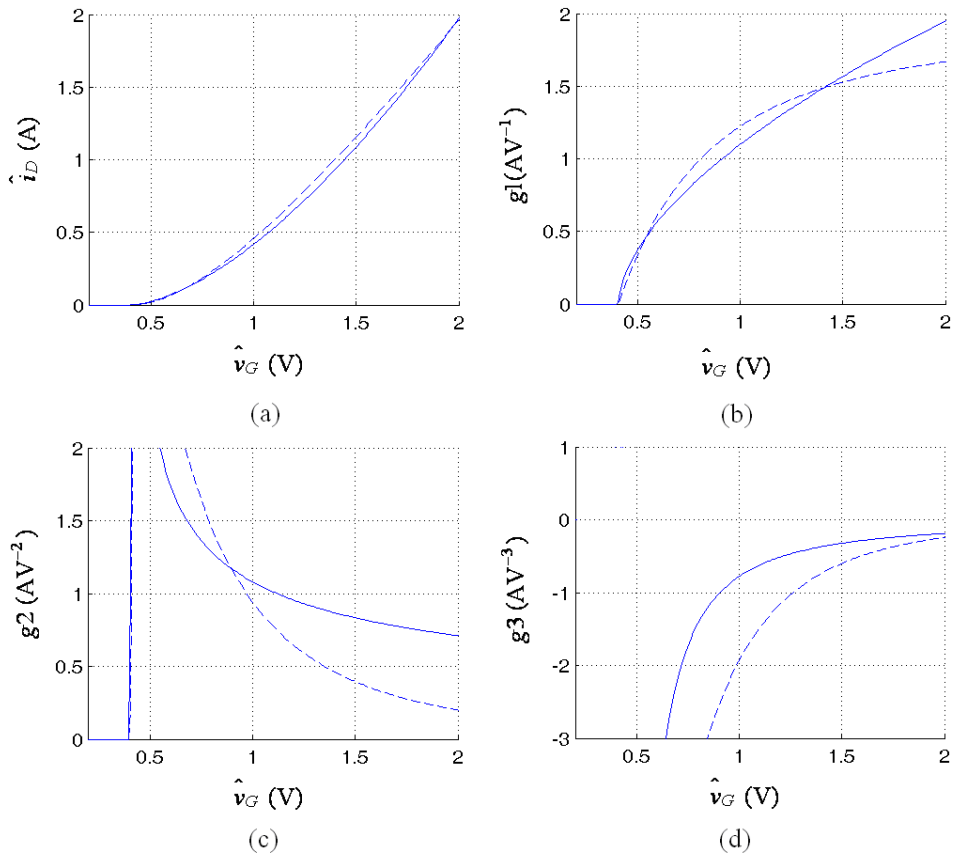

Figure 7.11 Comparison of transitional models for Q = 1.58 (−−) and θ = 0.30 (- -), (a) i_D, (b) first derivative, (c) second derivative, (d) third derivative.

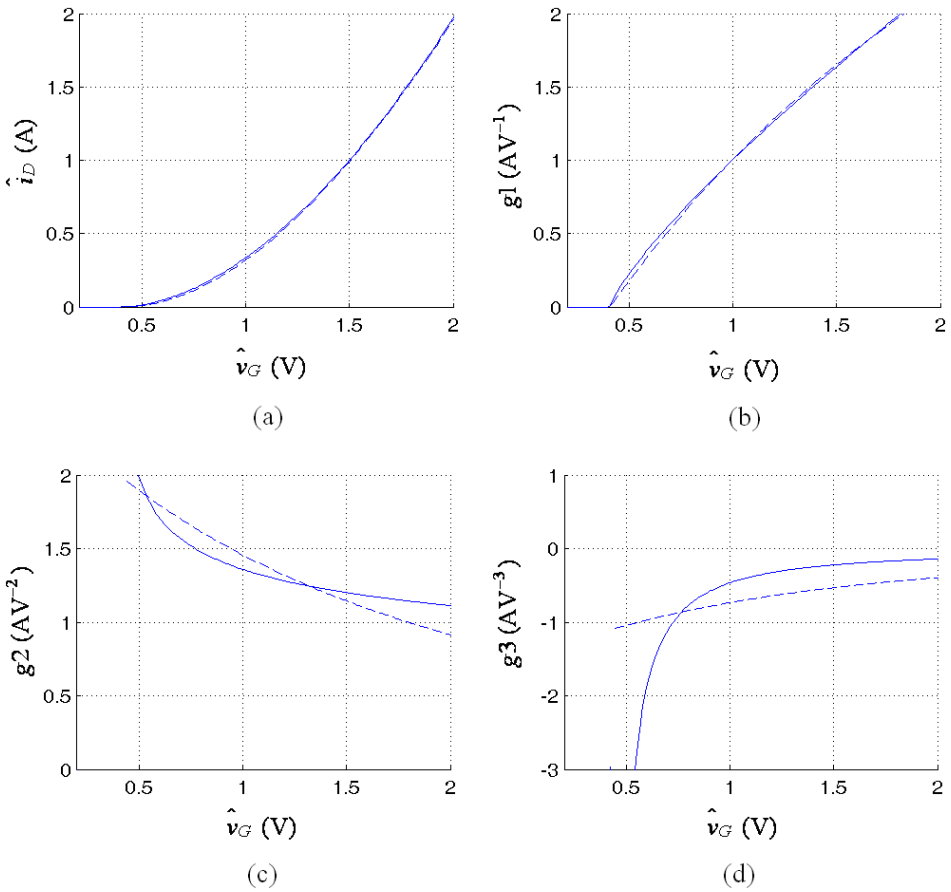

Figure 7.12 Comparison of transitional models for Q = 1.8 (—) and θ = 0.05 (- -), (a) i_D, (b) first order derivative, (c) second order derivative, (d) third order derivative.

range in Figure 7.9(b), and two alternative Q-values of 1.45 and 1.58, respectively, were chosen. It can be seen from Figure 7.10 that, for Q = 1.45, the i_D values from the two models agree well at moderate i_D values but not for low i_D values. For Q = 1.58, it is clear from Figure 7.11 that the model i_D values agree well for low i_D values. However, whether the fit of i_D is good at low or at moderate i_D values, the small signal bias-dependent derivatives for the two models differ considerably, especially the 3rd derivative. This point is emphasised further in Figure 7.12, which shows the comparison for a θ value of 0.05, quite close to square law. It can be seen that choice of Q = 1.8 gives a good fit of i_D for all i_D values. However, in spite of this, there are considerable differences in the 3rd derivatives.

It is clear from Figures 7.10 and 7.11, that for θ = 0.3, a choice of Q = 1.45 (Figure 7.10) would lead to much closer values of effective threshold voltage for the two models than Q = 1.58 (Figure 7.11), since effective threshold voltage is governed

by moderate and high i_D values, and is relatively independent of the shape of the curve for low values of i_D. Figure 7.12 shows that for $\theta = 0.05$, the choice of Q = 1.8, that provides close i_D matching at all i_D levels, will give good matching of effective threshold voltages also.

These observations suggest that models with the same effective threshold voltages may have transfer characteristics that are not particularly well matched around the cut-off point. They also may have quite different small signal bias-dependent 3rd derivative characteristics.

7.5.4. Fourier series Coefficients for Transitional Models

The 3rd order Fourier series coefficients F_3 of the drain current waveforms for the two transitional models can be derived by substituting (7.2) and (7.4) into the integral expression I_3 in (5.13) with $k = 3$, which in turn is substituted into (5.12). However, in contrast with the cases of the linear and square law models considered in Chapters 5 and 6, the integrals I_3 obtained from both (7.2) and (7.4) do not have closed-form solutions. Therefore, numerical integration using MATLAB is employed for these transitional models. For every point in the $\hat{v}_G$ and γ_F space, one period of the drain current waveform i_D as a function of $\varphi = \omega_o t$ is evaluated and the Fourier series coefficient determined numerically. The MATLAB program used to accomplish this task is the same program as that used to verify the analytically derived Fourier coefficients in Chapters 5 and 6.

7.6. Examples of 3-D Distortion Plots

Examples of 3-D PA 3rd order distortion plots using transitional device models, obtained as described above, are given in Figures 7.13 and 7.14 for the Q-law and velocity saturation models, respectively. The curves in Figures 7.13(b) and 7.14(b) are for Q = 1.8 and $\theta = 0.05$, respectively, and are therefore towards the square law end of the transition range (for square law characteristic, Q = 2 and $\theta = 0$). The curves in Figures 7.13(a) and 7.14(a) are for Q = 1.45 and $\theta = 0.3$, respectively, and are close to the middle of the model transition range, as can be seen from the model transfer

characteristics in Figure 7.9. The reason for the choice of these precise values for Q and θ will be explained in section 7.7.

Some important conclusions can be drawn from the 3-D distortion plots in Figures 7.13 and 7.14. The hypothesis in section 7.3, using the concepts of effective threshold voltage and effective conduction angle that a transitional model will rotate and make curved the class B valley, of the linear model shown in Figure 7.1(a), as predicted, is clearly shown to be true. Secondly, the amount of rotation and curvature increases for models that are closer to the square law model, as is the case in Figures 7.13(b) and 7.14(b). Thirdly, the extension of the class BC part of the valley to meet up with the rotated and curved class B part of the valley, as required by the principle

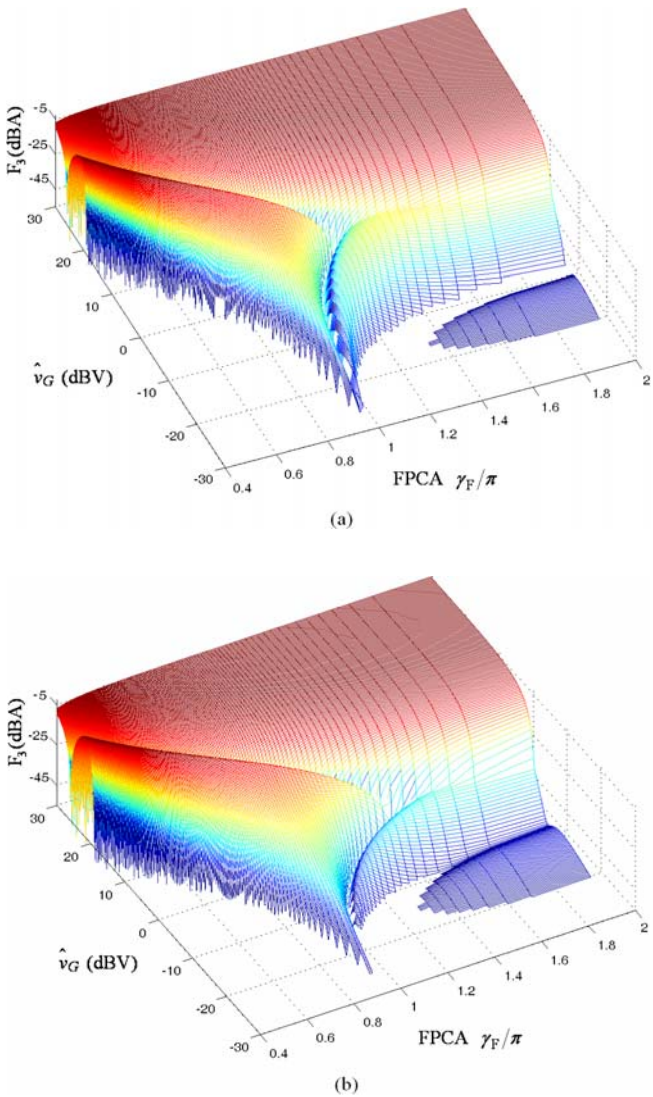

Figure 7.13 3-D plot of 3rd order distortion for the Q-law transitional model, (a) Q = 1.45 and (b) Q = 1.8.

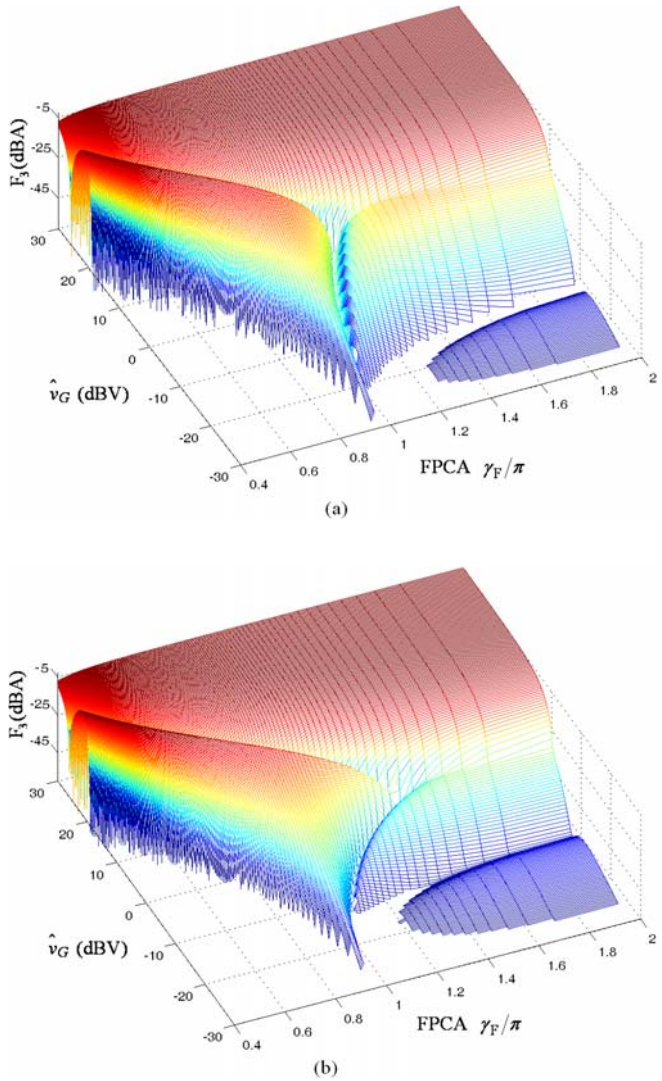

Figure 7.14 3-D plot of 3rd order distortion for the velocity saturation transitional model, (a) θ = 0.3 and (b) θ = 0.05.

of valley continuity of section 7.2.2, is clearly confirmed. Fourthly, we can see that the effect on the valley in Figures 7.13(a) and 7.14(a) is similar. Also, the effect in Figures 7.13(b) and 7.14(b) is similar. Note that the transfer characteristic and derivatives of the models used in Figures 7.13(a) and 7.14(a) are given in Figure 7.10 and those used in Figures 7.13(b) and 7.14(b) in Figure 7.12. We did note in section 7.5.3 that the effective threshold voltages for the models in Figure 7.10 were similar and those for the models in Figure 7.12 were similar. However, the corresponding models have very different 3rd derivatives and, in Figure 7.10, the model transfer characteristics differ considerably near cut-off. These considerations suggest that the

effective threshold voltage of a device is a more important factor affecting PA distortion than the precise form of the small signal bias-dependent 3rd derivatives or the precise shape of the transfer characteristic near cut-off.

Finally, it can be observed from Figures 7.13 and 7.14 that distortion is not zero in the R0 region, where there is no clipping. This is because the transitional model equations, (7.2) and (7.4), unlike the equations for the linear and square law models, (5.15) and (6.2), have 3rd derivatives that, in general, are not zero. However, Figures 7.13 and 7.14 show that distortion due to this effect is relatively small, and that distortion is principally determined by the high levels of distortion in the R1 and R2 regions of the $\hat{v}_G - \gamma_F$ plane that are due to clipping.

7.7. Examples of Distortion Contour Plots

Contour plots show the path of a deep valley more clearly than 3-D plots. Contour plots corresponding to the 3-D plots of Figures 7.13 and 7.14 are given in Figures 7.15 and 7.16, respectively. From these figures, the value of γ_F that corresponds to the 'corner' of the valley, denoted γ_{FT1} in Figure 7.8(a), can be determined quite precisely. Figures 7.15 and 7.16 reveal the principle that has been behind the choice of Q and θ values in Figures 7.13 − 7.16. This is that γ_{FT1} in the lower plots of these figures has been set to be 1.5π and in the upper plots, it has been set to be 1.2π.

Since the plots in Figures 7.15(a) and 7.16(a) have the same γ_{FT1} values, and those in Figures 7.15(b) and 7.16(b), have the same γ_{FT1} values, then we should expect that the upper end-points of the curved and rotated class B parts of the deep valleys must occur at the same point in the $\hat{v}_G - \gamma_F$ plane. It can be seen from Figures 7.15 and 7.16 that this is the case.

Consider now the lower end-points of these parts of the valleys in Figures 7.15 and 7.16. It can be seen from Figure 7.6 that, for very small input signal amplitude, all of the constant γ contours approach the same limit value, namely $\gamma_F = \pi$. It follows that irrespective of transition model type and the value of the transition parameter,

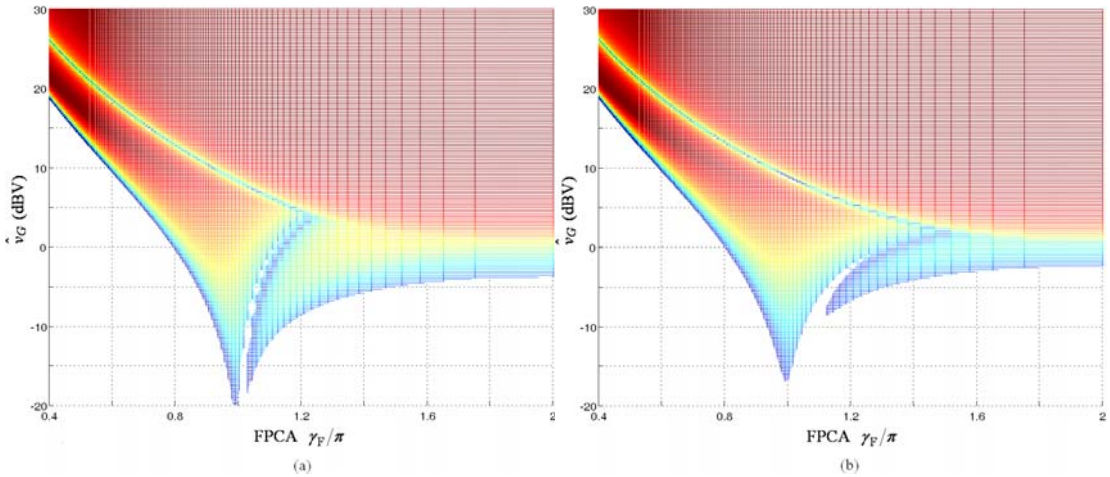

Figure 7.15 Contour plot corresponding to Figure 7.13, (a) Q = 1.45; (b) Q = 1.80.

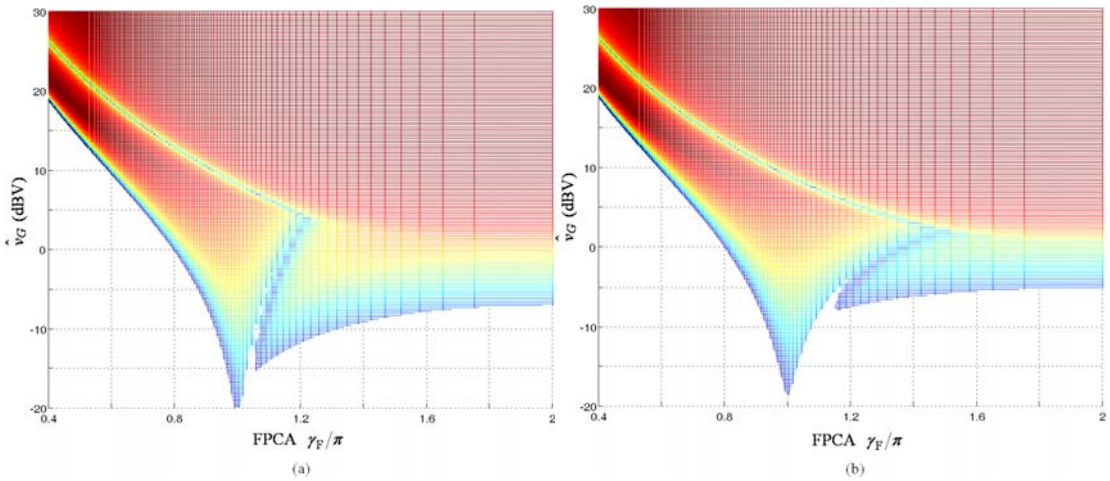

Figure 7.16 Contour plot corresponding to Figure 7.14, (a) θ = 0.30; (b) θ = 0.05.

and the effect of these on effective conduction angle, the rotated and curve class B part of the deep valley is expected to tend to follow the line $\gamma_F = \pi$ as signal amplitude is reduced. The contour plots in Figures 7.15 and 7.16 are consistent with this limit case.

Thus, we confirm that the two end-points of the rotated curved class B part of the valley in Figures 7.15(a) and 7.16(a) are the same, and likewise for Figures 7.15(b) and 7.16(b). We recall that the device models in Figure 7.10 that produced the distortion plots in Figures 7.15(a) and 7.16(a) have similar effective threshold voltages. The same comment applies to the models in Figure 7.12 that produced the

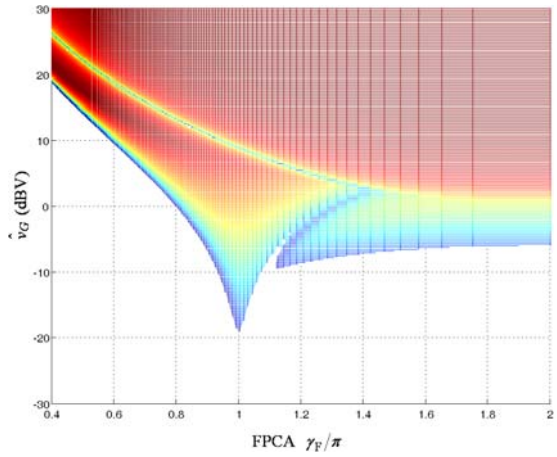

Figure 7.17 Contour plot of 3rd order distortion for Q-law model with Q = 1.58.

distortion plots in Figures 7.15(b) and 7.16(b). Thus we see that models with similar effective threshold voltages lead to similar γ_{FT1} and similar end points for the curved and rotated class B parts of the distortion valley.

Consider now the model characteristics in Figure 7.11, where Q was raised from Q = 1.45 used in Figure 7.10 to Q = 1.58, in order to give best matching of the i_D curves near the cut-off point, but leading to very different values for effective threshold voltage. The distortion contour plot for the Q = 1.58 model is shown in Figure 7.17. It can be seen that γ_{FT1} has changed from $\gamma_{FT1} = 1.2\pi$ in Figures 7.15(a) and 7.16(a) to around 1.4π. Thus is it confirmed that models with dissimilar effective threshold voltages lead to end points of the rotated curved Class B part of the distortion valley that are also dissimilar. It follows that neither modelling the precise shape of the device transfer characteristic in the cut-off region nor matching the small signal bias dependent 3rd derivative of current are the most critical factors for distortion prediction. Device current clipping is the dominant cause of distortion in PAs, and the key device model parameter that governs clipping is effective threshold voltage. This has important implications for modelling of devices for distortion prediction.

In spite of the fact that the end-points of the rotated and curved class B part of the deep valleys in Figures 7.15(a) and 7.16(a), and in Figures 7.15(b) and 7.16(b), are the same, yet the valleys are different. The difference is that the valley paths for

the Q-law model in Figure 7.15 are more curved than the corresponding valley paths for the velocity saturation model in Figure 7.16.

The fact that different transition models that produce the same γ_{FT1} have different degrees of curvature of the shifted class B part of the deep valley implies that the valleys can not simply be following constant γ contours in Figure 7.6. The reason that this might be so could be understood as follows.

Consider the device current waveform for a linear and for a nonlinear model in Figure 7.5. Since the difference between the waveforms is due to device nonlinearity, it is clear that if the signal amplitude is changed, the degree of nonlinearity of the nonlinear model will also change and the effective conduction angle will change too with respect to the actual conduction angle.

The implications of this argument may be understood in Figure 7.6. At high signal power close to the FPP, the effective conduction angle for the device output current waveform must determine the corner point, γ_{FT1}, of the L-shaped valley. However, as signal amplitude is reduced, effective conduction angle will change and this must change the γ contour that is being followed. Hence, models whose effective conduction angles vary with respect to signal amplitude in different ways may have rotated valleys in their distortion plots with different degrees of curvature, even though their γ_{FT1} values are the same. This has implications for device modelling that will be discussed later.

7.8. Distortion Contour Plots for Complete Range of Transition Parameters

Contour plots of distortion for the Q-law and velocity saturation transitional models are given for a wide range of values of transitional parameters in Figures 7.18 and 7.19. The values used for the transitional parameters are the same as those used for the transfer characteristic plots of Figure 7.9. In Figures 7.18 and 7.19, the first plot (Figures 7.18(a) and 7.19(a)) is the limiting case where the transitional models behave as the linear model and the last plot (Figures 7.18(f) and 7.19(f)) is the other

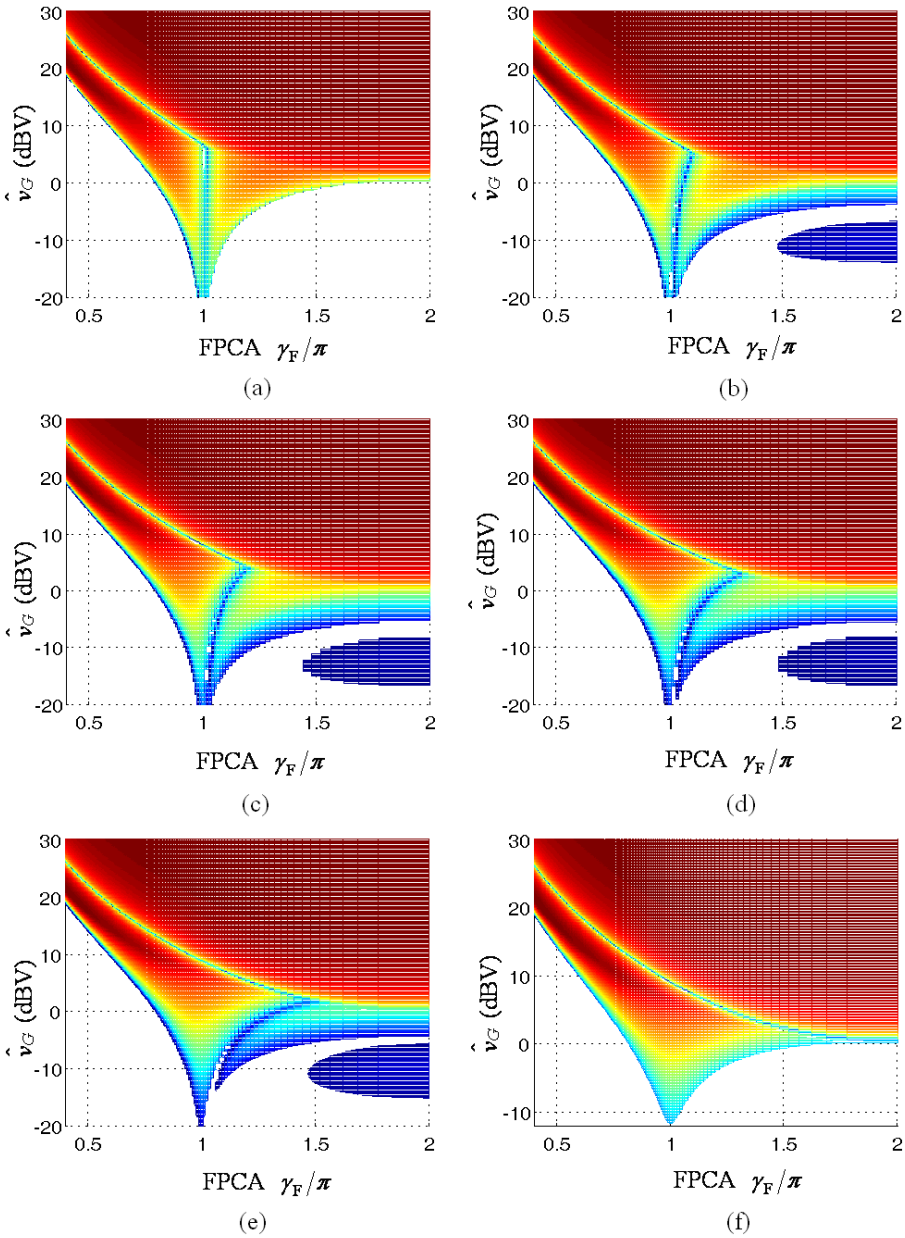

Figure 7.18 Contour plots of 3rd order distortion for the Q-law model versus FPCA and input signal amplitude, (a)-(f), Q = 1, 1.2, 1.4, 1.6, 1.8, 2.

limiting case where they behave as the square law model. The contour plots in Figures 7.18 and 7.19 show a number of things.

Firstly, the theory presented in section 7.2 to explain the relationship between the linear and square law model distortion plots in Figure 7.2 is confirmed. Figures 7.18 and 7.19 make it clear beyond question that the class B part of the deep valley, that is parallel to the $\hat{v}_G$ axis for the linear model in Figure 7.2(a), progressively

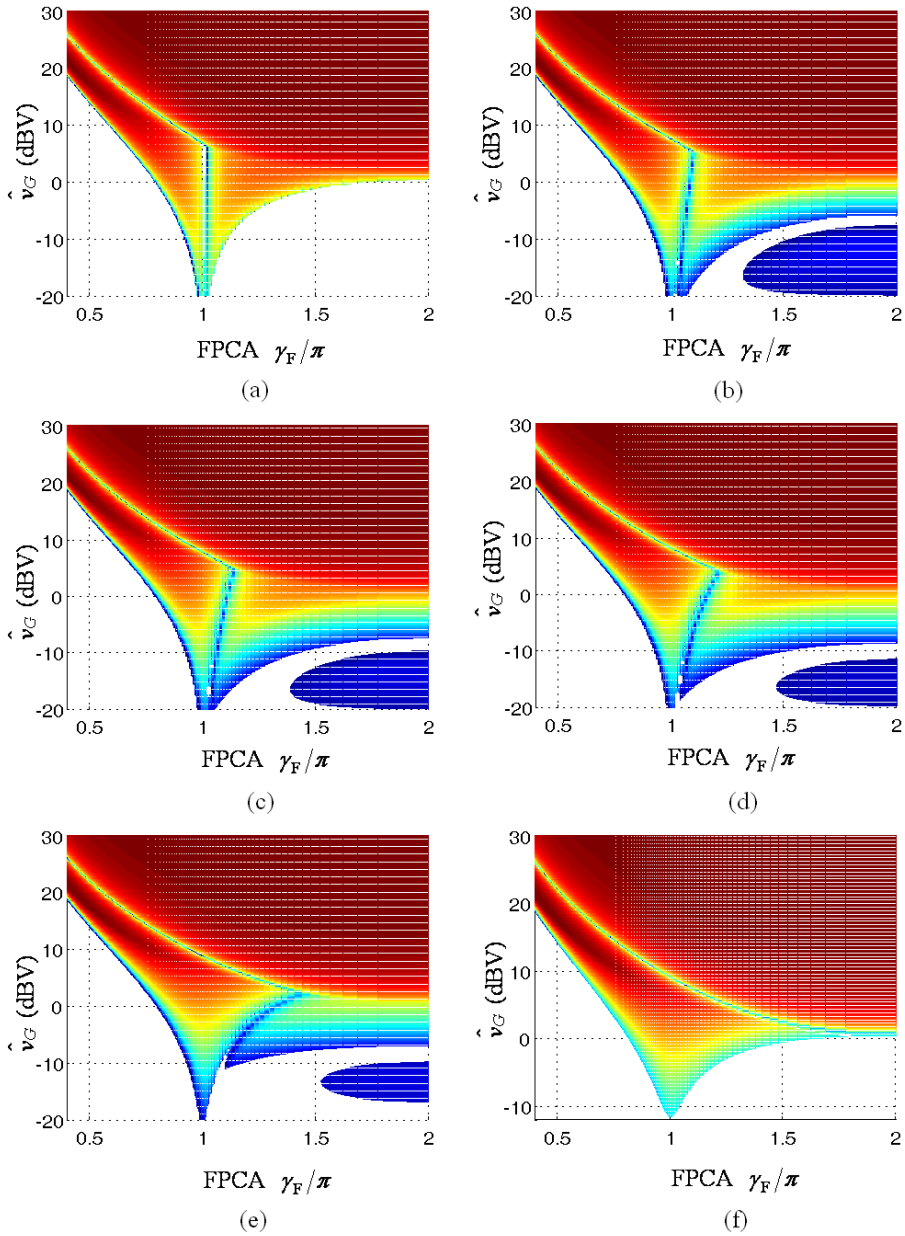

Figure 7.19 Contour plots of 3rd order distortion for the velocity saturation model versus FPCA and input signal amplitude. (a)-(f), θ = 39, 1, 0.6, 0.3, 0.06, 0.006.

rotates clockwise and becomes curved and then eventually disappears into the no-distortion R0 region when the models become square law in Figure 7.2(b).

Secondly, the plots in Figures 7.18 and 7.19 show that, whereas the linear and square law models produce no 3rd order distortion in the R0 region where there is no clipping, this is not the case for the intermediate plots (b) to (e). However, this distortion due to the model characteristic is less than the distortion in the R1 and R2

regions that is due to clipping. Even using a transitional device model, the primary factor causing distortion is device current waveform clipping.

7.9. Distortion − Power Sweeps

3rd order distortion power sweeps for a PA may be obtained from a distortion surface, as in Figure 7.13, by taking a vertical cross-section, or slice, parallel to the $\hat{v}_G$ axis, for the corresponding class, or value of γ_F, as was done is Chapters 5 and 6 for the linear and square law models. The distortion-power sweeps for the Q-law and the velocity saturation transitional device models are given in Figures 7.20 and 7.21, respectively.

The transitional model parameters chosen, Q = 1.4 and θ = 0.3, are in the middle of the transition ranges and close to the values used in Figures 7.13 (a), 7.14(a), 7.15(a) and 7.16(a). The γ_F values used may be divided into ranges, as shown in Table 7.1. The distortion-power sweeps in Figures 7.20 and 7.21 are in three parts, (a), (b) and (c), which correspond with the ranges for γ_F given in Table 7.1; ranges

Table 7.1 FPCA γ_F values used for distortion power sweeps using Q-law model in Figure 7.20 and velocity saturation model in Figure 7.21.

Range	Curve	γ_F / π	
		Q-law model	Velocity saturation model
AB(A)	A	2.00	2.00
	AB(A)	1.36	1.34
AB(AB)	AB(AB)1	1.26	1.24
	AB(AB)2	1.20	1.20
	AB(T1)	1.19	1.18
AB(B)	AB(B)1	1.13	1.13
	AB(B)2	1.10	1.06
	B	1.00	1.00
BC	BC1	0.94	0.94
	BC2	0.87	0.86

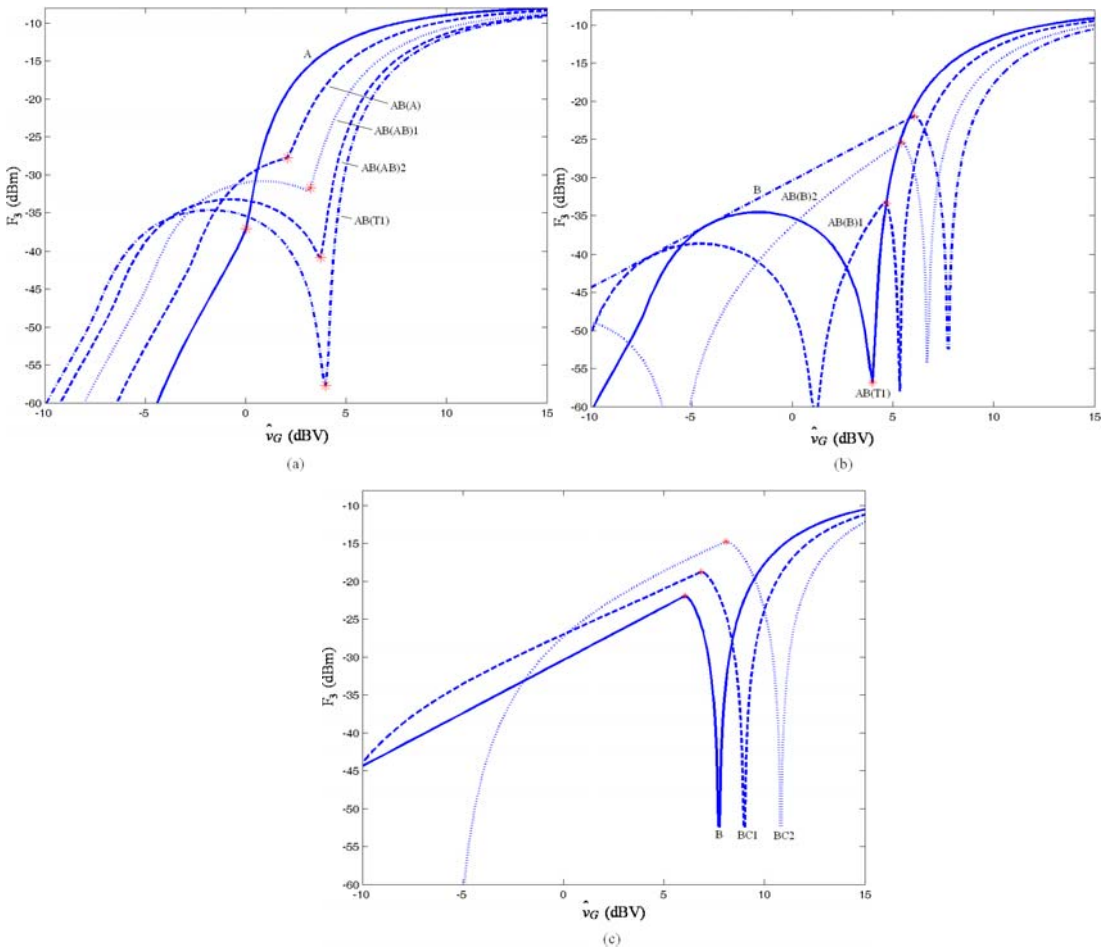

Figure 7.20 Distortion power sweeps for Q-law model with Q = 1.4, (a) AB(A) and AB(AB) class ranges; (b) AB(B) class range; (c) BC class range.

AB(A) and AB(AB) are plotted together. Since the sweeps for Q-law and velocity saturation models in Figures 7.20 and 7.21 have many similar features, we first make points that apply for both models and discuss differences later. In all sweeps in Figures 7.20 and 7.21, the FPP is indicated by the symbol '*'.

Distortion power sweeps for the AB(A) and AB(AB) class ranges are plotted in Figures 7.20(a) and 7.21(a) and begin with Class A. For class A, distortion is not zero at the FPP and in the R0 region, as it was for the linear and square law models (Figures 5.11(a) and 6.9(a)). As described in section 7.4.2 in the AB(A) range there is a ledge and in the AB(AB) range there is a shallow null. These two cases are exemplified by curves AB(A), AB(AB)1 and AB(AB)2, in Figures 7.20(a) and 7.21(a), respectively. The second transition point in the AB class range, γ_{FT2} in

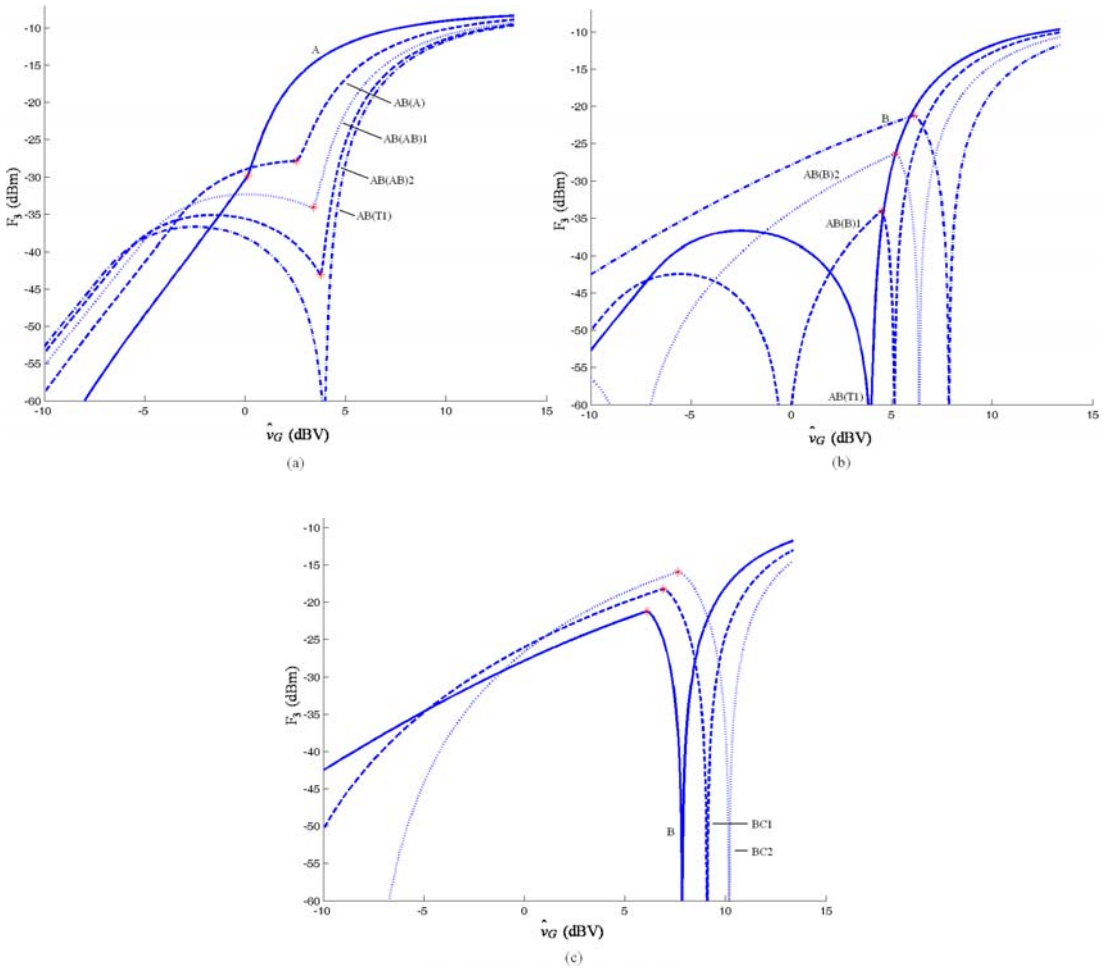

Figure 7.21 Distortion power sweeps for velocity saturation model with θ = 0.3, (a) AB($\overline{\mathrm{B}}$) class ranges; (b) AB(B) class range; (c) BC class range.

Figure 7.8(b), lies between the AB(A) and AB(AB)1 curves. The last curve in Figures 7.20(a) and 7.21(a) is the curve for the end of the AB(A) range, AB(T1) and it is repeated in Figures 7.20(b) and 7.21(b).

Distortion power sweeps for the AB(B) class range are given in Figures 7.20(b) and 7.21(b). The range starts from $\gamma = \gamma_{FT1}$ with curve labelled AB(T1), which marks the boundary between the AB(AB) and AB(B) class ranges and which has a wide and deep null, as predicted in section 7.4. As γ_F is reduced from this point, the wide deep null splits into two deep nulls whose separation increases; this can be understood by looking at Figures 7.8(b), 7.13(a) or 7.15(a). The wide deep null for curve AB(T1) can be seen as a merging, that occurs for $\gamma_F = \gamma_{FT1}$, of the two deep nulls. The end of the AB(B) range corresponds to class B which provides a single null at high power.

We may treat this class as the limiting case of the two deep null situations where the lower power null has moved to an input signal power level of zero − see Figures 7.8 or 7.13.

The BC class range distortion sweeps are given in Figures 7.20(c) and 7.21(c) and include the case of class B. They are quite similar to the corresponding sweeps for the linear and square law models in Figures 5.11(b) and 6.9(b), respectively.

The distortion-power sweeps for the Q-law and velocity saturation device models in Figures 7.20 and 7.21 are quite similar and do not show any strong differentiating behaviour in the dominant distortion features. However, at low distortion levels, there are some differences which are now discussed.

The low level distortion that occurs in the R0 region where there is no clipping is different for the velocity saturation model and for the Q-law model, For example, for class A, distortion at the FPP is − 30 dBV for the velocity saturation model (Figure 7.21(a)) and is − 37 dBV for the Q-law model (Figure 7.20(a)). Below the FPP, the class A distortion curve becomes approximately linear. And the curves for other classes in the AB(A) and AB(AB) range become approximately parallel to the class A curve, in both Figures 7.20(a) and 7.21(a). Here, in the R0 region, there is no clipping and this distortion is entirely due to small-signal model derivatives. However, the gradients of the curves differ. For the Q-law model in Figure 7.20(a), it is 5, but for the velocity saturation model in Figure 7.21(a), it is 3. The greater steepness of the curves for the Q-law model can be clearly seen in the 3-D plots in Figures 7.13(a) and 7.14(a), where this is seen as an increased slope of the low level planar surface in the AB(A) and AB(AB) class ranges.

However, Figures 7.13(a) and 7.14(a) show that this planar surface leads down into a low level valley, or secondary valley, approximately parallel to the γ_F axis in the middle of the R0 region. This secondary valley occurs at different input signal amplitude levels for the two models, at − 10 dBV for the Q-law model and at − 15 dBV for the velocity saturation model. This shows that the slope of the approximately planar region above this valley is determined principally by the position of the valley, rather than by a particular power dependence on input signal amplitude. It should be noted that, although there are these differences in the low level distortion behaviour obtained for the two transition models, these levels of distortion are very low.

Observable PA distortion behaviour is governed by the principal 'L'-shaped valley that cuts through the R2 and R1 regions. The secondary valley in the R0 region in Figures 7.13 and 7.14 has not been observed in practice, probably because the levels of the distortion surrounding it are so low. Nevertheless, the difference in the slope of the planar surface that leads down to the secondary valley could lead to observable effects, as seen in Figures 7.20(a) and 7.21(a). This difference in slope could be a factor in choosing one model in preference to another for fitting the distortion characteristics of practical PAs. The task of fitting these distortion predictions to the characteristics of real PAs will be undertaken in the following chapter.

7.10. Conclusion

In Chapters 5 and 6, 3rd order distortion surfaces, as functions of γ_F (PA class) and input voltage amplitude $\hat{v}_G$, have been predicted for the linear and square law device models. For both models, the area of high distortion in the double and single clipping regions (R2 and R1, respectively) is crossed by a deep valley, but the path of valley is quite different for the two models. But slices taken from either of the 3-D distortion surfaces cannot predict the distortion power sweeps of real PAs, especially the double null in the class AB region. That has led to the aim of this chapter of trying to discover a device model that has a distortion surface that can yield the forms of distortion power sweep observed in real PAs.

The aim of this chapter has been met by the identification of a type of device model that can predict the distortion power sweeps of real PAs, including the double null in the AB range. This model is called a transitional model in that is can be varied, by means of a transition parameter, between the abrupt cut-off characteristic of the linear model and the smooth cut-off characteristic of the square law model. The two examples of transitional models studied in this chapter will be used to fit published PA distortion data in the following chapter. In the process of meeting the aims of this chapter, a lot has been discovered about the nature of distortion in PAs, and this may be summarised as follows.

The starting point for understanding distortion in PAs is the surface of 3rd order distortion versus γ_F, PA class, and $\hat{v}_G$, input voltage amplitude, for the case of the linear device model. This distortion surface is cut by the 'L'-shaped valley which is straight and follows the line $\gamma_F = \pi$ in the quasi-linear range and turns to the left at the FPP to cross the BC class saturation range in a curve. The resulting power-distortion sweeps will give a single deep null in the saturation power range in the BC class range, which agrees with published data. However, for Class B, the straight part of the valley predicts a no-distortion sweet spot that is not observed in practice. In the AB class range, a ledge is predicted throughout the range, whereas, in practice, a double null is most often observed. In order to obtain correct distortion predictions, the transitional device model is introduced.

The transitional model has a softer cut-off than the linear model. As a result, the part of the transfer characteristic for moderate and high values of output current may be extrapolated to the $\hat{v}_G$ axis in order to define an effective threshold voltage that is always greater than actual threshold voltage. The clipping theory of Chapter 4 shows that increase of effective threshold voltage reduces conduction angle, γ. Hence, a given distortion feature with a linear model will occur with a transitional model for a higher value of γ. A plot in Chapter 4 of constant γ contours in the γ_F - $\hat{v}_G$ plane shows that as γ is increased above π, the straight contour for $\gamma = \pi$ turns to the right and becomes curved. It follows that the straight part of the class B distortion valley, obtained with the linear device model, turns to the right and becomes curved with a transitional device model.

The principle of valley continuity, proposed in this chapter, requires that as the straight valley turns to the right and curves, the Class BC part of the valley, obtained for the linear model, must extend so that the two parts of the valley remain connected. The result is that with a transitional device model, the 'L'-shaped distortion valley obtained with the linear model rotates clockwise and curves to the right. The rotation of the 'L' shaped valley to the right has important consequences. It implies that a distortion power sweep can have two deep nulls, which is the type of sweep most frequently observed for practical PAs operating in Class AB.

The rotation of the 'L'-shaped valley leads to a sub-division of the AB-Class range of PA operation depending on type of distortion characteristic. The value of γ_F

that corresponds to the corner of the rotated 'L'-shaped valley is denoted a transition value of γ_F, γ_{FT1}. The first part of the AB class range is from $\gamma_F = \pi$ (Class B) to $\gamma_F = \gamma_{FT1}$. In this range, called AB(B), the distortion power sweep will cross the rotated valley twice giving rise to two deep nulls in the distortion characteristic. As γ_F is increased above γ_{FT1}, there will be a shallow valley, due to proximity to the deep valley at γ_{FT1}, and as γ_F is increased, moving away from γ_{FT1}, the depth of the valley will reduce. A second transition point, γ_{FT2}, is the point where there just ceases to be a shallow valley. The range $\gamma_{FT2} \leq \gamma_F \leq \gamma_{FT1}$, where there is a shallow valley is denoted the AB(AB) class range. Finally, the range from $\gamma_F = \gamma_{FT2}$ to $\gamma_F = 2\pi$ (Class A) is called the Class AB(A) range. In this range, the distortion characteristic exhibits a ledge feature and there is no change in sign of its gradient.

Ideas have been proposed that lead to predicted distortion characteristics that have the same general from as those observed for practical PAs. Furthermore, a very general theory has emerged that can explain the dependence of PA 3rd order distortion on input signal amplitude and class, and how this dependence is affected by device model. In the next chapter, these ideas are put to the test by carrying out precise fitting of the predicted PA performance curves to published performance curves for PAs implemented with different technologies.

CHAPTER 8

PERFORMANCE PREDICTION AND COMPARISON WITH PUBLISHED DATA

8.1. Introduction

In order to verify that the device current clipping theory developed in Chapters 3 and 4 of this thesis is the major factor determining PA performance including distortion, performance predictions using the theory with the transitional device models of Chapter 7 will be fitted to published PA performance curves.

This Chapter begins with overview of the published measured and simulated performance data for PAs using CMOS, LDMOS and MESFET devices. The performance data includes 3rd intermodulation distortion and, in most cases, output power. Then the choice of criteria for fitting will be discussed and different styles for fitting the performance curves and optimising the device models will be illustrated. Finally, performance predictions will be presented and compared with published simulation and measurement data for different PA device technologies.

8.2. Published PA Performance Data

The published PA performance curves that will be fitted using the transitional

models of Chapter 7 were presented in Chapter 2 as Figures 2.19 − 2.22. The data in Figures 2.19, 2.20 and 2.21 is measured output power and IMD3 for three different technologies, namely CMOS, LDMOS and GaAs MESFET. The data in Figure 2.22 is IMD3 simulated using harmonic balance for the CMOS PA whose measured data is given in Figure 2.19. The bias voltages used for all the published data were stated in Table 2.2.

The simulated and measured data for the CMOS PA in Figures 2.22 and 2.19 includes four different gate bias conditions; one is class BC (called Class C in [83]), two are Class AB (AB_- and AB_+) and one is Class A. It can be seen from Figures 2.22(b) and 2.19(b) that the Class AB design with lower bias voltage (AB_-) has an IMD3 curve with two nulls. From the theory developed in Chapter 7 and illustrated in Figure 7.8 (b), it is evident that this design is operating in the AB(B) class range. From Figures 2.22(c) and 2.19(c), the class AB design with higher bias voltage (AB_+) has an IMD3 curve with a ledge; from Figure 7.8(b), it can now be stated that this design is operating in the AB(A) class range.

The measured data for the LDMOS PA in Figure 2.20 includes four different gate bias conditions; one is a Class BC, two are Class AB (AB_- and AB_+) and one is Class A, as for the CMOS PA. However, Figures 2.20(b) and (c) show that in both cases of Class AB, there are two deep nulls. From the theory in Chapter 7, they are therefore both operating in the AB(B) Class range. The spacing of the nulls is much less for the case of the higher bias voltage (AB_+).

The measured data for the GaAs MESFET PA in Figure 2.21 includes just two gate bias conditions, Class AB and Class B. From Figure 2.21(a) and Figure 7.8(b), it is clear that the Class AB case, that has a ledge, is operating in the AB(A) class range.

In Chapter 4 of this thesis, a strict definition of the class of a PA has been proposed based on full power conduction angle, γ_F. However, as shown in Figures 4.5 and 4.6, conduction angle γ varies greatly with input signal amplitude, and this means that in the literature, there is no accepted strict definition of the class of a PA. Therefore, in fitting the published curves, the class quoted in the literature, such as A or B, is ignored. For each performance curve, γ_F is optimised to obtain the best curve fit. This actually leads to the determination of the class of the PA according to the strict definition in this thesis.

This approach can be justified by comparison of the simulated and measured distortion curves for the CMOS PA in Figures 2.22 and 2.19. For the measured Class AB$_-$ data in Figure 2.19(b), the two nulls are not very deep, and yet it is possible to establish the spacing of the nulls to be close to 10 dB. For the simulated Class AB$_-$ data in Figure 2.22(b), the null spacing is clearly about 15 dB. Again, for the simulated class AB$_-$ data in Figure 2.22(c), the difference between the distortion on the ledge and the maximum limit of distortion is about 20 dB but for the corresponding measured data in Figure 2.19(c), this difference is about 35 dB. In view of these major differences between measured and simulated IMD3 in [83], it is right to make no assumption that the class, as defined in this thesis using γ_F, is the same for the simulated and measured data that is presented as corresponding.

Furthermore, it will not be assumed in this chapter that the device model that best fits the measured and simulated CMOS data is the same. The device model will be optimised against each set of performance data independently and then a comparison of the models will be made.

Note that, in the published PA data for fitting that is available, there is no distortion curve that has a shallow valley, as exemplified by curves AB(AB)1 and AB(AB)2 in Figures 7.20(a) and 7.21(a), which are for the AB(AB) class range. Table 7.1, that shows the data used for the typical distortion curves in Figures 7.20(a) and 7.21(a), indicates that the AB(AB) class range covers a range of γ_F of about 0.25π. This range is not unduly narrow and therefore the lack, in the literature, of distortion curves showing a single shallow null for this region of PA operation must be attributed to co-incidence.

8.3. A Method for Fitting Model Predictions to Published Data

8.3.1. Methods of Approach

Published distortion data for a PA using a particular device, examples of which have been shown in Figures 2.19 − 2.22, typically consist of a set of distortion-power sweeps, each for a different value of input voltage DC bias, which sets the class of the PA. These sweeps could be stood-up vertically and assembled along an axis with a

scale of input voltage bias, and then they could be regarded as cross-sections of a distortion surface that is plotted against two axes, one of which is PA input voltage amplitude and the other is bias voltage, or PA class. In principle, measurements could be made to establish the form of the whole of this distortion surface. This would describe distortion as a function of input voltage amplitude for any bias that may be chosen, *i.e.* for any class of operation. However, this has never been done because the number of measurements needed would be prohibitively high. So we have to work with a limited number of cross-sections, or slices, through such a distortion surface, as are given in Figures 2.19 − 2.22.

The prediction of PA 3rd order distortion due to device current clipping, as has been proposed in this thesis, leads also to a 3-D plot of distortion. The surface depends on the value of the model transition parameter, as seen for example by comparing Figures 7.13(a) and (b). The predicted distortion surface also depends on the form of the model, but for good models the differences should not be too great, as seen for example by comparing the Q-law model in Figure 7.13 with the θ model in Figure 7.14. Optimising the form of the model is a very important task in general, but in this thesis, only the two transition models introduced in Chapter 7, the Q-law and velocity saturation models, will be used, and both will be used for fitting, so it is not necessary to consider the form of the model further here. So, as far as these models that will be used here are concerned, just the transition parameters of the models (Q and θ) must be optimised as part of the process of fitting the model predictions to the published data.

The task of modelling distortion can now be formulated. Ideally, the predicted distortion surface should be the best possible fit to the measured distortion surface for the whole range of PA class ($0 \leq \gamma_F \leq 2\pi$) and for the range of input voltage amplitude that is of interest. Since, in practice, the measured distortion surface is only available as sample slices for a few discrete values of PA bias voltage, the best possible approach to the ideal is to fit the predicted distortion surface to the available distortion power sweeps. If the given sweeps span the whole class range from A to BC, then they may be regarded as reasonable samples of the whole distortion surface. Thus the variables for the optimisation are the transition parameter of the model and the values of γ_F (or class, according to the formal definition of this thesis) for each

given distortion-power sweep. Such a multi-variable optimisation requires a numerical method, and this is regarded as outside the scope of this thesis for the following reasons:

1) Fitting to the published PA data to a very high standard, well sufficient to confirm the validity of the theory presented, can be performed by a much simpler method, as will be shown.
2) The focus of this thesis is on developing the clipping theory and using it to explain observed PA behaviour using two basic transition device models. Detailed numerical optimisation is a task for future work.
3) Detailed numerical optimisation should include a wider range of models than the basic ones considered here; this also is outside the scope of the thesis.

The alternative and simple method of fitting distortion predictions to published data consists in using just one of the given distortion-power sweeps in order to determine the device model transition parameter. Since the FPCA, γ_F, for the given sweep is not known, this is a 2-variable optimisation. A method of handling this without resorting to numerical optimisation will be presented. But first, the choice of which of the given distortion-power sweeps to use in order to optimise the transition parameter of the device model is considered.

8.3.2. Choice of Best Distortion Sweep for Simple Method

Predicted distortion plots generated by the clipping theory of this thesis are for normalised PA input voltage and normalised device output current, and denormalisation for application to a practical PA requires knowledge of maximum device current, effective load resistance at the device output port and average device transconductance, as described in Appendix A. Since these parameters are often not available in the literature, it is not practical to predict an absolute value of distortion or an absolute value of input voltage amplitude for which a particular distortion feature occurs. It is necessary, therefore, to use, as criteria for curve fitting, differences of distortion levels and differences of PA input voltage amplitude that correspond to particular distortion features. We refer to such differences as *relative fitting criteria*.

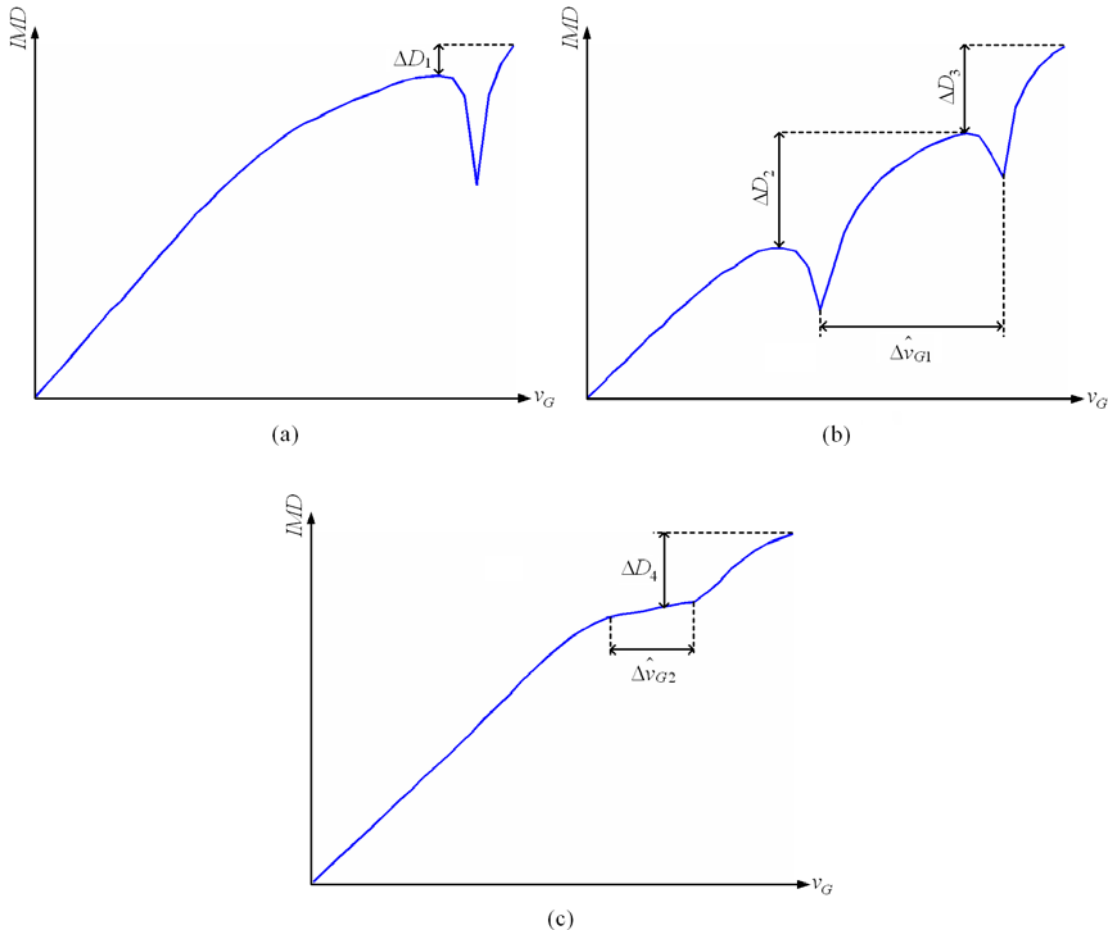

Figure 8.1 Fitting criteria for distortion-power sweeps, (a) Class BC; (b) Class AB(B); (c) Class AB(A).

The published distortion-power sweeps in Figures 2.19 − 2.22 have distinctive characteristics. All of the sweeps for class C and class B have a single null (*e.g.* Figures 2.19(a), 2.20(a), 2.21(a) and 2.22(a)). The sweeps for class range AB(B) (*e.g.* Figures 2.19(b), 2.20(b), 2.21(b) and 2.22(b)) have two nulls. The sweep for class range AB(A) (*e.g.* Figures 2.19(c), 2.20(c), 2.21(c) and 2.22(c)) has a ledge and the curve for class A (*e.g.* Figures 2.19(d), 2.20(d), 2.21(d) and 2.22(d)) is monotonic. It is now necessary to decide the type of curve that should be used to optimise the device model transition parameter.

First consider the Class BC distortion curve that has a single null. There is just one possible relative fitting criterion, and that is the difference between the minimum

distortion below the null and the distortion limit for large input voltage, as indicated by ΔD_1 in the sketch in Figure 8.1(a).

Now consider the distortion curve, for the Class AB(B) that has two nulls. For this type of curve, there are two possible distortion criteria, shown as ΔD_2 and ΔD_3 in Figure 8.1(b). There is also a possible criterion for input voltage amplitude. This is the spacing $\Delta\hat{v}_{G1}$ between the two nulls, as also illustrated in Figure 8.1(b).

Next consider the distortion curve for Class AB(A) that has a ledge. Clearly, the width of the ledge could be a criterion, as indicated in the sketch in Figure 8.1(c). Also, the difference ΔD_4 between the distortion on the ledge and the limit of the distortion for large input voltage amplitude is also a candidate criterion.

Consider finally the distortion curve for Class A that is monotonic. The shape of the curve is relatively featureless and it is not possible to establish any relative criterion, either of distortion or input voltage amplitude.

The curve types and fitting criteria in Figure 8.1 now can be assessed for suitability for determining device model transition parameters. The width of the ledge $\Delta\hat{v}_{G2}$ in Figure 8.1(c) has the problem that width of ledge is difficult to define precisely. This excludes the class AB(A) curve as unsuitable. That leaves the Class BC and AB(B) curves in Figure 8.1(a) and (b). Since the Class AB(B) type of curve in Figure 8.1(b) has three possible relative criteria for fitting and the BC curve has only one criterion, the Class AB(B) is preferred. The fit of the predicted distortion to the Class AB(B) published data will be used to establish the device model transition parameter that is used to model the distortion curves for all other classes as well. As mentioned in section 8.3.1, the fitting of the model to one of the given distortion-power sweeps, now chosen to be the class AB(B) curve, is a 2-variable optimisation problem. In obtaining the model transition parameter, Q or θ, the FPCA, γ_F, for the given AB(B) distortion curve is treated as un-known. A method of handling this without recourse to numerical optimisation is now discussed.

8.3.3. A Method for By-Hand Fitting of Distortion Data

A simple by-hand method of curve fitting is possible when there is a single optimisation variable, as then a family of curves for different values of the parameter

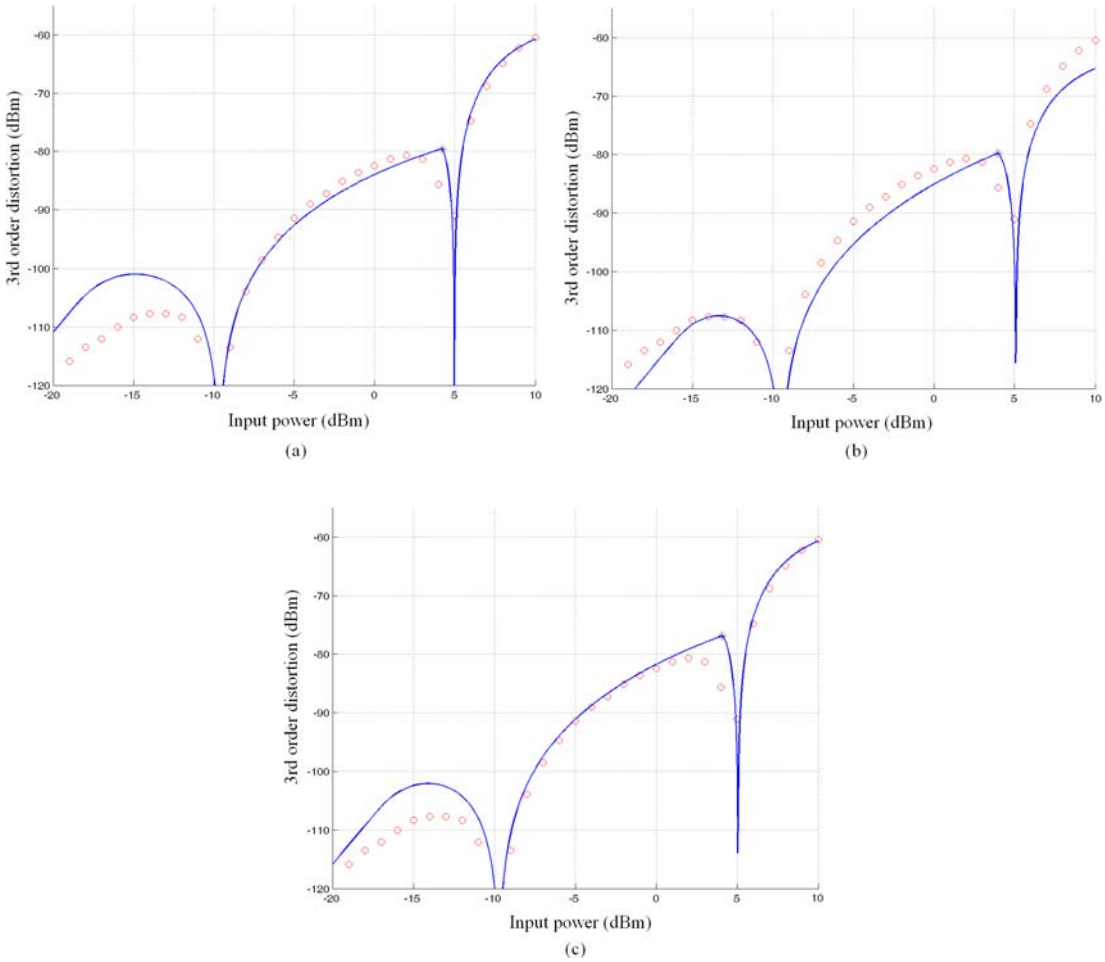

Figure 8.2 Fitting procedure illustrated for the velocity saturation model, (a) best fitting at high power, θ = 0.74; (b) best fitting at low power, θ = 0.36; (c) compromise fitting, θ = 0.50.

may be plotted and the best one chosen. A 2-variable optimisation problem may be reduced to a single variable problem if a constraint is introduced.

Consider now the families of predicted distortion contour plots in Figures 7.18 and 7.19. For any value of device model transition parameter, Q or θ, in the AB(B) class range, where there are two nulls, the FPCA γ_F has a strong effect on the null spacing. If $\gamma_F = \gamma_{FT1}$, then the nulls are co-incident and the spacing is 0 dBV. If $\gamma_F = \pi$, then the lower null is at $-\infty$ on the dBV scale, *i.e.* at $\Delta\hat{v}_G = 0$ V. Hence, the spacing between the two deep nulls in the AB(B) class range may be set to any given value by means of γ_F, and, consequently, the fitting criterion Δv_{G1} in Figure 8.1(b) may always be satisfied exactly. Thus, the satisfaction of this criterion may be built-in, and then,

there is left only a single optimisation variable, for which families of curves may be plotted and the best one chosen, using the criteria ΔD_2 and ΔD_3 in Figure 8.1(b). The process of optimisation will now be illustrated using an example.

Figures 8.2(a) − (c) show the curve of Figure 2.22(b), of simulated IMD3 for a CMOS PA from [83] in the class AB(B) region, with fits of three different predictions. Each fit is obtained with the different pair of θ and γ_F values given in Table 8.1. In Figure 8.2(a), the fit is very good at the higher end of the input power range, above the higher null. In Figure 8.2(b), a much better fit is obtained at low power level, around the lower null. But the fit at high power levels is not nearly as good as that in Figure 8.2(a). In Figure 8.2(c), the fit is a compromise fit that gives the best fit over a range of input signal amplitudes. Notice that in all three fits in Figure 8.2, the spacing of the nulls is kept constant and matches the spacing for the published curve. Because of the difficulty of obtaining data from publications for correctly denormalising the predicted curve, the fitting of all curves involves introducing horizontal and vertical shifts in order to optimise the fit, and these shifts are given in Table 8.1.

A process such as that illustrated in Figure 8.2 can be used to determine what is regarded as the best fit. That process leads to a value for the device model transition parameter, Q or θ, which establishes the device model. Using this model, FPCA γ_F alone is then used to fit the published curves for the given PA device for all other classes for which data is provided. Fitting of the published PA data in Figures 2.19 − 2.22 using the transitional models in Chapter 7 by the simple method of by-hand optimisation can now be carried out.

Table 8.1 Parameters for fitting in Figure 8.2.

Figure 8.2	θ	γ_F / π	ΔD (dB)	Δv_G (dBV)
(a)	0.74	1.05	− 48.0	− 1.30
(b)	0.50	1.06	− 48.0	− 1.30
(c)	0.36	1.06	− 52.7	− 1.30

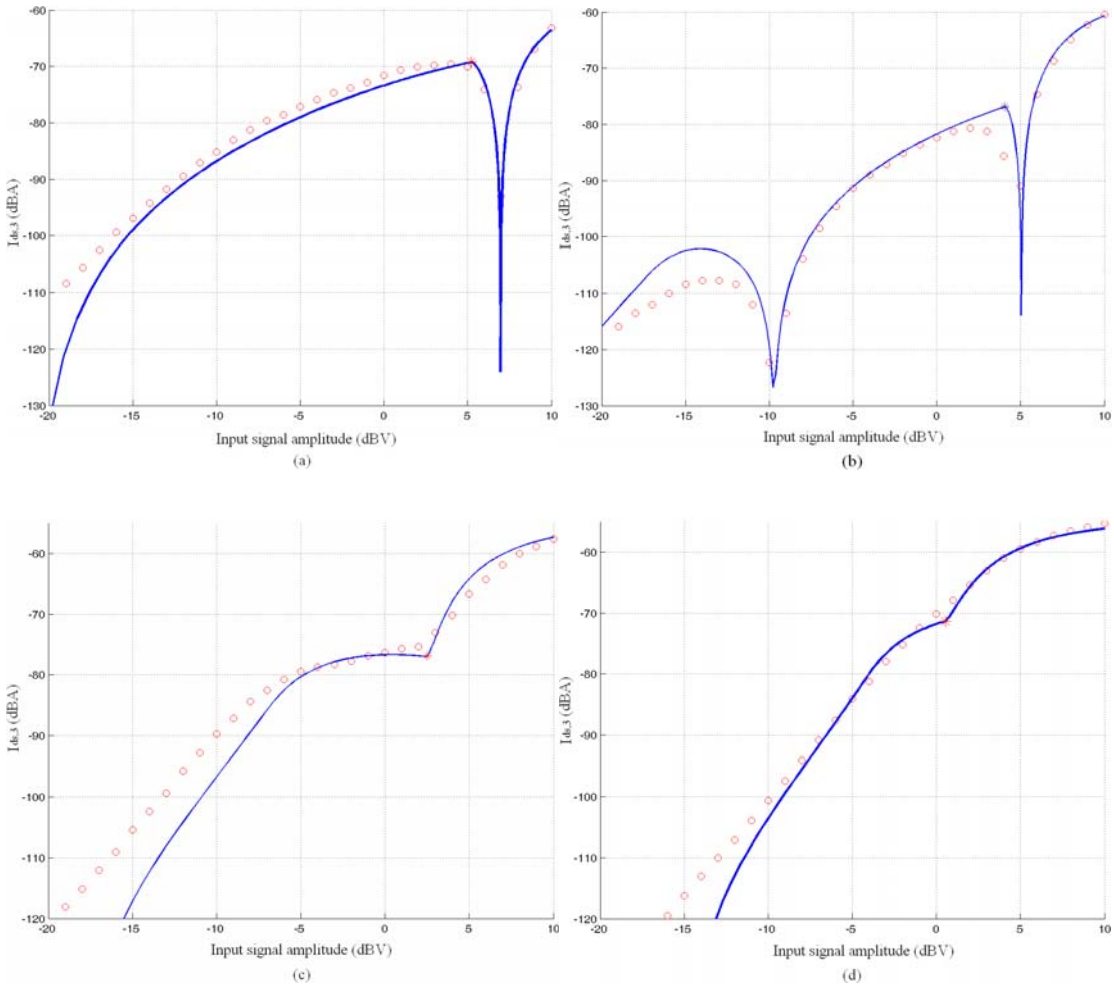

Figure 8.3 Velocity saturation model fitting for simulated data for CMOS PA of [83], (a) Class BC, (b) Class AB$_-$, (c) Class AB$_+$, (d) Class A.

8.4. Fitting Simulated Distortion Data for CMOS PA from [83]

In this section, the simulated IMD3 curves for a CMOS PA from [83], which were shown in Figure 2.22, are fitted with curves for predicted 3rd order distortion due to device current clipping using the velocity saturation and Q-law device models. The fits using these two models are shown in Figures 8.3 and 8.4, respectively. In Figures 8.3 and 8.4, and in all remaining figures in this chapter, the published data points are indicated by symbols 'o' and the predicted data by a continuous curve. For each predicted curve, the FPP is indicated by the symbol '*'. As mentioned is section 8.3, the fit to the class AB(B) published curve, in Figures 8.3(b) and 8.4(b), was used to define the device model transition parameter; for other classes, the same model was

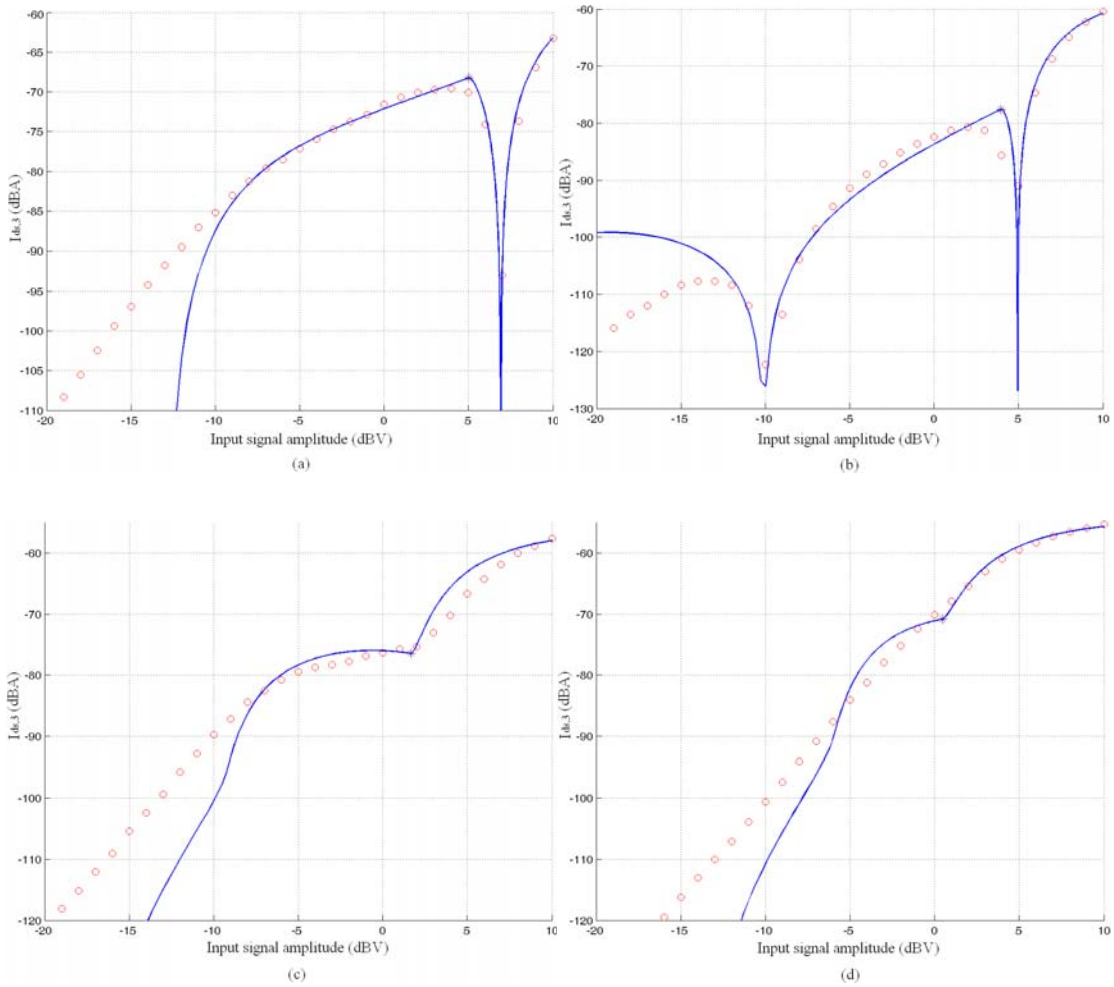

Figure 8.4 Q-law model fitting for simulated data for CMOS PA of [83], (a) Class BC, (b) Class AB$_-$, (c) Class AB$_+$, (d) Class A.

used and only the γ_F value was altered. As mentioned in section 8.2, it is difficult to obtain from publications sufficient data to correctly denormalise the predicted curves. Therefore, the predicted curves were subject to shifting vertically and horizontally in order to optimise their fit to the published curves. The horizontal and vertical scales in Figures 8.3 and 8.4, and in all the remaining figures in this chapter, are the scales for the published performance data. Data about the optimisation, including device model transition parameter, values of γ_F and shifts introduced are given in Table 8.2.

The fits used are 'compromise fits' that take into account the whole curve, but give rather more weight to the parts of the curve where the distortion is highest. For fitting the Class AB(B) curves in Figures 8.3(b) and 8.4(b) that are used to define the

Table 8.2 Parameters for fitting simulated data for CMOS PA of [83].

	$\theta = 0.50$ (for Figure 8.3)			Q = 1.20 (for Figure 8.4)		
	γ_F / π	ΔD(dB)	Δv_G(dB)	γ_F / π	ΔD(dB)	Δv_G(dB)
C	0.97	− 48.0	− 1.30	0.93	− 48.0	− 2.20
AB_-	1.06	− 48.0	− 1.30	1.02	− 48.0	− 1.80
AB_+	1.22	− 47.0	− 1.10	1.18	− 48.0	− 2.20
A	1.47	− 47.0	− 1.10	1.31	− 46.5	− 2.20

device model, , the predicted curve is chosen to model the spacing of the nulls precisely, as outlined in section 8.3.3.

The predicted curves in Figure 8.3(a) − (c) for the velocity saturation model clearly display the distinct curves types observed for the different classes, namely single deep null, double null and ledge. In Figure 8.3(d), the predicted curve has a small ledge that is not in the published curve in order to optimise the fit. But, nevertheless, the curves are very close to each other. At low power levels, where device model small-signal derivatives begin to have a significant effect, the predicted and published curves in Figure 8.3 do diverge, but it should be observed that the distortion power levels where this occurs are very low. For the Class AB(B) case in Figure 8.3(b), there is a significant difference between the curves at the FPP. This is possibly due to the fact that the device models used in the predictions have abrupt knee clipping whereas the real device, and a full model for a real device, has smooth knee clipping. Apart from the discrepancy around the FPP for the AB(B) curve, and discrepancies at very low power levels for all classes, the fits to the published data are good.

The fits in Figure 8.4 for the Q-law model are very similar to those for the velocity saturation model in Figure 8.3, except that at very low power level the differences between the curves are much greater. This suggests that the small-signal derivatives for the Q-law model are less realistic. However, at medium and high power levels, where device current clipping is the dominant factor, there is little to choose between the two models.

The optimisation data in Table 8.2 comes out of the process of fitting the distortion predictions to the published data in Figures 8.3 and 8.4. From this data, we can make interesting comparison between transition parameter values, Q and θ, of the

Q-law and velocity saturation device models and between the γ_F value for each class of operation and the class stated in the publication [83].

The values for the device model transition parameter, Q and θ, in Table 8.2, θ = 0.5 and Q = 1.2, are both towards the linear end of the transition range, with the Q-law model closer to the linear case. The values of γ_F for classes BC, AB_- and AB_+ are quite similar for the two models. Both Class BC and Class AB_- whose distortion curve exhibits two nulls, are in fact very close to Class B ($\gamma_F = \pi$). For Class A, the γ_F values for the two models differ to same extent from each other and differ considerably from the true Class A value, $\gamma_F = 2\pi$. This serves to emphasise that there is a lack of a precise criterion in the literature for the class of a PA.

8.5. Fitting Measured Performance Data for CMOS PA from [83]

This section presents fits of predicted output power and 3rd order distortion to the corresponding measured curves from [83] for a CMOS PA, as have been presented in Figure 2.19. These fits for the velocity saturation and Q-law models are given in Figures 8.5 and 8.6, respectively. Prediction of output power is carried out in the same way as 3rd order distortion described in Chapter 7, except that the fundamental Fourier component is used in place of the 3rd order component. The difficult of denormalising predicted distortion data due to insufficient information about the published data has been mentioned. For output power data, there are further unknowns, such as whether the test is a 2-tone test using the IMD3 test set-up or whether it is a single-tone test (network analyser set-up). Consequently it was decided to introduce vertical and horizontal shifts for the output power curves that are independent of those used for the distortion curves. Data relating to the curve fits in Figures 8.5 and 8.6, including these shifts for the output power curves are given in Table 8.3.

As mentioned in section 8.2, it was decided to optimise the device models for the fit to the measured CMOS data independently of the model optimisation for fitting the simulated CMOS data that was described in section 8.4. It was also

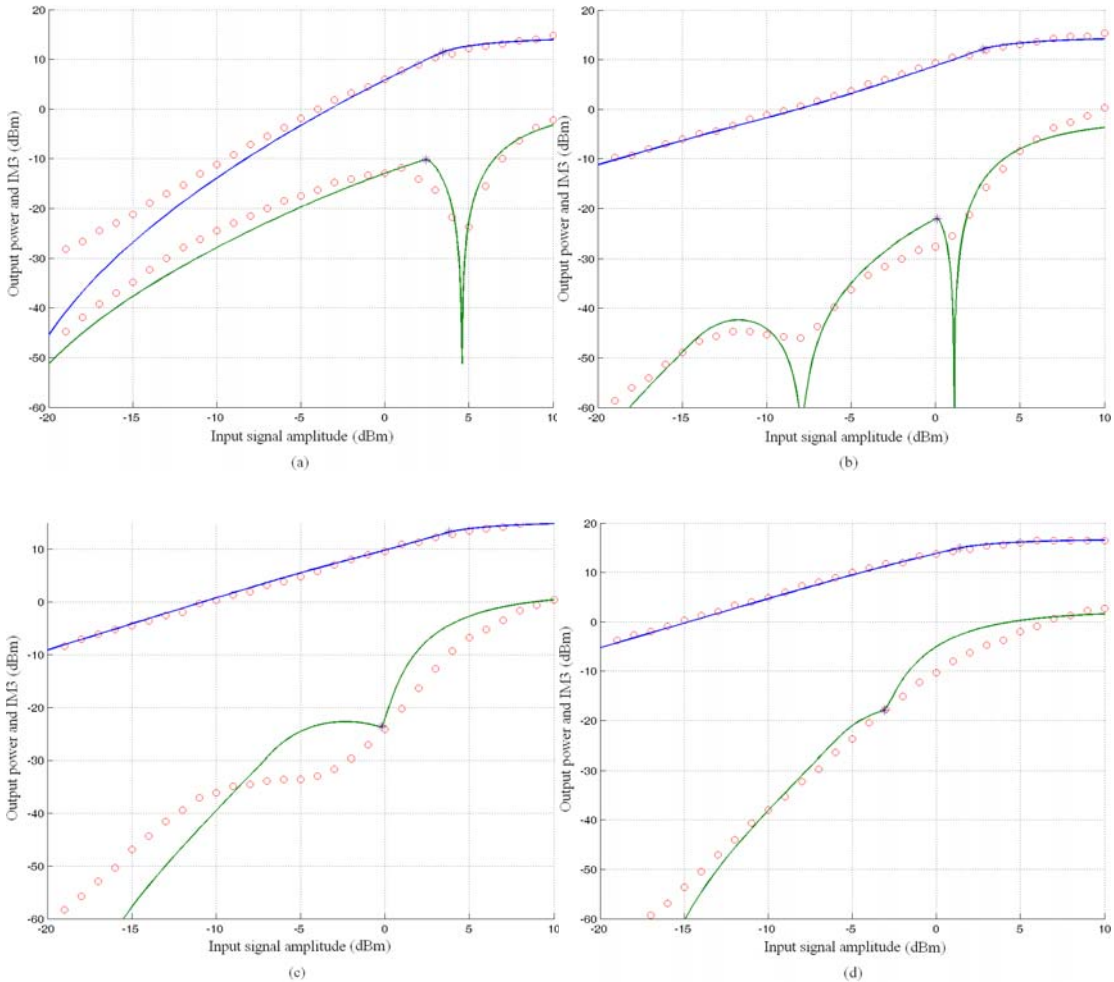

Figure 8.5 Velocity saturation model fitting for measured data for CMOS PA of [83], (a) Class BC, (b) Class AB$_-$, (c) Class AB$_+$, (d) Class A.

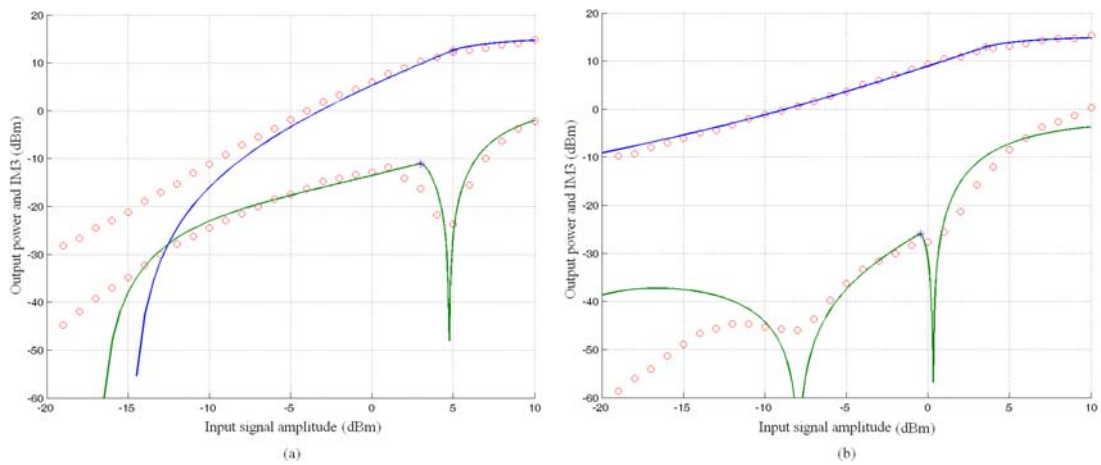

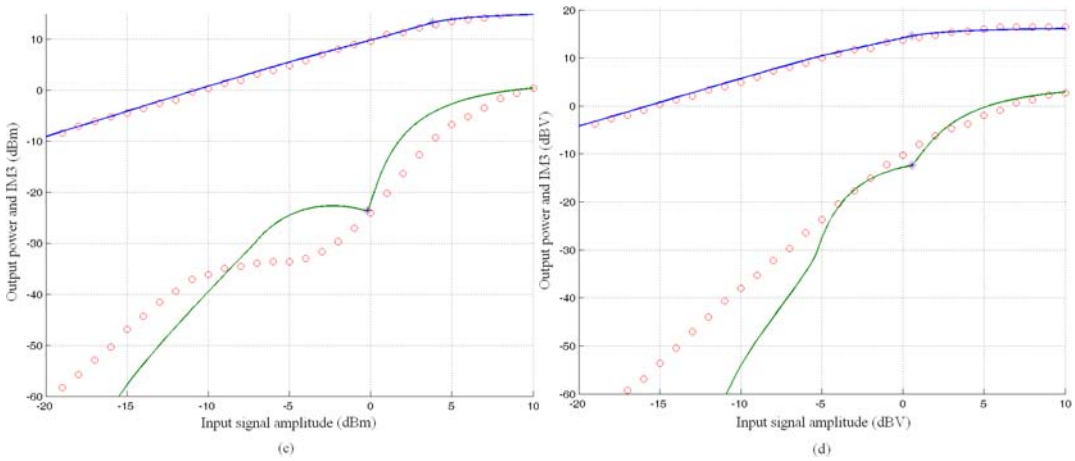

Figure 8.6 Q-law model fitting for measured data for CMOS PA of [83], (a) Class BC, (b) Class AB$_-$, (c) Class AB$_+$, (d) Class A.

Table 8.3 Parameters for fitting measured data for CMOS PA of [83].

	θ = 0.20 (for Figure 8.5)					Q = 1.22 (for Figure 8.6)				
	γ_F / π	P_{out}		IMD3		γ_F / π	P_{out}		IMD3	
		ΔP (dB)	Δv_G (dB)	ΔD (dB)	Δv_G (dB)		ΔP (dB)	Δv_G (dB)	ΔD (dB)	Δv_G (dB)
C	0.98	13.0	− 3.00	8.50	− 4.00	0.93	10.0	− 2.00	10.0	− 4.00
AB$_-$	1.12	13.0	− 1.80	6.00	− 4.50	1.03	14.0	− 2.00	6.00	− 6.00
AB$_+$	1.31	13.5	1.00	0.00	− 7.00	1.20	14.5	2.00	− 6.00	− 8.00
A	1.51	15.0	0.00	11.0	− 4.00	1.34	14.5	− 2.00	12.0	− 2.00

mentioned in section 8.2 that, in view of significant differences between the published simulated and measured data for the CMOS PA, γ_F would be optimised independently for the two cases. The fits of predicted 3rd order distortion to the measured curves for the CMOS PA in Figures 8.5 and 8.6 are now considered.

Excluding the curves in Figures 8.5(c) and 8.6(c) for the Class AB(A) case, the fits at medium and high power levels are reasonable. At low power levels, there are two issues. The curves in Figures 8.5(b) and (d), and those in Figures 8.6(b) and (d), do diverge at low power levels, and the divergence is much less for the velocity saturation model in Figure 8.5 than for the Q-law model in Figure 8.6. This confirms the conclusion from the previous section that very low levels of distortion obtained where there is no clipping are predicted better by the velocity saturation model.

The fits for the Class BC case in Figure 8.5(a) and Figure 8.6(a) are now discussed. For this class alone, there is a considerable divergence in the output power

curves that occurs at low power levels and affects distortion fit too, especially for the Q-law model in Figure 8.6(a). For low power levels the predicted output power curves in Figures 8.5(a) and 8.6(a) show a strong expansion. The expansion effect was already observed for low γ_F in the peak clipped gate voltage plot of Figure 4.4, and the effect is further enhanced by model non-linearity and by the Fourier series co-efficient for the output current. The published measured curve of output power in Figures 8.5(a) and 8.6(a) does not follow this expansion but instead is more linear. The reason for this is that the real device never cuts-off completely; its behaviour at low power in class BC is governed by its sub-threshold behaviour, which requires the soft pinch-off function for its accurate representation [92][94]. This difference between published and predicted output power curves for Class BC at low input power levels applies to all technologies that will be considered, and also applies to the fits to the simulated CMOS data in Figures 8.3(a) and 8.4(a).

The fits in Figures 8.5(c) and 8.6(c) for the Class AB(A) case are now discussed. It was observed in section 8.2 that there was a large difference between the simulated and measured distortion curves for the AB_- class curve in Figures 2.26(c) and 2.23(c), respectively. The difference between the distortion at the ledge and the maximum limit of distortion was 20 dB for the simulated curve (Figure 2.22 (c)) and 35 dB for the measured curve (Figure 2.19(c)) − a very large difference. The simulated curve has been fitted well using both device models, as shown in Figures 8.3(c) and 8.4(c). Turning now to the fitting of the measured class AB(A) data in Figures 8.5(c) and 8.6(c), it can be seen that is has been found to be impossible to fit the low level of distortion on the ledge. In fact, the best fits to the measured curve are similar to the fits to the simulated curve, for which the distortion at the ledge is about 20 dB below maximum. The fact that neither the simulation by the author of [83], or the clipping theory proposed in this thesis using two different transitional device models can predict the low level of distortion of 35 dB below maximum on the ledge of the measured data from [83] suggests that there must be a factor affecting the Class AB_- measurement results that is outside the scope of the simulations of the author of [83] and also outside the scope of the clipping theory proposed in this thesis. Comparing to the two fitting criteria for the case of Class AB(A) in Figure 8.1(c), Δv_{G2} can be fitted but ΔD_4 is impossible to fit. As a result, ledge width is the main figure of merit

in fitting the measured CMOS IMD3 data for Class AB_+ in Figures 8.5(c) and 8.6(c). Ignoring these known issues of the distortion level on the ledge for Class AB(A) and the output power at low input power for Class BC, the fits to the measured data in Figures 8.5 and 8.6 are satisfactory.

It is now possible to compare the values of the device model transition parameters in Tables 8.2 and 8.3 for the fitting of the simulated and measured PA data. It can be seen that θ for the measured data has reduced considerably and the model is close to square law compared with the case of the simulated data. The value of Q, on the other hand is about the same for fitting simulated and measured data.

It is now possible to compare the γ_F values in Table 8.3 with those in Table 8.2 for fitting the simulated data. The γ_F values for the Q law model are very similar. For the velocity saturation device model, larger differences occur in the middle of the γ_F range. Note that, on account of the complex form of the distortion surface in the AB class range, especially in or near the AB(B) part, even small changes in γ_F have a very large effect on the shape of the distortion-power sweep.

8.6. Fitting Measured Performance Data for LDMOS PA from [87]

Curves of measured output power and 3rd order distortion for a LDMOS PA from [87] have been shown in Figure 2.20(a) − (d) for four classes of operation. This section presents fits to this data based on the clipping theory with the velocity saturation and Q-law models. The fits for these models are shown in Figures 8.7 and

Table 8.4 Parameters for fitting measured data for LDMOS PA of [87].

	θ = 0.30 (for Figure 8.7)					Q = 1.24 (for Figure 8.8)				
		P_{out}		IMD3			P_{out}		IMD3	
	γ_F / π	ΔP (dB)	Δv_G (dB)	ΔD (dB)	Δv_G (dB)	γ_F / π	ΔP (dB)	Δv_G (dB)	ΔD (dB)	Δv_G (dB)
C	0.97	21.0	4.50	17.0	5.50	0.90	22.0	4.50	15.5	4.10
AB_-	1.05	20.0	4.50	16.0	4.50	1.02	21.5	6.00	15.5	4.00
AB_+	1.08	20.0	4.50	15.0	4.50	1.04	21.0	6.00	14.0	4.00
A	1.62	20.0	9.00	17.0	8.50	1.40	21.3	10.0	17.0	7.40

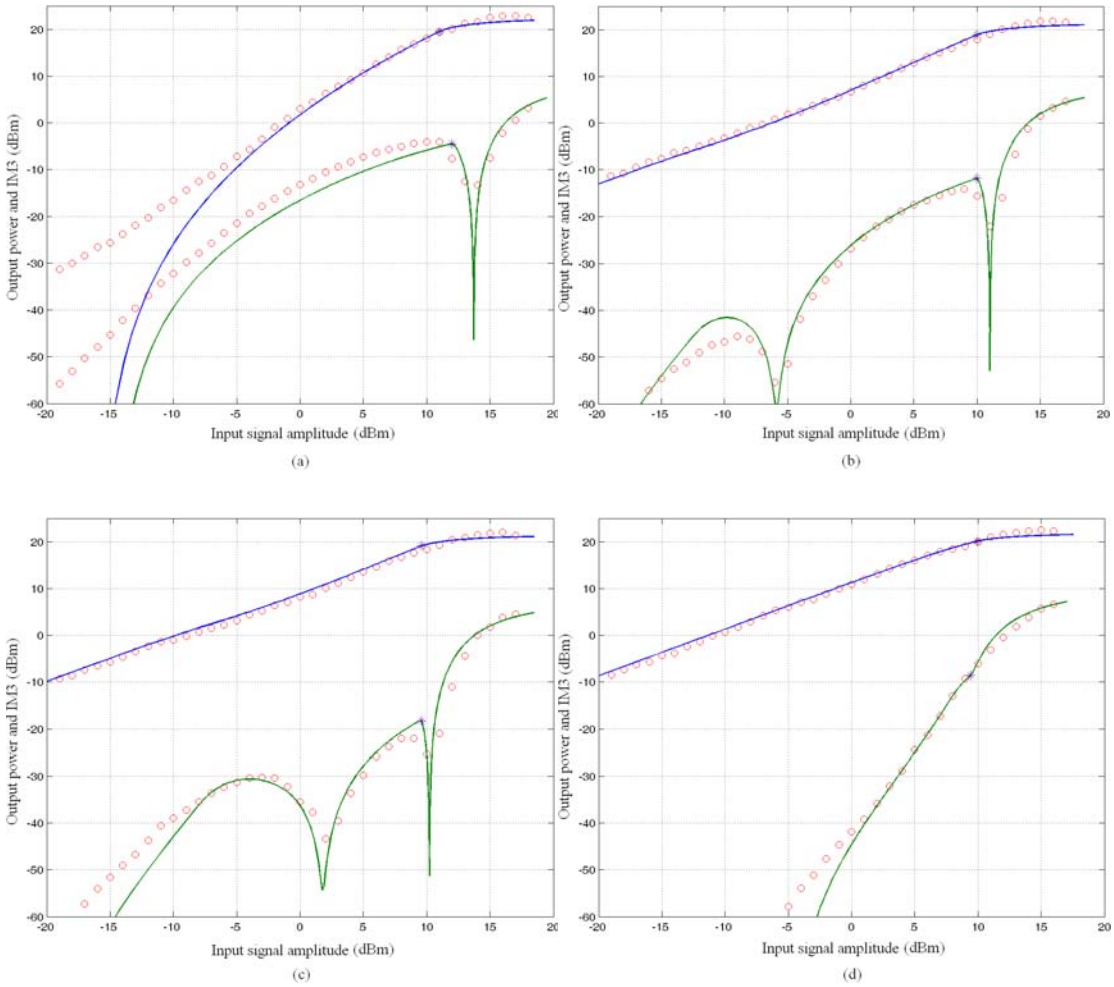

Figure 8.7 Velocity saturation model fitting for measured data for LDMOS PA of [87], (a) Class BC, (b) Class AB$_-$, (c) Class AB$_+$, (d) Class A.

8.8. Data for the optimisation of these fits is contained in Table 8.4.

As mentioned in section 8.2, both of the Class AB operating conductions for the LDMOS PA in [87] are in the AB(B) range and have a distortion characteristic with two deep nulls but with very different null spacings. As shown in Figures 8.7(b), (c) and 8.8(b), (c), it has been possible to meet both null spacing requirements exactly.

The results in Figures 8.7(a) and 8.8(a) exhibit the divergence at low input power levels of the predicted and measured output power for Class BC and associated divergence of the distortion characteristics, the reason for which has explained in section 8.5. Apart from this effect, the fits for the velocity saturation model in Figure 8.7 are very good. This fitting is assisted by the apparent high quality of the measured

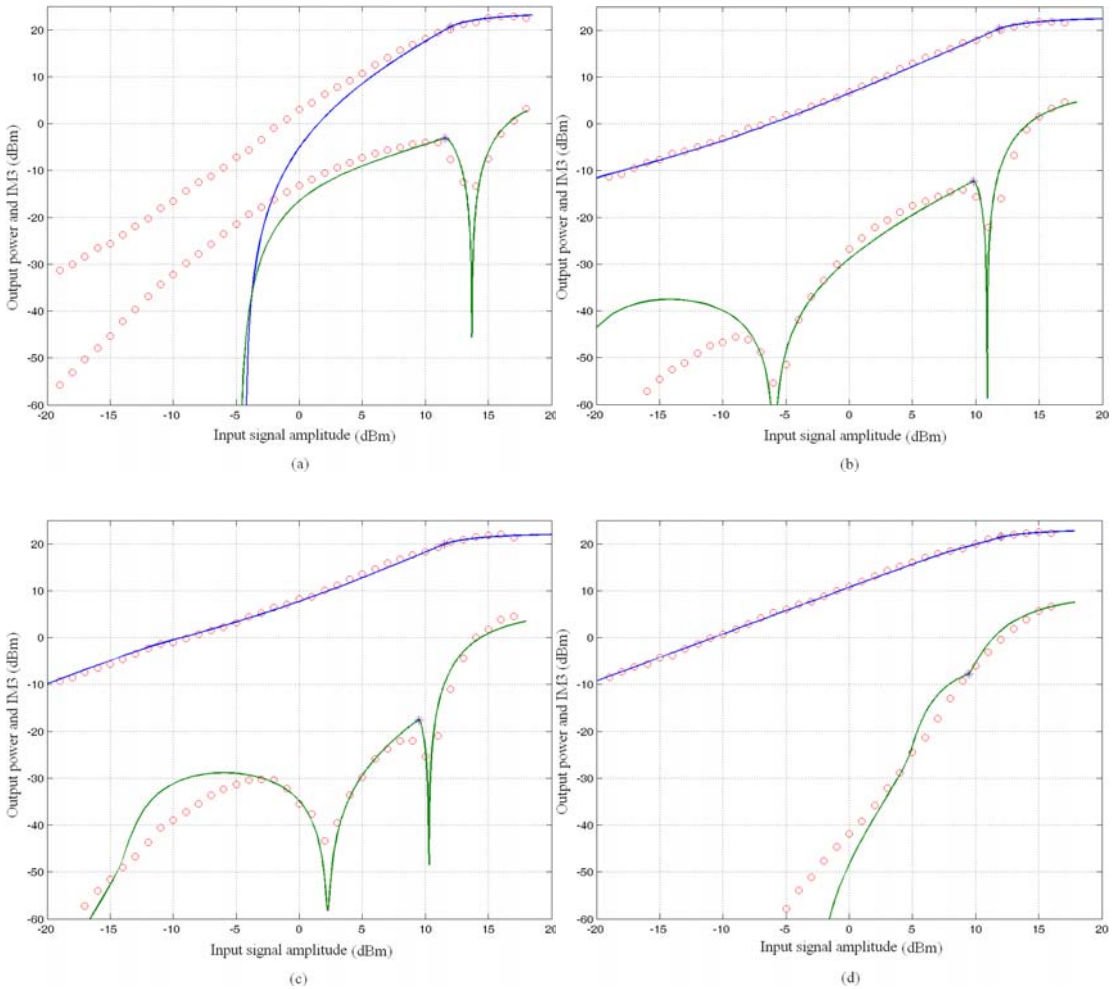

Figure 8.8 Q-law model fitting for measured data for LDMOS PA of [87], (a) Class BC, (b) Class AB$_-$, (c) Class AB$_+$, (d) Class A.

data for the LDMOS PA which exhibits mulls that are relatively deep, and therefore clearly defined.

At low input power, the predicted curves for the Q-law model in Figure 8.8 deviate from the measured data to a much greater extent than for the velocity saturation model in Figure 8.7. This suggest again that although both models predict well the moderate and high levels of distortion where clipping occurs, for the low levels of distortion, where there is no clipping, the velocity saturation model gives a better fit, which suggests that its small-signal derivative are more realistic.

Comparing the θ and Q values in Table 8.4 for fitting the LDMOS data with those for the CMOS data in Tables 8.2 and 8.3, the Q-law model for the LDMOS case

is very similar to that for CMOS. On the other hand, for the velocity saturation model, the value of θ for the LDMOS data lies in between the rather different values obtained for fitting simulated and measured CMOS data. As mentioned in section 7.7, the two models do cause different degrees of curvature of the rotated Class B part of the distortion valley. Therefore it is mot surprising that in order to fit a given set of PA data, the model parameters come out differently.

Consider the γ_F values in Table 8.4 for fitting the two models to the LDMOS data. It can be observed that the two cases of Class AB that have distortion characteristics with very different null spacing have values of γ_F that are very close to each other. This emphasises the high sensitivity of the distortion characteristic, especially in the AB(B) class range. As was the case for fitting the simulated and measured CMOS data, the Class BC PA is very close to Class B operation and what is described as a Class A PA, is, on the basis of the clipping theory and fitting distortion characteristics, in fact operating in the AB(A) class range and close to the middle of the AB class range.

8.7. Fitting Measured Performance Data for GaAs MESFET PA from [89]

Curves of measured output power and 3rd order distortion for a GaAs MESFET PA from [89] have been shown in Figure 2.21(a) and (b) for Class B and AB operation. This section presents fits to this data based on the clipping theory with the velocity saturation and Q-law models. The fits for these models are shown in Figures 8.9 and 8.10. Data for the optimisation of these fits is contained in Table 8.5.

Table 8.5 Parameters for fitting measured data for MESFET PA of [89].

	θ = 0.35 (for Figure 8.9)					Q = 1.70 (for Figure 8.10)				
	γ_F / π	P_{out}		IMD3		γ_F / π	P_{out}		IMD3	
		ΔP (dB)	Δv_G (dB)	ΔD (dB)	Δv_G (dB)		ΔP dB)	Δv_G (dB)	ΔD (dB)	Δv_G (dB)
B	1.01	12.0	−0.50	11.0	− 0.70	1.02	12.5	0.00	11.0	− 1.0
AB_+	1.43	12.0	0.50	8.50	− 0.70	1.37	12.5	0.00	11.0	− 1.0

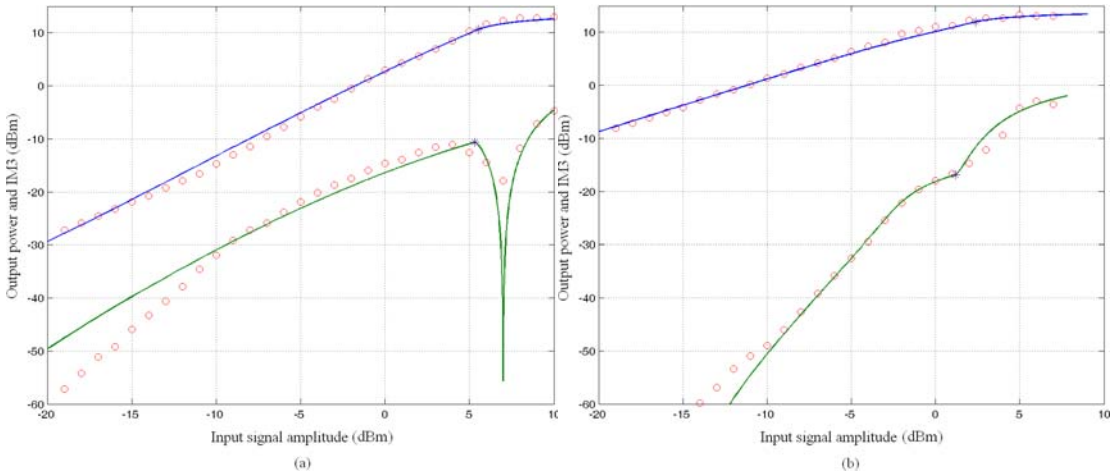

Figure 8.9 Velocity saturation model fitting for measured data for MESFET PA of [89], (a) Class B, (b) Class AB.

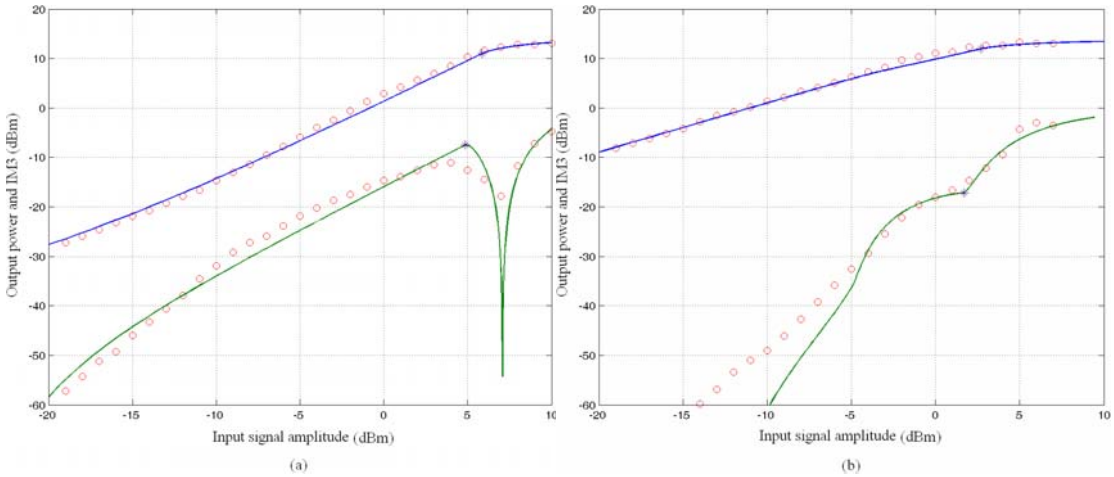

Figure 8.10 Q-law model fitting for measured data for MESFET PA of [89], (a) Class B, (b) Class AB.

The fact that the published distortion-power sweep for the Class AB GaAs MESFET PA in [89] shown in Figure 2.21(b) has a ledge shows that, according to the classification based on clipping theory in section 7.4, it is actually operating in the AB(A) class range. Thus the GaAs MESFET PA data does not include a sweep for the AB(B) class range that would exhibit two deep nulls. Since it is the Class AB(B) sweep with two deep nulls that has been used to define the device model transition parameters in the fitting to other technologies in sections 8.4 − 8.6, a different approach is necessary in order to define the model to best fit the GaAs MESFET data. Instead, a more empirical approach was adopted, in which the device model transition

parameter was stepped through a sequence of values, and, in each case, the two values of γ_F were adjusted to optimise the fitting criteria shown in Figures 8.1(a) and (c) for Class B and Class AB(A). As a result of this process, an optimum value of device model transition parameter, that gave the best fits when γ_F was optimised, was chosen.

It can be seen from Figures 8.9 and 8.10 that the fits to the GaAs MESFET data are reasonably good. The single null for Class B and the ledge for Class AB(A) are predicted well. At low power levels, the Q-law model fit for Class B in Figure 8.10(a) is of similar quality to that for the velocity saturation model fit in Figure 8.9(a).

Consider now the optimisation data for the GaAs MESFET PA in Table 8.5. It can be seen that the Q-law model, with Q = 1.7, is much closer to square-law than the models that best fit other technologies. For the velocity saturation model, the difference is not so great.

From the γ_F values in Table 8.5, it can be seen that there is reasonable agreement between the values for the two models. To best fit the data described in [89] as Class B, it has in fact been necessary to increase γ_F slightly above π. Thus, what is described as the Class B design is actually operating in the AB(B) class range, but γ_F is so close to π that the second null as at a very low input power and is not visible. What is described as the Class AB design, which as has been stated is actually operating in Class AB(A) according to the distortion characteristic, is around the middle of the AB class range.

8.8. Conclusion

A theory was proposed in Chapter 7 to explain the different forms of distortion-power sweep obtained for different classes of PA. The theory was based on an analysis of device output current clipping assuming a transitional device model. The general form of the distortion surface was validated using two different examples of transitional device models. The theory predicts the following:

The class of a PA is defined by FPCA, γ_F. The complete range of γ_F, with its two end points $\gamma_F = 0$ (Class C) and $\gamma_F = 2\pi$ (Class A), is divided by 3 transition points into 4 sub-ranges. In the BC class range, $0 \leq \gamma_F \leq \pi$, distortion-power sweeps exhibit a

single deep null above the FPP. At the Class B transition point, $\gamma_F = \pi$, there is a single deep null at the FPP and a low distortion sweet spot for very low input voltage amplitude. The Class B transition point is the beginning of the AB(B) class range, $\pi \leq \gamma_F \leq \gamma_{FT1}$, where the distortion-power sweep exhibit two deep nulls, whose spacing reduces, as γ_F increases. The two nulls merge into a single wide deep null at the transition point $\gamma_F = \gamma_{FT1}$. The γ_{FT1} transition point leads to the AB(AB) class range, $\gamma_{FT1} \leq \gamma_F \leq \gamma_{FT2}$, where there is a shallow null, whose depth reduces as γ_F increases. The transition point at which the shallow null ceases to exist is denoted γ_{FT2}. For $\gamma_{FT2} \leq \gamma_F \leq 2\pi$, the class range is denoted AB(A) and the distortion power sweeps exhibit a ledge that becomes narrower and lower as γ_F increases. The transition point $\gamma_F = \gamma_{FT1}$ is dependent on the effective threshold voltage of the device model transfer characteristic which may be set for any transitional device model by means of the transition parameter.

In Chapter 8, predicted distortion-power sweeps from the device current clipping theory using two examples of transitional device model have been fitted to published measured and simulated data for three different PA technologies. The published measured and simulated PA distortion-power sweeps clearly exhibit the expected patterns of behaviour in three of the class ranges, single null (BC), double null (AB(B)) and ledge (AB(A)). The fact that no published data showing the shallow null (AB(AB)) was found is attributed to co-incidence. The quality of the fits of the predictions to the published data, for the case of both transitional device models, confirms the validity of the theory of the rotated 'L'-shaped distortion valley produced by device current clipping and a transitional device model, as the principal determining factor of distortion and its dependence on input signal amplitude, class and device model.

It was mentioned in section 8.3.1 that, in principle, 3rd order distortion sweeps could be measured for a PA at a range of values of input signal bias voltage (*i.e.* class) and used to produce a 3-D plot showing a distortion surface. In this chapter, published distortion-power sweeps for PAs using CMOS, LDMOS and GaAs MESFET technologies have been fitted well by slices, or cross-sections, taken from the surface of 3rd order distortion predicted from device current clipping and use of a transitional model. The form of the predicted distortion surface has an area of high distortion in

the R1 and R2 clipping regions, which is intersected by a rotated 'L'-shaped valley. It follows from the quality of the fits presented in this chapter that, if it was possible to make sufficient number of measurements on a PA of any technology in order to establish a measured surface of 3rd order distortion, then that surface too would be intersected by a rotated 'L'-shaped valley.

Likewise, a computer simulation of the 3rd order distortion of a PA that correctly predicted distortion power sweeps for a number of classes of operation would, if run enough times to establish the distortion surface, yield a surface that is intersected by the rotated 'L'-shaped valleys; this is true whether the model has continuous derivatives, as in [92][95][96], or if it has discontinuous derivatives, like the models used in this thesis.

Thus the rotated 'L'-shaped valley in the distortion surface of a PA is a very fundamental feature underlying the actual performance of a PA using a device of any technology. And it underlies also any simulation of a PA that gives realistic distortion-power seeps for different classes of operation.

As reviewed in section 1.3, the essential difference between PAs of different classes is the extent of the clipping of the device output current. It has been shown in this thesis that clipping introduces a continuous valley that cuts across the surface of 3rd order distortion. Moreover, it has been shown that the form of the model affects the path of the valley. In particular, the effective threshold voltage of the device transfer characteristic (actual and simulated) governs a rotation of the valley that determines the diverse pattern of distortion-power sweeps obtained for different classes of operation.

Therefore the device current clipping theory proposed in this thesis, the transitional device model and the rotated 'L'-shaped 3rd order distortion valley that they lead to form the corner-stone of true understanding of PA operation and performance both in an educational setting and for practical PA design in industry.

The results obtained in this thesis have important implications for modelling of devices for simulation of PA distortion.

In an ideal situation, the transfer characteristic for the device model would be identical with that for the real PA device. In that case, the measured and simulated 3rd order distortion surfaces, and the distortion-power sweeps for any class, would also

be identical. The derivatives and effective threshold voltage for the transfer characteristics of the model and the real device would also be identical.

In practice, the transfer characteristic for the device model cannot be the same as that of the real device. Then the interesting question of device modelling arises, namely, how should the model be optimised? One approach is to obtain the best fit of the two transfer characteristic curves [87]. Another is to introduce the soft pinch-off function [77][80] into the model equation in order to obtain bounded derivatives that give the best match to those for the real device, especially in the cut-off region. Although such advances are significant, they are not successful enough that they have permitted prediction of the 3rd order distortion-power sweeps of a PA at different classes of operation over the full range of input voltage amplitude with any accuracy. In order to do that, the understanding gained through the work described in this thesis may be used to propose novel criteria for device modelling.

Up until now, the selection of PA input signal bias voltage, or class of operation, for the measurement of distortion power sweeps for evaluating simulator device models has been rather haphazard. For example, the two Class AB distortion-power sweep in [87] each has two nulls but, in [83], one has two nulls and the other has a ledge. The rotated 'L'-shaped valley theory of PA distortion proposed in this thesis allows a systematic approach to the gathering of measured distortion data.

First the class B point may be determined, either by adjusting PA input signal bias voltage to obtain a sweep spot at very low input signal amplitude or by setting the bias voltage to equal the device threshold voltage. Some representative distortion power sweeps in the BC class range may be measured, all of which exhibits a single null.

If input signal bias voltage is increased above the Class B point, then two nulls appear in the distortion-power sweep. The input signal bias voltage that corresponds to the transitional point γ_{FT1} may be found by observing the point at which the two nulls just merge to create a single wide deep null. Then a number of representative distortion power sweeps in the AB(B) class range ($\pi \leq \gamma_F \leq \gamma_{FT1}$), all of which exhibit two deep nulls, may be made.

Then the input signal bias voltage may be increased further until the point where the shallow null just disappears, establishing the transition point γ_{FT2}. Now

representative distortion-power sweeps may be made in the AB(AB) class range ($\gamma_{FT1} \leq \gamma_F \leq \gamma_{FT2}$ – shallow null) and in the AB(A) class range ($\gamma_{FT1} \leq \gamma_F \leq 2\pi$ – ledge). Such comprehensive distortion measurements covering all class ranges would form a good set of data for evaluating simulator device models.

The rotated 'L'- shaped distortion valley theory of PA behaviour based on device current clipping and the transitional device model provides novel criteria for developing the form of device model and optimising its parameters. The most significant feature of the surface of PA 3rd order distortion is the rotated 'L'-shaped valley. This suggests that the primary device modelling criterion should be the correct bias for the corner of the valley, γ_{FT1}, which gives a single wide deep null and separates the AB(B) and AB(AB) class ranges, where there are two deep nulls and a single shallow null, respectively. The results in Chapter 7 suggest that the effective threshold voltage of the device model transfer characteristic plays the major role in determining the degree of rotation of the valley and hence γ_{FT1}. Perhaps the second most important device modelling criterion is the correct input signal bias for the transition point γ_{FT2}, between the AB(AB) and AB(A) class ranges, where the distortion-power sweep has a single shallow null and a ledge, respectively. It has been shown in Chapter 7 (section 7.8) that different transitional device models give different curvature of the 'L'-shaped valley in the class AB(B) class range. This curvature could be optimised in order to predict correctly the way in which the spacing of the two nulls in the AB(B) class range varies with PA input signal bias voltage.

Finally, it has been shown (Chapter 7) that the low levels of distortion obtained where there is no clipping can be rather different for different transitional device models, and this might also be a criterion for optimising the form selected for device model. Thus it can be seen that understanding of the cause of PA distortion gained from the device current clipping theory, transitional device model and rotated 'L'-shaped distortion valley as developed in this thesis leads to novel criteria for optimisation of simulator device models.

CHAPTER 9 CONCLUSION AND FUTURE WORK

9.1. Conclusion

Theories that explain key aspects of PA performance, such as output power, efficiency and gain, by analysis of device current clipping have been proposed in previous work by Pedro [51] and Cripps [52]. In this thesis, a new device current clipping theory has been proposed with clear advantages over the previous ones. These are that a very systematic approach to the analysis enables PA performance metrics of output power, efficiency and gain to be plotted as 3-D surfaces with PA class and input signal power as independent variables, offering considerable insight, and that the critical PA performance parameter of 3rd order intermodulation distortion is now included.

The development of the new device current clipping theory rests on a number of original concepts and definitions. These are:

- full power point (section 3.2.3)
- full power conduction angle (section 3.2.4)
- equivalent system model for PA that considers clipping to the applied to the input voltage (section 3.3)
- definition and use of the extrapolation function as the ratio of peak clipped input voltage to peak input voltage (section 4.3)
- partition of the $\gamma_F - \hat{v}_G$ (*i.e.* class – input signal amplitude) space into regions R2, R1, R0 and Rf, according to type of clipping, double, single, no and full clipping (sections 4.4 and 4.5)

- understanding variation of knee and cut-off clipping angles and conduction angle versus γ_F and $\hat{v}_G$ (section 4.7)
- identifying form of constant γ (conduction angle) contours in $\gamma_F - \hat{v}_G$ plane (section 4.7)
- significance and effect of transitional device model that can be changed by means of a transition parameter between the linear and square law model (Chapter 7)
- principle of valley continuity in a distortion surface (section 7.2.2)
- idea and application of effective threshold voltage (section 7.2.3) and effective conduction angle (section 7.2.4)

The theory presented in this thesis sheds understanding on PA 3rd order distortion in two ways. The first is on the general form of the distortion surface when plotted against input voltage amplitude $\hat{v}_G$ and class of operation, FPCA γ_F. The surface shows high distortion both above the full power point (FPP) in the double clipping R2 region and below the FPP in the single clipping R1 region. The combined area of high distortion is crossed by a deep valley. In the BC class range ($0 \leq \gamma_F \leq \pi$), the valley is gently curved and its path is relatively independent of PA device model. In the AB class range ($\pi \leq \gamma_F \leq 2\pi$), the path of the valley is critically dependent on device model. For a linear device model, this part of the valley is straight, parallel to the $\hat{v}_G$ axis and follows the line $\gamma_F = \pi$ rads. For a transitional device model, this part of the valley curves to the right as $\hat{v}_G$ increases, following, approximately, a constant γ contour. As the device model cut-off becomes increasingly soft, the curvature increases. In the limit, for a square law model, this part of the valley reaches the edge of the R1 region, *i.e.* the R1 − R0 boundary, and disappears into the no distortion R0 region. The extent of the rotation of this part of valley depends on the effective threshold voltage of the device model transfer characteristic. The principle of valley continuity requires that, as this part of the valley turns and rotates; the BC part of the valley must extend across the AB region to keep its connection with it. Thus, device current clipping in a PA causes the region of high distortion around the full-power point to be intersected by an 'L'-shaped valley that has a clockwise rotation, the

degree of rotation depending on the effective threshold voltage of the device transfer characteristic.

The second contribution to understanding of PA distortion is on the forms obtained for 3rd order distortion-power sweeps. Since the power sweeps are simply cross-sections of the 3-D distortion surface, the forms of the power sweeps follow from the form of the distortion surface, having a rotated 'L'-shaped valley, as discussed in the last paragraph. The entire class range ($0 \leq \gamma_F \leq 2\pi$) is divided into four sub-ranges by three transition points. The transition points are the Class B point ($\gamma_F = \pi$), the corner of the rotated 'L'-shaped valley ($\gamma_F = \gamma_{FT1}$) and the point where the shallow valley just disappears ($\gamma_F = \gamma_{FT2}$). Each class sub-range has a distinctive form of distortion power sweep. In the BC Class range ($0 \leq \gamma_F \leq \pi$), there is a single deep null in the saturation range. Throughout the AB(B) class range ($\pi \leq \gamma_F \leq \gamma_{FT1}$), there are two deep nulls, whose spacing reduces as γ_F increases. At $\gamma_F = \gamma_{FT1}$, the two nulls merge to give a single wide deep null. In the AB(AB) class range ($\gamma_{FT1} \leq \gamma_F \leq \gamma_{FT2}$), there is a shallow null, whose depth reduces as γ_F increases. Finally, in the AB(A) class range ($\gamma_{FT2} \leq \gamma_F \leq 2\pi$), there is a ledge whose width reduces and depth increases as γ_F increases. Since, irrespective of PA device technology, device current clipping is the factor that distinguishes PAs of different classes [47], as shown in Figure 1.9, the four distinctive forms of distortion-power sweep, single null, double null, shallow null and ledge for the four class ranges, BC, AB(B), AB(AB) and AB(A) should be exhibited by PAs of any technology. These different forms of distortion power sweep have been observed in published measured distortion sweeps for CMOS, LDMOS and GaAs MESFET PAs, and the clipping theory presented in this thesis provides good fits to this published data using two different transitional device models.

The class of operation of a PA is set by the input signal bias voltage. Changes in input signal bias voltage to set the class cause considerable changes in PA device current clipping characteristics, as shown in Figure 1.9. Indeed, it is the change in device current clipping with class that leads to the differences in performance metrics such as efficiency. Thus device current clipping is a primary aspect of PA operation. In this thesis, it has been shown that device current clipping causes high levels of intermodulation distortion and the clipping theory provides good fits to published measured distortion characteristics of CMOS, LDMOS and GaAs MESFET PAs. The

quality of the fits provides further confirmation that device current clipping is the primary cause of distortion in PAs. Therefore, the clipping theory presented in this thesis should be of key interest to those in industry who design and optimise PAs and also to those engaged in teaching an understanding of PA design and performance. Of course, PA distortion must be affected by phenomena other than device current clipping, but it is believed that these effects are secondary as they can only modify the path and the depth of the rotated 'L'-shaped valley that is caused by device current clipping. Some of these secondary influences on distortion will be mentioned in the following sub-section on future work.

9.2. Future Work

9.2.1. Confirmation of Form of 3-D Surface for IMD3 of PAs

It has been shown, in this thesis, that published measured distortion-power sweeps for PAs of different technologies can be fitted by slices from a predicted 3-D distortion surface that contains a rotated, curved 'L'-shaped valley. The published measured data, however, is limited since only four different classes are considered for each technology and no curve has been found for the predicted AB(AB) class range, which has a shallow null. It would be very interesting to confirm the form of the whole of the distortion surface, including rotated 'L'-shaped valley, by measurements on PAs of different technologies. In view of the quantity of measured data required to define the distortion surface, a fully automated test system would need to be utilized.

The form of the surface of PA distortion, including the rotated 'L'-shaped valley, has been predicted in this thesis using very simple device models that are transitional between the linear and square-law models. It would also be very interesting to derive the distortion surface by circuit simulation using full models for devices, such as the Parker-Skellern [79], EKV model [78] or other models, such as those used in Cadence. Harmonic balance [51][97] might be a suitable analysis method. In view of the very large amount of computation needed to define the distortion surface, the simulation would need to be set up to run fully automatically.

Comparison of measured distortion surface for a PA with that predicted using a particular device model could provide a very stringent method for assessing device models. Correct prediction of the path of the valley can be used as an initial criterion for selecting forms of device models and optimising their parameters. The valley paths can be obtained by generating contour plots from the 3-D distortion surfaces. Looking at distortion 3-D and contour plot, rather than at only distortion power sweeps, provides a higher level of view that would settle in a very clear way many question about accuracy of device models for distortion prediction.

9.2.2. Extension of the Clipping Theory

In this thesis, a basic form of PA device current clipping theory has been presented that can predict the measured distortion-power sweeps of practical PAs. However, there are several obvious ways in which it might be interesting and useful to extend the theory.

1. Derivation of the relationship between the full power point (FPP) for a PA, as introduced in this thesis and the 1 dB compression point [52], and thus introduce 1 dB compression point into the theory.
2. Introduction of a soft type of knee clipping, perhaps using the function in [77] and find the effect of this on the 'L'-shaped distortion valley. Also, investigation of effect on distortion valley of modelling device cut-off using the soft pinch-off function [77], that makes derivatives finite and continuous.
3. Formal definition of effective threshold voltage and effective conduction angle and hence derivative of mathematical expressions for the transitional values of $\gamma_F - \gamma_{FT1}$ and γ_{FT2} (divides AB(B) from AB(AB) and AB(AB) from AB(A) class ranges, respectively).
4. It has been shown that FET source access resistance has a considerable effect on small-signal distortion of the common-source FET amplifier [82]. Inclusion of device source resistance as separate from device model and determine its effect on the distortion surface.
5. Investigation by computer simulation of the effect of the parasitic capacitance of the PA device on the form of the distortion surface for very high

frequencies of operation. Aim for an analytical treatment of the observed effect.

9.2.3. CAD Package for PA Design

In the design of a practical PA, many design decisions have to be made, including device size scaling, class (*i.e.* input signal bias voltage) and degree of back-off (*i.e.* input signal amplitude). These decisions will affect output power, efficiency and gain. They also affect distortion that in turn affects ACI and EVM, both of which affect bit error rate (BER). Thus the design of a practical PA involves trade-offs between many factors, and, is therefore time consuming and there is not guarantee of optimality.

It has been shown in this thesis that device current clipping can predict the distortion characteristics of practical PAs, even using simple transitional device models. Therefore, it would be attractive to produce a CAD package based on device current clipping and a simple device model that could improve and speed up the work of a PA designer. The simplicity of the model of could allow rapid calculation and display of multiple sets of PA performance parameters, such as efficiency and BER, and allow the designer to adjust design parameters, such as bias and back-off, in order to obtain an optimum solution for a given modulation format. Use of such a package could form a very useful first stage of the PA design process that allows the designer to make optimum choice of the key parameters of PA design before then transforming the design to a conventional design package such as Cadence for detailed design at component level and layout.

9.2.4. Effect of Load

The device current clipping theory presented in this thesis has been based on the assumption of a device transfer characteristic that implies a maximum current limit value (i_{DL} in Figure 3.2) that is independent of PA input signal amplitude and class of operation. In reality, the maximum limit current is not exactly constant, and including this effect in the theory could improve the quality of the fit of PA performance predictions to measured data.

As stated in section 3.2.1, the maximum limit current depends on the intersection of the load line (or load plane) with the outer edge of the triode region part of the device transfer characteristics, as can be envisaged using Figure 1.6 (or Figure 1.7). Although not yet quantified analytically, it is often stated in the literature that the position of the load line does vary with the amplitude of the PA input signal [52][98]. This will cause the maximum limit current of the device i_{DL} to be dependent on the amplitude of the PA input signal. When different classes of operation for a PA are being compared, it may be the case that the effective load resistance at the device output terminal and the supply voltage are changed in such a way that i_{DL} is not exactly constant. So it is likely that the quality of the predictions of PA performance made by the device current clipping theory would be improved if dependence of i_{DL} on input voltage amplitude ($\hat{v}_G$) and class (γ_{F}) was included. Other factors that could affect predictions from the theory and should be investigated include the use of a tuned load coupling matching circuit (as in Figure 1.5(b)) and the use of harmonic terminations [76].

REFERENCES

[1] S.-W. Chen, W. Panton, R. Gilmore, "Effects of Nonlinear Distortion on CDMA Communication Systems," *IEEE. Symp. Microwave*, Vol. 2, PP. 775-778, June 1996.

[2] J. F. Sevic, "Statistical Characterization of RF Power Amplifier Efficiency for CDMA Wireless Communication Systems," *Conf. Wireless Communications*, PP. 110-113, Aug. 1997.

[3] M. Uhlirz, "Concept of a GSM-Based Communications System for High-Speed Trains," *IEEE Conf. Vehicular Technology*, Vol. 2, PP. 1130-1134, June 1994.

[4] W. Zhao, R. Tafazolli and B. G. Evans, "Internetwoek Handover Performance Analysis in GSM-Satelliter in Integrated Mobile Communication Systems," *IEEE Jour. Selected Areas in Communications*, Vol. 15, PP. 1567-1671, Oct. 1997.

[5] Jun-Zhao Sun, J. Sauvola and D. Howie, "Features in Future: 4G visions from a Technical Perspective," *IEEE Conf. Global Telecommunications*, Vol. 6 PP. 3533-3537, Nov. 2001.

[6] B. G. Evans and K. Baughan, "Visions of 4G," *Journ. Electronics & Communication Engineering*, Vol. 12, PP. 293-303, Dec. 2000.

[7] L. E. Larson, "Microwave Device and Circuit Challenges for Next Generation Wireless Applications," *IEEE. Conf. Wireless Communication Technology*, PP. 74-77, 2003.

[8] F. Aclachi, "New Direction of Wireless Technology," *Workshop on Signal Design and Its Application in Communications*, PP. 1-1, Sept. 2007.

[9] P. R. Gray and A. Niknejad, "CMOS Power Amplifier in High-Integration RF Transceivers," *IEEE Conf. Consume Electronic, NorChip*, Nov. 2006.

[10] M. Feng, S-Ch Shen, D. C. Caruth, and J-J Huang, "Device Technologies for RF Front-End Circuits in Next-Generation Wireless Communications," *IEEE The Priceedings*, Vol. 92, No. 2, PP. 354-375, Feb. 2004.

[11] L. E. Larson, "Radio Frequency Integrated Circuit Technilogy for Low-Powqer Wireless Communications," *IEEE Journ. Personal Communications*, PP. 11-19, June 1998.

[12] L. E. Larson, "Circuit and System Design for Future Microwave Systems," *IEEE Symp. Microwave*, PP. 913-916, June 2005.

[13] H. S. Bennett, R. Brederlow, J. Costa, M. Huang, A. A. Immorlica, Jr. Jan-Erik Mueller, M. Racanelli, C. E. Weitzel and Bin Zhao, "RF and AMS," *IEEE Maga. Circuits & Devices*, PP. 38-51, Nov./Dec. 2004.

[14] Y.-H. Chen, Ch.-W. Wang, Ch.-F. Lee; T.-Y. Yang, Ch.-F. Liao, G. –K. Ma and Sh.-I. Liu, "A 0.18 /spl mu/m CMOS receiver for 3.1 to 10.6GHz MB-OFDM UWB communication systems," *IEEE Symp. Radio Frequency Integrated Circuits*, June, 2006.

[15] R. Gilmore and L. Besser, "Practical RF circuit design for modern wireless systems volume II Active circuits and systems," *Artch House*, 2003.

[16] J. Lee and J. D. Cressler, "Analysis and Design of an Ultra-Wideband Low-Noise Amplifier Using Resistive Feedback in SiGe HBT Technology," *IEEE Trans. Microwave Theory and Techniques*, Vol. 54, PP. 1261-1268, March 2006.

[17] S. Tiuraniemi, L. Stoica, A. Rabbachin and I. Oppermann, "Front-End Receiver for Low Power, Low Complexity Non-Coherent UWB Communications System," *IEEE Conf. International Ultra-Wideband*, 5th, PP. 339-343, Sept. 2005.

[18] Ch.-W. Lin, Y.-Z. Liu and K. Y. Josn, "A low distortion and fast settling automatic gain control amplifier in CMOS technology," *International Symp. Circuits and systems*, Vol. 1, PP. 541-543, May 2004.

[19] Ch.-Ch. Lin, M.-T. Shieu and Ch.-K. Wang, "A dual-loop automatic gain control for infrared communication system," *IEEE Proceedings. ASIC*, PP. 125 – 128 Aug. 2002.

[20] U. L. Rohde and A. K. Poddar, "Reconfigurable, Power Efficient, and High IP3 Passive FET Mixers for Wideband Communication Systems Wireless Communication Systems," *IEEE Symp. ISWCS*, PP. 433 − 437, Sept. 2006.

[21] I. Nam, B. Kim and K. Lee, "CMOS RF Amplifier and Mixer Circuits Utilizing Complementary Characteristics of Parallel Comboned NMOS and PMOS Devices," *IEEE Trans. Microwave Theory and Techniques*, Vol. 52, PP. 1662-1671, May 2005.

[22] S. H. Dahlan and M. Esa, "Miniaturized Low Pass Filter Using Modified Unifolded Single Hairpin-Line Resonator for Microwave Communication Systems," *IEEE Conf. RF and Microwave*, PP. 16-20, Sept. 2006.

[23] Shi. Nagaoka, "Compact Latching-Type Single-Model-Fiber Switches Fabricated by a Fiber-Micromaching Technique and Their Practical Applications," *IEEE Jour. Quantum Electronicsm,* Vol. 5, No.1, Jan./Feb. 1999.

[24] F. H. Raab, P. Asbeck, S. Cripps, P. B. Kenington, Z. B. Popovic, N. Pothecary, J. F. Sevic and N. O. Sokal, "Power Amplifiers and Transmitters for RF and Microwave," *IEEE Trans., Microwave Theory and Tech., vol 50, pp. 814-826, March. 2002.*

[25] H.-M. Park, D.-H. Baek, K.-I. Jeon and S. Hong, "A Predistortion Linearizer Using Envelope-Feedback Technique with Simplified Carrier Cancellation Scheme for Class-A and Class-B Power Amplifiers," *IEEE Trans. Microwave Theory and Techniques*, Vol. 48, PP. 898-904, June 2000.

[26] M. Faulkner, "Amplifier Linearization Using RF Feedback and Feedforward Techiques," *IEEE Trans, Vehicular Tech.,* Vol.47, PP.209-215, FEB, 1998.

[27] D. Webster, J. Scott and D. G. Haigh, "Control of Circuit Distortion by the Derivative Superposition Method," *IEEE Lett. Microwave and Guided Wave,* Vol. 6, PP.123-125, March 1996.

[28] D. R. Webster, G. Ataei and D. G. Haign, "Low-Distortion MMIC Power Amplifier Using a New Form of Derivative Superposition," *IEEE Trans., Microwave Theory and Tech.,* Vol 45, PP. 328-332, FEB. 2001.

[29] M. Iwamoto, A. Williams, P.-F. Chen, A. D. Metzger, L. E. Larson and P. M. Asbeck, "An Extended Doherty Amplifier with High Efficiency Over a Wide Power Range," *IEEE Trans. Mocrowave Theory and Technolog,* Vol.49, PP. 2472-2479, Dec. 2001.

[30] J. Kang, K. Lee, J. Yoon, Y. Chung, S. Hwang and B. Kim, "Differential CMOS linear power amplifier with 2nd harmonic termination at common source node," *IEEE Symp. Radio Frequency Integrated Circuits*, PP. 443-446, June, 2005.

[31] V. W.Leung, JunXiong Deng, P. S. Gudern and L. E. Larson, "Analysis of Envelop Signal Injection for Improvement of RF Amplifier Intermodulation Distortion," *IEEE J.Solid-State Circuits,* Vol.40, PP.1888-1894, Sep. 2005.

[32] Ch.Zh. Wang, L. E. Larson and P. M. Asbeck, "A Nonlinear Capacitance Cancellation Techniques and its Application to a CMOS Class AB Power Amplifier," *IEEE symp. Radio Frequency Integrated Circuits,* PP. 39-42, 2001.

[33] Ch.Zh. Wang, M. Vaidyanathan and L. E. Larson, "A Capacitance-Compensation Technique for Improved Linearity in CMOS Class-AB Power Amplifiers," *IEEE Journ. Sloid-State Circuits*, Vol. 39, PP. 1927-1937, Nov. 2004.

[34] M. P. van der Heijden, H. C. de Graaff, L. C. N. de Vreede, J. R. Gajaharsing and J. N. Burghartz, "Theory and Design of an Ultra-Linear Square-Law Approximated LDMOS Power Amplifier in Class-AB Operation," *IEEE Trans. Microwave Thoery and Techniques*, Vol. 50, PP. 2176-2185, Sept. 2002.

[35] T. W. Kim, B. Kim, I. Nam and K. Lee, "A Low-Power Highly Linear Cascoded Multiple-Gated Transistor CMOS RF Amplifier with 10 dB IP3 Improvement," *IEEE Lett. Microwave and Wireless Components*, Vol. 13, PP.205-207, June 2003.

[36] R. Gupta, B. M. Ballweber and D. J. Allstot, "Design and Optimization of CMOS RF Power Amplifiers," *IEEE Journ. Solid-State Circuits*, Vol. 36, PP. 166-175, Feb. 2001.

[37] Y.W. Ding and R. Harjani, "A High-Wfficiency CMOS +22-dBm Liner Power Amplifier," *IEEE Journ. Solid-State Circuits*, Vol. 40, PP. 1895-1902, Sept. 2005.

[38] A. N.D'Andra, V. Lottici, and R. Reggiannini, "RF Power Amplifier Linearization through Amplitude and Phase Predistortion", *IEEE Trans. Communication,* Vol.44, PP. 1477-1484, 1996.

[39] B. Wilson and M. Al-Gahtani, "Improved Logarithmic Converter Based On A Transconductance Feedback Amplifier", *IEEE Sym. Circuits and System,*Vol.1, PP. 651-654,2001.

[40] B. Wilson, "Transconductance Feedback Amplifier Configuration Exhibiting Bandwidth-Independent Voltage gain," *IEE proc.-Circuits Devices Sys*., Vol.146, PP. 242-248, OCT, 1999.

[41] T. H. Lee, "The Design of CMOS Radio-Frequency Integrated Circuits-second edition," *Cambridge,* 2004.

[42] Ch. Fager, J. C. Pedro Nuno Borges de Carvalh, H. Zirath and M. J. Rosario, "A Comprehensive Analysis if IMD Behavior if RF CMOS Power Amplifier," *IEEE Journ. Solid-State Circuits,* Vol.39, PP. 24-34, Jan., 2004.

[43] S. A. Maas, "Nonlinear Microwave Circuits", *Artech House,* 1988.

[44] D. Webster, M. Darvishzadeh and D. G. Haigh, "Total Charge Capacitor Model for Short-Channel MESFET's", *IEEE Lett. Microwave and Guided Wave,* Vol.6, PP. 351-353, Oct., 1996.

[45] S. Kang, B. Choi and B. Kim, "Linearity Analysis of CMOS for RF Application," *IEEE Conf. MTT-S,* PP.279-282, 2002.

[46] A. Marzuki, T. A. Zulkifli, N. Mohd noh, and Z. A. Abdul Aziz, " A Broadband RF Feedback Amplifier Design with Simple Feedback Network," *Conf. RF and Microwave*, PP. 1-4, Oct. 2004.

[47] P. B. Kenington, "High-Linearity RF Amplifier Design," *Artech House*, 2000.

[48] A. Moschitta and D. Petri, "Wideband Communication System Sensitivity to Overloading Quantization Noise [ADC Characterization]," *IEEE Trans. Instrumentation and Measurement,* Vol. 52, PP. 1302-1307, Aug. 2003.

[49] H. T. Jensen and I. Galton, "A Low-Complexity Dynamic Element Matching DAC for Direct Digital Synthesis," *IEEE Trans. Circuits and Systems − II: Analog and Digital Signal Processing,* Vol. 45, No. 1, PP. 13-27, Jan. 1998.

[50] H. Shafiess, B. Nourani and M. Khoshgard, "Joint Compression and Tracking of Frequency Offsets in RF Mixers and DAC/ADC Clocks in OFDM," *Conf. Commnications Systems,* PP. 150-154, Sept. 2004.

[51] J. C. Pedro and N. B. Carvalho, "Intermodulation Distortion in Microwave and Wireless Circuits," *Artech House*, 2003.

[52] S. C. Cripps, "RF Power Amplifiers for Wireless Communications," *Artech House*, 1999.

[53] S. C. Cripps, "Advance Techniques in RF Power Amplifier Design," *Artech House*, 2000.

[54] R. Gilmore and L. Besser, "Practical RF circuit design for modern wireless systems volume I Passive circuits" *Artech House*, 2003.

[55] A. Stephenne, F. Bellili and S. Affes, "Moment-Based SNR Estimation for SIMO Wireless Communication Systems Using Arbitrary QAM," *Conf. Signals, Systems and Computers*, PP. 601-605, Nov. 2007.

[56] A. V. Dinh and R. J. Bolton, "A High-Speed Baseband Transceiver for Wireless Communication Using QAM," *IEEE Conf. Communications, Computers and Signal Processing*, Vol. 2, PP. 631-634, Aug. 2001.

[57] S. Mirabbasi and K. Martin, "Classical and Modern Receiver Architectures," *IEEE Magazine Communications*, Vol. 38, PP. 132-139, Nov. 2000.

[58] W. Struble, F. McGranth, I. Harrington and P. Nagle, "Understanding Linearity in Wireless Communication Amplifiers," *IEEE Journ. Solid-State Circuits*, Vol. 32, PP. 1310-1318, Sept. 1997.

[59] J. F. Sevic and J. Staudinger, "Simulation of Power Amplifier Adjacent-channel Power Ratio for Digital Wireless Communication Systems," *IEEE Conf. Vehicular Technology*, Vol. 2, PP. 681-685, May 1997.

[60] Q.Ch. Liu and J. Li, "Quasi-Constant Envelop OQPSK through Nonlinear Radio and AWGN Channel," *Proceeding MILCOM*, Vol.1, PP. 715-720, Oct. 2002.

[61] Ch.-H. Chen and Ch.-Ch. Chiu, "Novel Radiation Pattern by Genetic Algorithms, in Wireless Communication," *IEEE Conf. Cehicular Technology*, Vol. 1, PP. 8-12, May 2001.

[62] A. Sampath and D. R. Jeske, "Analysis of Signal-to-Interfernce Ration Estimation Methods for Wireless Communication Systems," *IEEE Conf. Communications*, Vol. 8, PP. 2499-2503, June 2001.

[63] A. C. McCormick and E. A. Al-Susa, "Multicarrier CDMA for Future Generation Mobile Communication," *Journ. Electronics & Communication Engineering*, Vol. 14, PP. 52 – 60, April 2002.

[64] Je-Kuan Jar and T.-Sh. Horng, "Linear Interpolation Scheme for Compersation of Path Delay Difference in an Envelope Elimination and Restoration Transmitter," *IEEE Conf. Asia-Pacific Microwave*, Vol. 3, PP. 1072-1075, Dec. 2001.

[65] F.-L. Lin, Sh.-F. Chen, L.-F.Chen and H.-R. Chuang, "Computer Simulation and Measurement of Error Vector Magnitude (EVM) and adjacent-Channel Power

Amplifiers," *IEEE Conf. Vehicular Technology*, Vol. 4, 19 − 22, PP. 2024-2028, Sept. 1999.

[66] S. Tanaka, F.Behbahani, and A.A.Abidi, "A Linearization Technique for CMOS RF Power Amplifier," *Symp. VLSI Circuit*, PP. 93-94, June, 1997.

[67] F. H. Raab, P. Asbeck, S. Cripps, P B. Kenington, Z B. Popovic, N. Pothecary, J F. Sevic and N O. Sokal, " Power amplifiers and Transmitters for RF and Microwave," *IEEE Trans. Microwave and Techniques*, Vol. 50, No. 3, PP. 814-826, March, 2002.

[68] M. A. Jang, S. Y. Kim, K. K. Jeon, Y. Kim and Y. C. Jeong, "Linearity Improvement of Power Amplifier Using Modulation of Low Frequency IMD Signals," *Conf. APMC*, Vol. 2, PP. 4-8, Dec., 2005.

[69] F.-J. Gonzalex-Serrano, J. J. Murillo-Fuentes and A. Artes-Roderiguez, "GCMAC-Based Prediction for Digital Modulations," *IEEE Trans. Communications*, Vol. 49, No.9, PP. 1679-1689, Sept. 2001.

[70] M. S. O'Droma, N. Mgebrishvili, "On Quantifying the Benefits of SSPA Linearization in UMC-136 Sysstems," *IEEE Trans. Signal Processing*, Vol. 53, PP. 2470-2476, July 2005.

[71] H.-G. Ryu, Y. Sh. Li and J.-S. Park, "Nonlinear Analysis of the Phase Noise in the OFDM Communication System," *IEEE Trans. Consumer Electronics*, Vol. 50, PP. 54-63, Feb. 2004.

[72] T. Wang, Zh. Chen and K. Chen, "Effect of Selecting Antenna and Template on BER Performance in Pulsed UWB Wireless Communication Systems," *IEEE Workshop Antenna Technology: Small Antennas and Novel Metamaterials*, PP. 446-449, March 2005.

[73] Jia Li and Qingchong Liu, "PSK Communicatios Systems Using Fully Saturated Power Amplifiers," *IEEE Trans. Aerospace and Electronic Systems*, Vol. 42, PP. 464-477, April 2006.

[74] Y.-J. Tian, D. G. Haigh, "Investigation into RF Feedback for Improving the Efficiency-Linearity Trade-off in Power Amplifiers," *Conf. APMC*, PP. 449-452, Dec., 2006.

[75] Y.-J. Tian, D. G Haigh, "Optimum Design of Power Amplifier for Wireless Communications," *Thesis on Transfer*, Dec, 2007.

[76] R. Lugwig and P. Bretchko, "RF Circuit Design _ Theory and Application", *Prentice-Hall*, 2000.

[77] D. G. Haigh, D. R. Webster, R Ataei, T E Parker and J B Scott, " Issues in Nonolinear Circuit Theory and Application To High Frequency Linear Amplifier Design," *http://www.elec.mq.edu.au/cnerf/papers/pdf/ndes01.pdf*, Dec. 2001.

[78] G. A. S. Machado, "Low-power HF MicroElectronics: A Unified Approach," *The Institution of Electrical Engineering,* 1998.

[79] A. E. Parker and J. B. Scott, "A Realistic Large-Signal MESFET Mosel for SPICE," *IEEE Trans. MTT.*, Vol. 45, No.9, PP. 1563-1571, Sept. 1997.

[80] D. R. Webster, A.E.Parker, M.T.Hutabarat, D.G.Haigh and J.G.Rathmell, "Modifying the Parker Skellern MESFET SPICE Model to have Continuous Derivatives at Zero Drain Bias," *IEE Intertional Workshop on High Performance Electron Device for Microwave and Optoelectronic Applications*, Nov 1998.

[81] S. Kang, B. Choi, and B. Kim, "Linearity analysis of CMOS for RF application," *IEEE Trans. Microwave Theory and Techniques*, Vol. 51, PP. 972 − 977, March 2002.

[82] G. Passiopoulos, D.R. Webster, A.E.Parker and D.G. Haigh, "Nonlinear Common Source MESFET Behaviour and Model Validation," *IEEE Workshop High Performance Electron Device for Microwave and Optoelectronic Application*, PP. 118 −123, Nov. 1995.

[83] C. Fager, J. C. Pedro, N. B. ds Carvalho, H. Zirath, F. Fortes, and M. J. Rosaria, "A Comprehensive Analysis of IMD behaviour in RF CMOS Power Amplifiers," *IEEE Journ. Solid-State Circuits*, Vol. 39, No. 1, PP. 24-33, Jan. 2004.

[84] N. Srirattana, A. Raghavan, D. Heo, P. E. Allen, J. Laskar, "Analysis and Design of a High-Efficiency Multistage Doherty Power Amplifier for Wireless Communicatios," *IEEE. Trans. Microwave Theory and Techniques*, Vol. 53, No. 3, March, 2005.

[85] N. Moseley, R. Schiphorst and K. Slump, "The effects of nonlinear power amplifiers on the of a HIperL|AN/2 system," *IEE/EURASIP Conf. DSPenabledRadio*, Sept. 2005.

[86] S.-Y. Lee, K.-I. Jeon, Y.-S. Lee, K.-S. Lee, and Y.-H. Jeong, "The IMD Sweet Spots Varied with Gate Bias Voltages and Input Powers in RF LDMOS Power Amplifiers," *Conf. 33rd Euro. Microwave*, PP. 1353-1356, Oct. 2003.

[87] C. Fager, J. C. Pedro, N. B. and H. Zirath, "Prediction of IMD in LDMOS Transistor Amplifiers Using a New Large-Signal Model," *IEEE Trans. Microwave Theory and Techniques*, Vol. 50, No.12, PP. 2834-2842, Dec. 2002.

[88] P. J. Gonzalez, L.F.Herrant, J.A.Garcia, T.Fernandez, A.Tazon, A.Mediavilla and J.L.Garcia, "Detecting IMD Sweet Spots in LDMOS Devices through and Accurate Nonlinear Characterization," *Conf. European Microwave*, Vol. 1, PP.105-107, Oct. 2000.

[89] N. B. ds Carvalho, and J. C. Pedro, " Large- and Small- Signal IMD Behaviour of Microwave Power Amplifiers," *IEEE Trans. Microwave Theory and Techniques*, Vol. 47, No. 12, PP. 2364-2374, Dec. 1999.

[90] G. Stephenson, "Mathematical Methods for Science Students," *Pearson Prenticd Hall*, 1973.

[91] Bronshtein, Semendyayev, "A Guide Book to Mathematics," *Springer-Verlag New York Inc*, 1973.

[92] A. E. Parker and D.J.Skellern, "A realistic Large-Signal MESFET Model for SPICE", *IEEE Trans. MTT*, Vol. 45, No. 9, PP. 1563-1571, Sept. 1997.

[93] P. E. Allen, D. R. Holberg, "CMOS Analog Circuit Design," *Oxford University Press*, 2002.

[94] A. E. Parker and Guoli Qu, "Intermodulation nulling in HEMT Common Source Amplifiers," *IEEE Lett. Microwave and Wireless Component*, Vol. 11, No. 3, PP. 109 −111, March 2001.

[95] M. T. Hutabarat, D.R. Webster, D.G. Haigh, "Variation of pinch-off Modulation with Drain Bias in MESFET and HEMTs," *Electronic Letters*, Vol. 35, No. 9, PP. 755-756, April 1999.

[96] A. E. Parker and J. B. Scott, "Intermodulation Nulling in GaAs MESFETs", *IEE Electronics Letter*s, Vol. 29, No.22, PP. 1961-1962, Oct. 1993.

[97] S. A. Maas, " Nonlinear Microwave Circuits," *Artech House*, 1988.

[98] G. Passiopoulos, D.R. Webster, A.E. Parker, D.G. Haigh and I.D. Robertson, “Effect of bias and load on MESFET nonlinear characteristics,” *Electronic Letter*, Vol. 32, No. 8, PP.741 − 743, April 1996.

APPENDIX

A. Relationship between HD3 and IMD3

Single tone input signal can be described by, such as

$$v_G = \hat{v} \cdot \cos\phi, \quad \phi = \omega t \tag{A. 1}$$

Let device be described by

$$i_D = g_1 v_G + g_2 v_G^2 + g_3 v_G^3 + \cdots \tag{A. 2}$$

Then,

$$\begin{aligned} i_D &= g_1 \hat{v} \cdot \cos\phi + g_2 \hat{v}^2 \cdot \cos^2\phi + g_3 \hat{v}^3 \cdot \cos^3\phi + \cdots \\ &= g_1 \hat{v} \cdot \cos\phi + \frac{1}{2} g_2 \hat{v}^2 \cdot \left(1 + \cos 2\phi\right) + \frac{1}{4} g_3 \hat{v}^3 \cdot \left(\cos 3\phi + 3\cos\phi\right) + \cdots \\ &= \frac{1}{2} g_2 \hat{v}^2 + \left(g_1 \hat{v} + \frac{3}{4} g_3 \hat{v}^3 \right) \cos\phi + \frac{1}{2} g_2 \hat{v}^2 \cos 2\phi + \frac{1}{4} g_3 \hat{v}^3 \cos 3\phi + \cdots \end{aligned} \tag{A. 3}$$

Ratio of 3rd harmonic component to fundamental component is given by

$$\begin{aligned} R_{HD} &= \frac{1}{4} \frac{g_3 \hat{v}^3}{g_1 \hat{v} + \frac{3}{4} g_3 \hat{v}^3} \\ &= \frac{g_3 \hat{v}^2}{4 g_1 + 3 g_3 \hat{v}^2} \end{aligned} \tag{A. 4}$$

A 2-tone input signal may be described by

$$v_G = \hat{v}\left(\cos\phi_1 + \cos\phi_2\right), \quad \phi_1 = \omega_1 t, \quad \phi_2 = \omega_2 t \tag{A. 5}$$

Then drain current with two-tone input signals would become,

$$
\begin{aligned}
i_D &= g_1\hat{v}\left(\cos\phi_1+\cos\phi_2\right)+g_2\hat{v}^2\left(\cos\phi_1+\cos\phi_2\right)^2+g_3\hat{v}^3\left(\cos\phi_1+\cos\phi_2\right)^3+\cdots \\
&= g_1\hat{v}\left(\cos\phi_1+\cos\phi_2\right)+g_2\hat{v}^2\left(\cos^2\phi_1+\cos^2\phi_2+2\cos\phi_1\cos\phi_2\right) \\
&\quad g_3\hat{v}^3\left(\cos^3\phi_1+\cos^3\phi_2+3\cos^2\phi_1\cos\phi_2+3\cos^2\phi_2\cos\phi_1\right)+\cdots \\
&= \left(g_1\hat{v}+\frac{3}{4}g_3\hat{v}^3\right)\left(\cos\phi_1+\cos\phi_2\right)+\frac{1}{4}g_3\hat{v}^3\left(\cos 3\phi_1+\cos 3\phi_2\right)+ \\
&\quad \frac{1}{2}g_2\hat{v}^2\left(1+\cos 2\phi_1+1+\cos 2\phi_2\right)+g_2\hat{v}^2\left[\cos\left(\phi_1-\phi_2\right)+\cos\left(\phi_1+\phi_2\right)\right] \\
&\quad \frac{3}{4}g_3\hat{v}^3\left[\cos\left(2\phi_1-\phi_2\right)+\cos\left(2\phi_1+\phi_2\right)+\cos\left(2\phi_2-\phi_1\right)+\cos\left(2\phi_2+\phi_1\right)\right]+\cdots
\end{aligned}
\tag{A. 6}
$$

Ratio of each IMD3 sideband (*e.g.* $\cos(2\Phi_1-\Phi_2)$ term) to wanted o/p tone (*e.g.* $\cos(\Phi_1)$ term):

$$
\begin{aligned}
R_{IMD} &= \frac{1}{4}\frac{3g_3\hat{v}^3}{g_1\hat{v}+\frac{3}{4}g_3\hat{v}^3} \\
&= \frac{g_3\hat{v}^2}{4g_1+3g_3\hat{v}^2}
\end{aligned}
\tag{A. 7}
$$

B. Denormalisation OF Predicted PA Performance Metrics

B1. Device Output Current

Drain current (fundamental and 3rd harmonic) can be converted to voltage using the actual load resistance R_L and allow for the actual maximum current i_{DM}, by introducing a shift along the dBA scale for F_1 and F_3 of:

$$\Delta i_D = 20\log_{10}\left(\frac{i_{DM}R_L}{2}\right) \quad dB \tag{A. 8}$$

B2. Device Input Current

A transconductance G_{MM} corresponding to maximum v_G and i_D swings for a device may be defined as

$$G_{MM} = \frac{i_{DM}}{\left(v_{GM} - V_T\right)} \tag{A. 9}$$

In order to denormalise the input voltage scales in dBV, we may introduce a shift of,

$$\begin{aligned}\Delta v_G &= 20\log_{10}\left(\frac{v_{GM} - V_T}{2}\right) \\ &= 20\log_{10}\left(\frac{i_{DM}}{2G_{MM}}\right) \quad dB\end{aligned} \tag{A. 10}$$

B3. Gain

In order to denormalise gain, (A.8) and (A.10) can be combined to yield a shift of

$$\begin{aligned}\Delta_{Gain} &= 20\log_{10}\left(\frac{i_{GM}R_L/2}{i_{DB}/2G_{MM}}\right) \\ &= 20\log_{10}\left(R_L G_{MM}\right) \quad dB\end{aligned} \tag{A. 11}$$